

Studies on Phase Transformations in Zr-1 wt.% Nb and U-9 wt.% Mo Alloys and their Metallurgical Interaction

By

SUMAN NEOGY

ENGG01200904027

Bhabha Atomic Research Centre, Mumbai

A thesis submitted to the

Board of Studies in Engineering Sciences

In partial fulfillment of requirements

for the Degree of

DOCTOR OF PHILOSOPHY

of

HOMI BHABHA NATIONAL INSTITUTE

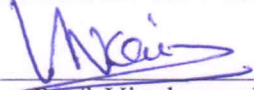


June, 2017

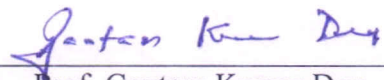
Homi Bhabha National Institute

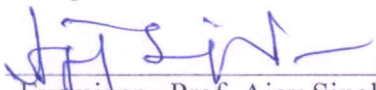
Recommendations of the Viva Voce Committee

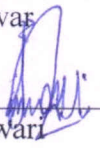
As members of the Viva Voce Committee, we certify that we have read the dissertation prepared by Suman Neogy entitled "Studies on Phase Transformations in Zr-1 wt.% Nb and U-9 wt.% Mo Alloys and their Metallurgical Interaction" and recommend that it may be accepted as fulfilling the thesis requirement for the award of Degree of Doctor of Philosophy.


Chairman - Prof. Vivekanand Kain **Date:** 12/06/2017


Guide / Convener - Prof. Dinesh Srivastava **Date:** 12/06/2017


Co-guide - Prof. Gautam Kumar Dey **Date:** 12/06/2017


Examiner - Prof. Ajay Singh Panwar **Date:** 12/06/2017


Member 1- Prof. Raghvendra Tewari **Date:** 12/06/2017


Member 2- Prof. Alok Awasthi **Date:** 12/06/2017

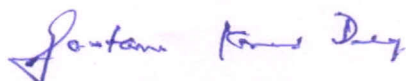

Member 3- Prof. Jung Bahadur Singh **Date:** 12/06/2017

Final approval and acceptance of this thesis is contingent upon the candidate's submission of the final copies of the thesis to HBNI.

I/We hereby certify that I/we have read this thesis prepared under my/our direction and recommend that it may be accepted as fulfilling the thesis requirement.

Date: 12/06/2017

Place: Mumbai



Co-guide



Guide

STATEMENT BY AUTHOR

This dissertation has been submitted in partial fulfillment of requirements for an advanced degree at Homi Bhabha National Institute (HBNI) and is deposited in the Library to be made available to borrowers under rules of the HBNI.

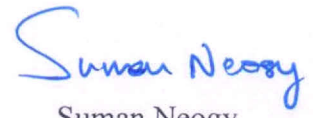
Brief quotations from this dissertation are allowable without special permission, provided that accurate acknowledgement of source is made. Requests for permission for extended quotation from or reproduction of this manuscript in whole or in part may be granted by the Competent Authority of HBNI when in his or her judgment the proposed use of the material is in the interests of scholarship. In all other instances, however, permission must be obtained from the author.



Suman Neogy

DECLARATION

I, hereby declare that the investigation presented in the thesis has been carried out by me. The work is original and has not been submitted earlier as a whole or in part for a degree / diploma at this or any other Institution / University.


Suman Neogy

List of Publications arising from the thesis

Journal

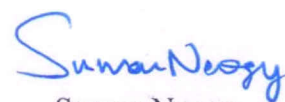
1. "A study of morphological and compositional evolution of nano-precipitates in Zr-Nb system and their transformational behavior", S. Neogy, K. V. Mani Krishna, D. Srivastava and G. K. Dey, *Philosophical Magazine*, **2011**, 91, 4447–4464.

2. "Microstructural Study of Gamma Phase Stability in U-9 wt.% Mo Alloy", S. Neogy, M. T. Saify, S. K. Jha, D. Srivastava, M. M. Hussain, G. K. Dey and R. P. Singh, *Journal of Nuclear Materials*, **2012**, 422, 77–85.

3. "Interplay of diffusion and phase transformations in microstructural evolution of the interaction zone between U-9 wt.% Mo and Zr-1 wt.% Nb alloys", S. Neogy, A. Laik, M. T. Saify, D. Srivastava, S. K. Jha and G. K. Dey, *Philosophical Magazine Letters*, **2014**, 94, 163–171.

4. "Ageing Characteristics of the Metastable Gamma Phase in U-9 wt.% Mo Alloy: Experimental Observations and Thermodynamic Validation", S. Neogy, M. T. Saify, S. K. Jha, D. Srivastava and G. K. Dey, *Philosophical Magazine*, **2015**, 95, 2866–2884.

5. "Microstructural Evolution of the Interdiffusion Zone between U-9 Wt Pct Mo Fuel Alloy and Zr-1 Wt Pct Nb Cladding Alloy Upon Annealing", S. Neogy, A. Laik, M.T. Saify, S.K. Jha, D. Srivastava, and G.K. Dey, *Metallurgical and Materials Transactions A*, **2017**, 48, 2819–2833.


Suman Neogy



Homi Bhabha National Institute

SYNOPSIS OF Ph. D. THESIS

- 1. Name of the Student: Suman Neogy**
- 2. Name of the Constituent Institution: Bhabha Atomic Research Centre**
- 3. Enrolment No. : ENGG01200904027**
- 4. Title of the Thesis: Studies on phase transformations in Zr-1 wt.% Nb and U-9 wt.% Mo alloys and their metallurgical interaction**
- 5. Board of Studies: Engineering Sciences**

SYNOPSIS

Nuclear research and test reactors are used worldwide to assess the irradiation withstanding capabilities of various in-core reactor structural materials, besides basic and applied research work. Such reactors use U-based fuels in two different forms viz., dispersion and monolithic, both of which are encapsulated in Al or Al-alloy cladding.

There are primarily two issues of concern with these research reactor fuels. First is the proliferation issue associated with the highly enriched U-fuels used in these reactors. The second issue is associated with the metallurgical interaction between the fuel material and the Al or Al-alloy matrix/cladding, both during fabrication and in-reactor operation, resulting in generation of phases which degrade fuel performance [1,2].

The first issue calls for the development of alternative high U-density reduced enrichment fuels ($U^{235} < 20$ wt.%) to keep the effective concentration of the fissile U^{235} isotope same [3,4]. Body centered cubic (bcc) γ -phase stabilized U–Mo alloys with Mo in the range of 8 to 10 wt.% have shown considerable prospect in this regard [1,5-7]. As far as the second issue is concerned, addition of a diffusion barrier element, like Zr, either by directly alloying in the fuel, in case of

dispersion fuel geometry, or as a liner between the fuel and the clad, in case of monolithic fuel geometry, has been envisaged to mitigate the fuel and Al/Al-alloy interaction [8].

In this backdrop, the present research work is focused on evaluating two binary alloys, viz., U–9 wt.% Mo and Zr–1 wt.% Nb as research reactor monolithic fuel and clad, respectively. The envision of Zr–1Nb alloy, a power reactor fuel cladding alloy [9-11], over the currently used Al/Al-alloy cladding will eliminate the need for a separate liner material, and hence additional fuel–liner and liner–clad interactions, with Zr being the major constituent of the alloy.

In nuclear research reactors frequent shut-downs and ramping in power during operation can lead to rapid rise and fall of temperatures in the fuel assemblies. This can not only alter the initial microstructural features of the fuel or the fuel cladding, but also introduce undesirable metastable phase(s) in the microstructures. In this work, therefore, the microstructural stabilities of Zr–1Nb and U–9Mo alloys have been investigated. In doing so, phase transformations in these alloys have been explored under thermal conditions which emulate the above-mentioned off-normal reactor operating scenarios.

The desired microstructure of Zr–1Nb alloy for cladding application constitutes a two-phase ($\alpha + \beta$) structure with the bcc β -phase present in form of precipitates in a recrystallized hexagonal closed packed (hcp) α -Zr matrix [12-16]. The morphological and compositional evolutions of this Nb-rich β -phase have been investigated in this alloy. In addition, under rapid cooling the athermal transformation of the β -phase to hcp martensite (α') and/or hexagonal omega (ω) metastable phases has been explored depending on its composition and size [17,18].

The irradiation stability of γ -phase stabilized U–Mo alloys is linked to their ability to retain the γ -phase in metastable equilibrium at the reactor operating temperature. Thus, in U–9Mo alloy the stability of the γ -phase has been assessed in different as-processed conditions of the alloy and also under isothermal ageing. The decomposition of the γ -phase occurs eutectoidally forming the orthorhombic α -U and the tetragonal γ' (U_2Mo) phases [19]. Attempts have been made as well to decipher the pathway of this decomposition.

In addition to microstructural modifications, a rise in the temperature of the fuel assemblies can enhance the interaction between the fuel and the clad. Thus, the metallurgical interaction and the microstructural evolution at the interdiffusion zone between Zr–1Nb and

U–9Mo alloys have been evaluated. The effect of in-reactor temperature excursion on the stability of the interdiffusion zone has also been investigated.

In all, the objectives of this dissertation are to investigate:

- (i) Morphological and compositional evolution of β -phase in Zr–1Nb alloy as a function of temperature and time in the $(\alpha + \beta_{Zr})$ phase field and feasibility of metastable phase transformations, like the martensitic and omega, in β -phase of different length scales.
- (ii) Stability of the γ -phase in U–9Mo alloy under various conditions of thermomechanical treatments and examination of the factors affecting it.
- (iii) Mechanism of decomposition of the metastable γ -phase into the α -U and γ' phases in U–9Mo alloy from its ageing characteristics.
- (iv) Metallurgical interaction between U–9Mo and Zr–1Nb alloys by means of solid-state diffusion bonding.
- (v) Stability of the interdiffusion zone formed between U–9Mo and Zr–1Nb alloys under different annealing conditions.

All the results have been presented in form of separate chapters in the thesis. As a whole, the thesis comprises of nine chapters. Chapter 1 defines the issues to be addressed under this research work and details out the scope of the investigations undertaken therein. Chapter 2 is focused on literature review of alloy systems dealt with in the present work and also on the nature of studies performed in these systems. All experimental details are presented in chapter 3. The experimental findings and their analyses towards realizing each of the outlined research objectives have been discussed independently in chapters 4 to 8, gist of which are given below paragraph wise. The salient outcomes of the entire research work are summarized collectively in chapter 9.

In Zr–1Nb alloy, the β -phase present in the starting microstructure in form of spherical β_{Nb} -precipitates was found to evolve both morphologically and compositionally during heat treatment in the $(\alpha + \beta_{Zr})$ phase-field above the monotectoid temperature. This evolution of the β -phase was driven by a need to reduce its Nb-content accompanied by a corresponding increase in the volume fraction. The reduction in the Nb-content of the β_{Nb} -precipitates ultimately led to their dissolution into the α -phase matrix which, in turn, prompted the nucleation of fresh β -phase in form of intergranular patches and intragranular precipitates (Figure 1a). The nucleated β -precipitates exhibited a needle-shaped morphology which could be attributed to their growth

following the invariant line strain (ILS) criteria. The morphological changes in the β -phase were found to be associated with the attainment of intermediate metastable compositions (higher than equilibrium) during the initial stages of heat treatments at higher temperatures. This was rationalized thermodynamically on the basis of maximization of driving force for nucleation using free energy–composition (G–X) diagrams. In the course of quenching of the alloy after the heat treatment, metastable phase transformations, like martensitic or omega, within the β -needles, as compared to patches, were found to be governed by their sizes besides the composition of the β -phase (Figure 1b). Thermodynamics and micromechanical modeling established the dominant role of interfacial energy behind it. In addition, the modeling could predict the requirement of a critical dimension of nearly 150 nm in all the directions of a β -precipitate to allow the martensitic transformation at the maximum possible undercooling, which was in close agreement with the experimental findings. The omega transformation, in comparison to martensitic, showed less dependency on the size of the β -phase.

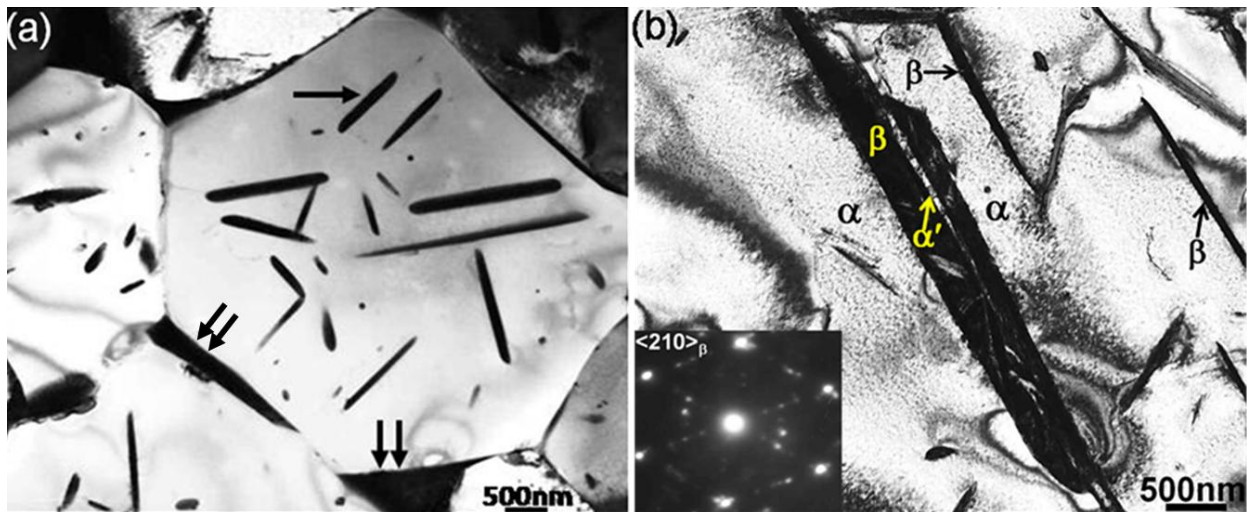


Figure 1 (a) A typical bright-field TEM micrograph representing the microstructures of samples heat treated at 800 °C for different durations. Single and double arrows indicate the needle and patch morphologies of the β -phase, respectively. (b) Bright-field TEM micrograph showing the formation of acicular α' -plates (marked by an arrow) within an elongated β -precipitate, having comparatively larger dimensions with respect to other precipitates, present in the sample heat treated at 832 °C for 5 mins. The SAED pattern (Zone Axis = $\langle 210 \rangle_{\beta}$) obtained from this precipitate (given as inset) shows the simultaneous occurrence of ω -phase within it.

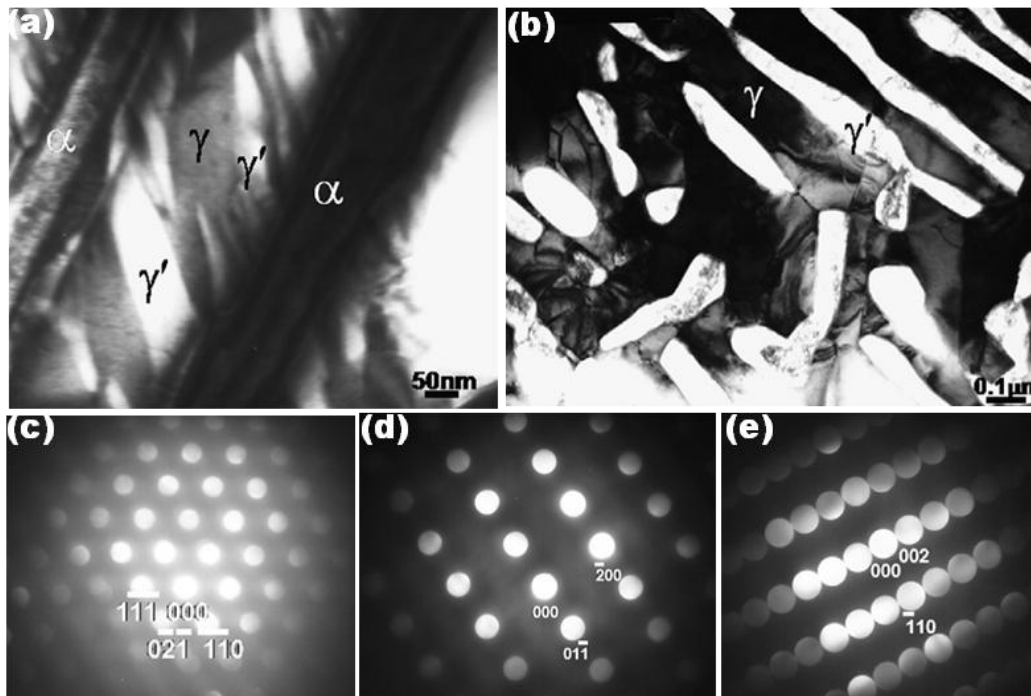


Figure 2 (a) A typical bright-field TEM micrograph showing the occasional presence of the γ' -phase in the γ -interlamellar region between α -phase lamellae in partially decomposed ($\gamma + \alpha$) colony. (b) A typical bright-field TEM micrograph showing the partially decomposed ($\gamma + \gamma'$) colony comprising of γ' -phase lamellae and γ -interlamellar regions. (c-e) Typical microdiffraction patterns of α (Zone Axis = $[\bar{1}\bar{1}\bar{2}]$), γ (Zone Axis = $[011]$) and γ' (Zone Axis = $[110]$) phases, respectively.

In U-9Mo alloy the γ -phase was found to be retained in a metastable state in the as-cast condition by suppressing the equilibrium eutectoid decomposition to α - and γ' - phases. The decomposition of the γ -phase did not occur even in furnace cooled samples after homogenization at 1000 °C for 24 h. The decomposition of the metastable γ -phase could only be set in by ageing and was found to depend on the grain size. A larger grain size in the homogenized samples resulted in lesser decomposition in comparison to the fine-grained as-rolled material. The extent of the decomposition reaction was again found to depend on the temperature of ageing. Microstructural characterization of the aged samples revealed the decomposition characteristics of the γ -phase. Partially transformed cellular colonies, comprising of either the α -phase or the γ' -phase as lamellae and a compositionally different γ -phase as interlamellar region, was observed on carrying out ageing below the eutectoid temperature (Figure 2). In addition to this, γ' -phase was

found to be present occasionally between α -phase lamellae in $(\gamma + \alpha)$ colonies. Development of $(\alpha + \gamma')$ lamellar colonies was noticed upon prolonged ageing. Discontinuous coarsening of the lamellar colonies to some extent has occurred in all the aged samples. Ageing above the eutectoid temperature resulted in a non-lamellar $(\alpha + \gamma)$ structure, wherein α -phase needles were found to be distributed within the γ -matrix.

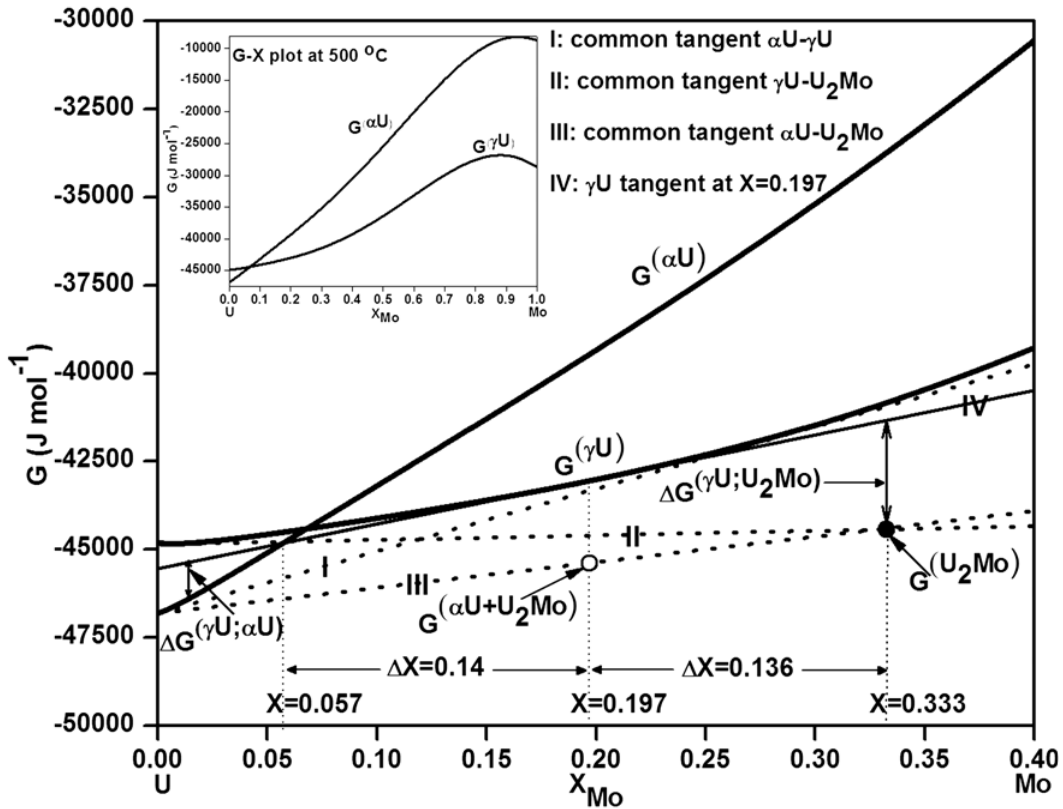


Figure 3 Free energy–composition diagram at 500 °C showing the variation of free energies of α -U and γ -U phases as a function of Mo-content in U–Mo system. The inset shows the same diagram for the entire U–Mo composition range. The free energy of the stoichiometric γ' (U_2Mo) phase of 33.3 at.% Mo is marked in the diagram by the filled circle.

The mechanism of decomposition of the γ -phase in U–9Mo alloy was delineated from its ageing characteristics by invoking a thermodynamic assessment of the U–Mo system at the different ageing temperatures. In doing so, free energy–composition (G–X) diagrams constructed using the regular solution thermodynamics model were employed (Figure 3). The correlation existing between the decomposed γ -phase fraction and the ageing temperature could be explained based on G–X diagrams. A reduction in the decomposed fraction at 565 °C, as compared to 500 °C, could be related to the extent of Mo-segregation required in the γ -matrix for

the nucleation of α - and γ' - phases and the chemical free energy change associated with their nucleation. The same thermodynamic analyses could also corroborate the occurrences of partially transformed ($\gamma + \gamma'$) and ($\alpha + \gamma$) cellular colonies in the microstructures of 500 °C and 565 °C aged samples. A discontinuous precipitation (or cellular) reaction was found to operative as opposed to a pearlitic-type of decomposition of the γ -phase to ($\alpha + \gamma'$) lamellar colonies. This was followed by an in-situ transformation of the γ -interlamellar regions to α - and γ' - phases in ($\gamma + \gamma'$) and ($\alpha + \gamma$) colonies, respectively, resulting in the development of ($\alpha + \gamma'$) lamellar colonies. Such a transformation was driven by reduction in free energy on forming an equilibrium mixture of α - and γ' - phases. Discontinuous coarsening of the colonies was prompted by reduction of both the interfacial free energy and the supersaturation remaining in the lamellar decomposition products. In the 575 °C aged sample, the needle-like morphology of the α -phase, which exhibits an orientation relationship with the γ -matrix, was attributed to the strain energy minimization.

Out-of-pile diffusion bonding studies are usually carried out to assess the interaction and the mechanism of evolution of the interdiffusion zone developing at the interfaces of fuel and cladding materials while in contact [20-23]. Thus, the metallurgical interaction between U-9Mo and Zr-1Nb alloys has been assessed by forming solid-to-solid interdiffusion couple. The interdiffusion of the constituent elements of these alloys during diffusion bonding at 800 °C led to the development of a layered interdiffusion zone at the joint interface (Figure 4). The expected “down-the-gradient” concentration profiles of U, Mo and Zr across the bonded interface got modified near the U-9Mo side of the couple (region-A) due to the formation of Mo_2Zr spheroids in the γ -U(Mo,Zr) matrix. The depletion of Mo and Zr on account of the formation of the Mo_2Zr phase promoted instability in the γ -U(Mo,Zr) matrix, and got it partially transformed to α -U phase during the cooling of the couple. Decomposition of the γ -U(Mo,Zr) phase to α -U and α -Zr phases was also noticed in this part of the interdiffusion zone. A two-phase ($\alpha + \beta$)-Zr layer in Widmanstatten morphology was formed near the Zr-1Nb side of the interdiffusion zone (region-C). The in-between region of the interdiffusion zone was found to exist as a single bcc solid solution phase (region-B). The presence of 1 wt.% of Nb in the cladding alloy was found to have an insignificant influence on the microstructural evolution of the interdiffusion zone, emphasizing the advantage of having Zr-1Nb alloy as clad.

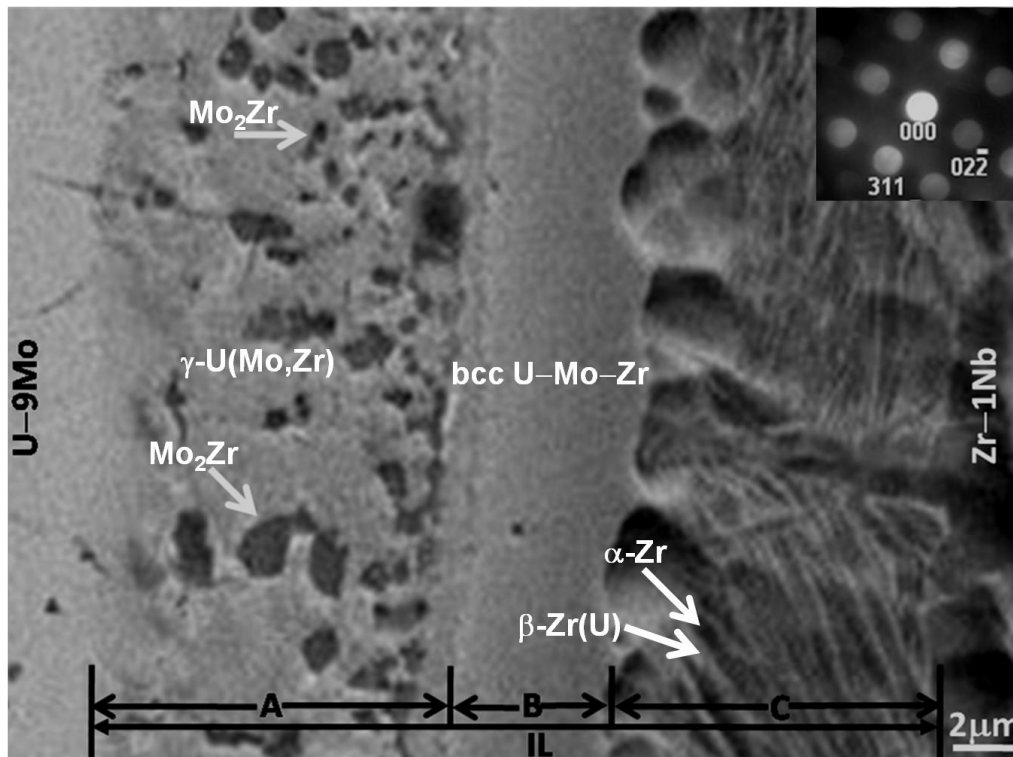


Figure 4 Back scattered electron image of the interaction layer formed between U-9Mo and Zr-1Nb alloys during the diffusion bonding operation at 800 °C. The interaction layer could be divided into three distinct regions as marked by A, B and C in the figure. The inset shows a microdiffraction pattern corresponding to the Mo₂Zr phase.

Annealing studies were performed to investigate the stability of the interdiffusion zone, formed between U-9Mo and Zr-1Nb alloys during the diffusion bonding operation, in terms of further growth and plausible microstructural modifications. Annealing heat treatments increased the width of the as-bonded interdiffusion zone preserving its layered-type microstructural features (Figure 5). On annealing the as-bonded couple at 800 °C, 900 °C and 1000 °C, the Mo₂Zr phase was found to evolve in form of a continuous layer and also in a ‘massive’ morphology. A discontinuous precipitation reaction in the matrix adjoining the Mo₂Zr phase, instigated by Mo-depletion, led to the formation of lamellar α -U phase within the γ -U(Mo,Zr) matrix. Precipitation of α -Zr(U) phase in U-Mo-Zr matrix was observed towards the U-9Mo side end of the interdiffusion zone. The morphology of the α -Zr(U) precipitates changed from thin needle-like to voluminous particulates with the increase in the annealing temperature. A two-phase ($\alpha + \beta$)-Zr layer formed near the Zr-1Nb side of the interdiffusion zone in the as-bonded couple became much wider during annealing, engulfing most of the Zr-1Nb base material, and

exhibited a “basket weave” microstructure with α -Zr laths and β -Zr(Nb,U) interlath regions. A β - to ω - transformation was also observed within the interlath regions. The mid-section of the interdiffusion zone was found to exist as a single bcc solid solution phase even in the annealed samples. The growth rate of the interdiffusion zone was found to be orders of magnitude lower in comparison of the growth rates in diffusion couples formed between compositionally similar U–10 wt.% Mo and Al or Al–Si cladding alloys, thus establishing a lower U–9Mo/Zr–1Nb interaction.

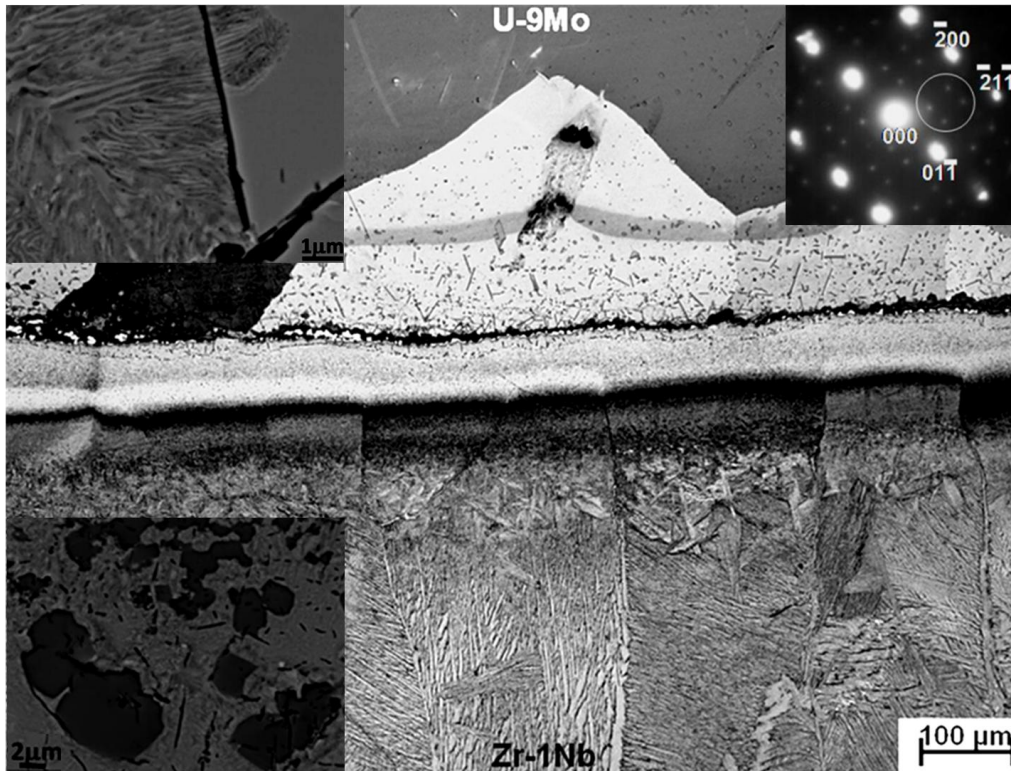


Figure 5 A typical optical microscopy image representing the overall microstructural features of the interdiffusion zones of all the annealed U–9Mo/Zr–1Nb bonded samples. The top-left inset depicts the lamellar region present adjacent to Mo_2Zr phase (shown in bottom inset), whereas, the SAED pattern of the top-right inset shows the superimposition of omega-type reflections (encircled) with reflections of the β -Zr interlath regions of the “basket weave” microstructure.

Conclusions

The β -phase in Zr–1Nb alloy forms as Nb-rich precipitates below 610 °C. This β -phase changed its morphology, along with composition, to needle-shaped precipitates and grain boundary patches above 610 °C. Further, the morphologically and compositionally evolved β -phase upon water quenching transformed athermally to α' and/or ω metastable phases depending on the

composition and size. The binary U–Mo system shows a eutectoid decomposition of the γ -phase to α - and γ' - phases below ~ 570 °C. However, the γ -phase in U–9Mo alloy did not exhibit this reaction even under the slowest cooling rate (furnace cooling) used in the present study. This metastable γ -phase upon ageing at 500 °C and above decomposed into α - and γ' - phases through the mechanism of discontinuous precipitation (or cellular) reaction. The metallurgical interactions of these alloys in the temperature range of 800 °C to 1000 °C resulted in the formation of a layered interdiffusion zone comprising of multiple phases at the interface. All these salient findings have been summarized schematically in Figure 6.

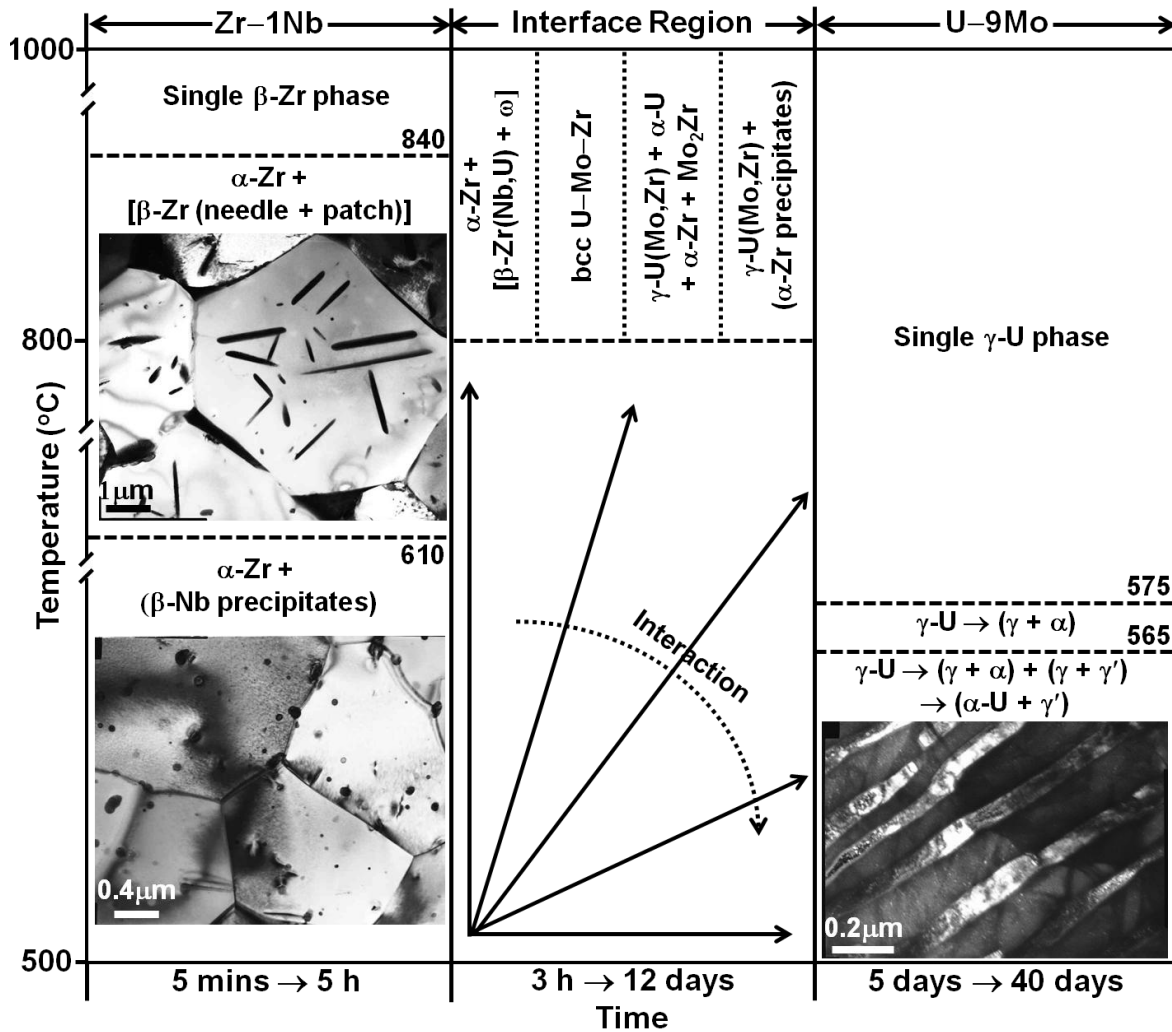


Figure 6 A schematic representations of different reaction sequences exhibited by Zr–1Nb and U–9Mo alloys over different temperature ranges, and their metallurgical interaction, in the present work. The β -Zr needle/patch in the Zr–1Nb alloy would transform to α' - and/or ω - metastable phases depending on the composition and size.

This study could throw important light on the behavior of these alloys during reactor operations, particularly during the off-normal scenarios of temperature excursions and rapid cooling. The formation of α' and/or ω metastable phases in the Zr–1Nb alloy in situations of temperature excursions followed by rapid cooling can cause mechanical instability in the alloy. In the case of U–9Mo alloy temperature excursions alone would not have much of an effect as appreciable time would be required to have a reasonable decomposition fraction of the γ -phase. In respect of the metallurgical interactions between Zr–1Nb and U–9Mo alloys, the phases generated at the interface, being stable under irradiation [24], would not degrade the performance of the fuel.

References

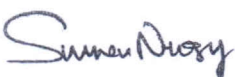
- [1] “Development status of metallic, dispersion and non-oxide advanced and alternative fuels for power and research reactors”, *IAEA-TECDOC-1374*, International Atomic Energy Agency, Vienna, **2003**.
- [2] “Interdiffusion between Zr diffusion barrier and U–Mo alloy”, K. Huang, Y. Park, D. D. Keiser Jr. and Y. H. Sohn, *J. Phase Equilib. Diffus.*, **2012**, *33*, 443-449.
- [3] “Limiting the use of highly enriched uranium in domestically licensed research and test reactors”, *U. S. Nuclear Regulatory Commission 10 CFR Part 50, Federal Register (Rules and Regulations)*, **1986**, *51 (37)*. Available at <http://www.nrc.gov/REFDOCS/NRCRULE.pdf>
- [4] “Development of very-high-density low-enriched-uranium fuels”, J. L. Snelgrove, G. L. Hofman, M. K. Meyer, C. L. Trybus and T. C. Wiencek, *Nucl. Eng. Des.*, **1997**, *178*, 119-126.
- [5] “Low-temperature irradiation behavior of uranium–molybdenum alloy dispersion fuel”, M. K. Meyer, G. L. Hofman, S. L. Hayes, C. R. Clark, T. C. Wiencek, J. L. Snelgrove, R. V. Strain and K. H. Kim, *J. Nucl. Mater.*, **2002**, *304*, 221-236.
- [6] “Development of Uranium-Silicide and U–Mo alloy fuels by centrifugal atomization, Studies on Fuels with Low Fission Gas Release”, K. Kim, D. B. Lee, C. K. Kim, I. H. Kuk and K. W. Baek, *IAEA-TECDOC-970*, Vienna, **1997**, 77-86. Available at http://www-pub.iaea.org/MTCD/publications/PDF/te_970_prn.pdf
- [7] “Neutron diffraction study of U–10 wt.% Mo alloy”, B. S. Seong, C. H. Lee, J. S. Lee, H. S. Shim, J. H. Lee, K. H. Kim, C. K. Kim and V. Em, *J. Nucl. Mater.*, **2000**, *277*, 274-279.

- [8] “Irradiation performance of U–Mo–Ti and U–Mo–Zr dispersion fuels in Al–Si matrixes”, Y. S. Kim, G. L. Hofman, A. B. Robinson, D. M. Wachs, H. J. Ryu, J. M. Park and J. H. Yang, *J. Nucl. Mater.*, **2012**, 427, 233-238.
- [9] “Development of a Cladding Alloy for High Burnup”, G. P. Sabol, G. R. Kilp, M. G. Balfour and E. Roberts, *ASTM STP 1023*, Zirconium in the Nuclear Industry: Eighth International Symposium, L. F. P. Van Swam and C. M. Eucken (Eds.), ASTM, Philadelphia, PA, **1989**, 227-244.
- [10] “Improved PWR Fuel Cladding”, G. P. Sabol, G. Schoenberger and M. G. Balfour, *IAEA-TECDOC-665*, Proceedings of IAEA Technical Committee Meeting on Materials for Advanced Water Cooled Reactors, International Atomic Energy Agency, Vienna, **1992**.
- [11] “Zirconium alloys in nuclear applications”, C. Lemaignan and A. T. Motta, *Nuclear Materials II, Materials Science and Technology, A Comprehensive Treatment, 10B*, in: R. W. Cahn, P. Hassen and E. J. Kramer (Eds.), VCH, **1994**, 1-51.
- [12] “Corrosion and microstructural characteristics of Zr–Nb alloys with different Nb contents”, H. G. Kim, S. Y. Park, M. H. Lee, Y. H. Jeong and S. D. Kim, *J. Nucl. Mater.*, **2008**, 373, 429-432.
- [13] “Effect of isothermal annealing on the corrosion behavior of Zr–xNb alloys”, H. G. Kim, Y. H. Jeong and T. H. Kim, *J. Nucl. Mater.*, **2004**, 326, 125-131.
- [14] “Correlation between microstructure and corrosion behavior of Zr–Nb binary alloy”, Y. H. Jeong, K. O. Lee and H. G. Kim, *J. Nucl. Mater.*, **2002**, 302, 9-19.
- [15] “Corrosion behavior of Zr alloys with a high Nb content”, J. Y. Park, B. K. Choi, Y. H. Jeong and Y. H. Jung, *J. Nucl. Mater.*, **2005**, 340, 237-246.
- [16] “Effect of β phase, precipitate and Nb-concentration in matrix on corrosion and oxide characteristics of Zr–xNb alloys”, Y. H. Jeong, H. G. Kim and T. H. Kim, *J. Nucl. Mater.*, **2003**, 317, 1-12.
- [17] “Transformations in zirconium-niobium alloys”, R. F. Hehemann, *Can. Metall. Q.*, **1972**, 11, 201-211.
- [18] S. Banerjee and P. Mukhopadhyay, *Phase transformations: examples from titanium and zirconium alloys*, Pergamon Press, Oxford, **2004**.
- [19] T. B. Massalski, H. Okamoto, P. R. Subramanian and L. Kacprzak, *Binary Alloy Phase Diagrams*, 2nd ed., ASM International, Materials Park, OH, **1990**.

- [20] “Characterization of the reaction layer in U–7wt%Mo/Al diffusion couples”, M. I. Mirandou, S. N. Balart, M. Ortiz and M. S. Granovsky, *J. Nucl. Mater.*, **2003**, 323, 29-35.
- [21] “Phase Constituents and Microstructure of Interaction Layer Formed in U-Mo Alloys vs Al Diffusion Couples Annealed at 873 K (600 °C)”, E. Perez, D. D. Keiser Jr. and Y. H. Sohn, *Metall. Mater. Trans. A*, **2011**, 42, 3071-3083.
- [22] “Selected Observations in Phase Constituents, Growth Kinetics and Microstructural Development of Aluminides in U-Mo vs. Al and 6061 Diffusion Couples Annealed at 600 °C”, E. Perez, D. D. Keiser and Y. H. Sohn, *Defect Diffus. Forum*, **2009**, 289-292, 41-49.
- [23] “Characterization of the interaction layer grown by interdiffusion between U–7wt%Mo and Al A356 alloy at 550 and 340 °C”, M. Mirandou, S. Aricó, M. Rosenbusch, M. Ortiz, S. Balart and L. Gribaudo, *J. Nucl. Mater.*, **2009**, 384, 268-273.
- [24] “US RERTR Fuel Development Post-Irradiation Examination Results”, A. B. Robinson, D. M. Wachs, D. E. Burkes and D. D. Keiser, *Proceedings of the 30th International Meeting on RERTR-2008*, Report No. INL/CON-08-14916 (Preprint), **2008**. Available at <http://www.inl.gov/technicalpublications/Documents/4282340.pdf>

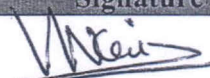
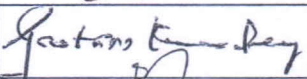
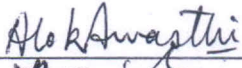
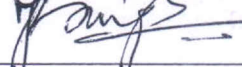
Publications in Refereed Journal:

- [1] "A study of morphological and compositional evolution of nano-precipitates in Zr-Nb system and their transformational behavior", S. Neogy, K. V. Mani Krishna, D. Srivastava and G. K. Dey, *Philos. Mag.*, **2011**, *91*, 4447-4464.
- [2] "Microstructural Study of Gamma Phase Stability in U-9 wt.% Mo Alloy", S. Neogy, M. T. Saify, S. K. Jha, D. Srivastava, M. M. Hussain, G. K. Dey and R. P. Singh, *J. Nucl. Mater.*, **2012**, *422*, 77-85.
- [3] "Interplay of diffusion and phase transformations in microstructural evolution of the interaction zone between U-9 wt.% Mo and Zr-1 wt.% Nb alloys", S. Neogy, A. Laik, M. T. Saify, D. Srivastava, S. K. Jha and G. K. Dey, *Phil. Mag. Lett.*, **2014**, *94*, 163-171.
- [4] "Ageing characteristics of the metastable gamma phase in U-9 wt.% Mo alloy: Experimental observations and thermodynamic validation", S. Neogy, M. T. Saify, S. K. Jha, D. Srivastava and G. K. Dey, *Philos. Mag.*, **2015**, *95*, 2866-2884.

Signature of Student: 

Date: 01/08/2016

Doctoral Committee:

S. No.	Name	Designation	Signature	Date
1.	Dr. V. Kain	Chairman		1-8-2016
2.	Dr. D. Srivastava	Guide/ Convener		1-8-2016
3.	Dr. G. K. Dey	Co-guide (if any)		1/8/16
4.	Dr. R. Tewari	Member		01/08/2016
5.	Dr. A. Awasthi	Member		01/08/2016
6.	Dr. J. B. Singh	Member		01/08/2016

Contents

	Page
Abstract	iv
List of Figures	vi
List of Tables	xx
List of Abbreviations	xxii
Chapter 1 Introduction	1
1.1 Background	1
1.2 Motivation	2
1.3 Objectives	3
1.4 Structure of the thesis	4
Chapter 2 Literature Review	5
2.1 Development of Zr–Nb alloy as cladding material	5
2.2 Phase transformations exhibited by the binary Zr–Nb system	6
2.2.1 A brief review on martensitic phase transformation	9
2.2.1.1 Driving force for martensitic transformation	9
2.2.1.2 Phenomenological theory of martensite crystallography (PTMC)	11
2.2.1.3 Martensite morphology and substructure	14
2.2.1.4 Self accommodating morphologies of martensites	17
2.2.2 A brief review on omega phase transformation	18
2.2.2.1 Characteristics	18
2.2.2.2 Thermally induced omega phase formation	18
2.2.2.3 Crystallographic basis of $\beta \rightarrow \omega$ transformation	19
2.3 Martensitic and Omega phase transformations in nano-dimension	24
2.4 Development of U–Mo alloy as nuclear research and test reactor fuel	25
2.5 Phase transformations exhibited by the binary U–Mo system	27
2.5.1 Decomposition aspects of the metastable γ -phase in binary U–Mo	30

	Alloys	
	2.6 Fuel-clad chemical interaction issues with γ -phase U–Mo alloys and its mitigation	32
	2.7 Thermodynamic assessment of binary systems employing free energy-composition (G–X) diagrams	37
	2.8 Compatibility study of dissimilar materials – Diffusion bonding	39
Chapter 3	Experimental methodology	42
	3.1 Sample details	42
	3.1.1 Zr–1 wt.% Nb alloy	42
	3.1.2 U–9 wt.% Mo alloy	43
	3.2 Diffusion bonding of Zr–1Nb and U–9Mo alloys	43
	3.3 Heat treatments	43
	3.4 Sample preparation	44
	3.4.1 Metallography	44
	3.4.2 Sample preparation for transmission electron microscopy	45
	3.5 Characterization techniques	45
Chapter 4	Microstructural and phase transformation aspects of Zr–1Nb alloy	47
	4.1 Background	47
	4.2 Experimental observations	49
	4.2.1 Morphological evolution of the β -phase	49
	4.2.2 Transformations within the β -phase	55
	4.3 Discussion	63
	4.3.1 Chemical and morphological evolution of the β -phase	63
	4.3.2 Size dependency of β -phase transformations	72
	4.4 Summary	76
Chapter 5	Study on γ-phase stability in U–9Mo alloy	78
	5.1 Background	78
	5.2 Experimental observations	79
	5.3 Discussion	106
	5.4 Summary	110

Chapter 6	Decomposition pathway of the metastable γ-phase in U–9Mo alloy	112
	6.1 Background	112
	6.2 Thermodynamic evaluation of γ -phase decomposition	113
	6.3 Discussion	120
	6.4 Summary	124
Chapter 7	Interaction between U–9Mo fuel alloy and Zr–1Nb cladding alloy	126
	7.1 Background	126
	7.2 Experimental observations	127
	7.3 Discussion	135
	7.4 Summary	137
Chapter 8	Assessment of U–9Mo/Zr–1Nb interdiffusion zone stability	139
	8.1 Background	139
	8.2 Experimental observations	139
	8.3 Discussion	165
	8.3.1 Morphological evolution of the Mo ₂ Zr phase	166
	8.3.2 Genesis of the lamellar ‘halo’ structure	167
	8.3.3 Evolution of the “basket weave” microstructural zone	169
	8.3.4 Precipitation of the Zr-rich phase in the U–9Mo side of the interdiffusion zone	171
	8.3.5 Growth rate of the interdiffusion zone	174
	8.4 Summary	178
Chapter 9	Conclusions	180
	References	185
	APPENDIX-I (Binary equilibrium phase diagrams)	209
	APPENDIX-II (Free energy (G)–Composition (X) diagrams)	228
	Scope of further work	231

Abstract

Solid-state phase transformation studies in Zr–1 wt.% Nb and U–9 wt.% Mo alloys, proposed to be used as clad and fuel materials, respectively, in nuclear research reactors have formed the basis of the present research work. Phase transformation aspects of these alloys under conditions similar to off-normal conditions of reactor operation, like temperature excursions, rapid cooling, have been assessed. In doing so, the relevant temperature domains over which these alloys are expected to show phase transitions have been considered. In addition, metallurgical interaction of these alloys has been investigated, as fuel and clad are likely to interact both during fuel-plate fabrication and in-reactor operation.

The microstructure of the Zr–1Nb alloy comprising of a uniform distribution of Nb-rich β_{Nb} second phase precipitates in a recrystallized α -Zr matrix, desirable for optimum in-reactor performance, underwent considerable modifications on heat treating the alloy in the $(\alpha + \beta_{\text{Zr}})$ phase-field. The spherical second phase precipitates were found to be gradually replaced with needle-like precipitates of the β_{Zr} -phase, accompanied by formation of β_{Zr} -patches at the α/α grain boundaries and tri-junctions, with the increase in heat treatment temperature and time. The chemical composition of the β_{Zr} - needles and patches showed a time-dependent evolution suggesting preference towards metastable compositions with Nb higher than the equilibrium value during the early stages of heat treatment. This was rationalized thermodynamically using free energy–composition diagrams. The β_{Zr} - needles and patches depending on composition showed martensitic and/or omega metastable phase transformations on rapid cooling of the alloy from the heat treatment temperature. In the case of β_{Zr} - needles, size of the needles was found to dictate the occurrences of these transformations over and above the needle composition. Micromechanical modeling was done to estimate the critical size of β -phase required to induce martensitic transformation and the model predictions were found to be in close agreement with the experimental observations. Omega transformation, in contrast, showed less size-dependency.

In the case of U-based metallic fuel alloys stabilization of the high temperature γ -U phase at temperatures in the vicinity of reactor operating temperature bears immense significance due to the stability of the γ -U phase under irradiation. Thus, in the present work, stability of the γ -

phase has been examined in U–9Mo alloy under different microstructural conditions. The γ -phase was found to be retained even under very slow conditions of cooling without decomposing into the α -U and γ' (U_2Mo) phases eutectoidally. The decomposition of the metastable γ -phase on isothermal holding was assessed through ageing of the alloy in the ($\alpha + \gamma'$) and ($\alpha + \gamma$) phase-fields. It was observed that homogenization of the alloy at 1000 °C for 24 h increased the stability of the γ -phase against decomposition. Analyses of the aged microstructures revealed the decomposition mechanism of the γ -phase to α -U and γ' phases. A discontinuous precipitation reaction led to the formation of partially transformed cellular colonies with lamellae of either the α -phase or the γ' -phase in γ -phase matrix. This was followed by “in-situ transformation” of the γ -interlamellar regions to α - and γ' - phases in ($\gamma + \gamma'$) and ($\alpha + \gamma$) colonies, respectively. This decomposition pathway was explained on the basis of extent of Mo-segregation and the driving force required for the nucleation of α - and γ' - phases in the γ -matrix using free energy–composition diagrams.

The metallurgical interaction between U–9Mo and Zr–1Nb alloys has been assessed through diffusion bonding. Interdiffusion of the constituent elements of these alloys resulted in the development of a layered interdiffusion zone. The as-bonded couple was further annealed at different temperatures to investigate the microstructural stability of this zone. Annealing operation led to an increase in the width of the interdiffusion zone preserving its layered-type microstructural features. The diffusion reaction in the U-rich part of the interdiffusion zone during the bonding operation was dominated by the formation of the Mo_2Zr phase in the γ -U(Mo,Zr) matrix. α -U and α -Zr phases were also found to be present in the same matrix arising out of the phase separation of the γ -U(Mo,Zr) phase. The Mo_2Zr phase present as dispersoids in the as-bonded couple was found to evolve in form of a continuous layer and also in a ‘massive’ morphology in all the annealed couples. Precipitates of α -Zr(U) phase in U–Mo–Zr matrix was observed in the U–9Mo side end of the interdiffusion zone in all the annealed couples. The Zr–1Nb side end of the interdiffusion zone was characterized by the presence of a two-phase ($\alpha + \beta$)-Zr layer. The growth rate of the interdiffusion zone was found to be orders of magnitude lower in comparison of growth rates in diffusion couples formed between compositionally similar U–10 wt.% Mo and Al or Al–Si cladding alloys, thus establishing a lower U–9Mo/Zr–1Nb interaction.

List of Figures

	Page No.
2.1 (a) Schematic equilibrium phase diagram of binary Zr–Nb system (marked by solid lines). Superimposed metastable phase boundaries have also been shown by broken lines. (b) Schematic free energy curves for the α -, ω - and the β - phases [23].	8
2.2 Schematic diagram showing the free energy change for a martensitic transformation.	10
2.3 Atomistic representation of the bcc \rightarrow hcp transformation on the matching $(0002)_M/(110)_b$ planes, with the corresponding two-dimensional shape change given by the circle to ellipse transformation, before (a), (b), and after (c), (d) the rigid body rotation required to produce an invariant line [59].	13
2.4 A bright-field TEM micrograph showing the mutually twin-related three variant lath martensite grouping in Zr–1Nb alloy water-quenched from the high temperature β -phase field. The three lath variants are marked as 1, 2 and 3 in the figure. The inset shows a typical twin related SAED pattern corresponding to 1-2, 2-3 and 3-1 lath-lath interfaces. The SAED pattern resembled $\{1\bar{1}01\}_\alpha$ type twinning [45].	15
2.5 Bright-field TEM micrograph showing the typical morphology of plate martensite in a Zr–2.5Nb alloy water-quenched from the high temperature β -phase field [56].	16
2.6 Bright-field TEM micrograph showing internally twinned plate martensites in a Zr–2.5Nb alloy water-quenched from the high temperature β -phase field [56].	16
2.7 A bright-field TEM micrograph showing the presence of large number of self-accommodating mutually twin-related three variant martensite plate clusters of “indentation morphology” in Zr–2.5Nb alloy water-quenched from the high temperature β -phase field [56]. The three plate variants are marked as 1, 2 and 3 in the figure.	17

- 2.8 (a) Geometrical relations between the hexagonal representation of the bcc structure and the traditional cubic cell. (b) The unit cell of the trigonal ω phase. Light grey spheres and dark grey spheres represent the A-type and B-type sites, respectively. The z parameter determines the position of the B-type sites. The lattice parameters, as well as the d_{A-A} , d_{A-B} and d_{B-B} interatomic distances are indicated [39]. 20
- 2.9 Lattice collapse mechanism of $\beta \rightarrow \omega$ transformation [65]. 22
- 2.10 Simulated composite SAED patterns from (a) [100], (b) [110], (c) [111], (d) [211], (e) [210] and (f) [311] zone axes of the β -phase. Filled circles represent reflections corresponding to the β -phase, whereas, open circles represent those due to the ω -phase. The indices corresponding to the β - and ω - phase reflections have been marked in the figures. Numbers 1, 2, 3 and 4 in the figures represent variant number of the ω -phase as per Table 2.1. 23
- 4.1 A schematic Zr-rich portion of the binary Zr–Nb equilibrium phase diagram. The Zr–Nb alloy composition and the heat treatment temperatures have been marked in the figure. The equilibrium compositions of the β -phase at the heat treatment temperatures, and its expected metastable transformation on quenching, have also been indicated in the figure. 49
- 4.2 Bright-field TEM micrograph showing the microstructure of recrystallized Zr–1 wt.% Nb alloy. A uniform distribution of spherical β_{Nb} -precipitates could be seen with the α -Zr grains. 50
- 4.3 Bright-field TEM micrograph showing the typical microstructure of Zr–1 wt.% Nb alloy sample heat treated at 675 °C for 1 h. Inset shows the typical SAED pattern [Zone Axis = $\langle 110 \rangle_{\beta}$] obtained from β -patches superimposed with reflections of the ω -phase, the indexing of which can be referred from Figure 2.10. Single and double arrows indicate the needle and patch morphologies of the β -phase, respectively. 51
- 4.4 A typical bright-field TEM micrograph representing the microstructures of Zr–1 wt.% Nb alloy samples heat treated at 800 °C for different durations. Single and 52

- double arrows indicate the needle and patch morphologies of the β -phase, respectively.
- 4.5 A typical bright-field TEM micrograph representing the microstructure of Zr-1 wt.% Nb alloy sample heat treated at 825 °C for 10 mins. 53
- 4.6 A typical bright-field TEM micrograph representing the microstructure of Zr-1 wt.% Nb alloy sample heat treated at 832 °C for 5 mins. 54
- 4.7 Composite SAED pattern showing reflections from both the α - and the β - phases in Zr-1 wt.% Nb alloy. $[\bar{1}2\bar{1}3]_{\alpha} // [111]_{\beta}$; $(0\bar{1}1)_{\alpha} // (\bar{1}10)_{\beta}$. 55
- 4.8 A HREM micrograph showing an untransformed spherical β -precipitate present in the α -matrix in Zr-1 wt.% Nb alloy. Inset at the top shows a magnified view of the precipitate-matrix interface, while the insets at the bottom show a Fast Fourier Transform (FFT) from the precipitate (left) and its inverse (right). 56
- 4.9 A HREM micrograph showing an untransformed elongated β -precipitate present in the α -matrix in Zr-1 wt.% Nb alloy. 57
- 4.10 SAED patterns obtained along different zone axes from an elongated β -precipitate present in the Zr-1 wt.% Nb alloy sample heat treated at 800 °C for 30 mins. Superposition of ω -phase reflections could be seen along the $[110]$, $[210]$, $[311]$ and $[211]$ β -zone axes. Indexing of the patterns can be referred from Figure 2.10. 58
- 4.11 Bright-field TEM micrograph showing the β -precipitate in the Zr-1 wt.% Nb alloy sample heat treated at 800 °C for 30 mins (marked by an arrow) from which the SAED patterns in Figure 4.10 are obtained. 59
- 4.12 HREM micrograph showing the lattices of ω - and β - phases (marked in the figure) in Zr-1 wt.% Nb alloy. The $[10\bar{1}]$ section of the β -reciprocal lattice superimposed with ω -phase reflections and its key are given as insets. 60
- 4.13 A dark-field TEM micrograph of a β -patch present in the Zr-1 wt.% Nb alloy sample heat treated at 800 °C for 30 mins. ω -particles corresponding to one crystallographic variant could be seen highlighted in the micrograph, as marked by arrows. 61

- 4.14 A typical bright-field TEM micrograph of a β -patch present in the Zr-1 wt.% Nb alloy sample heat treated at 800 °C for 5 h showing the occurrence of α' -needles within it, as marked by arrows. 61
- 4.15 Bright-field TEM micrograph showing the formation of acicular α' -plates (marked by an arrow) within an elongated β -precipitate, having comparatively larger dimensions with respect to other precipitates, present in the Zr-1 wt.% Nb alloy sample heat treated at 832 °C for 5 mins. The SAED pattern (Zone Axis = $\langle 210 \rangle_{\beta}$) obtained from this precipitate (given as inset) shows the simultaneous occurrence of ω within it, the indexing of which can be referred from Figure 2.10. 62
- 4.16 Free energy–composition diagram showing the variation of free energies of α - and the β - phases as a function of Nb-content in Zr–Nb system at 675 °C. The inset shows the same diagram for the entire Zr–Nb composition range. X_1 represents the composition of α -matrix and X_0 the composition where the free energies of α - and β - phases become equal. X_2 represents the limiting composition of a β -precipitate for nucleation in a α -matrix of composition X_1 , obtained by the intersection of the tangent drawn to the free energy curve of the α -phase at X_1 with the free energy curve of the β -phase. $\Delta G^{\alpha}(0.01;X)$ represents the activation energy associated with the nucleation of a β -precipitate of composition X in a α -matrix of composition X_1 , whereas, $\Delta G^{\alpha\beta}(0.01;X)$ the driving force for the same. $\Delta G_{\max}^{\alpha\beta}(0.01;0.22)$ represents the maximum driving force with which a β -precipitate can nucleate in a α -matrix of composition X_1 . 66
- 4.17 Free energy–composition diagram showing the variation of free energies of α - and the β - phases as a function of Nb-content in Zr–Nb system at 800 °C. The inset shows the same diagram for the entire Zr–Nb composition range. X_0 represents the composition at which the free energies of α - and β - phases are equal, and also the limiting composition of α -matrix for nucleation of β -precipitate. X_m represents the maximum Nb-content that a nucleated β -precipitate can achieve, and is obtained by maximizing the driving force of nucleation 68

- ($\Delta G_{\max}^{\alpha\beta}$ (0.012;0.15)) in respect of the tangent drawn to the free energy curve of the α -phase at X_0 .
- 4.18 Bright-field TEM micrograph showing an elongated β -precipitate in Zr-1 wt.% Nb alloy (marked by an arrow) exhibiting Moire contrast and strain field. 70
- 4.19 A plot of the maximum half-length of the precipitates against the square root of time at 800 °C in Zr-1 wt.% Nb alloy. The corresponding maximum aspect ratio (A) of the precipitates has been indicated in the plot. 71
- 4.20 Effect of strain energy accommodation on the feasibility of martensite formation inside β -precipitate as a function of the size of the precipitate (assuming an undercooling of ΔM_s : 50 °C and precipitate composition of Zr-8 wt.% Nb). 74
- 4.21 The net energy change associated with martensitic transformation against various assumed values of β -precipitate size and undercooling (ΔM_s) (assuming a precipitate composition of Zr-8 wt.% Nb). 75
- 5.1 X-ray diffraction pattern obtained from the vacuum induction melted and cast U-9 wt.% Mo alloy. 80
- 5.2 X-ray diffraction patterns obtained from the homogenized, furnace-cooled and as-rolled samples of U-9 wt.% Mo alloy. 81
- 5.3 A typical bright-field TEM micrograph representing the microstructure of the as-rolled U-9 wt.% Mo alloy sample furnace-cooled after being homogenized at 1000 °C for 24 h. 81
- 5.4 A typical SAED pattern (Zone Axis = $[001]_{\gamma}$) obtained from the γ -phase present in the microstructure of the as-rolled U-9 wt.% Mo alloy sample furnace-cooled after being homogenized at 1000 °C for 24 h. 82
- 5.5 Optical micrograph showing the microstructure of vacuum induction melted and cast U-9 wt.% Mo alloy. 83
- 5.6 Optical micrograph showing the microstructure of as-rolled U-9 wt.% Mo alloy. 83
- 5.7 Optical micrograph showing the microstructure of homogenized U-9 wt.% Mo alloy. Boxes marked in the figure indicate abnormal grain coarsening noticed in the microstructure. 84

- 5.8 Optical micrograph of as-rolled U–9 wt.% Mo alloy after ageing at 500 °C for 5 85 days.
- 5.9 Optical micrograph of homogenized U–9 wt.% Mo alloy after ageing at 500 °C 85 for 5 days. The regions marked by arrow indicate undecomposed γ -phase.
- 5.10 Optical micrograph of as-rolled U–9 wt.% Mo alloy after ageing at 500 °C for 40 86 days.
- 5.11 Optical micrograph of as-rolled U–9 wt.% Mo alloy after ageing at 565 °C for 7 87 days.
- 5.12 Optical micrograph of as-rolled U–9 wt.% Mo alloy after ageing at 565 °C for 14 88 days.
- 5.13 Optical micrograph of as-rolled U–9 wt.% Mo alloy after ageing at 575 °C for 14 88 days.
- 5.14 XRD pattern obtained from the as-rolled U–9 wt.% Mo alloy after ageing at 500 89 °C for 5 days.
- 5.15 XRD pattern obtained from the as-rolled U–9 wt.% Mo alloy after ageing at 500 90 °C for 40 days.
- 5.16 XRD pattern obtained from homogenized U–9 wt.% Mo alloy after ageing at 500 91 °C for 5 days.
- 5.17 XRD pattern obtained from as-rolled U–9 wt.% Mo alloy after ageing at 565 °C 92 for 7 days.
- 5.18 XRD pattern obtained from as-rolled U–9 wt.% Mo alloy after ageing at 565 °C 93 for 14 days.
- 5.19 XRD pattern obtained from as-rolled U–9 wt.% Mo alloy after ageing at 575 °C 94 for 14 days.
- 5.20 SEM micrograph showing BSE image of the U–9 wt.% Mo alloy sample aged at 96 565 °C for 14 days. The labels indicate the features from which EDS analysis was carried out. Single arrow and double arrows indicate long and short lamellae types, respectively.
- 5.21 SEM micrograph showing BSE image of the U–9 wt.% Mo alloy sample aged at 97

- 565 °C for 14 days. The labels indicate the features from which EDS analysis was carried out. Single arrow and double arrows indicate long and short lamellae types, respectively.
- 5.22 A typical bright-field TEM micrograph showing the partially decomposed type-I $(\gamma + \alpha)$ lamellar colony comprising of long α -phase lamellae and γ -interlamellar regions in U–9 wt.% Mo alloy. 100
- 5.23 A typical bright-field TEM micrograph showing the partially decomposed type-II $(\gamma + \gamma')$ lamellar colony comprising of long γ' -phase lamellae and γ -interlamellar regions in U–9 wt.% Mo alloy. 101
- 5.24 A typical bright-field TEM micrograph showing the partially decomposed type-III $(\gamma + \gamma')$ lamellar colony comprising of short γ' -phase lamellae and γ -interlamellar regions in U–9 wt.% Mo alloy. 102
- 5.25 A typical bright-field TEM micrograph showing the occasional presence of the γ' -phase in the γ -interlamellar region between two α -phase lamellae in partially decomposed type-I $(\gamma + \alpha)$ lamellar colony in U–9 wt.% Mo alloy. 103
- 5.26 Typical micro-diffraction patterns of (a) α (Zone Axis = $[\bar{1}\bar{1}\bar{2}]_{\alpha}$), (b), γ (Zone Axis = $[011]_{\gamma}$) and (c) γ' (Zone Axis = $[110]_{\gamma'}$) phases. 103
- 5.27 *Typical SAED patterns of (a) α -U, (b) γ -U and (c) γ' phases.* 104
- 5.28 Composite SAED pattern (along with its key) showing reflections from the α -, γ - and γ' -phases. $[001]_{\alpha} // [011]_{\gamma} // [110]_{\gamma'}$; $(\bar{1}\bar{1}0)_{\alpha} // (0\bar{1}\bar{1})_{\gamma} // (\bar{1}\bar{1}0)_{\gamma'}$. 104
- 5.29 SEM micrograph showing the BSE image of the as-rolled U–9 wt.% Mo alloy sample aged at 500 °C for 40 days. 106
- 6.1 Free energy–composition diagram at 500 °C showing the variation of free energies of α -U and γ -U phases as a function of Mo-content in U–Mo system. The inset shows the same diagram for the entire U–Mo composition range. The free energy of the stoichiometric γ' (U_2Mo) phase of 33.3 at.% Mo (G^{U_2Mo}) is marked in the diagram by the filled circle. The free energy of the U-19.7 at.% Mo alloy existing as a mixture of α -U phase, of equilibrium composition, and stoichiometric γ' phase ($G^{\alpha U + U_2Mo}$) is indicated in the diagram by the open circle 115

on tangent-III. $\Delta X = 0.14$ (or 14 at.% Mo) represents the minimum amount of Mo-depletion required in the 19.7 at.% Mo γ -matrix to nucleate the α -U phase, whereas, $\Delta X = 0.136$ (or 13.6 at.% Mo) represents the minimum amount of Mo-enrichment required in the same γ -matrix to nucleate the γ' phase. $X = 0.057$ (or 5.7 at.% Mo) represents the maximum Mo-content with which the α -U phase can nucleate, and is given by the intersection of tangent-IV and free energy curve of α -U phase.

- 6.2 Free energy–composition diagram at 565 °C showing the variation of free 116
energies of α -U and γ -U phases as a function of Mo-content in U–Mo system. The inset shows the same diagram for the entire U–Mo composition range. The free energy of the stoichiometric γ' (U_2Mo) phase of 33.3 at.% Mo (G^{U_2Mo}) is marked in the diagram by the filled circle. The free energy of the U-19.7 at.% Mo alloy existing as a mixture of α -U phase, of equilibrium composition, and stoichiometric γ' phase ($G^{\alpha U+U_2Mo}$) is indicated in the diagram by the open circle on tangent-III. $X = 0.027$ (or 2.7 at.% Mo) represents the maximum Mo-content with which the α -U phase can nucleate, and is given by the intersection of tangent-IV and free energy curve of α -U phase.
- 6.3 Free energy–composition diagram at 575 °C showing the variation of free 120
energies of α -U and γ -U phases as a function of Mo-content in U–Mo system. The inset shows the same diagram for the entire U–Mo composition range. The free energy of the stoichiometric γ' (U_2Mo) phase of 33.3 at.% Mo (G^{U_2Mo}) is marked in the diagram by the filled circle.
- 7.1 Optical micrograph depicting the microstructure of the cross-section of as-bonded 127
U–9Mo/Zr–1Nb sample.
- 7.2 Back scattered electron image of the interaction layer (IL) formed between U– 128
9Mo and Zr–1Nb alloys during the diffusion bonding operation at 800 °C. The compositions at regions labeled 1, 2, 3, ..., 14 are given in Table 7.1. The interaction layer could be divided into three distinct regions as marked by A, B and C in the figure. Labels 3, 5 and 6 correspond to the Mo_2Zr phase present in

- region-A as dispersoids. Labels 12 and 13 in region-C correspond to β -Zr(U) and α -Zr phases, respectively.
- 7.3 Concentration-distance profiles of U, Mo and Zr across the interaction layer (IL) 130
formed between U-9Mo and Zr-1Nb alloys during the diffusion bonding
operation at 800 °C, as determined by EPMA. The profiles have been divided into
three zones viz., A, B and C (as marked in the figure) in accordance with the
classification of the interaction layer (IL) carried out on the basis of
microstructural features (Figure 7.2) and EDS analysis (Table 7.1).
- 7.4 (a-d) Typical microdiffraction patterns of α -Zr, Mo₂Zr, γ -U(Mo,Zr) and α -U 132
phases present in the interdiffusion zone of the as-bonded U-9Mo/Zr-1Nb
sample.
- 7.5 Typical composite SAED patterns showing reflections from (a) γ -U(Mo,Zr), α -Zr 133
and Mo₂Zr phases, (b) γ -U(Mo,Zr), α -U and Mo₂Zr phases present in the
interdiffusion zone of the as-bonded U-9Mo/Zr-1Nb sample. Cells constituting
of diffracting planes for each of the phases have been outlined in the patterns.
- 7.6 Typical bright-field TEM micrographs representing the microstructure of (a) 135
region-A near the U-9Mo/IL interface and (b) region-A near the interface with
region-B in the interdiffusion zone of the as-bonded U-9Mo/Zr-1Nb sample.
Mo₂Zr precipitates are indicated by arrows in the micrographs.
- 8.1 A typical optical microscopy image representing the overall microstructural 141
features of the interdiffusion zones of all the annealed U-9Mo/Zr-1Nb bonded
samples.
- 8.2 Backscattered electron image of the interdiffusion zone of U-9Mo/Zr-1Nb 142
bonded sample annealed at 800 °C for 10 days followed by water quenching.
Labels 1 and 2 represent the ‘massive’ morphological feature of the Mo₂Zr phase.
- 8.3 Backscattered electron image of the interdiffusion zone of U-9Mo/Zr-1Nb 143
bonded sample annealed at 800 °C for 10 days followed by furnace cooling. Label
1 represents the ‘massive’ morphological feature of the Mo₂Zr phase. Label 3
represents the Zr-rich precipitate phase.
- 8.4 Backscattered electron image of the interdiffusion zone of U-9Mo/Zr-1Nb 144

- bonded sample annealed at 800 °C for 10 days followed by furnace cooling depicting the lamellar ‘halo’ region adjoining the Mo₂Zr phase.
- 8.5 Backscattered electron image of the interdiffusion zone of U–9Mo/Zr–1Nb 145 bonded sample annealed at 900 °C for 10 days followed by furnace cooling. Labels 3 and 5 represent the continuous layer of Mo₂Zr phase running parallel to the as-bonded interface. Labels 7 and 8 represent the ‘massive’ morphological feature of the Mo₂Zr phase. Labels 6, 9 and 10 represent the ‘halo’ region adjoining the Mo₂Zr phase.
- 8.6 Backscattered electron image of the interdiffusion zone further deep into the U– 146 9Mo side of U–9Mo/Zr–1Nb bonded sample annealed at 900 °C for 10 days followed by furnace cooling. Labels 1, 2, 3 and 5 represent the Zr-rich precipitate phase.
- 8.7 Backscattered electron image of the interdiffusion zone of U–9Mo/Zr–1Nb 147 bonded sample annealed at 900 °C for 12 days followed by furnace cooling. Label 1 represents the continuous layer of Mo₂Zr phase running parallel to the as-bonded interface. Labels 5 represents the ‘halo’ region adjoining the Mo₂Zr phase.
- 8.8 Backscattered electron image of the interdiffusion zone further deep into the U– 148 9Mo side of U–9Mo/Zr–1Nb bonded sample annealed at 900 °C for 12 days followed by furnace cooling. Labels 1, 2 and 3 represent the Zr-rich precipitate phase.
- 8.9 Backscattered electron image of the interdiffusion zone of U–9Mo/Zr–1Nb 149 bonded sample annealed at 1000 °C for 10 days followed by furnace cooling. Labels 1, 2, 3 and 5 represent the Zr-rich precipitate phase.
- 8.10 (a) BSE-SEM image of the interdiffusion zone close to the U–9Mo side of U– 153 9Mo/Zr–1Nb bonded sample annealed at 800 °C for 10 days followed by furnace cooling. Mo₂Zr phase of ‘massive’ morphological feature and Zr-rich precipitates could be seen in this image, (b) qualitative U, Mo and Zr elemental concentration profiles across the line marked in (a), (c-e) elemental maps of (a) obtained with UM_{α1}, MoL_{α1} and ZrL_{α1} characteristic X-ray signals, respectively.

- 8.11 Concentration-distance profiles of U, Mo and Zr across the interdiffusion zone of U-9Mo/Zr-1Nb bonded sample annealed at 800 °C for 10 days followed by water quenching, as determined by EPMA. The inset shows an enlarged view of the profiles corresponding to the zone marked as A. 154
- 8.12 Concentration-distance profiles of U, Mo and Zr across the interdiffusion zone of U-9Mo/Zr-1Nb bonded sample annealed at 800 °C for 10 days followed by furnace cooling, as determined by EPMA. 155
- 8.13 Concentration-distance profiles of U, Mo and Zr across the interdiffusion zone of U-9Mo/Zr-1Nb bonded sample annealed at 900 °C for 10 days followed by furnace cooling, as determined by EPMA. The inset shows an enlarged view of the profiles corresponding to the zone marked as A. 156
- 8.14 Concentration-distance profiles of U, Mo and Zr across the interdiffusion zone of U-9Mo/Zr-1Nb bonded sample annealed at 900 °C for 12 days followed by furnace cooling, as determined by EPMA. The insets show an enlarged view of the profiles corresponding to the zones marked as A and B. 157
- 8.15 Concentration-distance profiles of U, Mo and Zr across the interdiffusion zone of U-9Mo/Zr-1Nb bonded sample annealed at 1000 °C for 10 days followed by furnace cooling, as determined by EPMA. The inset shows an enlarged view of the profiles corresponding to the zone marked as A. 158
- 8.16 (a,c) Typical SEM images of lamellar ‘halo’ regions noticed adjacent to the ‘massive’ Mo₂Zr phase in the interdiffusion zone of the annealed U-9Mo/Zr-1Nb bonded samples, (b) X-ray map of (a) using MoL_{α1} characteristic radiation, (d) magnified view of the white line, and its associated features, marked in (c), (e) X-ray profiles of Mo and Zr across the line marked in (c). 160
- 8.17 (a,b) Typical polarized light optical microscopy images depicting the “basket weave” microstructure noticed near the Zr-1Nb side of the interdiffusion zone of the annealed U-9Mo/Zr-1Nb bonded samples. 161
- 8.18 (a,b) Typical bright-field TEM micrographs showing the arrangement of laths in the “basket weave” microstructure, noticed near the Zr-1Nb side of the interdiffusion zone of the annealed U-9Mo/Zr-1Nb bonded samples. 162

8.19	Typical SAED patterns corresponding to (a) α -Zr phase obtained from the intralath regions and (b) β -Zr phase obtained from the interlath regions of the “basket weave” microstructure noticed near the Zr–1Nb side of the interdiffusion zone of the annealed U–9Mo/Zr–1Nb bonded samples. The circle in (b) shows the omega-type reflections, similar to Figure 2.10b, corresponding to the second phase present within the β -phase interlath boundaries.	163
8.20	Microdiffraction pattern obtained from the β -phase present in the interlath regions of the “basket weave” microstructure noticed near the Zr–1Nb side of the interdiffusion zone of the annealed U–9Mo/Zr–1Nb bonded samples. The black dots represent the omega-type reflections, similar to Figure 2.10f, corresponding to the second phase present within the β -phase interlath boundaries.	164
8.21	Optical microscopy image depicting the simultaneous formation of “basket weave” structure and Widmanstätten α -Zr laths at the α -Zr grain boundaries in the U–9Mo/Zr–1Nb bonded sample furnace-cooled after annealing at 800 °C.	170
8.22	Plot showing the Arrhenius temperature dependence of the growth rate of the interdiffusion zone in U–9Mo/Zr–1Nb bonded sample annealed at 800 °C, 900 °C and 1000 °C for 10 days followed by furnace cooling.	176
9.1	A schematic representation of different reaction sequences exhibited by Zr–1 wt.% Nb and U–9 wt.% Mo alloys over different temperature ranges, and their metallurgical interaction, in the present work. The β -Zr needle/patch in the Zr–1Nb alloy would transform to α' - and/or ω - metastable phases depending on the composition and size.	184
AI.1	The binary Zr–Nb equilibrium phase diagram [24].	209
AI.2	The binary Mo–U equilibrium phase diagram [24].	210
AI.3	The binary Nb–U equilibrium phase diagram [24].	211
AI.4	The binary Mo–Nb equilibrium phase diagram [24].	212
AI.5	The binary U–Zr equilibrium phase diagram [24].	213
AI.6	The binary Mo–Zr equilibrium phase diagram [24].	214
AI.7	The binary Al–Mo equilibrium phase diagram [24].	215

AI.8	The binary Mo–Si equilibrium phase diagram [24].	216
AI.9	The binary Nb–Al equilibrium phase diagram [24].	217
AI.10	The binary Nb–Si equilibrium phase diagram [24].	218
AI.11	The binary Zr–Al equilibrium phase diagram [24].	219
AI.12	The binary Si–Zr equilibrium phase diagram [24].	220
AI.13	The binary Mg–U equilibrium phase diagram [24].	221
AI.14	The binary Mg–Mo equilibrium phase diagram [24].	222
AI.15	The binary Al–Mg equilibrium phase diagram [24].	223
AI.16	The binary Mg–Si equilibrium phase diagram [24].	224
AI.17	The binary Ti–U equilibrium phase diagram [24].	225
AI.18	The binary Ti–Mo equilibrium phase diagram [24].	226
AI.19	The binary Ti–Al equilibrium phase diagram [24].	227
AII.1	Free energy–composition diagram at 500 °C showing the variation of free energies of α -U and γ -U phases as a function of Mo-content in U–Mo system constructed using the thermodynamic parameters of Zhang et al [135]. The free energy of the stoichiometric γ' (U_2Mo) phase of 33.3 at.% Mo (G^{U_2Mo}) is marked in the diagram by the filled circle. The free energy of the U-19.7 at.% Mo alloy existing as a mixture of α -U phase, of equilibrium composition, and stoichiometric γ' phase ($G^{\alpha U+U_2Mo}$) is indicated in the diagram by the open circle on the common tangent between the α -U and γ' phases. $X = 0.136$ (or 13.6 at.% Mo) represents the maximum Mo-content with which the α -U phase can nucleate.	228
AII.2	Free energy–composition diagram at 565 °C showing the variation of free energies of α -U and γ -U phases as a function of Mo-content in U–Mo system constructed using the thermodynamic parameters of Zhang et al [135]. The free energy of the stoichiometric γ' (U_2Mo) phase of 33.3 at.% Mo (G^{U_2Mo}) is marked in the diagram by the filled circle.	229
AII.3	Free energy–composition diagram at 575 °C showing the variation of free energies of α -U and γ -U phases as a function of Mo-content in U–Mo system constructed using the thermodynamic parameters of Berche et al [136]. The free	230

energy of the stoichiometric γ' (U_2Mo) phase of 33.3 at.% Mo ($G^{\text{U}_2\text{Mo}}$) is marked in the diagram by the filled circle. The free energy of the U-19.7 at.% Mo alloy existing as a mixture of α -U phase, of equilibrium composition, and stoichiometric γ' phase ($G^{\alpha\text{U}+\text{U}_2\text{Mo}}$) is indicated in the diagram by the open circle on the common tangent between the α -U and γ' phases. $X = 0.02$ (or 2 at.% Mo) represents the maximum Mo-content with which the α -U phase can nucleate.

List of Tables

	Page No.
2.1 Four possible orientation relationship in the bcc (β) and hexagonal (ω) crystal structures [74].	22
2.2 Invariant reactions in the Mo–U system.	27
2.3 Metastable phases in Mo–U system depending on the Mo-content and the rate of cooling from the γ -phase.	29
2.4 Physical properties of Mo, Nb and Zr as barrier material [200,202].	34
3.1 Detailed chemical composition of Zr–1 wt.% Nb alloy used in this work.	42
4.1 Heat treatment schedule of Zr–1 wt.% Nb alloy.	48
4.2 Nb contents of α - and β - phases in Zr–Nb system estimated from free energy–composition diagrams at 675 °C, 800 °C, 825 °C and 832 °C.	69
4.3 Morphological parameters of β -phase precipitates in 800 °C heat treated Zr–1 wt.% Nb alloy samples.	72
5.1 Space group, Wyckoff notation, atomic position and lattice parameter data of α -U, γ -U, γ' (U_2Mo), UO_2 and UO used for the analysis of X-ray diffraction patterns.	79
5.2 Ageing schedule of U–9 wt.% Mo alloy.	84
5.3 Volume fractions of γ -U, α -U and γ' (U_2Mo) phases present in the aged U–9 wt.% Mo alloy samples, as determined from XRD phase fraction analysis. For sake of comparison, expected equilibrium volume fractions of α - and γ' - phases, based on decomposed γ -phase fraction, have also been included in the table.	95
5.4 Chemical compositions of labeled regions in Figure 5.20, determined using SEM-EDS.	97
5.5 Chemical compositions of labeled regions in Figure 5.21, determined using SEM-EDS.	98
7.1 Chemical compositions of different regions, as labeled in Figure 7.2, within the interaction layer (IL) formed between U–9Mo and Zr–1Nb alloys during the	129

	diffusion bonding operation at 800 °C, determined using EDS in SEM.	
7.2	Orientation relationships between different phases present in the interdiffusion zone of the as-bonded U–9Mo/Zr–1Nb sample.	134
8.1	Annealing schedule of U–9Mo/ Zr–1Nb as-bonded diffusion couple.	139
8.2	Chemical compositions at different regions within the interdiffusion zone of the annealed U–9Mo/Zr–1Nb bonded samples as labeled in Figures 8.2 to 8.9, determined using EDS in SEM.	150
8.3	Interdiffusion zone width of annealed U–9Mo/Zr–1Nb bonded samples, as measured from the concentration-distance profiles determined by EPMA. For the sake of comparison, the width of the interdiffusion zone in the as-bonded sample is also included.	159
8.4	Chemical compositions of intralath and interlath regions of “basket weave” microstructure noticed near the Zr–1Nb side of the interdiffusion zone of the annealed U–9Mo/Zr–1Nb bonded samples, determined using EDS in TEM.	165
8.5	Chemical compositions of Zr-rich precipitates along with adjacent matrices noticed in the U-rich side of the interdiffusion zone of the annealed U–9Mo/Zr–1Nb bonded samples, determined using EDS in SEM.	171
8.6	Width of interdiffusion zone, developed during annealing of U–9Mo/Zr–1Nb bonded sample, and its growth rate as a function of annealing temperature together with pre-exponential factor and activation energy for growth.	175
8.7	A comparison of the growth rates of the interdiffusion zone in U–Mo vs. Al and U–Mo vs. Al–Si diffusion couples with those of the U–9Mo vs. Zr–1Nb diffusion couple.	177
8.8	A comparison of the growth rates of the interdiffusion zone in U–10 wt.% Mo vs. pure-Zr diffusion couple with those of the U–9 wt.% Mo vs. Zr–1 wt.% Nb diffusion couple.	178

List of Abbreviations

bcc	Body centered cubic
BR-3	Belgian Reactor 3
BSE	Backscattered electron
BWR	Boiling Water Reactor
DC	Discontinuous coarsening
DP	Discontinuous precipitation
DSA	Degree of self-accommodation
EDS	Energy dispersive spectroscopy
EPMA	Electron probe microanalyzer
FCCI	Fuel-clad chemical interaction
FFT	Fast Fourier Transform
GTRI	Global Threat Reduction Initiative
G-X	Free energy-composition
hcp	Hexagonal closed packed
HEU	High enriched uranium
HPU	Hydrogen pick-up
HREM	High resolution electron microscopy
IL	Interaction layer
ILS	Invariant Line Strain
IPS	Invariant Plane Strain
JEOL	Japan Electron Optics Limited
LEU	Low enriched uranium
LIS	Lattice Invariant Shear
LOCA	Loss of coolant accident
MeV	Million electron volt
OR	Orientation relationship
PET	Pentaerythritol

ppm	Parts per million
PTMC	Phenomenological theory of martensite crystallography
PWR	Pressurized Water Reactor
RBMK	Reaktor Bolshoi Mozhnosti Kanalov
RERTR	Reduced Enrichment for Research and Test Reactor
SAED	Selected area electron diffraction
SE	Secondary electron
SEM	Scanning electron microscope
SER	Standard Element Reference
SGTE	Scientific Group Thermodata Europe
TEM	Transmission electron microscope
T–T–T	Time–temperature–transformation
U–9Mo	U–9 wt.% Mo
VVER	Voda Voda Energo Reactor
WDS	Wavelength dispersive spectroscopy
wt.	Weight
XRD	X-ray diffraction
Zr–1Nb	Zr–1 wt.% Nb

Introduction

1.1 Background

Nuclear research and test reactors are used worldwide to assess the performance of various structural materials proposed to be used inside the core of a nuclear reactor, in terms of their irradiation withstanding capabilities, besides basic and applied research work. Such reactors use U-based fuels in two different geometries viz., dispersion and monolithic, both encapsulated in Al or Al-alloy cladding. In the former type, particulates of the fuel material are dispersed in a matrix of Al or Al-alloy, known as the fuel-meat, whereas, the same fuel material in the form a thin foil is used in the case of the latter.

There are primarily two issues with these research reactor fuels that are of concern. First is the proliferation issue, associated with the highly enriched U-fuels ($U^{235} > 20$ wt.%) used in these reactors, which calls for the development of alternative reduced enrichment fuels ($U^{235} < 20$ wt.%) with increased U-density so that the effective concentration of the fissile U^{235} isotope remain same [1,2]. Secondly, the fuel material and the Al or Al-alloy matrix/cladding metallurgically interact due to the interdiffusion of the constituent elements of fuel and clad. The phases generated out of such reactions, both during fabrication and in-reactor operation, degrade the fuel performance [3,4].

As far as the first issue is concerned, highly concentrated intermetallic compounds, like, U_3Si , U_6Me (where $Me = Fe, Mn, Ni, Co$ or Ge), and U-based alloys were considered as candidates for low enriched–high density fuels. However, due to the unsatisfactory irradiation behavior of these intermetallic compounds, U-based alloys emerged as the best alternative of high enriched uranium fuels [3,5-8]. Alloying of metallic-U arises from the need of stabilizing the high temperature bcc γ -allotrope of U due to its irradiation resistant properties and isotropic nature. Alloying U with Mo, as against the other common bcc-phase stabilizers like Zr, Nb, has shown considerable prospect, since Mo-addition in the range of 5.4 to 10 wt.% has been found sufficient in stabilizing the γ -phase while still maintaining a high U-density of the fuel [9,10]. The γ -phase stabilized by Mo possesses acceptable irradiation stability, mechanical properties

and corrosion resistance [3]. Thus, U–Mo alloys are a promising candidate for a fuel that offers a balance between high fissile material density and stable irradiation behavior [2,11]. In particular, U–Mo alloys containing between 8-10 wt.% of Mo are quite appealing on account of the sluggishness with which the γ -phase in these alloys has been found to decompose at lower temperatures [12].

With regard to the second issue, addition of a diffusion barrier element either by directly alloying in the fuel, in case of dispersion fuel geometry, or as a liner between the fuel and the clad, in case of monolithic fuel geometry, has been envisaged to mitigate the fuel and Al/Al-alloy interaction. Out of several plausible diffusion barrier elements like Mo [13], Nb [14,15], Zr [16], Mg [17] and Ti [18], Zr was found to be the most effective in reducing this deleterious interaction [16]. Since Zr-based alloys, like the zircalloys and the Zr-Nb alloys, are already in use as cladding in nuclear power reactors [19-21], the envision of same as fuel cladding in research reactor fuels of monolithic geometry can have the following advantages over the currently used Al/Al-alloy cladding:

(i) Utilization of diffusion barrier characteristics inherent in these alloys, as Zr is the major constituent in them. This will not only eliminate the need for a separate Zr-liner, and additional fuel–liner and liner–clad interactions, but will also lower the in-general thinning of the clad due to the reduced fuel–clad interaction.

(ii) Eradication of the unavoidable interaction likely to occur between the Zr-liner and the Al/Al-alloy cladding resulting in generation of unwanted phases.

In this backdrop, the present research work is focused on evaluating two binary alloys having potential of being used as a fuel–clad combination in research reactors, if conceived in monolithic form. The alloys selected are U–9 wt.% Mo, to be used as the fuel, and Zr–1 wt.% Nb, to be used as the clad. Zr–1Nb alloy having superior resistance to corrosion, hydrogen pick up and irradiation creep, in comparison of existing Zr-based fuel cladding alloys of power reactors, is being used extensively as fuel cladding in the Russian Pressurized Water Reactors (PWR) of VVER (Voda Voda Energo Reactor)-type [19-21].

1.2 Motivation

Nuclear research reactors experience frequent shut-downs and ramping in powers during operation. This leads to rapid rise and fall of temperatures in fuel assemblies. The sudden

changes in temperature can not only alter the initial microstructural features of the fuel or the fuel cladding, but also introduce undesirable metastable phase(s) in the microstructures. In this work, therefore, the phase transformation aspects of Zr–1Nb and U–9Mo alloys have been explored in temperature domains wherein these alloys are expected to show phase transitions relevant in context of the above-mentioned off-normal reactor operating scenarios.

The desired microstructure of Zr–1Nb alloy for reactor application necessitates the presence of Nb-rich bcc β -phase precipitates within a fully recrystallized hcp α -Zr matrix. In the present research work the morphological and compositional evolution alongside phase transformations which the constituents of this microstructure, especially the β -phase precipitates, might undergo in the reactor will be explored. The β -phase under rapid cooling transforms athermally to martensite and/or omega phases depending on its composition [22,23]. These metastable phases, especially the omega phase, are known to increase the hardness, and hence are undesirable as it may affect the post-irradiation ductility of the alloy.

The dimensional stability of γ -phase stabilized U–Mo alloys, in respect of irradiation induced growth and swelling, is related to their ability to retain the γ -phase in metastable equilibrium at the reactor operating condition. The γ -phase also decomposes to orthorhombic α -U and tetragonal γ' (U_2Mo) phases [24]. Thus, in the present study attempts will be made to assess the stability of the γ -phase in U–9Mo alloy under conditions which can influence its stability. In addition to this, the mechanism of decomposition of the metastable γ -phase into the stable α -U and γ' phases will also be investigated.

A rise in temperature in the fuel assemblies can enhance the fuel–clad interaction. Thus, the compatibility of Zr–1Nb and U–9Mo alloys will also be examined in the present work. The metallurgical interaction and the mechanism of evolution of the microstructure at the interdiffusion zone of these alloys will be ascertained. In addition, the stability of the interdiffusion zone will also be assessed at different temperatures.

1.3 Objectives

Objectives of the present work are to study:

1. Evolution of the β -phase in Zr–1Nb alloy in the ($\alpha + \beta_{Zr}$) phase field and its transformation into metastable phases as a function of size and composition.

2. Stability of the γ -phase in U–9Mo alloy and factors affecting it.
3. Decomposition mechanism of the metastable γ -phase in U–9Mo alloy during ageing.
4. Metallurgical interaction between U–9Mo and Zr–1Nb alloys.
5. Thermal stability of the interdiffusion zone formed between U–9Mo and Zr–1Nb alloys.

1.4 Structure of the thesis

The present thesis comprises nine chapters. The present chapter (Chapter 1) defines the issues to be addressed under this doctoral research work and details out the scope of the investigations undertaken therein. Chapter 2 is focused on literature review of alloy systems dealt with in the present work and also on the nature of studies performed in these systems. Experimental details related to alloy making, thermomechanical processing, heat treatments, specimen preparation and characterizations are presented in Chapter 3. The experimental findings and their analyses towards realizing each of the outlined research objectives have been discussed independently in Chapters 4 to 8. Chapter 4 addresses the microstructural and phase transformation aspects of Zr–1Nb fuel cladding alloy. Issues pertaining to the stability of the γ -phase of U–9Mo metallic fuel alloy are discussed in Chapter 5. Chapter 6 focuses on deciphering the mechanism of decomposition of the metastable γ -phase of U–9Mo alloy. The metallurgical interaction occurring during the solid-state diffusion bonding of U–9Mo and Zr–1Nb alloys is elaborated in Chapter 7. The response of the diffusion bonded U–9Mo/Zr–1Nb interaction zone microstructure to different annealing heat treatments is presented in Chapter 8. Finally, the salient outcomes of the entire research work are summarized collectively in Chapter 9. At the end, all the relevant binary equilibrium phase diagrams are presented in form of an Appendix.

Literature Review

This chapter entails a detailed literature survey conducted on the investigated alloy systems of Zr–Nb and U–Mo with due emphasis on the particular alloy compositions studied therein viz., Zr–1Nb and U–9Mo, respectively. The literature survey also gives a brief introduction to the phase transformation aspects which have been dealt with in the course of the investigations carried out with these two alloys. In addition, a review on the fuel–clad chemical interaction (FCCI) issues faced by U–9Mo fuel in contact with Al/Al-alloy clad has been presented. In this context, the role of Zr in mitigating such interactions and thus the conceptualization of Zr-based alloys, like in present case the Zr–1Nb alloy, as plausible cladding material has been elaborated upon.

2.1 Development of Zr–1Nb alloy as cladding material

Since the binary Zr–1Nb alloy studied in this work finds application as power reactor fuel cladding tube, it would be worth to review its genesis in brief. The development of Zr–Nb alloys for reactor application, in general, started in the former Soviet Union in the 1950's using iodide-Zr in the beginning, and then with Zr produced commercially by the molten salt electrolysis method. The objective was to obtain a corrosion resistant material with enhanced mechanical strength for the under construction VVER-PWR and RBMK (Reaktor Bolshoi Mozhnosti Kanalov) channel type BWR (Boiling Water Reactor). Out of the several elements which were considered as prospective alloying addition in Zr to achieve the above objective viz., Sn, Nb, Cr and Fe, focus was given to Nb as it helped in enhancing the corrosion resistance and reducing the pick-up of hydrogen [25]. Thus, a binary Zr–Nb alloy containing 1 wt.% of Nb, designated as E110, was developed. E110 was selected as the cladding material in VVER and RBMK [25,26]. E110 was also adopted as the cladding material for the naval reactors of Soviet Union [27]. The post-irradiation ductility of alloy E110 was found to be excellent [21]. The oxide layer build up and the hydrogen pick-up (HPU) in the E110 cladding tubes were usually extremely low except for a few reported cases of abnormally enhanced corrosion caused by coolant impurities. However, a poor corrosion behavior of E110 in high temperature steam during anticipated loss of

coolant accidents (LOCA) necessitated an improvement in the alloy. It was established eventually that the feed material used for alloy fabrication is actually responsible for this behavior, and the Zr source material was thus changed from (electrolytic + crystal bar) Zr to sponge-Zr to get rid of the high fluorine contamination from the former [28]. It was further found that an increase in the O and Fe contents of the alloy increased its creep strength and decreased its irradiation growth rate [29]. Hence, the O and Fe levels in E110 were specified between 600-990 ppm and 250-700 ppm, respectively [30,31].

Westinghouse started an irradiation program of Zr–Nb alloy in the experimental BR-3 PWR reactor in Mol, Belgium in 1976, which continued till 1985. Although the alloy showed a lower uniform oxide layer thickness, heavy nodular corrosion posed a problem for these alloys in the high O and low hydrogen containing coolant in few irradiation cycles [19,32,33].

Developmental activity of new cladding materials with improved performance was also initiated by Framatome (now Areva) in the early 1990's, which included studies on Zr–Nb alloys like the M5 [34]. Composition wise M5 is similar to the Russian E110 (Zr–Nb) alloy with extra additions of 0.125 wt.% of O and traces of S, and is processed with a special fabrication route involving all intermediate and final annealing heat treatments at 580 °C leading to a fully recrystallized microstructure with fine grains. Extensive in-pile test of M5 upto very high burn-ups in PWRs demonstrated its excellent corrosion resistance behavior [35]. The M5 alloy, once inducted on a commercial basis in PWRs by Framatome in 1996, has emerged as a cladding material of high corrosion resistance, low hydrogen pick up and low irradiation creep and irradiation growth.

2.2 Phase transformations exhibited by the binary Zr–Nb system

Since the present work is focused on the transformations of the β -phase in Zr–Nb alloy, it would be of worth to take a note on the different stable and metastable phase transformations exhibited by the binary Zr–Nb system.

The binary Zr–Nb equilibrium phase diagram [24] is shown in Figure AI.1. The various stable and metastable phase transformations which are possible in Zr–Nb alloys of different compositions are summarized in the following [22,23,36–39]. The allotropic transformation of the high temperature bcc β -phase into the hcp α -phase in un-alloyed Zr and in dilute Zr–Nb alloys results in the precipitation of α -phase in β -phase matrix in form of grain boundary

allotriomorphs, Widmanstätten side plates and intragranular plates (either in isolated manner or in a group giving rise to the “basket weave morphology”). The clustering tendency in the β -phase leads to its phase separation into β_{Zr} (Zr-rich) and β_{Nb} (Nb-rich) phases, thereby bringing about its spinodal decomposition in suitable temperature and composition regimes. In addition, the β -phase immiscibility is also responsible for the monotectoid reaction of $\beta_{Zr} \rightarrow \alpha + \beta_{Nb}$ at 610 °C and 20 wt.% Nb. Menon et al. [36] have shown that due to the large miscibility gap in the β -phase, the rate of monotectoid decomposition of the β_{Zr} -phase to β_{Nb} -phase depends strongly on the heat treatment temperature. In general, the β_{Zr} -phase is retained to a large fraction in samples annealed at temperatures higher than the monotectoid temperature (T_{mono}). Annealing at temperatures below T_{mono} , on the other hand, results in β -phase precipitates with composition varying between β_{Zr} and β_{Nb} . However, at $T \ll T_{mono}$, a long duration heat treatment results only in the formation of the equilibrium β_{Nb} -precipitates.

The desired microstructure of Zr–1Nb alloy for cladding application is the one in which the precipitation of the β_{Nb} -phase is nearly complete within the fully recrystallized grains of the α -Zr phase, as it significantly improves the corrosion resistance [40-44]. Thus, annealing studies of cold-worked Zr–1Nb alloy have been carried out to establish the recrystallization temperature on the basis of both microstructural observation and mechanical property evaluation and also to arrive at an annealing condition which maximizes the fraction of the β_{Nb} -precipitates. In the case of Zr–1Nb alloy, the role of the monotectoid reaction in evolution of β -phase precipitates has been clearly established, where annealing of cold worked alloy above and below T_{mono} exhibited substantially different compositions of the β -precipitates. β_{Zr} -precipitates have been observed when annealing was carried out above T_{mono} , while β_{Nb} -precipitates were noticed on annealing below T_{mono} [40,41,44,45]. With regard to recrystallization, it was found that in alloys which were deformed beyond 50% it is possible to obtain a fully recrystallized microstructure with annealing durations not exceeding 4h at temperatures lying just below T_{mono} , such as 580 °C [45-47]. However, annealing for a longer duration helped in generating a microstructure in which majority of the β -precipitates are Nb-rich [40,41,44].

The possibility of occurrences of displacive phase transformations also exists in Zr–Nb alloys containing Nb to a suitable level, like the β to hcp α' martensitic transformation in alloys

containing 0-8 wt.% Nb during β -quenching and the β to hexagonal omega (ω) transformation in alloys containing 4-17 wt.% Nb during β -quenching (athermal ω) or isothermal holding (ω precipitation). The significance of the composition of the β -phase in undergoing α' - and ω -phase transformations can be best comprehended from Figure 2.1. The figure schematically shows the Zr-rich side of the binary Zr–Nb system on which the metastable stability regimes of the α - and ω - phases are superimposed.

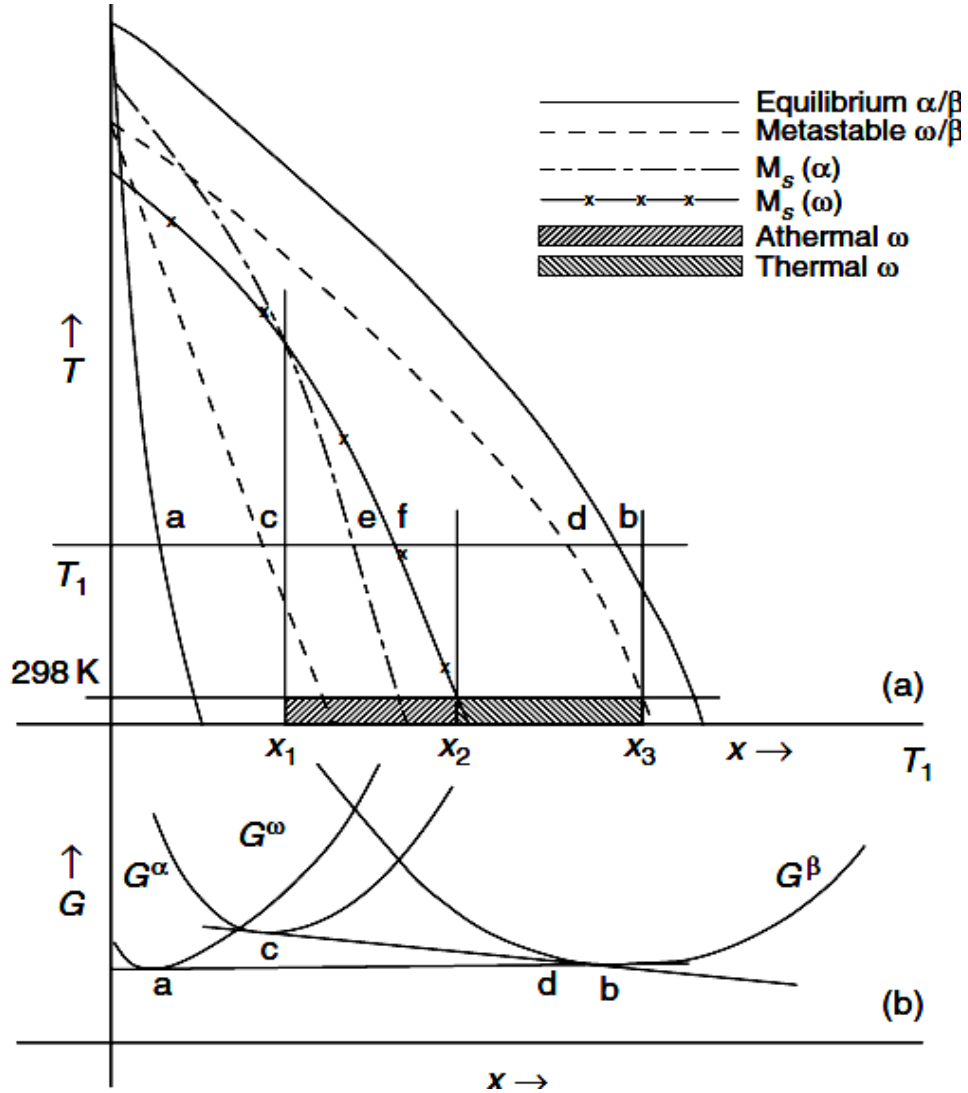


Figure 2.1 (a) Schematic equilibrium phase diagram of binary Zr–Nb system (marked by solid lines). Superimposed metastable phase boundaries have also been shown by broken lines. (b) Schematic free energy curves for the α -, ω - and the β - phases [23].

The M_s (transformation start) temperatures corresponding to the $\beta \rightarrow \alpha'$ martensitic ($M_s(\alpha)$) and athermal $\beta \rightarrow \omega$ ($M_s(\omega)$) are plotted against the concentration of Nb in Figure 2.1a. The composition, x_1 , at which the $M_s(\alpha)$ and the $M_s(\omega)$ lines intersect, defines the composition limit up to which the $\beta \rightarrow \alpha'$ martensitic transformation occurs on quenching an alloy from the β -phase field. In an alloy of composition x , where $x_2 > x > x_1$, formation of the athermal ω -phase inheriting the composition of the parent β -phase could be noticed on quenching from the β -phase field. This metastable product undergoes compositional changes during subsequent ageing when ω -particles depleted in the β -stabilizing element form, replacing the athermal ω -particles. The composition, x_2 , corresponds to the limiting composition for the formation of the athermal ω -phase. Beyond this composition, the β -phase can be retained at room temperature by quenching. Upon ageing these alloys formation of isothermal ω has been observed in the composition range of $x_1 < x < x_3$ [23].

2.2.1 A brief review on martensitic phase transformation

Mechanistically, a martensitic phase transformation is an example of a lattice strain dominated displacive transformation, wherein, the movements of atoms are accomplished by a homogeneous distortion of the parent lattice. These atoms move less than inter-atomic distances in a co-operative manner to bring in the required crystal structure of the product phase without changing its composition. The co-operative movement results in (i) inheritance of lattice correspondence, in which, a particular direction or plane in the parent crystal becomes a corresponding direction and plane in product crystal, respectively, (ii) inheritance of atomic coordination, in which, atom tries to retain the same set of neighbours both in the parent as well as in the product structures [48,49]. Such a transformation can be viewed as a homogeneous deformation of the parent lattice.

2.2.1.1 Driving force for martensitic transformation

Figure 2.2 schematically shows the change in chemical free energies of martensite and austenite (parent phase in Fe-based systems) with temperature. T_0 is the temperature at which the austenite and martensite are in thermodynamic equilibrium and M_s is the temperature at which the transformation starts upon cooling. The difference in free energies between austenite (γ) and martensite (α') at the M_s temperature, $\Delta G_{M_s}^{\gamma \rightarrow \alpha'}$, is the critical chemical driving force for the

onset of the martensitic transformation. In general, the free energy change associated with a martensitic transformation is given by:

$$\Delta G^{P \rightarrow M} = \Delta G_C^{P \rightarrow M} + \Delta G_{NC}^{P \rightarrow M} \quad (2.1)$$

$\Delta G_C^{P \rightarrow M}$ is the chemical free energy change (per unit volume of transformation) associated with the transformation from the parent phase to martensite, and $\Delta G_{NC}^{P \rightarrow M}$ is the nonchemical energy opposing the transformation (consisting of elastic strain and surface energy). Since the martensite-parent interface is semi-coherent the surface energy term should be small, and the elastic energy term will dominate. The chemical driving force can be assisted by externally applied stress ($<$ yield stress of parent phase). Referring to Figure 2.2, when a stress is applied to the austenite at T_1 (between M_s and T_0), the mechanical driving force, U , due to the stress is added to the chemical driving force, $\Delta G_{T_1}^{\gamma \rightarrow \alpha'}$, and the martensitic transformation starts at the critical stress where the total driving force is equal to $\Delta G_{M_s}^{\gamma \rightarrow \alpha'}$. U' ($=\Delta G_{M_s}^{\gamma \rightarrow \alpha'} - \Delta G_{T_1}^{\gamma \rightarrow \alpha'}$) in Figure 2.2 is the critical mechanical driving force needed for the stress-induced martensitic transformation at T_1 [50-52].

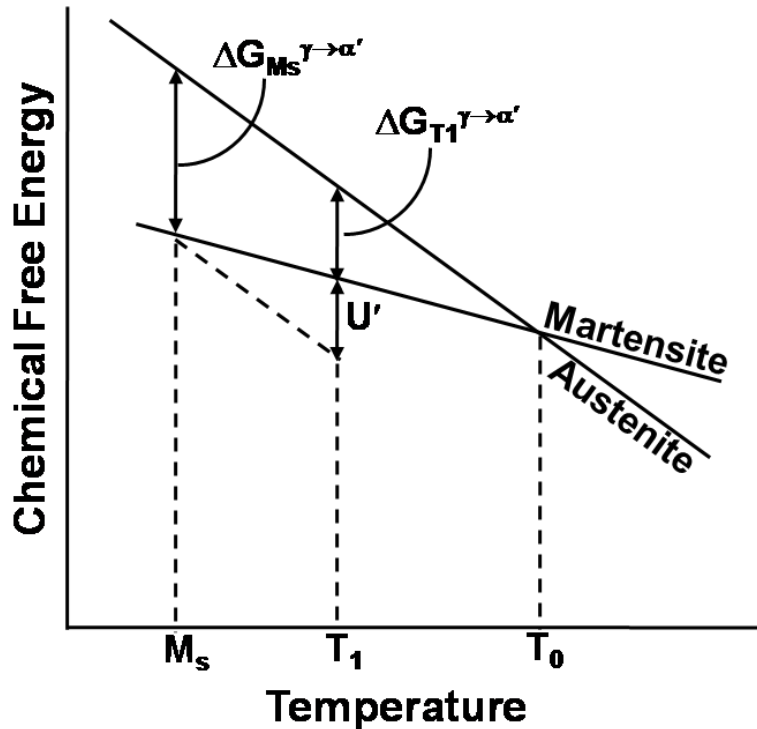


Figure 2.2 Schematic diagram showing the free energy change for a martensitic transformation.

2.2.1.2 Phenomenological theory of martensite crystallography (PTMC)

A martensitic transformation is always associated with a macroscopic shape deformation or shape strain, wherein, the interface plane or the habit plane remains (i) undistorted and (ii) unrotated i.e., it can be described in terms of an Invariant Plane Strain (IPS). The IPS can be accomplished by a simple shear (s). In general all martensitic transformations are associated with a volume change, which can be thought off as a dilatation normal to the shear. Hence the general IPS can be considered as a combination of a shear component and a dilatation component.

The total transformation crystallography accounting the observed IPS shape deformation, widely known as phenomenological theory of martensite crystallography (PTMC), constitute of three steps: (i) Bain Strain (B), (ii) Rigid Body Rotation (R) and (iii) Lattice Invariant Shear (LIS) [53-55]. Bain Strain is a homogeneous lattice distortion which brings about the required crystal structure change during the transformation involving smallest principal strains [53]. Bain Strain does not leave any plane invariant i.e., undistorted and unrotated. Hence an additional deformation is required to make a plane undistorted. This additional deformation must be lattice invariant, as it should not bring about any change in the crystal structure. This additional deformation normally comes in the form of a inhomogeneous shear, called as Lattice Invariant Shear (LIS) and gets manifested as slipped or twinned martensite substructure. Application of LIS leaves plane undistorted, but not unrotated. Hence a third operation known as Rigid Body Rotation is required to nullify the rotation effect of Bain Strain. Bain Strain (B) and Rigid Body Rotation (R) together constitute the net homogeneous lattice deformation which is also known as Invariant Line Strain (ILS). ILS leaves a single line undistorted and un-rotated in the interface between austenite and martensite.

The PTMC with respect to $bcc \rightarrow hcp$ martensitic transformation is illustrated in the following drawing reference to Zr-2.5Nb alloy. Figure 2.3a shows the, in general, atomistic representation of the $bcc \rightarrow hcp$ transformation maintaining the following lattice correspondence: $(110)_b \rightarrow (0001)_M$; $[001]_b \rightarrow [2\bar{1}\bar{1}0]_M$; $[\bar{1}\bar{1}0]_b \rightarrow [0\bar{1}\bar{1}0]_M$; $[110]_b \rightarrow [0001]_M$ ($b = bcc \beta$, $M = hcp \alpha'$). Based on this orientation relationship (OR) six different variants of the hcp phase can originate from the bcc phase. The six variants arise due to the difference in the multiplicity of (110) plane of bcc and (0001) of hcp. In the case of Zr-2.5Nb alloy the lattice parameters of α' are $a_M = 0.3211\text{nm}$, $c_M = 0.5115\text{nm}$ and that of β is $a_b = 0.3577\text{nm}$ [56].

The Bain Strain expressed along the principal axes of the hcp cell can be written as:

$$\varepsilon_1 = (a_M - a_b)/a_b = -10\% \quad (2.2)$$

$$\varepsilon_2 = (\sqrt{3}a_M - \sqrt{2}a_b)/(\sqrt{2}a_b) = +10\% \quad (2.3)$$

$$\varepsilon_3 = (c_M - \sqrt{2}a_b)/(\sqrt{2}a_b) = +1\% \quad (2.4)$$

Figure 2.3b represents the Bain deformation in form of shape change of a circle where one axis of the circle (X_2) is elongated by 10% and another axis (X_1), perpendicular to X_2 , is compressed by 10% resulting in its distortion into an ellipse. The third axis (X_3), which is perpendicular to both X_1 and X_2 , can be considered to have remained undistorted as it undergoes elongation by only 1% which can be approximated as zero. Hence, it can be seen that even without the application of LIS the criteria of an undistorted plane (viz., a combination of positive, negative and zero principal strains) gets satisfied. In other words, the amount of LIS that will be required to make the plane undistorted will be very small. OA' in Figure 2.3b represents the undistorted plane in two dimensions. A rigid body rotation of the ellipse by an angle γ about X_3 ($[0001]_M$) leads to an invariant plane (invariant line in two dimensions) associated with the phase transformation, as shown in Figure 2.3c. The atomic arrangement after the rigid body rotation is illustrated in Figure 2.3d. When the angle between $[\bar{1}\bar{1}0]_b$ and $[0\bar{1}\bar{1}0]_M$ i.e., γ becomes 5.26° the orientation relationship is known as Burgers orientation relationship and is most commonly observed in case of bcc \rightarrow hcp transformations [55,57,58].

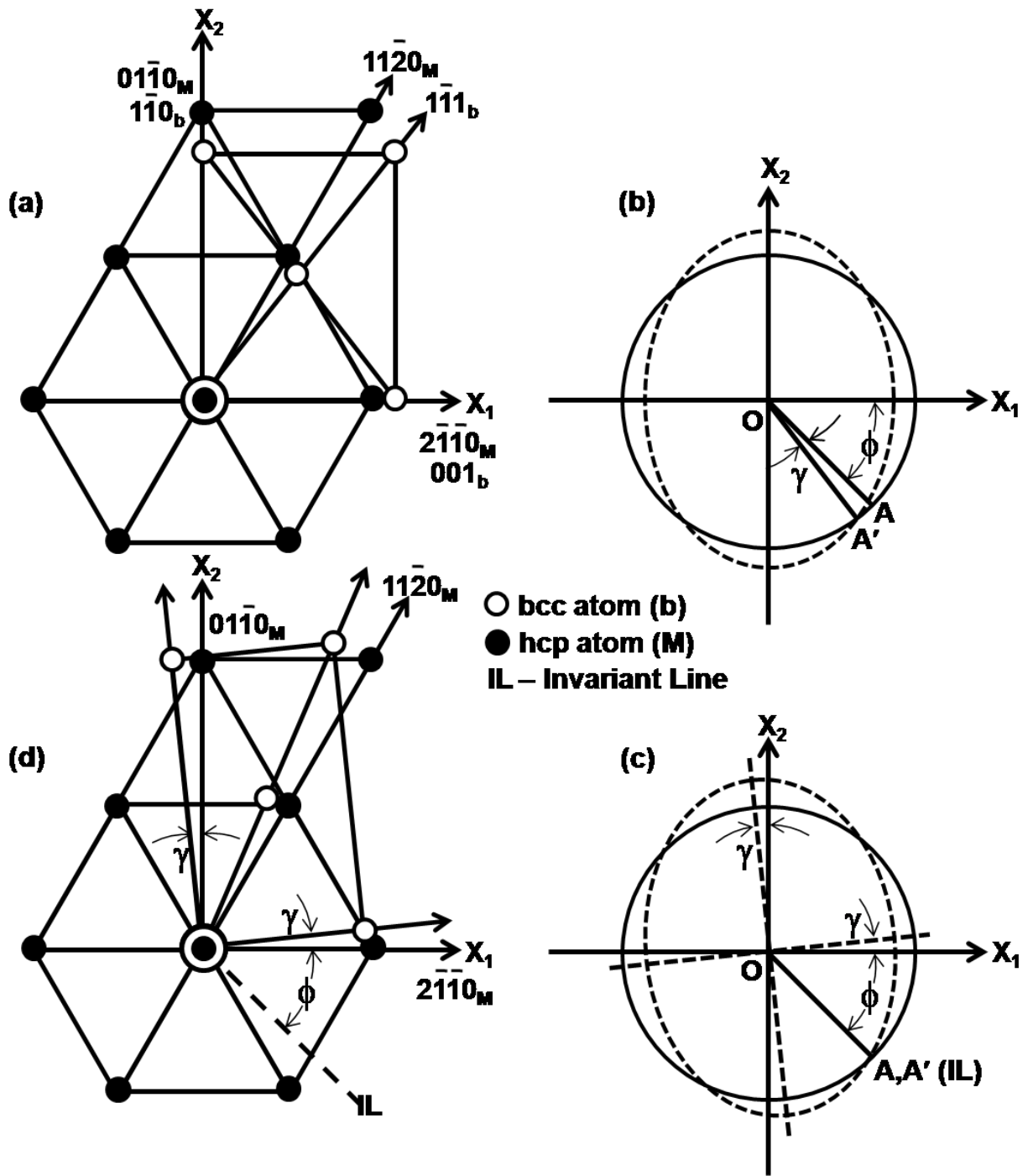


Figure 2.3 Atomistic representation of the $bcc \rightarrow hcp$ transformation on the matching $(0002)_M/(110)_b$ planes, with the corresponding two-dimensional shape change given by the circle to ellipse transformation, before (a), (b), and after (c), (d) the rigid body rotation required to produce an invariant line [59].

2.2.1.3 Martensite morphology and substructure

In general, martensite morphology can be classified under two broad headings viz., lath martensite and plate martensite.

(i) Lath martensite

The following are the characteristics of lath martensite [56,60,61]:

- High temperature product in dilute alloys.
- Morphology: thickness ($\sim 0.1\text{-}0.2\ \mu\text{m}$) < breadth ($10 \times$ thickness) < length (limited by parent phase grain size $\sim 30\text{-}40\ \mu\text{m}$).
- Individual laths arranged in parallel within a group.
- Several groups within a parent grain and units of a group non-parallel to units of adjacent group.
- Adjacent laths separated by high or low angle boundaries or twin related.

The substructure of lath martensite consists of network of tangled dislocations with dislocation density often reaching upto 10^{15}m^{-2} . Occasionally cell formation could be seen within the dislocation tangles. This high dislocation density may not be entirely related to transformation crystallography. Often strain energy due to the formation of martensite is accommodated in the martensite itself by its plastic deformation and this may lead to generation of high dislocations.

The β -quenched martensitic microstructure in Zr–1Nb alloy has been investigated and was found to be predominantly lath martensitic type with dislocated substructure. In addition to single variant, two and three variant groupings of mutually twin-related laths were also observed, which suggested the possibility of self-accommodation phenomenon coming into play (as explained in the following section). Figure 2.4 shows the arrangement of mutually twin related three variant lath martensite grouping in a Zr–1Nb alloy [45].

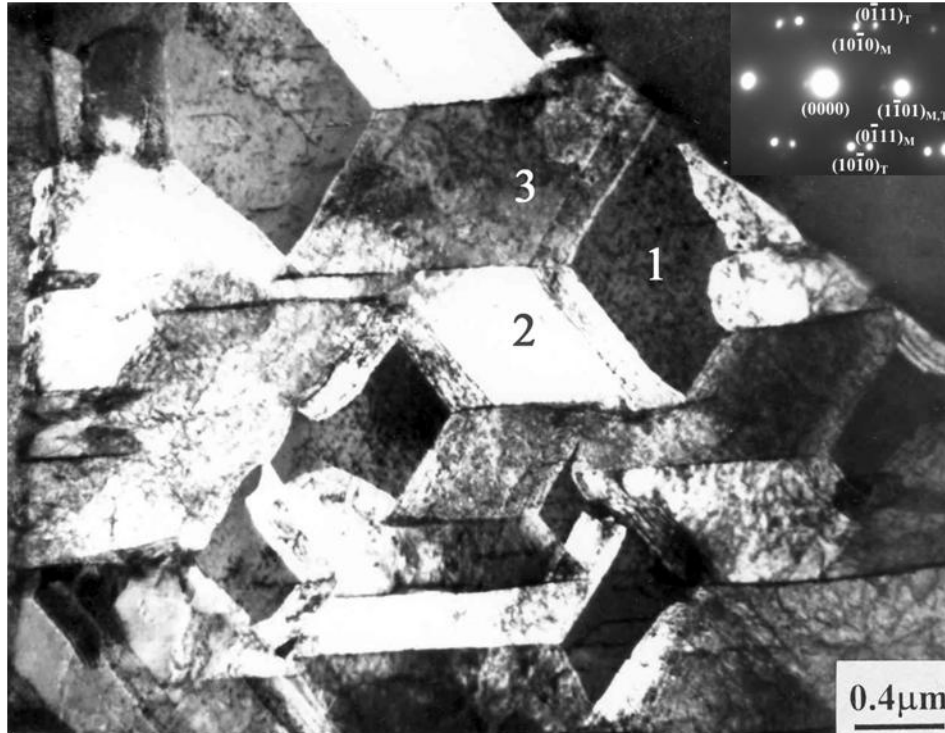


Figure 2.4 A bright-field TEM micrograph showing the mutually twin-related three variant lath martensite grouping in Zr–1Nb alloy water-quenched from the high temperature β -phase field. The three lath variants are marked as 1, 2 and 3 in the figure. The inset shows a typical twin related SAED pattern corresponding to 1-2, 2-3 and 3-1 lath-lath interfaces. The SAED pattern resembled $\{1\bar{1}01\}_\alpha$ type twinning [45].

(ii) Plate martensite

The following are the characteristics of plate martensite [56,60,61]:

- Low temperature product in concentrated alloys.
- Morphology: disc, lenticular plate - much thinner than lath martensite.
- Neighboring plates in a grain are non-parallel to one another and may be twin-related.
- Plates forming first partition parent grains into smaller pockets. Sub-partitioning by subsequently formed plates.

Figure 2.5 depicts the typical morphology of plate martensite observed in a Zr–2.5Nb alloy. The substructure of plate martensite consists of internal twins as shown in Figure 2.6.

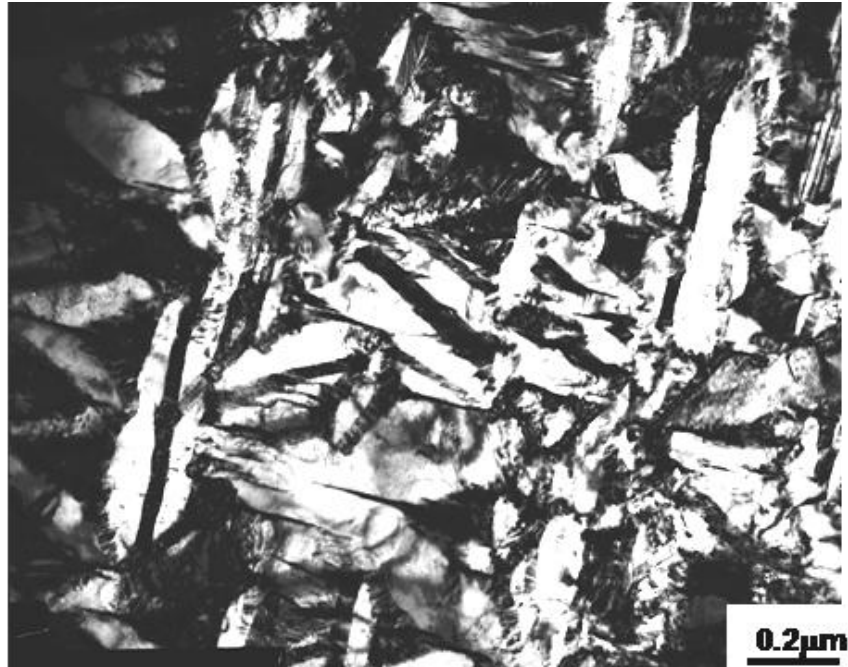


Figure 2.5 Bright-field TEM micrograph showing the typical morphology of plate martensite in a Zr-2.5Nb alloy water-quenched from the high temperature β -phase field [56].

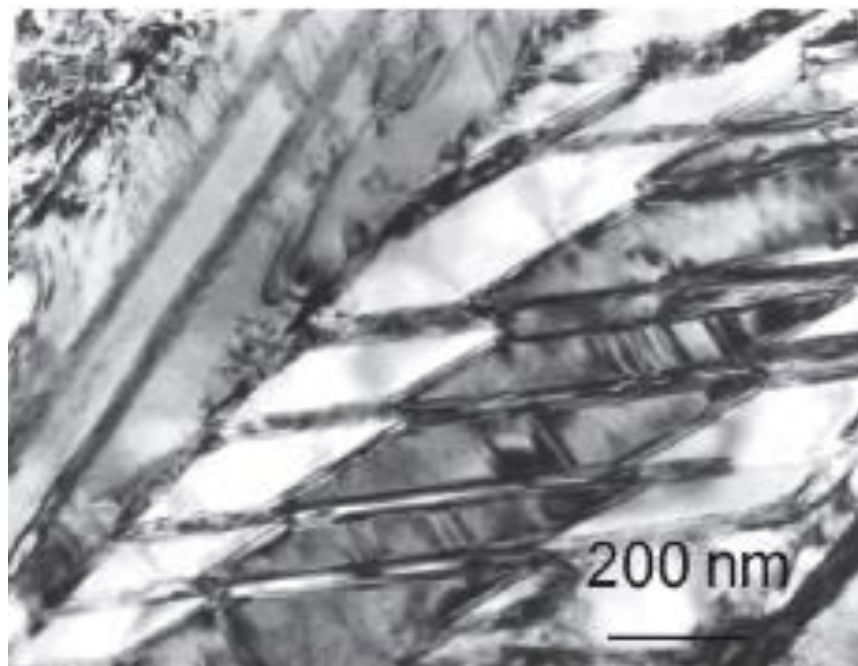


Figure 2.6 Bright-field TEM micrograph showing internally twinned plate martensites in a Zr-2.5Nb alloy water-quenched from the high temperature β -phase field [56].

2.2.1.4 Self accommodating morphologies of martensites

The process of minimization of strain energy does not remain confined to a individual martensite lath or plate. In a group of martensite laths or plates, mutual strain coupling can significantly reduce the overall strain energy. This is known as self-accommodation. The shape strain associated with ellipsoidal martensite plates causes an elastic strain field in the surrounding parent phase. The elastic strain fields of the different variants then interact with each other in such a manner that a maximum reduction in the strain energy density of the assembly of the plates and the matrix is achieved. The degree of self-accommodation (DSA) can be defined as:

$$DSA = 100 * (E^1 - E^N) / E^1 \quad (2.5)$$

where E^1 and E^N are strain energy density due to an isolated plate and group of 'n' plates, respectively. In case of Zr-2.5Nb alloy the strain energy accommodation was found to be ~ 62% for alternately twinned related laths and ~ 93% for alternately twin related three plate clusters (as shown in Figure 2.7) [56,60,61].

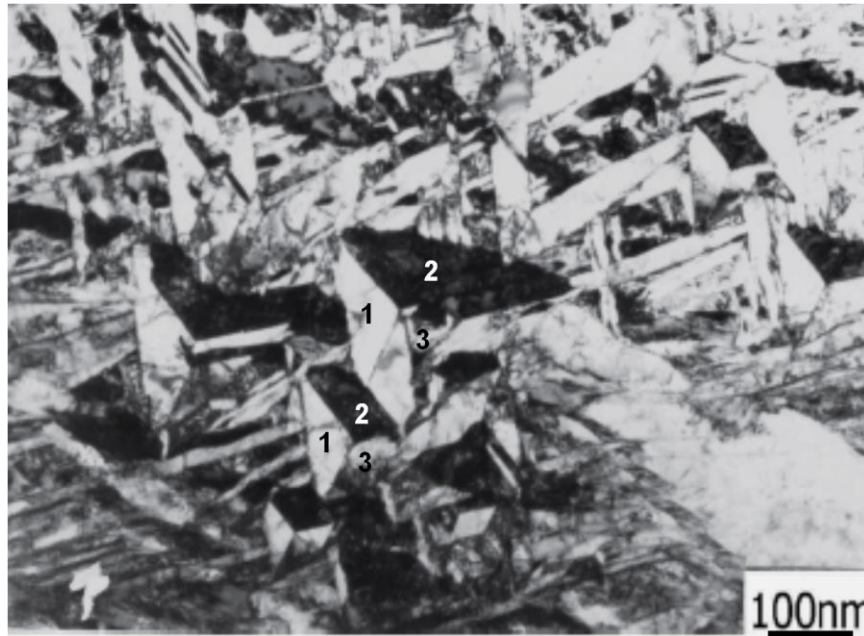


Figure 2.7 A bright-field TEM micrograph showing the presence of large number of self-accommodating mutually twin-related three variant martensite plate clusters of “indentation morphology” in Zr-2.5Nb alloy water-quenched from the high temperature β -phase field [56]. The three plate variants are marked as 1, 2 and 3 in the figure.

2.2.2 A brief review on omega phase transformation

In contrast to martensitic transformation, omega phase transformation is an example of a shuffle dominated displacive phase transformation wherein the atoms movements are accomplished by shuffling of lattice planes.

2.2.2.1 Characteristics

- First reported in Ti–8 wt.% Cr alloy by Frost et al. [62].
- Equilibrium phase under high-pressure in-group IV metals like Ti, Zr, Hf [63,64].
- Metastable phase in alloys of Ti, Zr, Hf containing β -phase stabilizing elements and other bcc alloys at ambient pressure [63,64].
- Occurrence [65]
 - Under high pressure (static pressure $\alpha \rightarrow \omega$; shock pressure $\alpha \rightarrow \omega$, $\beta \rightarrow \omega$)
 - Under thermal treatment $\beta \rightarrow \omega$ (athermal, isothermal)
 - Under deformation
 - Under irradiation

2.2.2.2 Thermally induced omega phase formation

The characteristics which qualify $\beta \rightarrow \omega$ transformation as an athermal process are listed in the following [66]:

- transformation is insuppressible even by extremely rapid quenching.
- large number density of particles (10^{18} - 10^{19} cm⁻³).
- inherits the composition of the parent phase.
- continuously and completely reversible.
- exhibits a well defined start temperature.
- appearance of extensive diffuse intensity distribution in diffraction pattern.

Similarly, the characteristics which qualify $\beta \rightarrow \omega$ transformation as an isothermal process constitute of following [66]:

- increase in volume fraction with time.
- composition of ω -phase is different from the β -phase.

The need of solute separation essentially arises due to the solute partitioning in the β -phase. The formation of the ω -phase, therefore, remains displacive in nature [66].

2.2.2.3 Crystallographic basis of $\beta \rightarrow \omega$ transformation

The crystallographic basis of the $\beta \rightarrow \omega$ transformation has been reviewed on various occasions [64,67,68]. The $\beta \rightarrow \omega$ transformation occurring on quenching of Zr–Nb alloys with low Nb content may be described by an hexagonal description of the parent β -phase as shown in Figure 2.8a. The β -phase, with a lattice parameter a_β , is represented by means of an hexagonal cell with lattice parameters a_{bcc} and c_{bcc} , which are related to a_β by: $a_{bcc} = \sqrt{2}a_\beta$ and $c_{bcc} = (\sqrt{3}/2)a_\beta$.

The lattice correspondence used in this description is as follows:

$$(111)_b // (0001)_h$$

$$[111]_b // [0001]_h \rightarrow Z$$

$$[\bar{1}\bar{1}0]_b // [11\bar{2}0]_h \rightarrow X$$

$$[0\bar{1}\bar{1}]_b // [\bar{2}110]_h \rightarrow Y$$

(b = bcc; h = hexagonal)

In this depiction there are three atom positions at $(0, 0, 0)$, $(1/3, 2/3, 1/3)$ and $(2/3, 1/3, 2/3)$ within the unit cell which represents the bcc lattice in hexagonal form. The atomic position at the origin will be referred to as an A-type site and the other two positions as B-type sites, as indicated in Figure 2.8b. During the $\beta \rightarrow \omega$ transformation, lattice dimensions do not vary too much but the atoms located at $(1/3, 2/3, 1/3)$ and $(2/3, 1/3, 2/3)$ moves towards each other. Therefore, lattice registry does not alter during the transformation, and the transformation ensues when the two atoms reach in the middle at $(1/3, 2/3, 1/2)$ and $(2/3, 1/3, 1/2)$ positions. Such structure with hexagonal symmetry ($P6/mmm$) is called as ‘ideal’ ω , which is observed in pure-Zr at high pressures. The athermal ω -phase in Zr–Nb alloys with up to about 8 wt.% Nb has been reported to have the ‘ideal’ structure. When the Nb-content of the alloy is as high as 15 wt.%, the $\beta \rightarrow \omega$ transformation leads to an ω -structure with trigonal symmetry ($P\bar{3}m1$), wherein, the atoms at the B-type sites are displaced slightly out of the (0001) plane alternately up and down in the direction of the c -axis of the structure. In general, the positions of the two B-type sites can be described by $(1/3, 2/3, 1/3 + z)$ and $(2/3, 1/3, 2/3 - z)$, where $0 \leq z \leq 1/6$. A value of $z = 1/6$ describes the ‘ideal’ ω -phase, $0 < z < 1/6$ the trigonal ω -phase and $z = 0$ the bcc β -structure ($Im\bar{3}m$) [69–71]. The $\beta \rightarrow \omega$ transformation is also associated with changes in the lattice parameters of the hexagonal cell as shown in Figure 2.8, i.e., $a_\omega \neq a_{bcc}$ and $c_\omega \neq c_{bcc}$ [39].

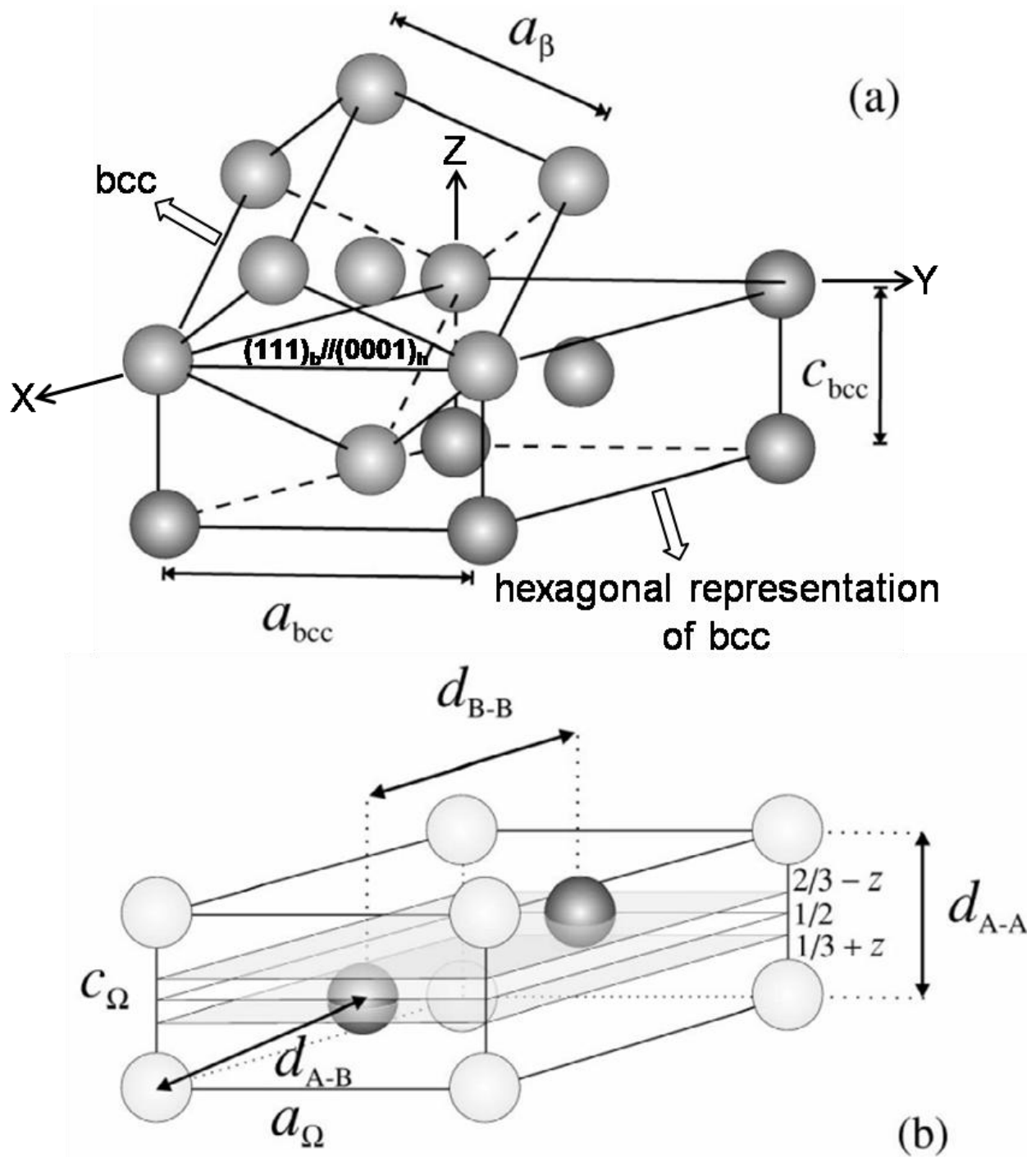


Figure 2.8 (a) Geometrical relations between the hexagonal representation of the bcc structure and the traditional cubic cell. (b) The unit cell of the trigonal ω phase. Light grey spheres and dark grey spheres represent the A-type and B-type sites, respectively. The z parameter determines the position of the B-type sites. The lattice parameters, as well as the $d_{\text{A-A}}$, $d_{\text{A-B}}$ and $d_{\text{B-B}}$ interatomic distances are indicated [39].

The atomic movements necessary to bring in the $\beta \rightarrow \omega$ transformation, based on the lattice correspondence between the β - and ω - structures mentioned above, can be viewed as collapsing of a pair of adjacent $(222)_\beta$ planes (e.g. “1” and “2” in Figure 2.9) leaving the “0” and “3” planes undisplaced. This results in a transition from the ABCABC..... stacking of the bcc-structure (in Figure 2.9, these three layers are depicted as “0 1 2”) into the AB’AB’..... stacking of the ω -structure (shown as “0 1.5 3” in Figure 2.9), where B’ planes correspond to the collapsed position located midway between B and C planes. A view along the $[111]_\beta$ direction shows how the threefold rotation symmetry changes to a six-fold symmetry where the collapse is complete (Figure 2.9). The ordered sequence of the displacement of the $\{111\}_\beta$ type planes which causes the $\beta \rightarrow \omega$ transition can be represented by a displacement wave with wavelength $\lambda = 3d_{222}$, the corresponding wave vector, K_ω , being equal to $2/3\langle 111 \rangle^*$ (where $\langle 111 \rangle^*$ is a vector in the reciprocal space). The development of the longitudinal displacement wave (Figure 2.9) along the $[111]$ direction can, therefore, formally describe the transformation [72,73].

The lattice correspondence of the $\beta \rightarrow \omega$ transformation invokes the possibility of formation of four distinct crystallographic variants of the ω -phase, as listed in Table 2.1 [74]. Based on this information composite simulated selected area electron diffraction (SAED) patterns containing reflections from both the β - and the ω - phases can be generated which could be used to identify the presence of different variants of the ω -phase. Figure 2.10 shows such simulated patterns of $(\beta + \omega)$ aggregates corresponding to the different zone axes of the β -phase. In fact, patterns corresponding to all zones excepting the $[100]_\beta$ and the $[111]_\beta$ invariably show extra diffraction spots of the ω -phase which divide all bcc reciprocal lattice vectors into three equal segments.

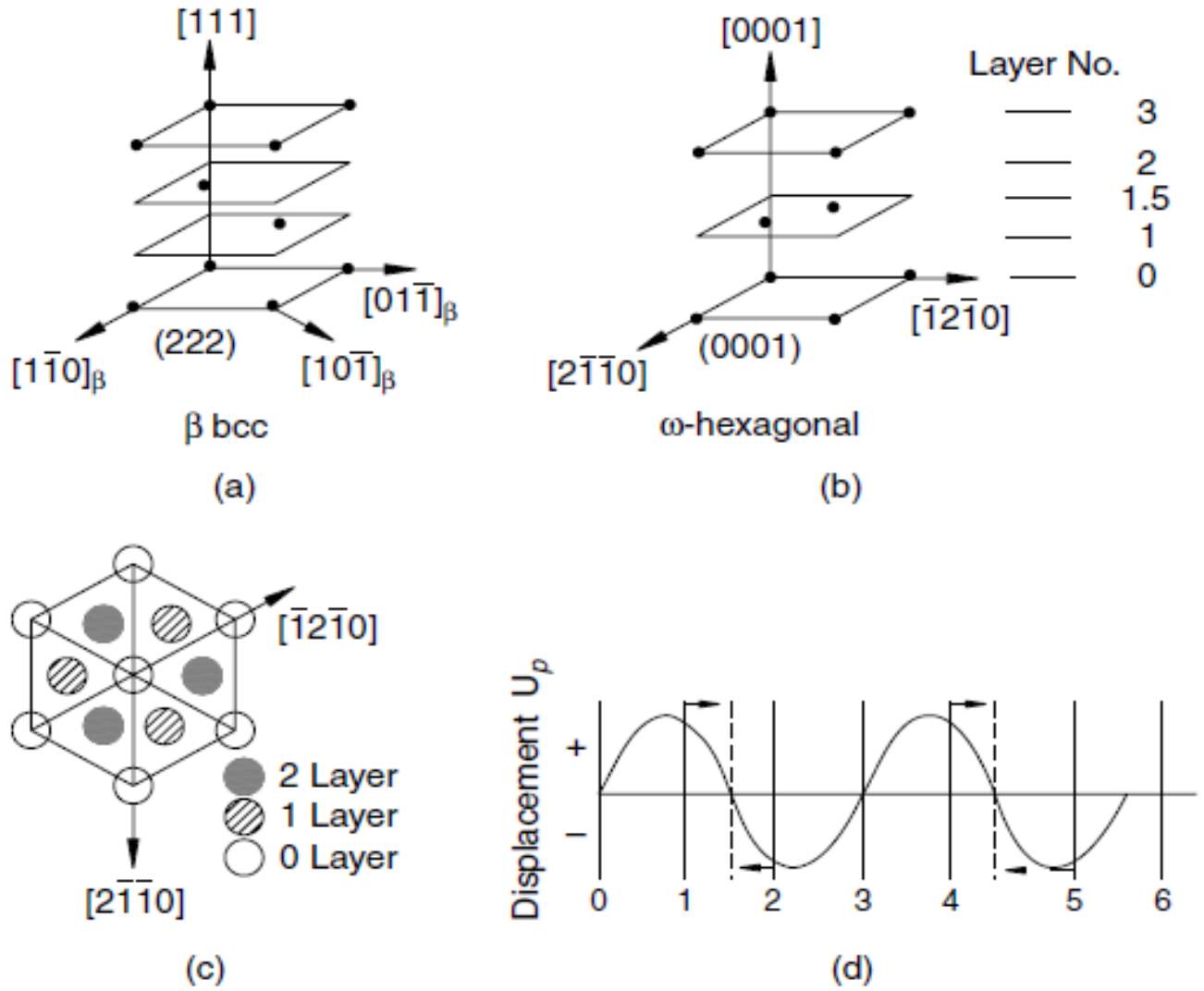


Figure 2.9 Lattice collapse mechanism of $\beta \rightarrow \omega$ transformation [65].

Table 2.1 Four possible orientation relationship in the bcc (β) and hexagonal (ω) crystal structures [74].

Variant	Orientation relationship	
	Planes	Directions
1	$(111)_\beta // (0001)_\omega$	$[\bar{1}10]_\beta // [1\bar{2}10]_\omega$
2	$(\bar{1}11)_\beta // (0001)_\omega$	$[\bar{1}\bar{1}0]_\beta // [1\bar{2}10]_\omega$
3	$(\bar{1}\bar{1}1)_\beta // (0001)_\omega$	$[1\bar{1}0]_\beta // [1\bar{2}10]_\omega$
4	$(1\bar{1}1)_\beta // (0001)_\omega$	$[110]_\beta // [1\bar{2}10]_\omega$

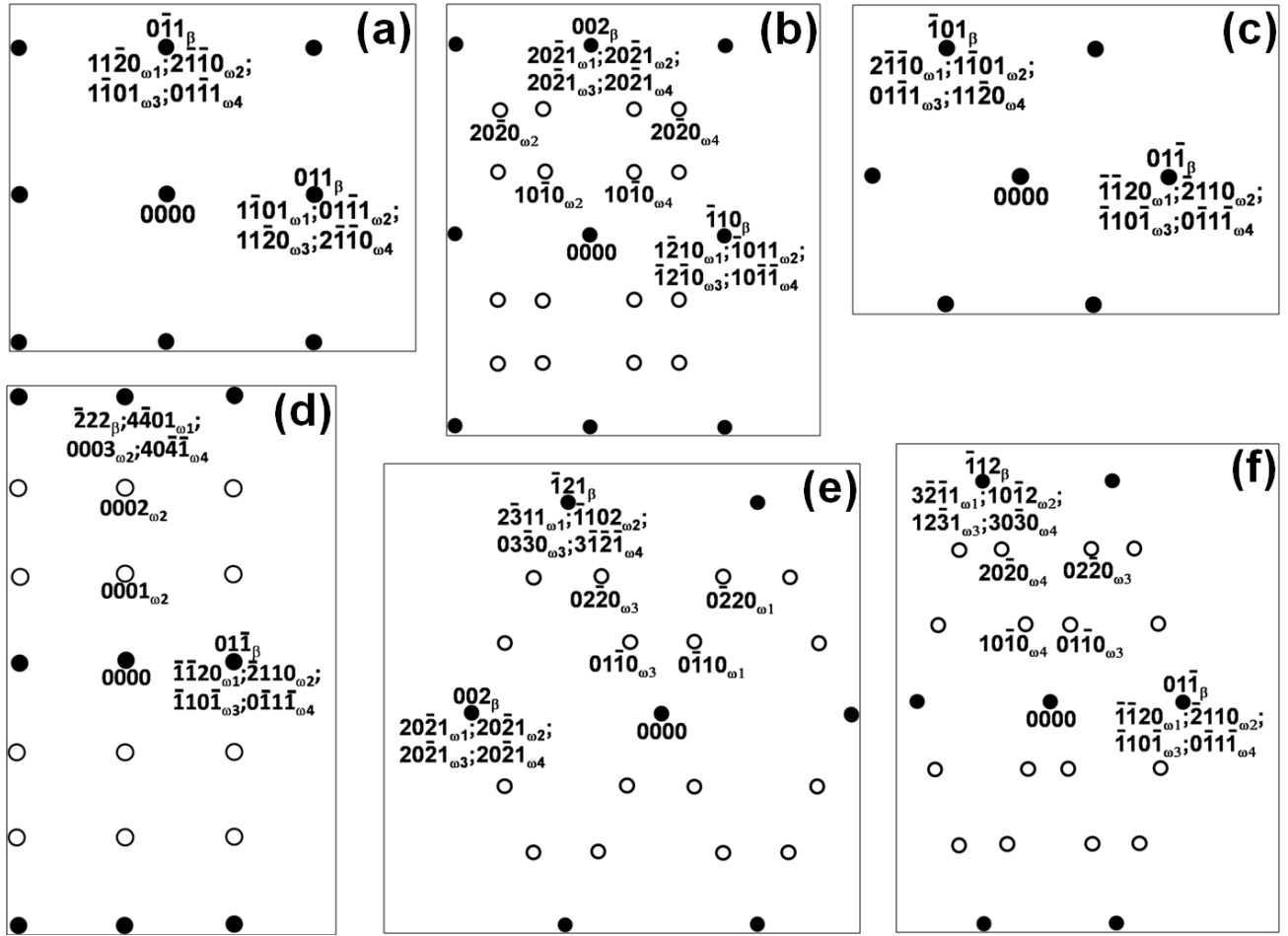


Figure 2.10 Simulated composite SAED patterns from (a) [100], (b) [110], (c) [111], (d) [211], (e) [210] and (f) [311] zone axes of the β -phase. Filled circles represent reflections corresponding to the β -phase, whereas, open circles represent those due to the ω -phase. The indices corresponding to the β - and ω -phase reflections have been marked in the figures. Numbers 1, 2, 3 and 4 in the figures represent variant number of the ω -phase as per Table 2.1.

2.3 Martensitic and Omega phase transformations in nano-dimension

A rich literature explaining the mechanisms of martensitic and omega phase transformations in Zr–Nb system and the various observed morphologies of the transformation products therein is already in existence [60,64,69-71,75-104]. However, it is worth emphasizing that all these studies have mostly considered transformations taking place within parent phase of few μm in size. Since one of the objectives of the present work is to examine the feasibility of martensitic and omega phase transformations in β -phase of different length scales ranging from micrometers to nanometers in Zr–Nb alloy, it would be meaningful to have a brief in general review of the occurrences of these transformations in parent phase of nano-dimension in different alloy systems.

Although, investigations with regard to martensitic transformation in nanometer-sized γ -Fe precipitates in dilute Cu–Fe alloys with or without Ni-addition have been reported by several researchers [105,106], studies dealing with omega phase transformation in nanometer-sized parent phase are not reported. Martensitic transformation could not be brought about in 2–200 nm sized austenitic fcc γ -Fe precipitates, present within the Cu-matrix of Cu–(1-2.5) wt.% Fe alloys, when quenched from a temperature higher than the M_s temperature for bulk γ -Fe phase of same composition. However, upon mechanical working the nano γ -Fe precipitates got transformed to bcc α -Fe martensitically. The dilatation accompanying the transformation caused considerable plastic deformation resulting in generation of dense dislocation tangles in the matrix. It was proposed that martensitic transformation in these precipitates got nucleated while dislocations were traversing the precipitate. In the strain field of a dislocation, atoms may attain such positions which assist them to adopt the bcc configuration. The additional force needed to induce the stable bcc configuration of α -Fe was assisted by the shear stress acting on the dislocations. With regard to the non-occurrence of the transformation upon quenching (even upto 1.43 K) it was suggested that the precipitates were either too small or too faultless to nucleate martensite. Suppression of the transformation despite of having a high thermodynamic driving force could be attributed to the dilatation accompanying the transformation which was opposed by the restraining forces of the surrounding Cu-matrix [106]. On removal of matrix constraints by partial or complete electrochemical isolation of the precipitates from the matrix led to the martensitic transformation of the precipitates into bcc α -Fe. The extraction of precipitates may as

well aid in the transformation due to the plausibility of any defect or deformation getting introduced into the precipitates during extraction. However, such contributions even if present are normally insignificant [105].

However, a critical size of the precipitate of ~ 20 nm also existed below which the transformation could not be induced even upon mechanical working [107]. The role of matrix constraints, in lending stability to the austenitic precipitates, was found to offer an unusually large temperature range over which austenite could be induced to transform to martensite by deformation, thus bringing about the dependence of martensite substructure on the transformation temperature. At temperatures in the vicinity of the bulk M_s temperature the precipitates were found to transform to single crystal of martensite in which the lattice invariant shear was accommodated by slip, whereas, near ambient temperatures the precipitates transformed to twinned martensite [108].

2.4 Development of U–9Mo alloy as nuclear research and test reactor fuel

U-based fuels in two different geometries, viz., dispersion and monolithic, are used in nuclear research and test reactors. In dispersion-type, particulates of fuel material are dispersed in a matrix of Al or Al-alloy to form a fuel-meat which is encapsulated in Al or Al-alloy cladding. In monolithic-type, the fuel comprises of a thin foil of the fuel material cladded in Al or Al-alloy.

The past three decades have seen a considerable drive in the direction of using low enriched U (LEU < 20 wt.% U^{235}) fuels in all new research reactors and for conversion of highly enriched U (HEU > 20 wt.% U^{235}) fuels of existing reactors to low enriched ones. Such efforts, under the umbrella of Global Threat Reduction Initiative (GTRI) and Reduced Enrichment for Research and Test Reactor (RERTR) programs, were initiated to address the concerns on nuclear proliferation and diversion [1,109]. The use of a low enriched U-core calls for a direct increase either in the fuel loading or in the total density of U-atoms in the fuel to keep the neutronics of the reactor unaffected [2,110]. The former option does not seem viable, as the roll bonding technique, which is an established fabrication methodology for making plate-type fuel, does not allow producing dispersoid fuel with volume of very high U-density fuel particle (> 15 g U cm^{-3}) exceeding 55% [111-114]. This volume limitation is further lowered in the case of extrusion, the other common commercial fabrication process of making rod-type and tube-type fuels [114]. Hence, increasing the U-density in the fuel itself to more than 15 g U cm^{-3} [9] or fabrication of

monolithic fuel, emerge as other alternatives. Pure U-metal, U-alloys and high-density intermetallic U-compounds are the promising candidates to be relied upon to explore as alternative options.

Dispersion fuels having intermetallic compounds like U_3Si_2 and U_3O_8 and densities of 4.8 and 3.2 g U cm^{-3} , respectively, were initially developed [115]. Although U_3Si_2 , exhibiting stable irradiation behavior [116,117], is being successfully used in many research reactors across the world, the reprocessing issue associated with it [118] and simultaneously the urge for further increase in the heavy metal density to increase the thermal neutron flux, led to the consideration of other intermetallic compounds like U_3Si and U_6Me , where $Me = Fe, Mn, Ni, Co$ or Ge . However, the poor irradiation behavior shown by plate-type dispersion fuels made out of these compounds, due to breakaway swelling at relatively low burn up, left fuel designers with the only option of using either metallic U or U-alloys [5-8].

Pure-U exhibits three polymorphic forms in solid-state viz., orthorhombic α -phase stable up to $667 \text{ }^\circ\text{C}$, tetragonal β -phase stable between $667 \text{ }^\circ\text{C}$ and $771 \text{ }^\circ\text{C}$ and bcc γ -phase stable above $771 \text{ }^\circ\text{C}$ [8,24]. Unalloyed U-metal cannot be considered as a fuel mainly because of the poor irradiation behavior exhibited by the α -phase. Cavitation swelling under irradiation and thermal and irradiation growth under power ramping are the main causes behind the poor irradiation behavior of the α -phase [119]. The high temperature isotropic γ -phase in pure-U is known to behave in a stable manner under low-burnup, high temperature irradiation conditions on account of swelling through fission gas nucleation and growth [115,120]. Moreover, the γ -phase is desirable from fuel fabrication point of view and for corrosion resistance in water and water steam environments [3]. The γ -phase in pure-U cannot be retained at low temperatures. U containing small amount of γ -U stabilizing element like Cr, Mo, Nb, Re, Ru, Ti, V or Zr provide good prospect in this respect [12,121]. U–Mo alloy is one of the promising candidate materials for low enrichment U-fuel with high U-loading, because γ -U with Mo in solid solution possesses acceptable irradiation stability, mechanical properties, corrosion resistance and the γ -phase shows wide phase-field in U–Mo binary system [3,120,122,123]. Besides, Mo has a lower parasitic absorption cross-section for neutrons [10].

Although the stability of the γ -phase increases with Mo-concentration, the maximum content of Mo in U–Mo alloy for LEU Fuel is set at 10 wt.%, so that the criterion of achieving

maximum U-density is met with [124]. Thus, Mo-addition in the range of 5.4 to 10 wt.% is sufficient in stabilizing the γ -phase thereby maintaining a high U-density in the fuel [9,10,12,115,122,124-126]. Densities of up to 8 and 17 g U cm⁻³ are achievable with U–Mo as dispersion fuel (in Al-matrix) and as monolithic fuel, respectively [125,126]. Hence, U–Mo alloys are a promising candidate for a fuel that offers a balance of high fissile material density and stable irradiation behavior [2,11,127-133].

2.5 Phase transformations exhibited by the binary U–Mo system

The binary Mo–U phase diagram [24] is shown in Figure AI.2, and the invariant phase reactions exhibited by it are listed in Table 2.2.

Table 2.2 Invariant reactions in the Mo–U system.

Reaction	Temperature (°C)	Phase composition (wt.% Mo)			Reference
Liquid + Mo \leftrightarrow γ -U	1284 \pm 2	16	93	22	[24]
β -U \leftrightarrow α -U + γ -U	639 \pm 5	0.5	0.04	5.6	[134]
γ -U \leftrightarrow γ' (U ₂ Mo)	625	16.5	16.5	-	[24]
γ -U \leftrightarrow Mo + γ' (U ₂ Mo)	580	18	98.5	17	[24]
γ -U \leftrightarrow α -U + γ' (U ₂ Mo)	565 \pm 5	10.5	0.02	16	[134]
	560	10.0	0.02	16	[24]
	556	9.7	0.02	16	[135]
	555	11.1	0.02	16	[136]

A number of metastable phases have also been reported in U–Mo system in U-rich alloys, viz., α' , α'' and γ^o , depending on the Mo-content and the cooling rate following solution treatment in the γ -phase, as listed in Table 2.3. U–Mo alloys containing up to 4.8 wt.% Mo when water-quenched from the γ -phase field are called “ α -phase” alloys, as the structure of the metastable phases obtained are slight variations of the orthorhombic lattice of unalloyed α -U [137]. U–Mo alloys containing upto 2.6 wt.% Mo assume a ‘distorted’ orthorhombic structure (α') with expanded and contracted ‘a’ and ‘b’ α -U lattice parameters, respectively [137,138]. Infact, the ‘a’ parameter increases only slightly with Mo-addition, whereas, the ‘b’ parameter

steadily decreases on increasing the Mo-content of the alloys to 2.9 wt.%, after which the rate of contraction decreases [137]. It was proposed that in U–Mo alloys with Mo-contents, such as 0.1, 0.2 and 0.3 wt.%, wherein the alloys pass through the single β -phase field in the course of cooling from the γ -phase transforms to α' via the formation of the β -phase in between [137]. This is because the formation of the intermediate β -phase is insuppressible even at cooling rates of 10^4 °C/s [139]. However, since in this case the formation of α' is not a result of direct shearing of the γ -lattice, rather a transformation of the retained β -phase, it would be rational to call it as α instead of α' . Tangri and Williams [137] and Hills et al. [140,141] have, however, shown that a direct transformation of the γ -phase to α' , by shear, occurs in U–Mo alloys with Mo-content not less than 1 wt.%, which also include compositions passing through the ($\beta + \gamma$) phase-field while cooling from the γ -phase. U–Mo alloys with $2.6 < \text{Mo} \leq 4.8$ wt.% transform into a monoclinic structure (α''), where in addition to a progressive decrease in the ‘b’ parameter and a slight increase in the ‘a’ and ‘c’ parameters of the α -U lattice, an abrupt increase in the angle γ (between ‘a’ and ‘b’ axes) from 90° occur [137,138,142,143]. Moreover, the volume of the monoclinic unit cell decreases on increasing the Mo-content of the alloy [142]. Similar to “ α -phase” alloys, U–Mo alloys containing more than 4.8 wt.% Mo are called “ γ -phase” alloys, since the structures obtained after γ -quenching are related to the bcc structure of the γ -phase in unalloyed-U [137,144-148]. For example, in U–Mo alloys containing Mo in the range of 4.9 wt.% to 5.6 wt.%, the water-quenched structure assume a body centered tetragonal unit cell (γ^0), which is obtained by doubling the ‘a’ and ‘b’ and contracting the ‘c’ axes of the bcc γ -phase cell [137,138,148]. It is to be further noted that the metastable structures γ^0 and α'' , in succession, are progressive stages in the generation of α' from the bcc γ -phase i.e., $\gamma \rightarrow \gamma^0 \rightarrow \alpha'' \rightarrow \alpha'$ [137]. This is due to the fact that the 4.8 wt.% Mo alloy, which on water quenching from the γ -phase field gave a α'' -structure, produced a γ^0 -structure when air-cooled [137]. Similarly, a 2.5 wt.% Mo alloy which formed α' on water-quenching, produced γ^0 on argon-quenching [137]. Moreover, Stewart and Williams [143] have shown that the monoclinic α'' -phase can be derived from a tetragonal phase, based on the bcc structure of γ -U, by a shear process. This tetragonal phase could be the γ^0 -phase. The γ -phase, in bcc form, could only be stabilized on water-quenching when the Mo-content of the alloy reached 5 wt.% [149,150]. Infact, stabilization of

the γ -phase as well on air-cooling has been reported to occur in a U-5.4 wt.% Mo alloy [147]. A further increase in the Mo-content of the alloy to 8 wt.% or beyond led to the stabilization of the γ -phase even on very slow cooling, like furnace cooling [115]. It is also to be noted that a very high cooling rate can also lead to the stabilization of the γ -phase in low Mo-containing alloys, as has been observed in U–Mo alloy powders prepared by centrifugal atomization with Mo-content ≥ 2 wt.% [10,122].

Table 2.3 Metastable phases in Mo–U system depending on the Mo-content and the rate of cooling from the γ -phase.

Wt.% Mo	Phase								
	Water quench ($\sim 10^3$ $^{\circ}\text{C/s}$) [137]	Water quench (~ 500 $^{\circ}\text{C/s}$) [151]	Mercury quench	Argon quench (~ 220 $^{\circ}\text{C/s}$) [137]	Iced brine quench (~ 50 $^{\circ}\text{C/s}$) [148]	Oil quench [140]	Air cool ($\sim 10^{\circ}\text{C/s}$) [137]	Air cool (~ 2.3 $^{\circ}\text{C/s}$) [148]	Air cool [140]
1.0			α' [140]						
1.2	α'								
1.4			α' [141]						
1.6	α'								
1.7			α' [141]						
2.0		α'							
2.1			α' [140]						
2.5	α'			α''	α' or α''			α' or α''	
2.6	α'								
3.0	α''						α''		
3.2			α'' [140]						
3.4					α'' or α'			α''	
3.6	α''								
3.8					α''			α''	
4.2	α''								

Table 2.3 (continued)

4.3			α'' [140]		α''			α''	γ°
4.7	α''				α''			γ° (c/a = 0.5)	
4.8	α''						γ° (c/a < 0.5)		
4.9	γ° (c/a < 0.5)						γ° (c/a = 0.5)		
5.0			γ° [140]			γ°			
5.4			γ° [140]						
5.6	γ°								

The dimensional stability of γ -phase stabilized U–Mo alloys, with respect to irradiation induced growth and swelling, is related to the ability of these alloys to retain the γ -phase at the temperature of interest. As mentioned in Table 2.2, the γ -phase eutectoidally decomposes to α -U and tetragonal γ' (U₂Mo) phases, for which several different values corresponding to the invariant temperature and composition are reported. Thus, from the data in Table 2.2 it may be assumed that the γ -phase can only exist in a metastable state below ~ 570 °C. Hence, an overview of different investigations carried out to examine the isothermal decomposition characteristics of the γ -phase has been presented in the following section.

2.5.1 Decomposition aspects of the metastable γ -phase in binary U–Mo alloys

The kinetics of decomposition of metastable γ -phase have been investigated widely in U–Mo alloys containing between 1.6 to 25 wt.% Mo [152-161]. All these studies have mostly determined the incubation time of the transformation at different temperatures employing experimental techniques ranging from metallography, hardness, resistivity, X-ray diffraction to dilatometry. The data was represented in form of time–temperature–transformation (T–T–T) diagrams. The initiation time of the decomposition reaction was found to vary for any given alloy composition and temperature depending upon the technique used to assess it. A few of these studies also attempted to work out the decomposition mechanism of the γ -phase depending upon the temperature of ageing and the Mo-content of the alloy.

In low Mo-content alloys, like U-1.6 wt.% Mo [152] and U-2.5 wt.% Mo [154], annealing at temperatures lying within the ($\beta + \gamma$) phase field proceeded with the nucleation of stringers of β -phase both at the grain boundaries as well as within the γ -grains. Similarly, annealing within the two-phase ($\alpha + \gamma$) phase field resulted in the nucleation of α -phase in form of lamellae both within the grains and at the grain boundaries of the γ -phase. Annealing in the ($\alpha + \gamma'$) phase field resulted in the following decomposition sequence of $\gamma \rightarrow (\alpha + \gamma) \rightarrow (\alpha + \gamma + \gamma') \rightarrow (\alpha + \gamma')$, provided the annealing temperature was above the M_s temperature for the formation of the α' -phase ($M_s(\alpha')$). Annealing at just below the $M_s(\alpha')$ the decomposition reaction proceeded as $\gamma \rightarrow (\alpha' + \gamma) \rightarrow (\alpha + \alpha' + \gamma) \rightarrow (\alpha + \alpha' + \gamma')$. On further lowering the annealing temperature the formation of the γ' -phase did not take place. The $M_s(\alpha')$ temperatures for 1.6 wt.% and 2.5 wt.% Mo alloys were found to lie between 520-550 °C [152] and 400-450 °C [154], respectively.

In respect of high Mo-containing U-Mo alloys, all studies carried out could arrive at a consensus with respect to the sluggish decomposition of the γ -phase, and the 'nose' of the 'C' curves of T-T-T diagrams for U-(8-10) wt.% Mo alloys lying close to 500 °C. In one of the study, U-10 wt.% Mo alloy was shown to be most resistant to decomposition at 550 °C amongst a range of U-Mo alloys containing between 5 to 16 wt.% Mo [156]. In few investigations, the γ -phase in 8 wt.% and 10.8 wt.% Mo alloys has been reported to transform directly to the ($\alpha + \gamma'$) phases at 550 °C, whereas, a gradual transformation of the γ -phase first to ($\alpha + \gamma$) and then to ($\alpha + \gamma'$) has been documented at 500 °C and below [162-164]. In the same alloys decomposition at lower temperatures, like 375 °C, has been found to proceed by the precipitation of γ' -phase followed by the formation of α -phase [164]. It has also been shown in some of the studies that the transition of γ to γ' takes place only after a certain degree of Mo-enrichment of the γ -phase [152,153]. Infact, a few annealing studies have made an attempt to understand the transition mechanism of γ to γ' by selecting alloy compositions close to that of the γ' (U_2Mo) phase, like U-(14.7, 16, 16.6 and 20) wt.% Mo [152,157,165]. In order to investigate the decomposition characteristics of the γ -phase in particulate form, ageing studies have been performed on γ -stabilized U-7 wt.% Mo powders at 340 °C, 450 °C, 550 °C [166], U-(7-10) wt.% Mo powders at 425 °C, 475 °C [167] and U-8 wt.% Mo powders at 450 °C [168]. The

transformation of the γ -phase has been explored as well in splat-cooled U–Mo alloys by carrying out ageing studies at room temperature and at 500 °C and 800 °C [169]. The effect on the decomposition of the γ -phase due to segregation of Mo in the as-cast structure has been dealt with recently in the work of Pedrosa et al. [170].

At this juncture it is worthwhile to mention the beneficial “phase reversal” phenomenon noticed in U–Mo system, where a microstructure consisting of lamellar α -U and γ' (U_2Mo) phases generated upon annealing of γ -phase stabilized samples reverts back to the γ -phase upon neutron irradiation. The degree of this reversal was shown to depend on the fission rate and the morphological features, especially the interlamellar spacing, of the lamellar α - and γ' - phases arranged alternately in the un-irradiated microstructure [171,172].

2.6 Fuel–clad chemical interaction issues with γ -phase U–Mo alloys and its mitigation

The performance of nuclear research and test reactor fuel plates, containing γ -phase U–(8-10) wt.% Mo alloy as dispersion or monolithic fuel, face utmost challenge from the chemical interactions that take place due to interdiffusion of the constituent elements of the fuel alloy and the Al-matrix or Al-cladding. Apart from thinning of the clad, the phases generated out of such reactions, both during fabrication and in-pile operation, like $(U,Mo)Al_3$ and $(U,Mo)Al_4$ are known to have undesirable properties, such as rapid growth kinetics, thermal expansion mismatch, low thermal conductivity and poor irradiation stability [3,4,9,124,173-187]. Several strategies have been adopted over the years to minimize these interactions; notable amongst which are application of silicide coating on the fuel surface [188], modification in the composition of the Al-matrix by alloying it with Si [127,181,187,189-193] and optimization of initial fuel-meat microstructure by suitable processing technique [194]. In addition, mitigation of the interaction between U and Al has also been attempted by increasing the stability of the γ -U phase by slowing down the rate of interdiffusion in U-alloy system. This is due to the fact that the decomposition of the γ -U phase, which is a diffusion-controlled process, triggers the interaction between the fuel elements and the clad. This is achieved by incorporating a “diffusion barrier” element capable of stabilizing the γ -U phase by remaining in solid solution, either as an

alloying addition in dispersion-fuel or as a liner between monolithic-fuel and clad [16,127,133,178,180,189,190,195-197].

An ideal barrier material for metallic fuel system must possess the following characteristics:

- (a) High melting point.
- (b) High thermal conductivity.
- (c) Low neutron absorption rate.
- (d) Good corrosion resistance.
- (e) Interdiffusion reactions between barrier and metallic fuel as well as between barrier and Al-alloy cladding should be moderate or slow. In this,
 - (i) None or insignificant amount of intermetallic phases should form for better structural integrity as thermal expansion coefficients and other thermomechanical properties of intermetallic phases may vary significantly. Hence, extensive solid solution is preferred because relevant properties would vary gradually with composition.
 - (ii) Intermetallic phases, if formed due to interdiffusion reaction, should have slow growth rates and stable irradiation behaviors.
 - (iii) Formation of no low melting eutectic phase(s).
- (f) Compliant with deformation and heat treatment processes.

Normally, refractory metals are considered as a preferred diffusion barrier owing to the sluggish diffusion of U in refractory metals [198]. Besides, refractory metals have high melting points and high thermal conductivities [199]. The diffusion of U in refractory metals is characterized by a high activation energy, which can be attributed to their high melting points [198,200]. Upon detailed evaluation of physical properties of different refractory metals, including irradiation behavior and the relevant equilibrium phase diagrams with U, three refractory metals viz., Mo, Nb, and Zr were found to have potential to be used as diffusion barrier material for the U–Mo fuel system. The physical properties of Mo, Nb and Zr in connection with their application as barrier material are compared in Table 2.4.

Table 2.4 Physical properties of Mo, Nb and Zr as barrier material [199,201].

Properties	Mo	Nb	Zr
Crystal structure	bcc	bcc	hcp (< 863 °C); bcc (> 863 °C)
Melting point	2623 °C	2477 °C	1855 °C
Neutron absorption rate	2.48 barn	1.15 barn	0.18 barn
Thermal conductivity	138 W/m/ K	53.7 W/m/K	22.6 W/m/K

Out of these three metals Mo has the highest melting point and thermal conductivity. Besides, using Mo as a barrier would also maintain the simple binary system between the fuel and the barrier, since Mo is already the alloying addition in U for stabilization of the γ -phase. In addition, only one intermetallic phase γ' (U_2Mo) exists below 625 °C (Figure AI.2) [24]. Interdiffusion studies between U–10 wt.% Mo alloy and pure-Mo were carried out in form of solid-to-solid diffusion couples in the temperature range of 600 °C to 1000 °C. No intermetallic phase formation could be observed at the interface of any of the couples [13].

Nb having melting point, neutron absorption cross-section and thermal conductivity values lying between Mo and Zr forms a solid solution with U, like Mo, and does not show the formation of any intermetallic phase (Figure AI.3) [24]. The Mo–Nb system on the other hand is a typical example of an isomorphous system displaying complete solubility in both the liquid and solid phases (Figure AI.4) [24]. Diffusion couple experiments conducted between U–10 wt.% Mo alloy and pure-Nb, again in the temperature range of 600 °C to 1000 °C, showed the formation of a two-phase region consisting of α -U or β -U precipitates in a Nb-rich matrix in the interdiffusion zone [14]. Thermal cracking at the interface between the U–Mo alloy and the interdiffusion zone, however, was consistently observed on quenching the couples from the annealing temperatures owing to the mismatch in the thermal expansion coefficient between the U–Mo fuel and the interaction product layer [14]. In another study the diffusional interaction between U–10 wt.% Mo alloy and pure-Nb was assessed in solid bonding diffusion couples made by cladding and hot rolling. Three types of solid-solutions viz., γ -U–Nb, γ' -U–Nb and α -U–Nb were found within the Nb-matrix in the interdiffusion zone [15].

Although Zr has a lower melting point and thermal conductivity as compared to Mo and Nb, its neutron absorption cross-section is lowest amongst the three. The choice of Zr as a barrier material for U–Mo alloy fuel satisfies most of the required conditions, viz., no eutectic reaction in U–Zr binary system and complete miscibility of γ -U and β -Zr over the entire composition range except for the presence of one intermetallic δ -U (UZr_2) phase (Figure AI.5) [24]. Similarly, Mo present in the fuel alloy also does not form any eutectic mixture with Zr till 1550 °C except for the formation of one intermetallic Mo_2Zr phase (Figure AI.6) [24]. The fabrication of Zr-barrier has also been found to be compatible with hot rolling practices adopted for the fabrication of U–Mo monolithic fuel [176]. In as-processed U–10 wt.% Mo monolithic fuel plate clad in AA6061 with Zr diffusion barrier, multiple phases were observed by Perez et al. [176] and Park et al. [202] at the interface of U–Mo with Zr. While phases like α -U, Mo_2Zr , Zr-solid solution, γ -UZr and UZr_2 were observed by the former, the latter did not observe Zr-solid solution and γ -UZr amongst these phases. Interdiffusion studies between U–10 wt.% Mo and pure-Zr, in form of solid-to-solid diffusion couple, were also conducted in the temperature range of 600 °C to 1000 °C [4,203]. A negligible diffusional interaction was noticed at 600 °C [4]. In couples annealed at 700 °C, 800 °C, 900 °C and 1000 °C only one intermetallic phase Mo_2Zr was found to exist as precipitates near the interface in addition to the presence of small α -Zr precipitates near the U–Mo side of the couple [4]. Within the diffusion zone of couples annealed at 650 °C single-phase layers of β -Zr and β -U were observed along with a discontinuous layer of Mo_2Zr between the β -Zr and β -U layers. In the vicinity of Mo_2Zr phase, islands of α -Zr phases were also found. In addition, acicular α -Zr and $\text{U}_6\text{Zr}_3\text{Mo}$ phases were observed within the γ -U(Mo) terminal alloy [203]. Hence, it may be seen that diffusional interaction between U–Mo fuel alloy and Zr diffusion barrier may lead to the generation of various interaction products at the interface depending on temperature. However, these interaction products do not pose significant problems as they have been found to remain stable under irradiation [196].

The abovementioned interdiffusion studies between U–10 wt.% Mo alloy and pure Nb, Mo and Zr showed diffusional interaction rates lower by almost 10^3 times for Zr, 10^5 times for Mo and 10^6 times for Nb when compared with those observed between U–Mo fuel and Al or Al–Si cladding [4,14]. Hence, this showed the efficacy of these metals in acting as diffusion

barrier material. A successful implementation of these metals as a barrier between the U–Mo fuel and Al or Al–Si clad will also depend on the nature of their interaction with Al and Si. Binary phase diagrams of these metals with Al and Si (Figures AI.7 to AI.12) show less intermetallic phase formation in case of Nb as compared to Mo or Zr [24].

Although Nb and Mo displayed lower growth rates of the interaction layer as compared to Zr, the presence of cracks in the interdiffusion zone in case of Nb and the poor formability and ductile-to-brittle transition of Mo near room temperature raised concern about the performance of these metals as diffusion barrier material [14]. Zr in this respect outperformed others, as it could reduce the rate of diffusional interaction by three orders of magnitude besides exhibiting excellent physical, thermo-mechanical and irradiation behaviors.

A recent study by Huang et al. [17] have also laid support to the use of Mg as a diffusion barrier material upon studying a U–7 wt.% Mo vs. pure-Mg diffusion couple assembled and annealed at 550 °C for 96 h. Although reactive in nature, Mg offers a high thermal conductivity of 156 W/m/K [204] along with a very low neutron absorption cross-section of 0.063 barn [205]. A negligible interdiffusion observed was consistent with the negligible solubilities between Mg and U or between Mg and Mo, as per their binary equilibrium phase diagrams (Figures AI.13 and AI.14, respectively) [24], apart from exhibiting a good bonded interface devoid of oxidation, cracks or pores. However, a significant interdiffusion reaction was found to occur between the Mg-matrix and the 6061Al-alloy cladding during the hot rolling operation at 415 °C in the course of U–Mo/Mg-matrix/6061Al-clad dispersion fuel fabrication [206]. Moreover, the presence of a eutectic point between Mg and Al at 437 °C remains a concern both during fuel processing and application [17,24]. The binary Al–Mg and Mg–Si equilibrium phase diagrams are given in Figures AI.15 and AI.16, respectively.

The effectiveness of Ti as a barrier material has also been probed recently in the form of a U–8 wt.% Mo/Ti/Al trilayer prepared by DC-magnetron sputtering [18]. Ti, like Zr, exhibits a hcp → bcc allotropic transformation at 882 °C [24] and has a melting point, thermal conductivity and neutron absorption cross-section of 1670 °C [24], 21.9 W/m/K [199] and 6.09 barn [205], respectively. Again, alike Zr, the binary phase diagram of Ti with U exhibits complete miscibility of bcc γ -U and β -Ti phases over the entire composition range and shows only one intermetallic U₂Ti-phase (Figure AI.17) [24]. The binary Ti–Mo phase diagram as well shows

complete solid solubility of bcc Mo and β -Ti over the entire composition range without any intermetallic phase (Figure AI.18). Upon irradiation of the trilayer by 80 MeV ^{127}I ions no interaction between U–Mo and Al could be noticed, although minimal interactions occurred at both the U–Mo/Ti and Ti/Al interfaces leading to the formation of an orthorhombic U–Ti compound at the former and an intermetallic phase at the latter. The binary Ti–Al equilibrium phase diagram is shown in Figure AI.19. It was however suggested that the formation of the U–Ti compound at the U–Mo/Ti interface could set off the decomposition of the γ -U(Mo) phase.

2.7 Thermodynamic assessment of binary systems employing free energy-composition (G–X) diagrams

G–X diagram finds application in providing a thermodynamic basis for predicting the sequence of various phase transformations and the same has been used quite extensively to rationalize many of the experimental observations made in Zr–1Nb and U–9Mo systems in the present study.

The free energies of solid-solution phases in any binary system, for instance A–B, can be estimated as a function of the concentration (x) of solute (B) by making use of the following expression on applying the regular solution thermodynamics model:

$$G_m^\phi = \sum_{i=A,B} x_i^\phi G_i^\phi + RT \sum_{i=A,B} x_i^\phi \ln x_i^\phi + E_m^\phi \quad (2.6)$$

where G_m^ϕ is the molar Gibbs free energy of a solid solution phase ϕ , R is the gas constant, T is the temperature in K, and x_i is the mole fraction of element i ($= A, B$). G_i^ϕ , the Gibbs free energy of a pure element in the structural state of ϕ , relative to the enthalpy of the “Standard Element Reference” i.e., the reference phase for the element at 298.15 K ($G\text{-H}_{\text{SER}}$), can be obtained from the Dinsdale’s compilation of SGTE (Scientific Group Thermodata Europe) data for pure elements [207]. In general, G_i^ϕ is represented in form of a power series of temperature as:

$$G_i^\phi = a + b T + c T \ln T + \sum d T^n \quad (2.7)$$

where ‘ a ’, ‘ b ’, ‘ c ’ and ‘ d ’ are coefficients and ‘ n ’ represents a set of integers, typically taking the values of 2, 3 and -1. The excess Gibbs free energy, E_m^ϕ , can be expressed by the Redlich–Kister polynomial function [208] as follows:

$$E_m^\phi = x_B x_A \sum_{j=0,1,\dots}^n {}^{(j)}L_{B,A}^\phi (x_B - x_A)^j \quad (2.8)$$

where ${}^{(j)}L_{B,A}^\phi$, the interaction parameter between B and A, is formulated as:

$${}^{(j)}L_{B,A}^\phi = A_j + B_j T + C_j T \ln T + D_j T^2 + E_j T^{-1} \quad (2.9)$$

where ‘ A_j ’, ‘ B_j ’, ‘ C_j ’, ‘ D_j ’ and ‘ E_j ’ are optimized model parameters.

The free energies of the solid-solution phases can be plotted as a function of solute content in a free energy–composition diagram or G–X diagram, depicting the variation of free energy as a function of composition at any temperature.

To emphasize the use of G–X diagram, some phase transition sequences in Zr–Nb system which have been rationalized utilizing G–X diagram are listed in the following [36,209]:

(i) Precipitation of β_{Zr} -precipitates, initially, and β_{Nb} -precipitates, later, on tempering supersaturated α' -martensites, produced on quenching dilute Zr–Nb alloys, at temperatures below but close to the monotectoid temperature ($T_{mono} = 610$ °C) provided their Nb-contents are less than that of the intersection of α - and β - free energy curves (X_o). For example, martensites in Zr–2.3 wt.% Nb and Zr–5.5 wt.% Nb alloys were found to follow this sequence on tempering at 550 and 600 °C and at 500 and 550°C, respectively.

(ii) Phase reversal of α' -martensites to β -phase initially on tempering at temperatures below but close to T_{mono} , provided their Nb-contents are more than X_o , and subsequently a sequential decomposition of the β -phase first to a mixture of $\alpha + \beta_{Zr}$ -precipitates and then to $\alpha + \beta_{Nb}$ -precipitates. Martensite in Zr–5.5 wt.% Nb alloy was found to exhibit this behavior during tempering at 600 °C.

(iii) Direct transformation of the α' -martensites to a mixture of α and β_{Nb} -precipitates on tempering at temperatures considerably below T_{mono} . This kind of precipitation sequence was observed during the tempering of Zr-2.3Nb and Zr-5.5Nb alloy martensites at temperatures up to 500 °C and 450 °C, respectively.

2.8 Compatibility study of dissimilar materials – Diffusion bonding

Since the present thesis has also focused on ascertaining the diffusion-reaction between the constituents of the U-9Mo fuel alloy and the Zr-1Nb cladding alloy through diffusion bonding of the two, it is imperative to have a brief general overview of the diffusion bonding technique.

Diffusion bonding is a solid-state joining process wherein the surfaces of the materials to be joined are put under a compressive stress at an elevated temperature for a finite time interval in a controlled atmosphere. The atomic diffusion of elements at the joining interface causes coalescence of the contacting surfaces [210-212]. Diffusion bonding is an attractive manufacturing option for joining of, in particular, dissimilar materials, which are otherwise difficult to join by conventional fusion welding due to (i) differences in their melting points and thermal conductivities and (ii) formation of brittle intermetallic compounds at the joint interface. In addition, low pressures and no localized thermal gradient are the key attributes of this process which minimize microstructural changes, build-up of residual stresses and distortions in the parts being joined.

The entire diffusion bonding operation can be mechanistically divided into three distinct stages, as follows [213]:

(i) The first stage comprises of plastic deformation of the contacting asperities primarily by yielding and by creep deformation mechanism to have an intimate contact over a large area of the interface. At the end of this stage, grain boundaries form at the areas of contact with voids in between.

(ii) In the second stage, diffusion dominates over deformation and many of the voids disappear on account of grain boundary diffusion of atoms.

(iii) During the third stage, elimination of the remaining voids occurs by volume diffusion of atoms to the void surface.

The quality of a diffusion bonded joint in terms of mechanical strength and leak tightness is governed both by the properties of materials being joined and the process parameters. Material properties include the surface, grain boundary and volume diffusion coefficients, creep properties and yield strength, whereas, the key process parameters are bonding pressure, bonding temperature and dwell time. The bonding pressure or the compressive stress helps to bring about the creep mechanisms in place, which assists the diffusion process in achieving the bonding at the interface. Pressure plays an important role in producing a large contact area at the joining temperature in the

first stage of joining. The bonding pressure should be so chosen that it is able to deform the surface asperities and fill all the voids at the interface by material flow, and at the same time must not exceed the yield strength of the weaker of the two materials at the bonding temperature so as to avoid macroscopic plastic deformation of the components. The other significant process variable is the temperature of bonding. Plastic deformation, creep and various diffusion mechanisms are temperature-dependent. The bonding temperature determines the extent of contact area in the first stage of joining and the rate of diffusion which governs void elimination in the second and third stages. An elevated bonding temperature of the order of $0.5-0.7T_m$ (T_m being the absolute melting point of the readily fusible material in the combination) is normally used to aid interdiffusion of atoms across the interface of the joint and also to aid in surface modification by elimination of asperities. Creep and diffusion mechanisms are time-dependent phenomena. The dwell time or the bonding time, the third process variable, should be such at a specified bonding temperature and pressure that an intimate contact is formed between the components by elimination of the asperities at the interface through the process of solid-state diffusion. The bonding time, in turn, is also affected by temperature, pressure, material and the specimen size. The width of the interdiffusion zone (w) formed at the interface of the two materials during diffusion bonding is given by:

$$w = k\sqrt{t} \quad (2.10)$$

where, k is the kinetic rate constant at the temperature of bonding and t is the duration of bonding.

Apart from the different material and process variables mentioned above, which affect the bonding operation, initial roughness and cleanliness of the joining surfaces also play important roles in the bonding operation. The surfaces should be free of oxides to ensure proper metal-to-metal contact. The degree of surface roughness determines the extent of initial surface contact and the size of voids, thereby affecting the rate of bonding. Rough initial surfaces impede the first stage of joining, leaving large voids to be eliminated during the later stages. In general, a surface finish of $\sim 0.4 \mu\text{m}$ or better ensures a good initial contact.

It is to be further noted that depending upon the materials to be joined, a thin interlayer is often introduced at the joining interface. An appropriate interlayer material can (i) accelerate diffusion, (ii) reduce the bonding temperature and/or pressure, (iii) prevent the formation of brittle intermetallic compounds at the joint, (iv) increase microdeformation in the joint to enhance contact

between the surfaces and (v) accommodate the residual stresses developed at the interface of dissimilar materials due to the mismatch in thermal expansion coefficients.

Experimental methodology

3.1 Sample details

3.1.1 Zr–1 wt.% Nb alloy

The material used was a finished Zr–1Nb fuel tube fabricated at Nuclear Fuel Complex, Hyderabad, India. The detailed chemical composition of the alloy is presented in Table 3.1. The fabrication process involved cold-deformation of a hot-extruded blank in seven steps through pilgering operation, with intermediate annealings at 580 °C for 4 h in between, to reach to the final dimension. The final deformation step was followed by a recrystallization annealing of the tube at 580 °C for 4 h. Small specimens from this recrystallized tube were cut for experimentation.

For the purpose of diffusion bonding with U–9 wt.% Mo alloy, Zr–1Nb sample in annealed condition was collected from an intermediate processing step of the above-mentioned fuel tube fabrication schedule. Samples of dimension 15 mm length × 10 mm width × 4 mm thickness were machined out from the annealed tube and their surfaces were prepared metallographically subsequently.

Table 3.1 Detailed chemical composition of Zr–1 wt.% Nb alloy used in this work.

<i>Al</i>	<i>B</i>	<i>Be</i>	<i>C</i>	<i>Ca</i>	<i>Cd</i>	<i>Cl</i>
66 ppm	0.5 ppm	25 ppm	43 ppm	25 ppm	0.3 ppm	20 ppm
<i>Cr</i>	<i>Cu</i>	<i>F</i>	<i>Fe</i>	<i>H</i>	<i>Hf</i>	<i>K</i>
140 ppm	30 ppm	30 ppm	480 ppm	3 ppm	50 ppm	20 ppm
<i>Li</i>	<i>Mn</i>	<i>Mo</i>	<i>N</i>	<i>Nb</i>	<i>Ni</i>	<i>O</i>
2 ppm	20 ppm	25 ppm	20 ppm	1.01 wt.%	70 ppm	851 ppm
<i>P</i>	<i>Pb</i>	<i>S</i>	<i>Si</i>	<i>Sn</i>	<i>Ti</i>	<i>Zr</i>
10 ppm	25 ppm	20 ppm	20 ppm	25 ppm	25 ppm	Balance

3.1.2 U–9 wt.% Mo alloy

The U–9Mo alloy was prepared by vacuum induction melting using magnesio-thermally reduced U and 99.9% pure Mo. The alloy button, obtained on casting the molten alloy in a copper hearth, had a dimension of 265 mm length \times 195 mm width \times 20 mm thickness and was subsequently rolled at 550 °C to break the as-cast structure. The rolling operation was carried out in several passes to achieve a final sheet thickness of 1 mm. The as-rolled sheet after the final pass was allowed to cool in air. Rectangular specimens with dimension of 17 mm length \times 14 mm width \times 1 mm thickness were cut out from an as-rolled sheet (500 mm length \times 80 mm width \times 1 mm thickness) for experimentation.

For the purpose of diffusion bonding with Zr–1Nb, U–9Mo samples of dimension 15 mm length \times 10 mm width \times 4 mm thickness were machined out from the as-cast alloy button. These samples after sealing in evacuated quartz capsules were homogenized at 1000 °C for 24 h followed by quenching in water. The capsules were broken to ensure a very high cooling rate. The sample surfaces were then prepared following standard metallographic practice.

3.2 Diffusion bonding of Zr–1Nb and U–9Mo alloys

Solid-state diffusion reaction was carried out between rectangular pieces of U–9Mo and Zr–1Nb alloy samples of dimension 15 mm length \times 10 mm width \times 4 mm thickness each in a vacuum hot press. The metallographically prepared surfaces of the samples were ultrasonically cleaned and were made to rest against each other on the anvil of the press by tying them together with a cotton thread. The temperature of the hot press was raised to 800 °C at a heating rate of 10 °C/min from room temperature after achieving a vacuum of 5×10^{-6} mbar inside the chamber. On attaining 800 °C a compressive stress of 20 MPa was applied for a duration of 3 h on the sample assembly by the help of a piston. The sample assembly was then allowed to cool in the hot press itself under vacuum by switching off the heat input to the press. The cooling rate was approximately 10 °C/min.

3.3 Heat treatments

Heat treatments of all samples in the present work were carried out after sealing individually all the samples in evacuated quartz capsule to prevent oxidation.

In the case of Zr–1Nb alloy, the encapsulated samples were heat treated in the ($\alpha + \beta_{\text{Zr}}$) phase field. After the heat treatment the samples were quenched in water and capsules were broken to ensure high cooling rate.

In the case of U–9Mo alloy, a few of the encapsulated as-rolled samples were homogenized at 1000 °C for 24 h followed by quenching in water. The capsules were broken to ensure a very high cooling rate. In one particular case after the homogenization the sample was allowed to cool in the furnace itself by switching off its power supply to achieve a very slow cooling rate. The homogenized samples, except for the furnace-cooled one, were again sealed in quartz capsules, and ageing heat treatments of both as-rolled and homogenized samples in encapsulated condition were carried out. After ageing the samples were quenched in water.

In the case of diffusion bonding of U–9Mo with Zr–1Nb, the as-bonded sample was sectioned into smaller pieces by a slow speed diamond cutting wheel. The pieces were then sealed individually in quartz capsules and annealed.

3.4 Sample preparation

3.4.1 Metallography

Samples were polished after mounting them in a hot mounting press using conducting Cu powders. This was followed by grinding on successively finer grit sized emery papers and final polishing in colloidal silica solution. Conducting mounting was done to avoid building up of charge during examination in scanning electron microscope (SEM) and electron probe microanalyzer (EPMA).

In the case of Zr–1Nb alloy, samples were swab etched using a solution comprising of 50% distilled water, 45% hydrochloric acid and 5% hydrofluoric acid by volume. In the case of U–9Mo alloy, no further etching of the samples was required as the microstructure could be revealed even in final polished condition.

The diffusion bonded samples were swab etched with the same solution used in the case of Zr–1Nb alloy.

The metallographically prepared sample surfaces were examined by optical microscopy, X-ray diffraction, SEM and EMPA.

3.4.2 Sample preparation for transmission electron microscopy

For transmission electron microscopy (TEM), at first, slices of ~ 0.3 mm thickness were cut from the mounted samples by a slow speed diamond cutting wheel. The thickness of the slices were further reduced to ~ 150 μm by grinding in emery paper, and 3 mm discs were then punched out from these slices. The discs were then thinned by twin-jet electropolishing till perforation occurred at the centre of the discs. In the case of Zr–1Nb samples the electrolyte consisted of 80% methanol and 20% perchloric acid by volume, whereas, the composition of the same for the U–9Mo samples was 95% methanol and 5% perchloric acid by volume. In both the cases polishing was carried out at 20 volts with the electrolyte temperature being maintained at $-45\text{ }^{\circ}\text{C}$. The electron transparent region surrounding the perforation was examined under the microscope.

In the case of the diffusion bonded samples rectangular cross sections of $3\text{ mm} \times 2\text{ mm}$ and 0.3 mm thickness were cut from the mounted samples in a slow speed diamond cutting wheel in such a manner that the bonded interface lies parallel to the longest dimension of the cut section. This was done to have an electron transparent area covering most of the adjacent region of the interface on either side. The cut sections were further reduced in thickness to 100 μm by grinding in fine grit sized emery paper (No. 1200 and above). Care was taken during cutting and grinding operations so as to avoid de-bonding at the interface. The thinned sections were then twin-jet electropolished under same set of conditions as that of U–9Mo.

3.5 Characterization techniques

Optical microscopy of all samples was carried out in a Carl Zeiss optical microscope under both bright field and polarized light conditions for preliminary microstructural examination. Polarized light was used to reveal any orientation information present in the microstructure.

X-ray diffraction experiment was performed in a Bruker D8 Advance X-ray diffractometer using Ni filtered CuK_{α} radiation of wavelength 1.54 \AA . A scan step of 0.02° and a collection time of 0.5 sec for each step were used. The instrumental broadening correction was done using a standard defect free Si sample. The XRD patterns obtained from different samples were analyzed using the PowderCell Program for identification of the phases constituting the microstructure and to quantify their respective volume fractions [214]. The space group, Wyckoff notation, atomic position and lattice parameter data of the probable phases present,

needed for the analysis, were collected from Pearson's Handbook [215]. Un-etched and un-mounted samples were used for XRD.

The optical microscopy samples were observed under SEM to reveal the microstructural details present in the samples at a finer scale. Imaging was carried out in both secondary electron (SE) and backscattered electron (BSE) modes at 5 kV and 30 kV accelerating voltages, respectively. Compositional analysis was performed using energy dispersive spectroscopy (EDS) detector attached with the instrument.

The diffusion bonded samples in mounted and etched conditions were analyzed in a Cameca SX100 electron probe microanalyzer, wherein, apart from site-specific compositional analysis, elemental concentration profiles were measured using wavelength dispersive spectroscopy (WDS) at an accelerating voltage of 20 kV and a beam current of 20 nA. A 1 μm diameter electron probe and a 0.5 μm step size were used to obtain the concentration profiles across the interface. Respective elements in pure form were used as standards for the analyses. Single crystals of PET were used to diffract the UM_{α} , MoL_{α} and ZrL_{α} X-ray lines in the three wavelength dispersive spectrometers of the instrument.

Conventional TEM analyses of all samples involving bright-field and dark-field imaging, selected area electron diffraction (SAED) and microdiffraction, and elemental quantification have been carried out in a JEOL 2000 FX instrument operated at an accelerating voltage of 160 kV. High resolution TEM (HRTEM) for imaging crystal lattice was carried out in a JEOL 3010 microscope operated at an accelerating voltage of 300 kV.

Microstructural and phase transformation aspects of Zr–1Nb alloy

4.1 Background

The stability of the microstructural constituents of an alloy, with respect to morphology, composition and phase transformation, in response to any thermal treatment decides its applicability under both normal and off-normal service conditions. As discussed in Section 2.2 the desirable microstructure of Zr–1Nb alloy for use as fuel cladding should comprise of a recrystallized α -Zr matrix with β_{Nb} -precipitates distributed uniformly within it. Such a microstructure is obtained via heat treatment of the alloy in the $(\alpha + \beta_{\text{Nb}})$ phase-field below the monotectoid temperature. Zr–1Nb alloy with this microstructure if, however, heat treated in the $(\alpha + \beta_{\text{Zr}})$ phase-field above the monotectoid temperature, may undergo a few microstructural modifications as hypothesized below:

- (i) A decrease in the Nb-content of the β_{Nb} -precipitates (as per the Zr–Nb phase diagram) by means of dissolution into the α -matrix leading to a reduction in their sizes.
- (ii) Excess Nb in the α -matrix, as a result of the above event, prompting nucleation of fresh β -precipitates of lower Nb-content both within the grains and at the grain boundaries.
- (iii) The occurrences of the above two events could result in a wider size distribution of the β -precipitates in comparison of the original microstructure.
- (iv) A likely exhibition of the phenomenon of Ostwald ripening during the later stages of the heat treatment.

Thus, the present chapter is focused on exploring the above-mentioned possibilities under various conditions of heat treatment in the $(\alpha + \beta_{\text{Zr}})$ phase-field of Zr–1Nb alloy. In addition, β -phase of suitable composition also undergoes metastable phase transformations like the martensitic (α') and omega (ω) as pointed out in Section 2.2. The mechanistic aspects of these transformations have been dealt with in considerable depth in literature, but mostly confined to transformations taking place within the bulk of the β -phase [23,60,64,69-71,75-104]. With diminishing size of the β -phase, the elastic strain energy and interfacial energy play crucial roles

in dictating the feasibility of these transformations apart from its composition and the thermodynamic driving force. This aspect is also assessed in the β -phase precipitates of Zr–1Nb alloy in the present study.

Accident scenarios, wherein, the temperature of the Zr–1Nb clad may exceed beyond the $(\alpha + \beta)$ phase-field can result in a single β -phase microstructure, which on subsequent rapid cooling can undergo α' -martensitic transformation. This aspect has already been investigated earlier [45] and hence is not dealt with in the present study.

Keeping the aforementioned views in consideration, the Zr–1Nb alloy was heat treated as per the schedule given in Table 4.1. Figure 4.1 shows a schematic Zr-rich portion of the binary Zr–Nb phase diagram. It may be apprehended from this figure that it is possible to generate β -phase of different volume fractions, and thus of Nb-contents, within the α -matrix of Zr–1Nb alloy by heat treating the alloy at different temperatures in the $(\alpha + \beta_{Zr})$ phase-field. The heat treatment temperatures employed in the present work, the composition of the β -phase at the heat treatment temperatures, and the anticipated metastable phase transformation of the β -phase on quenching from these temperatures have been indicated in Figure 4.1.

Table 4.1 Heat treatment schedule of Zr–1 wt.% Nb alloy.

<i>Temperature (°C)</i>	<i>Duration</i>
675	1 h
800	10 mins, 30 mins, 2 h, 5 h
825	10 mins
832	5 mins

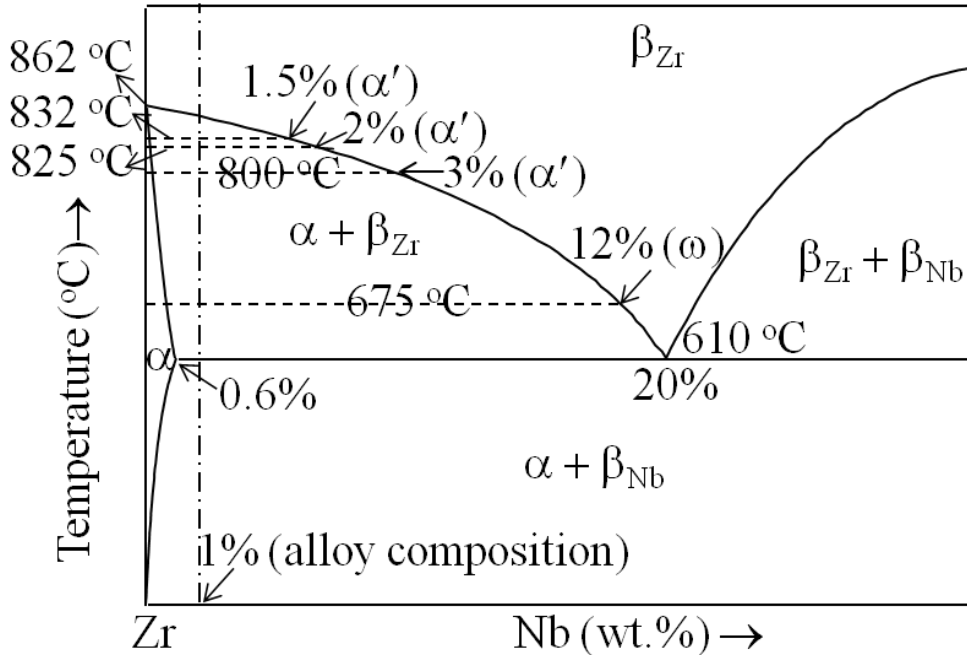


Figure 4.1 A schematic Zr-rich portion of the binary Zr–Nb equilibrium phase diagram. The Zr–Nb alloy composition and the heat treatment temperatures have been marked in the figure. The equilibrium compositions of the β -phase at the heat treatment temperatures, and its expected metastable transformation on quenching, have also been indicated in the figure.

4.2 Experimental observations

4.2.1 Morphological evolution of the β -phase

The microstructure of the starting material i.e., recrystallized Zr–1Nb consisted of spherical shaped β -precipitates with an average size of ~ 33 nm uniformly distributed within the α -grains (Figure 4.2). EDS measurements indicated Nb-content of the β -precipitates to vary between 53 to 75 wt.%, with the average being ~ 67 wt.%. This microstructure underwent substantial changes both in terms of morphology and size of the β -phase when samples of the starting material were subjected to different heat treatments as described below.

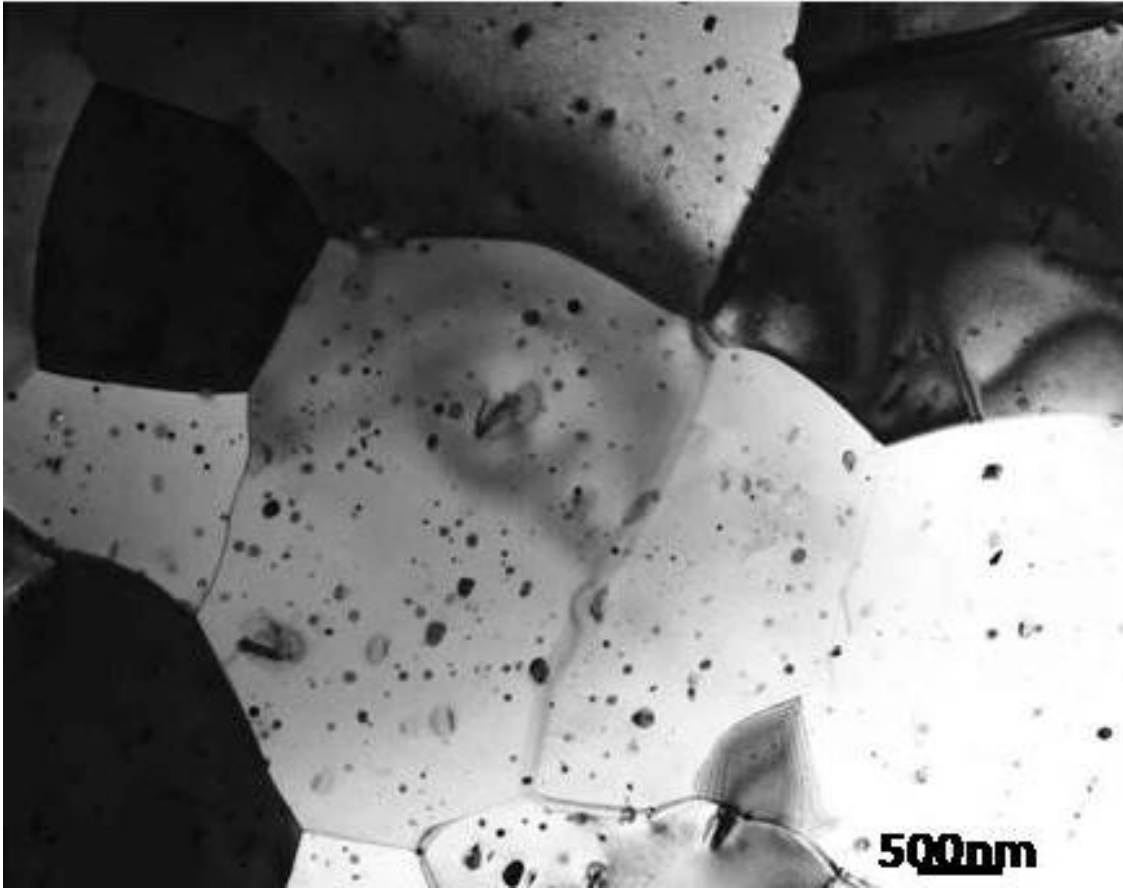


Figure 4.2 Bright-field TEM micrograph showing the microstructure of recrystallized Zr-1 wt.% Nb alloy. A uniform distribution of spherical β_{Nb} -precipitates could be seen with the α -Zr grains.

Heat-treatment at 675 °C for 1 h led to the formation of two distinctly different morphological features of the β -phase. These include irregular shaped β -regions at the α -grain boundaries and tri-junctions generically referred as ‘patch’ hereafter and elongated β -precipitates within the α -grains (Figure 4.3). The needle-like morphology of the elongated β -precipitates was ascertained through tilting experiment in TEM. The spherical β -precipitates as observed in the starting microstructure were also seen here.

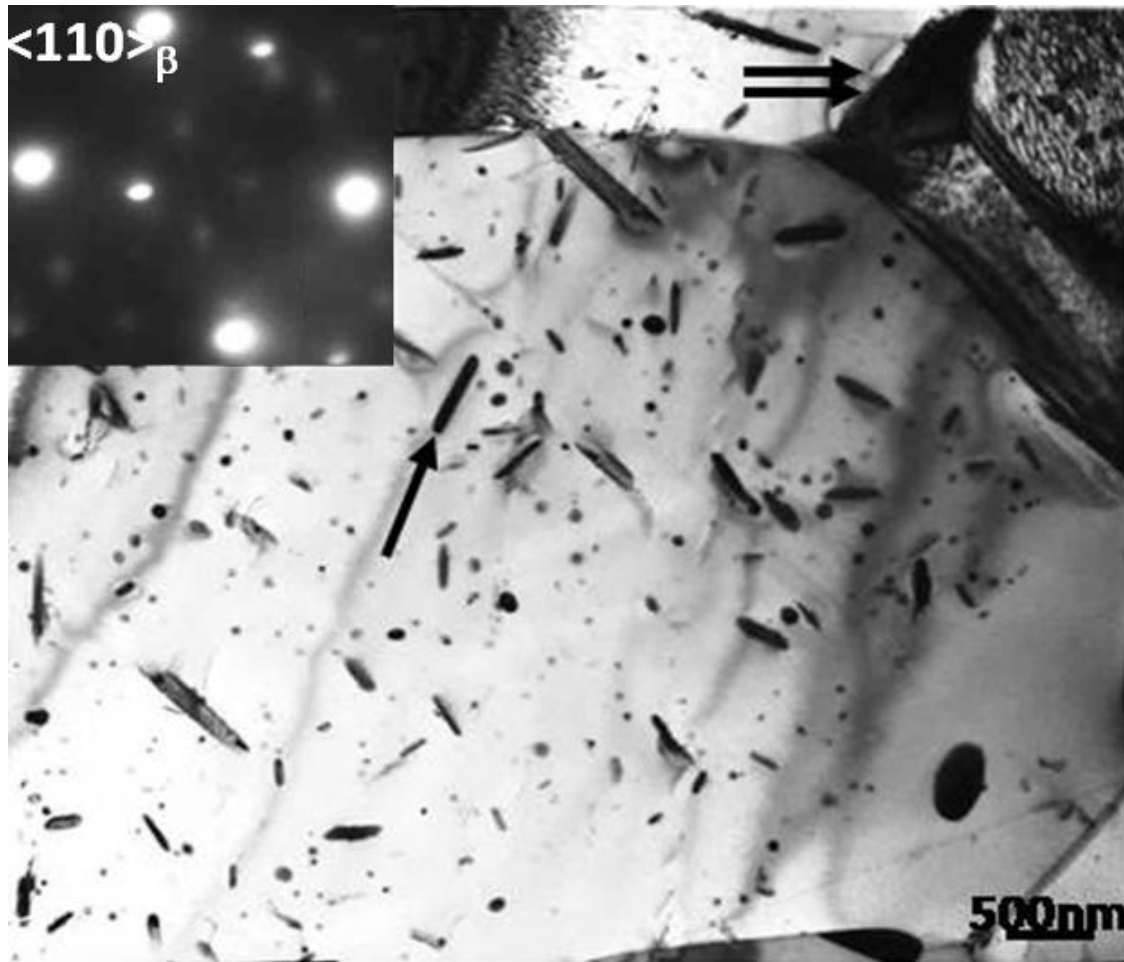


Figure 4.3 Bright-field TEM micrograph showing the typical microstructure of Zr-1 wt.% Nb alloy sample heat treated at 675 °C for 1 h. Inset shows the typical SAED pattern [Zone Axis = $\langle 110 \rangle_{\beta}$] obtained from β -patches superimposed with reflections of the ω -phase, the indexing of which can be referred from Figure 2.10. Single and double arrows indicate the needle and patch morphologies of the β -phase, respectively.

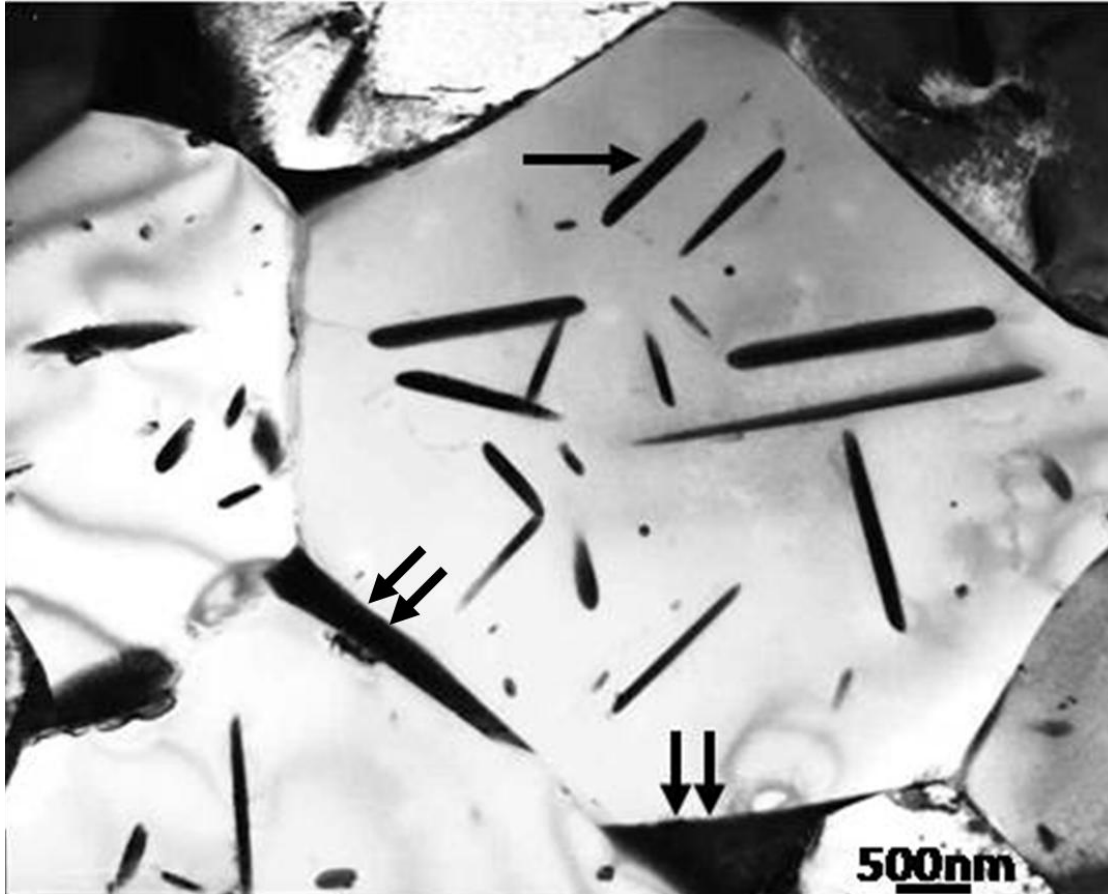


Figure 4.4 A typical bright-field TEM micrograph representing the microstructures of Zr-1 wt.% Nb alloy samples heat treated at 800 °C for different durations. Single and double arrows indicate the needle and patch morphologies of the β -phase, respectively.

The differences in microstructural features of the samples heat-treated at 800 °C for different time periods (starting from 10 mins up to 5 h), refer Figure 4.4, in comparison to the features of the sample treated at 675 °C can be summarized as:

(i) Formation of long β -needles inside α -grains with distinct morphological alignment with that of the matrix crystallographic planes suggestive of strong orientation relationship (OR) at 800 °C.

(ii) Increased size of the patches and noticeable decrease in the number density of the spherical β -precipitates of the starting microstructure at 800 °C. Progressively increased holding times at this temperature resulted in an increase in the size of the β -needles with corresponding decrease in their average number. On the contrary, the volume fraction of patches was found to increase with the hold time.

The morphological features of the β -phase in the samples heat treated at 825 °C for 10 mins (Figure 4.5) and 832 °C for 5 mins (Figure 4.6) were very similar to those of 800 °C.



Figure 4.5 A typical bright-field TEM micrograph representing the microstructure of Zr-1 wt.% Nb alloy sample heat treated at 825 °C for 10 mins.



Figure 4.6 A typical bright-field TEM micrograph representing the microstructure of Zr-1 wt.% Nb alloy sample heat treated at 832 °C for 5 mins.

The OR existing between the β -needles and the α -matrix corresponded to Burgers OR for bcc \leftrightarrow hcp transformation [57], as determined from composite SAED patterns containing reflections from both the phases (Figure 4.7). Single surface trace analysis was carried out to determine the habit plane of each orientation variant of the elongated precipitates keeping in mind the Burgers OR. The habit plane traces for all the variants were observed to lie close to $\{334\}_\beta$ type poles with some degree of scatter. The true crystallographic direction of all the variants analyzed was found to make angles ranging between 80° to 90° with $[0001]_\alpha$.

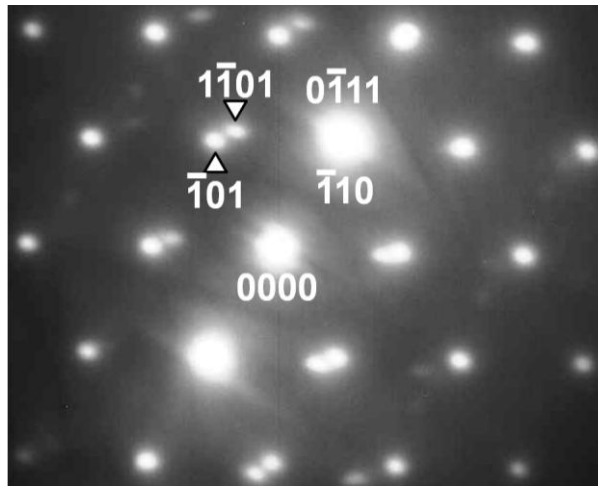


Figure 4.7 Composite SAED pattern showing reflections from both the α - and the β - phases in Zr-1 wt.% Nb alloy. $[\bar{1}\bar{2}\bar{1}3]_{\alpha} // [111]_{\beta}$; $(0\bar{1}11)_{\alpha} // (\bar{1}10)_{\beta}$.

4.2.2 Transformations within the β -phase

All the samples, which were subjected to heat treatments, were analyzed in detail (both by imaging and diffraction) to investigate the nature of transformations occurring inside the β -phase.

All of the spherical β -precipitates present in the initial microstructure (having Nb-content of more than 53 wt.%) were found to be essentially completely bcc- β with no transformation of any kind upon heat treatment. The above-mentioned chemical composition of the β -precipitates does not promote any transformation, neither α' or ω . Figure 4.8 shows a high resolution electron microscopy (HREM) image of an untransformed spherical β -precipitate present in the α -matrix. The needle shaped β -precipitates of the 675 °C heat-treated sample, whose length and width were found to be smaller than 200 nm and 40 nm respectively and having Nb in the range of 4-13 wt.%, did not exhibit any kind of transformation. The HREM image in Figure 4.9 shows one such precipitate where the β -lattice planes were found to run from one end of the plate to other without showing any discontinuity.

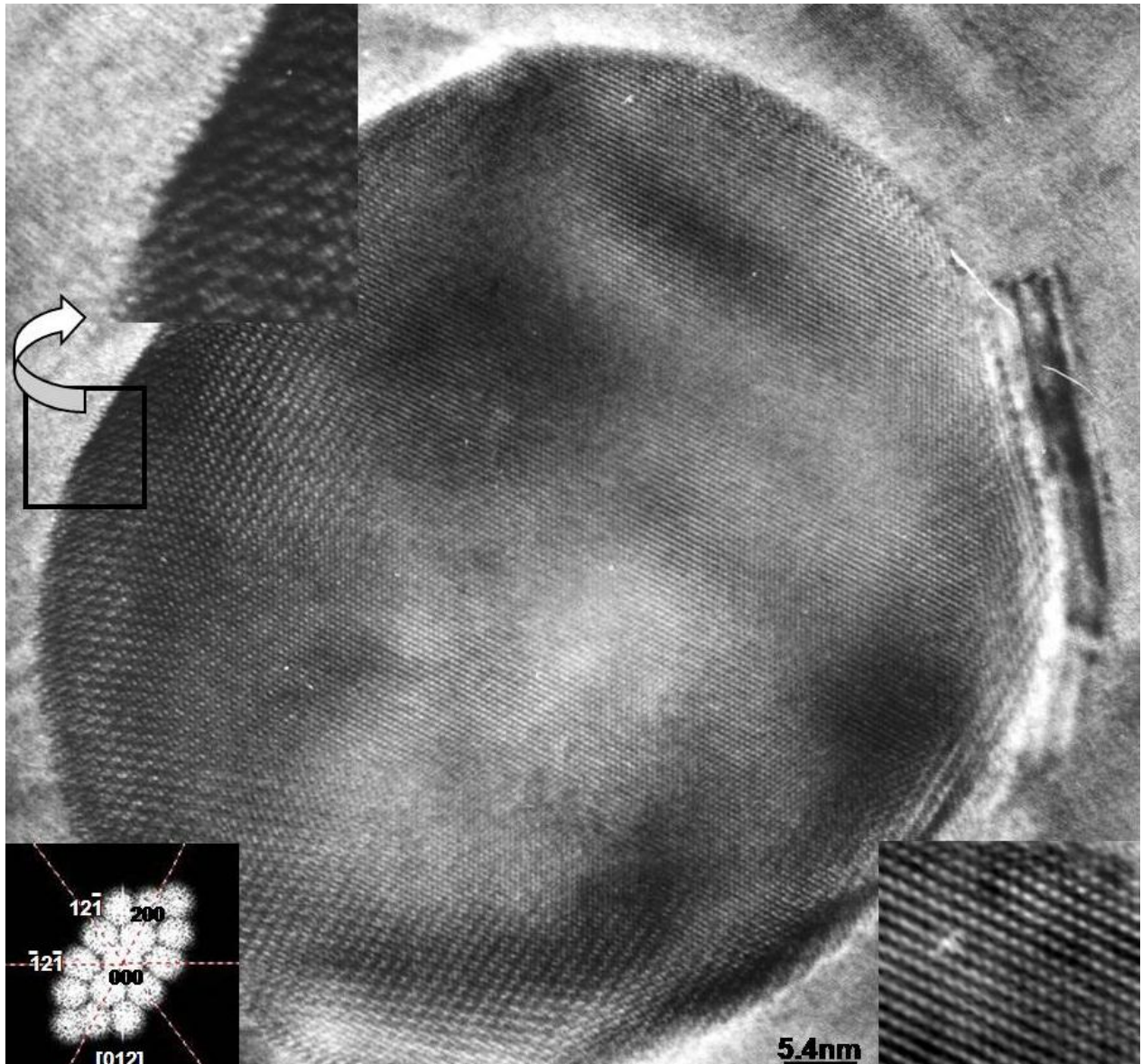


Figure 4.8 A HREM micrograph showing an untransformed spherical β -precipitate present in the α -matrix in Zr-1 wt.% Nb alloy. Inset at the top shows a magnified view of the precipitate-matrix interface, while the insets at the bottom show a Fast Fourier Transform (FFT) from the precipitate (left) and its inverse (right).

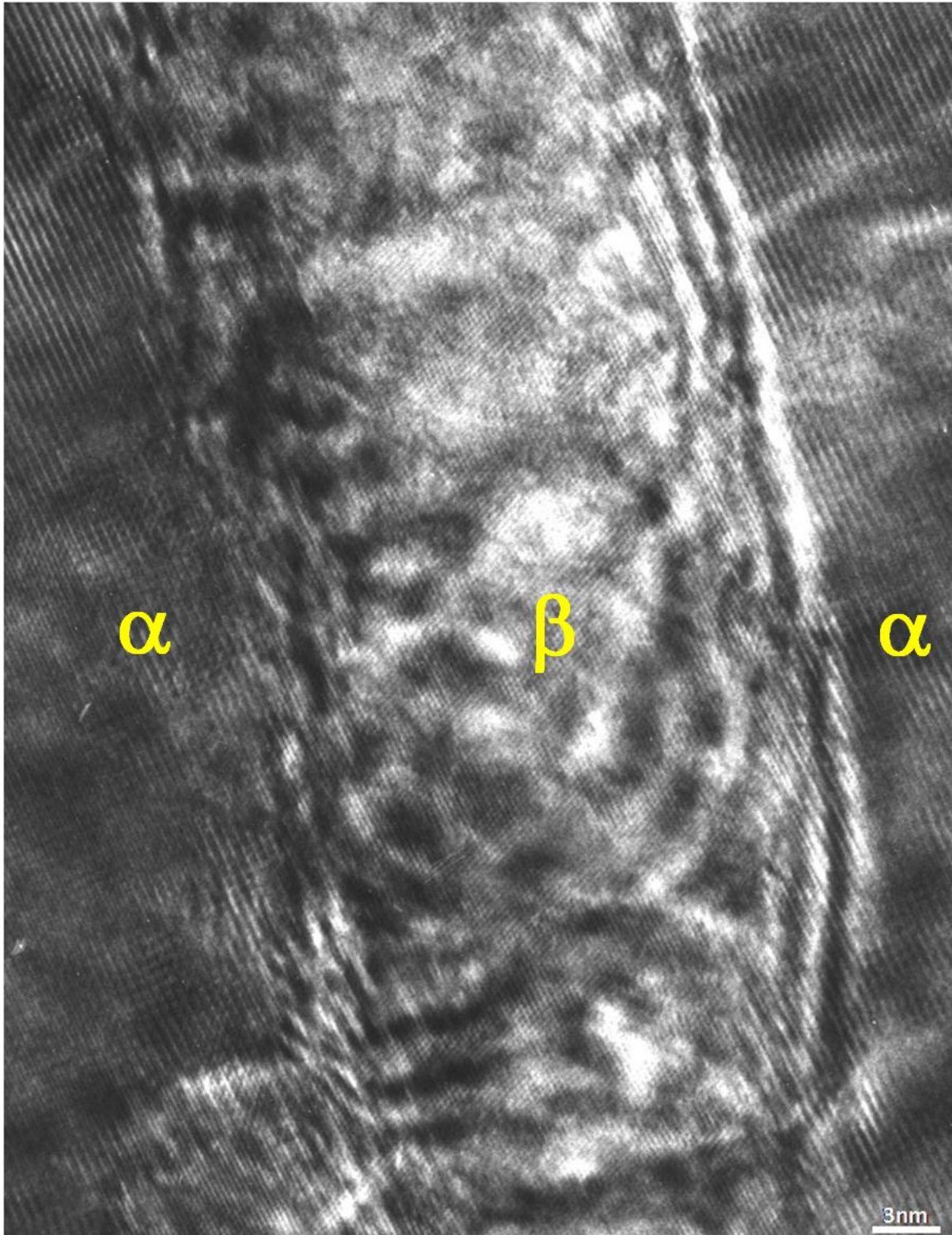


Figure 4.9 A HREM micrograph showing an untransformed elongated β -precipitate present in the α -matrix in Zr-1 wt.% Nb alloy.

It is to be noted that this composition range of the β -precipitates is expected to yield both α' - as well as ω - transformations under the present experimental conditions. On the other hand SAED patterns from the patches showed reflections pertaining to the ω -phase along with β -phase reflections (shown as inset in Figure 4.3).

Samples treated at 800 °C have shown β -precipitates with wide variation in composition. Those precipitates, which were found to have composition suitable for ω -transformation, did show ω -reflections even in very small β -needles. Figure 4.10 shows the sequence of diffraction patterns obtained from the β -precipitate, marked by an arrow in Figure 4.11, on tilting along the bcc stereographic triangle. The superimposition of the ω -reflections could be seen along with the β -reflections in $[110]$, $[210]$, $[311]$ and $[211]$ zone axes. These patterns matched well with the patterns shown in Figure 2.10.

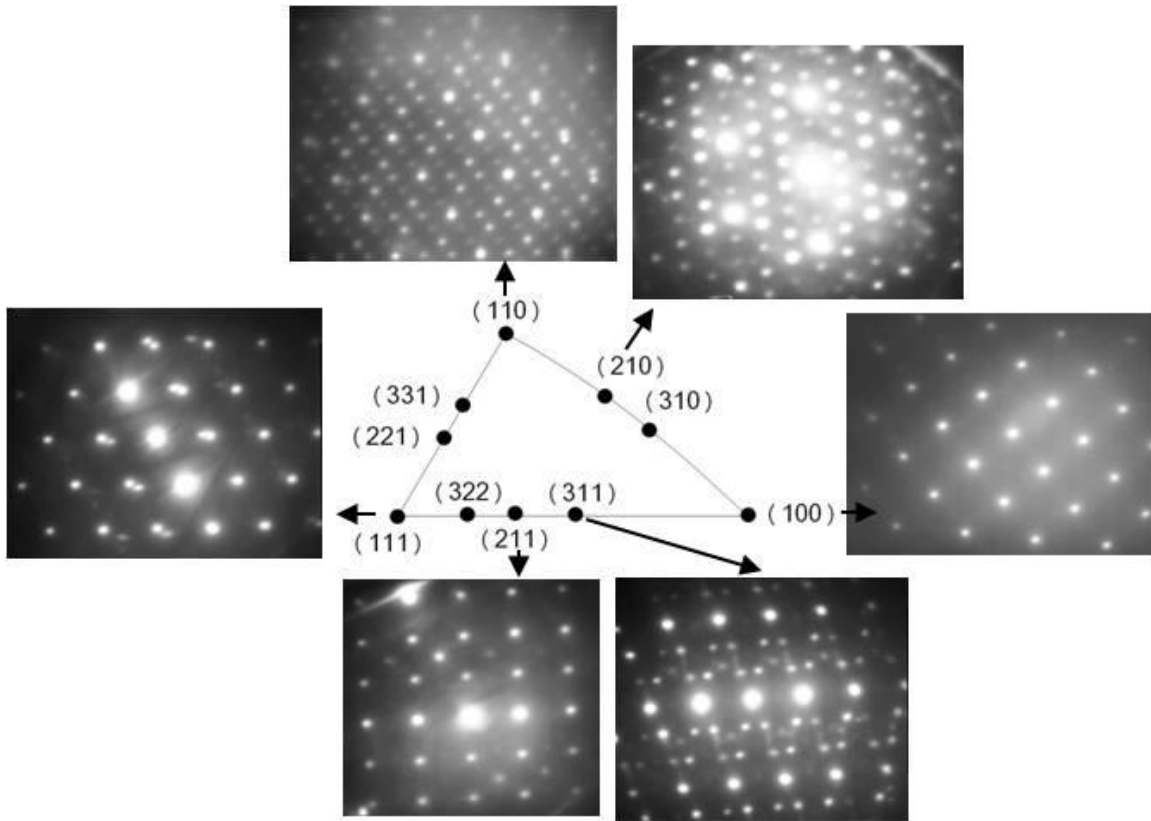


Figure 4.10 SAED patterns obtained along different zone axes from an elongated β -precipitate present in the Zr-1 wt.% Nb alloy sample heat treated at 800 °C for 30 mins. Superposition of ω -phase reflections could be seen along the $[110]$, $[210]$, $[311]$ and $[211]$ β -zone axes. Indexing of the patterns can be referred from Figure 2.10.



Figure 4.11 Bright-field TEM micrograph showing the β -precipitate in the Zr-1 wt.% Nb alloy sample heat treated at 800 °C for 30 mins (marked by an arrow) from which the SAED patterns in Figure 4.10 are obtained.

Those β -needles which are rich in Nb (more than 12 wt.%) were found to show no transformation, explainable from stabilization of β -phase at these high Nb contents. It is interesting to note that these precipitates have significantly higher Nb than what is expected under equilibrium conditions. However, holding for longer duration at this temperature did make composition of the β -phase to approach towards the expected equilibrium value. While the initial β -patches showed only ω -transformation, holding them for longer duration at this temperature resulted in the formation of α' too, thus indicating the shift of composition towards the equilibrium value of Zr-3 wt.% Nb. Figure 4.12 shows a high-resolution image of a β -patch having ω -particles within it. A dark-field TEM micrograph of this patch is given in Figure 4.13

where ω -particles corresponding to one crystallographic variant could be seen highlighted. A β -patch showing α' -martensite needles could be seen in the TEM micrograph of Figure 4.14.

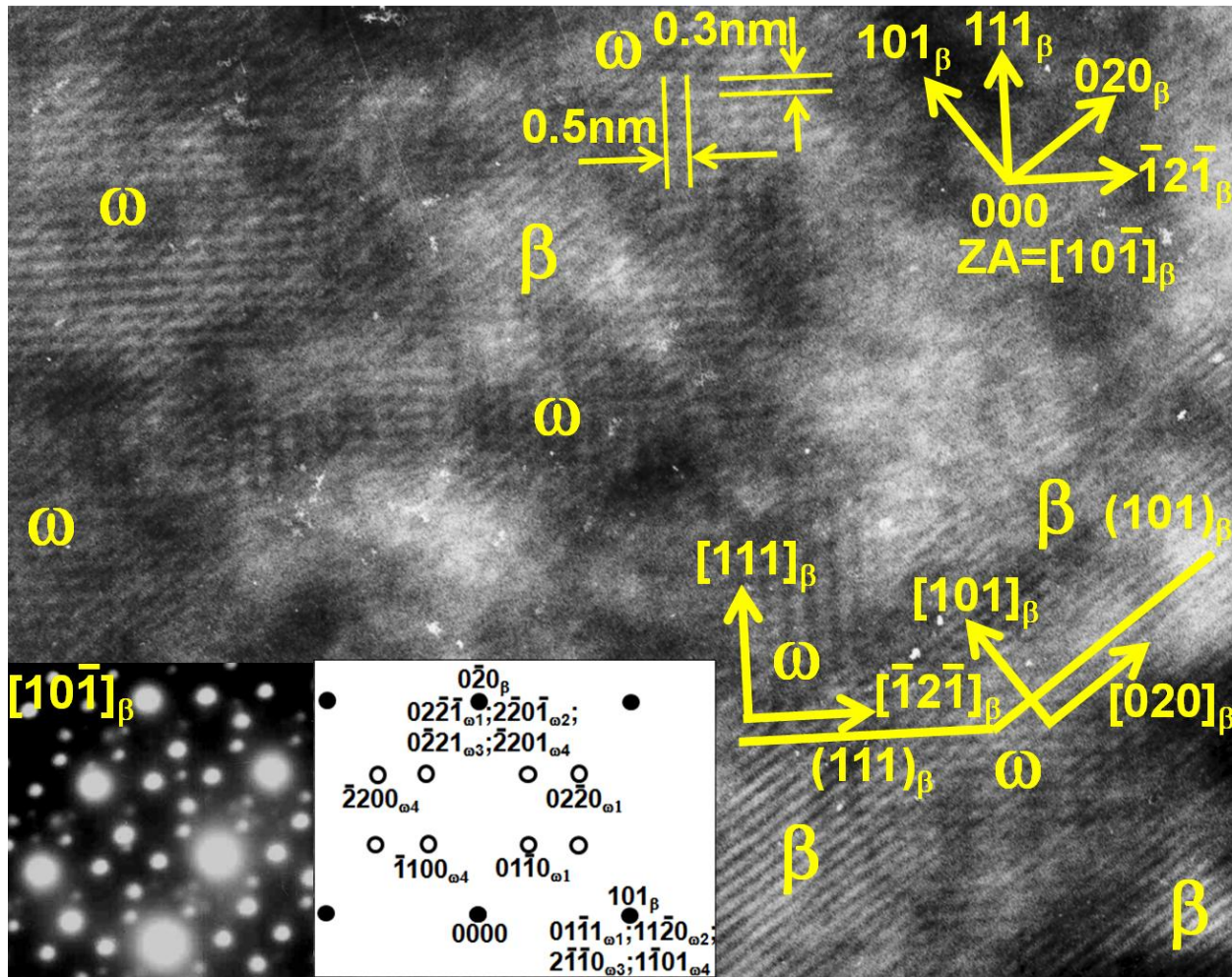


Figure 4.12 HREM micrograph showing the lattices of ω - and β - phases (marked in the figure) in Zr-1 wt.% Nb alloy. The $[10\bar{1}]$ section of the β -reciprocal lattice superimposed with ω -phase reflections and its key are given as insets.

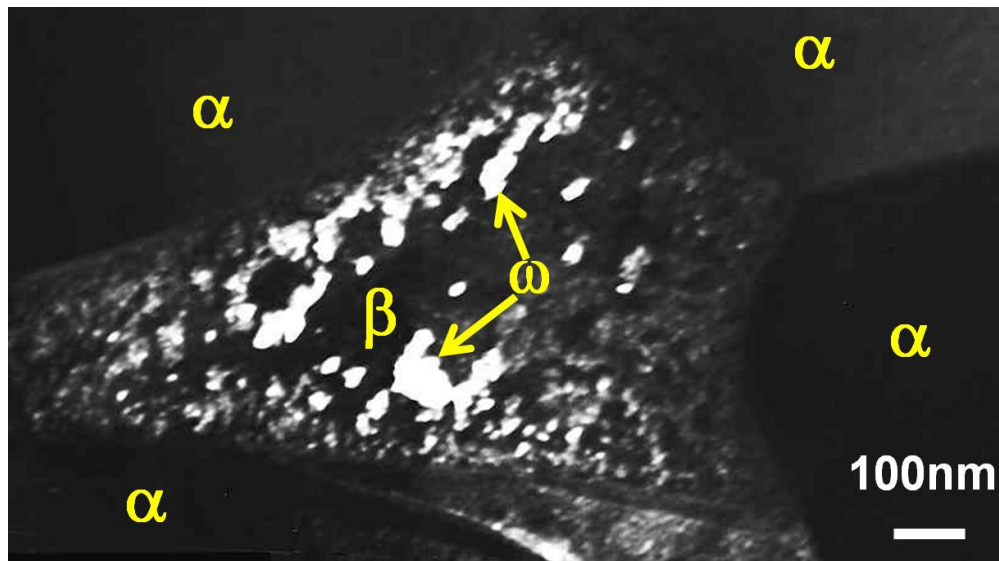


Figure 4.13 A dark-field TEM micrograph of a β -patch present in the Zr-1 wt.% Nb alloy sample heat treated at 800 °C for 30 mins. ω -particles corresponding to one crystallographic variant could be seen highlighted in the micrograph, as marked by arrows.

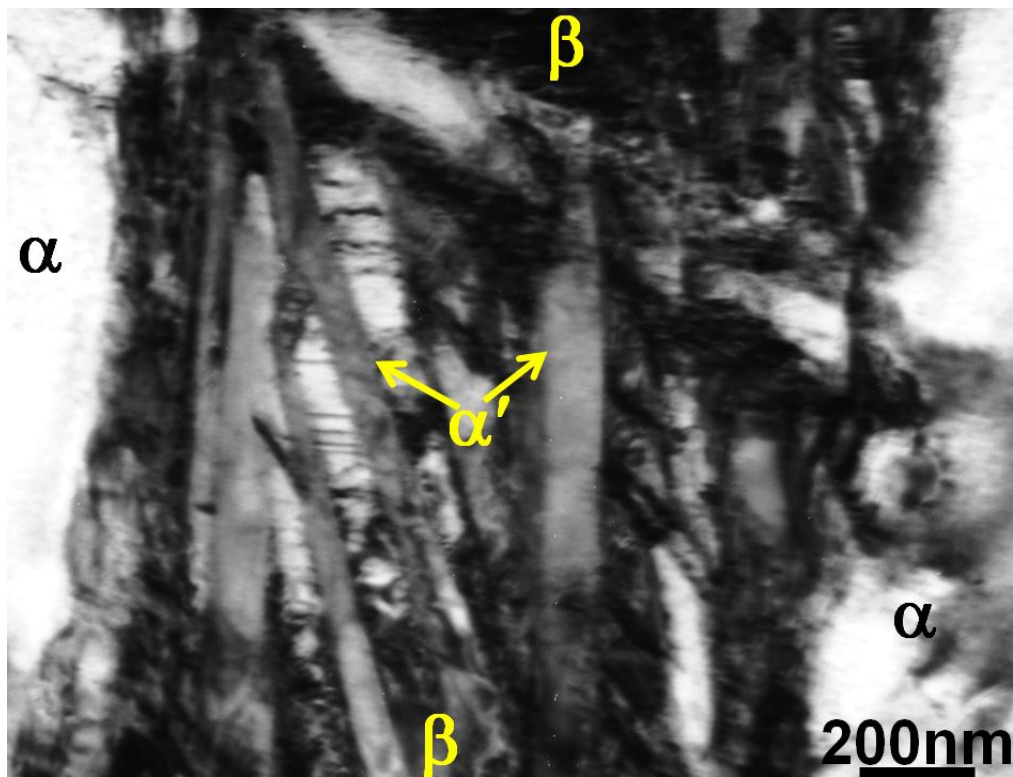


Figure 4.14 A typical bright-field TEM micrograph of a β -patch present in the Zr-1 wt.% Nb alloy sample heat treated at 800 °C for 5 h showing the occurrence of α' -needles within it, as marked by arrows.

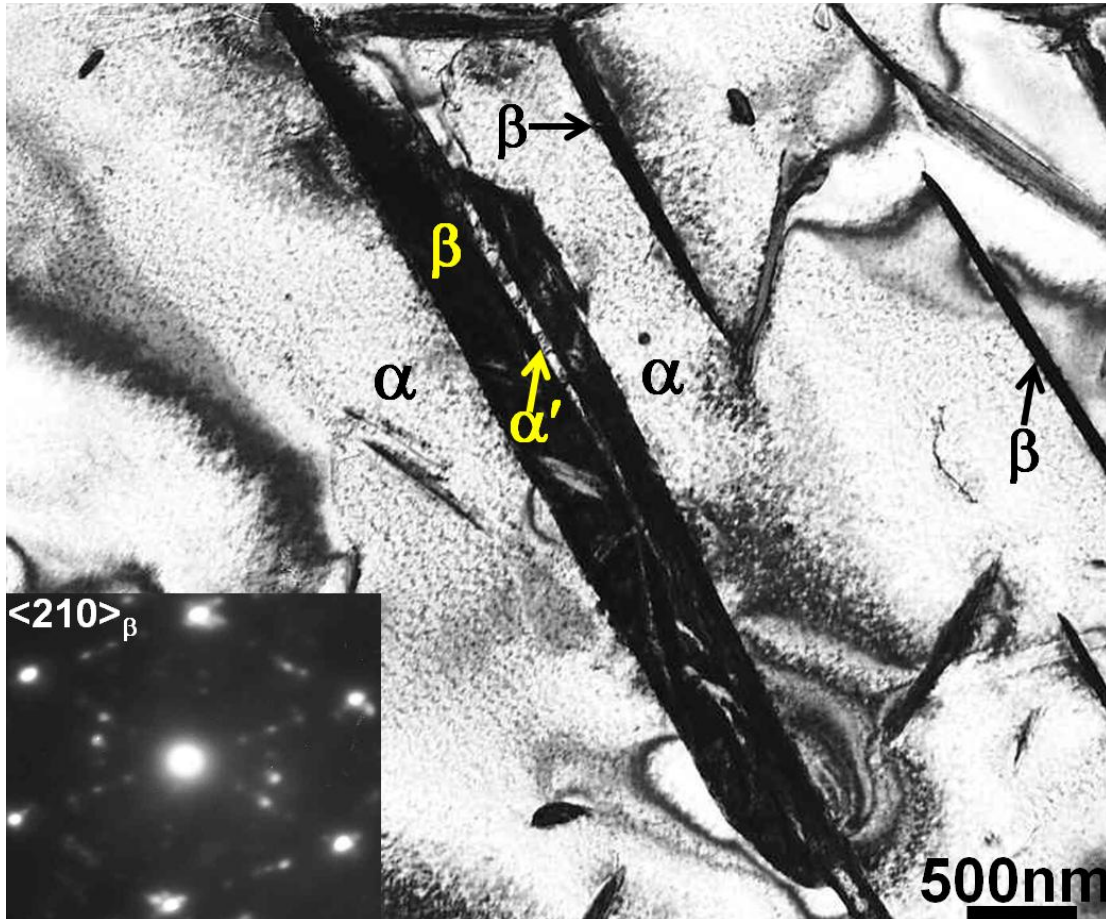


Figure 4.15 Bright-field TEM micrograph showing the formation of acicular α' -plates (marked by an arrow) within an elongated β -precipitate, having comparatively larger dimensions with respect to other precipitates, present in the Zr-1 wt.% Nb alloy sample heat treated at 832 °C for 5 mins. The SAED pattern (Zone Axis = $\langle 210 \rangle_{\beta}$) obtained from this precipitate (given as inset) shows the simultaneous occurrence of ω within it, the indexing of which can be referred from Figure 2.10.

Heat treatment at 832 °C gave rise to β -phase whose composition is conducive for both ω - as well as α' - transformations. This is reflected by the simultaneous presence of both α' - as well as ω - phases in β -patches as well as other coarser β -needles (Figure 4.15) forming inside the α -matrix. However, smaller β -needles with similar composition, showed only ω -transformation without any α' -transformation. In particular, a β -needle with 60 nm width showed only ω -phase formation while α' could be observed in β -precipitates only if their width exceeded 167 nm.

4.3 Discussion

The present study brings into light the following major points worth deeper consideration, as far as microstructural evolution in Zr–1Nb alloy as a function of heat treatment temperature and time in the ($\alpha + \beta_{Zr}$) phase-field is concerned.

1. The evolution of the chemical composition of the β -phase as a function of temperature and time suggested an intermediate favorable metastable composition which is quite different from what is expected from the Zr–Nb phase diagram.
2. The morphological evolution of β -phase in the form of needles and patches during heat treatment in contrast to the spherical precipitates present in the starting microstructure.
3. Some of the β -precipitates, with size less than an apparent critical size, in spite of having the composition favoring the α' -transformation, did not show any such transformation.
4. ω -transformation in general showed less size dependency in comparison to corresponding α' -transformation from the β -phase of suitable composition.

4.3.1 Chemical and morphological evolution of the β -phase

In the present study the Zr–1Nb starting material used for experimentation was a finished fuel tube which had been subjected to a recrystallization annealing heat treatment at 580 °C for 4 h after the final deformation step. This treatment would ideally lead to a microstructure comprising Nb-rich β_{Nb} precipitates in α_{Zr} matrix, as this temperature lies in the ($\alpha + \beta_{Nb}$) two phase-field (Figure AI.1). However, the presence of a miscibility gap between Zr-rich β_{Zr} and Nb-rich β_{Nb} phases in Zr–Nb system (Figure AI.1) results in a free energy barrier for the Nb-enrichment of the β -phase, thereby rendering the process sluggish. Thus, a range in Nb-content of β -phase precipitates, varying between 53 to 75 wt.%, was noticed in the starting microstructure signifying the gradual Nb-enrichment process of the β -phase precipitates. This microstructure, consisting of these uniformly dispersed spherical β -precipitates inside the α -matrix, evolved into an entirely different structure consisting of β -needles and patches during thermal treatments. The average composition of these original spherical β -precipitates was ~ Zr–67 wt.% Nb. This is higher than the equilibrium Nb-content of β -phase at any of the heat treatment temperatures considered in

the present study. This implies equilibrium composition can only be attained by rejection of Nb from the spherical β -precipitates in all cases of the present heat treatments, and the above process being a diffusion-controlled phenomenon is dependent on both temperature and time. This rejection of Nb should result in the dissolution of the pre-existing precipitates. Since the matrix has a very limited solubility of Nb (the maximum being 0.6 wt.% at 610 °C), such a rejection should be accompanied by re-precipitation of fresh β -phase whose morphology will be dictated by a combination of diffusional, strain energy and local microstructural conditions. This was achieved by two means: (i) precipitation in the form of patches at the α grain boundaries and tri-junctions and (ii) precipitation within the α -grains resulting in the formation of elongated precipitates. The processes of dissolution and re-precipitation have happened during all the heat treatments, only the kinetics has become faster at higher temperatures. At lower temperature like 675 °C the diffusivity of Nb in α -Zr is $3.6 \times 10^{-17} \text{ m}^2\text{s}^{-1}$ [216]. This shows that the typical diffusion length ($x = \sqrt{Dt}$) of Nb atoms would be $\sim 0.36 \mu\text{m}$ in 1h. Such low value of diffusion length would make the kinetics of dissolution and re-precipitation slow. This is the reason why substantial volume fraction of pre-existing β precipitates could be seen in the microstructure. This is also responsible for the small size of the elongated precipitates and also the formation of only few patches at the grain boundaries and tri-junctions. Higher temperatures like 800 °C or above made the kinetics faster ($2.5 \times 10^{-16} \text{ m}^2\text{s}^{-1}$) and hence only few spherical precipitates could be seen in the microstructure. This was associated with a corresponding increase in the size of the elongated precipitates and the number density of patches.

The TEM-EDS chemical analysis of the freshly nucleated β -precipitates has shown their composition to be spanning on either side of the equilibrium value. It is equally interesting to note that the lower temperature treatments yielded fresh β -precipitates whose composition is predominantly lower than the equilibrium value. On the other hand treatment at higher temperatures resulted in β -composition exceeding the equilibrium value in most of the cases. Although the former can be explained by the diffusional constraints at lower temperatures to attain the equilibrium compositions, exceeding the equilibrium composition at higher temperatures pointed towards the role of additional factors as discussed in the following.

The nucleation of a β -precipitate in the α -matrix involves (i) segregation of Nb-atoms and (ii) transformation of crystal structure from hcp to bcc [36]. G–X plots (X represents atomic fraction of Nb) have been calculated at all the heat treatment temperatures employing regular solution thermodynamics model by estimating the free energies of hcp α - and bcc β - phases by making use of expressions similar to Equations 2.6 to 2.9.

The expressions for G_{Zr}^{α} and G_{Nb}^{α} , used to calculate the free energy of the α -phase, and for G_{Zr}^{β} and G_{Nb}^{β} , used to calculate the free energy of the β -phase, in the temperature range investigated, are obtained from reference [207]:

$$G_{Zr}^{\alpha} = -7827.595 + 125.64905T - 24.1618T\ln(T) - 4.37791E-3T^2 + 34971T^{-1} \quad (4.1)$$

$$G_{Nb}^{\alpha} = 1480.647 + 144.445475T - 26.4711T\ln(T) + 0.203475E-3T^2 - 0.35012E-6T^3 + 93399T^{-1} \quad (4.2)$$

$$G_{Zr}^{\beta} = -525.539 + 124.9457T - 25.607406T\ln(T) - 0.340084E-3T^2 - 0.009729E-6T^3 + 25233T^{-1} - 0.076143E-9T^4 \quad (4.3)$$

$$G_{Nb}^{\beta} = -8519.353 + 142.045475T - 26.4711T\ln(T) + 0.203475E-3T^2 - 0.35012E-6T^3 + 93399T^{-1} \quad (4.4)$$

The interaction parameter data between Nb and Zr in the α - and β - phases have been obtained from the references [217,218] and are mentioned in the following.

Interaction parameter between Nb and Zr in the α -phase:

$${}^{(0)}L_{Nb,Zr}^{\alpha} = 24411 \quad (4.5)$$

Interaction parameter between Nb and Zr in the β -phase:

$${}^{(0)}L_{Nb,Zr}^{\beta} = 15911 + 3.35 T \quad (4.6)$$

$${}^{(1)}L_{Nb,Zr}^{\beta} = 3919 - 1.091 T \quad (4.7)$$

All thermodynamic data have been expressed in terms of $Jmol^{-1}$.

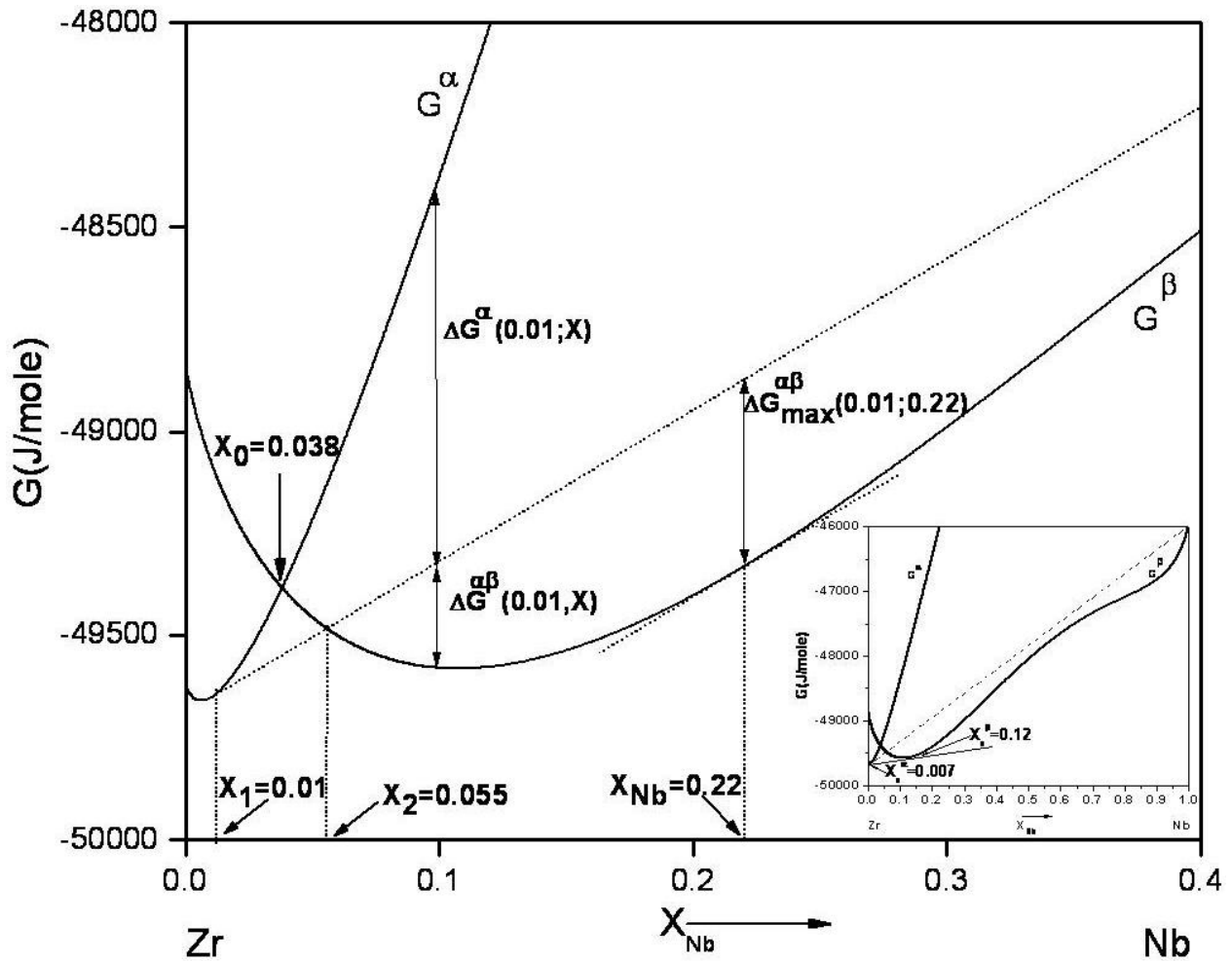


Figure 4.16 Free energy–composition diagram showing the variation of free energies of α - and the β - phases as a function of Nb-content in Zr–Nb system at 675 °C. The inset shows the same diagram for the entire Zr–Nb composition range. X_1 represents the composition of α -matrix and X_0 the composition where the free energies of α - and β - phases become equal. X_2 represents the limiting composition of a β -precipitate for nucleation in a α -matrix of composition X_1 , obtained by the intersection of the tangent drawn to the free energy curve of the α -phase at X_1 with the free energy curve of the β -phase. $\Delta G^\alpha(0.01;X)$ represents the activation energy associated with the nucleation of a β -precipitate of composition X in a α -matrix of composition X_1 , whereas, $\Delta G^{\alpha\beta}(0.01;X)$ the driving force for the same. $\Delta G_{\max}^{\alpha\beta}(0.01;0.22)$ represents the maximum driving force with which a β -precipitate can nucleate in a α -matrix of composition X_1 .

It could be seen from Figure 4.16 (at 675 °C) that, in the nucleation of a Nb-rich β -precipitate from α -matrix, of composition say Zr–1Nb (X_1), the occurrence of step (i) before step (ii) will involve a very large free energy barrier, as indicated in the figure by $\Delta G^\alpha(0.01;X)$. On the other hand, formation of β -nuclei having a Nb concentration of 5.5 wt.% (X_2) and a subsequent Nb-enrichment of these nuclei will involve a much smaller free energy barrier. In fact the driving force for nucleation becomes maximum ($\Delta G_{\max}^{\alpha\beta}$) for a precipitate containing 22 wt.% of Nb, as shown in Figure 4.16, which is higher than the equilibrium Nb-content of 12 wt.%. If one considers the possible local variation in the matrix composition (due to Nb-rejection from spherical precipitates), different values of X_1 , thus X_2 , and thus β -precipitates with different Nb-contents can be attained. Hence precipitates with varying Nb-contents may develop at different heat treatment temperatures depending on (i) the local composition of the matrix from where the precipitate is nucleating, (ii) diffusional and (iii) the nucleation being an early or a delayed event with respect to heat treatment duration. The Nb-content of a β -precipitate can reach to its maximum possible value (X_m) if it (i) nucleates in a matrix, having Nb-content just lower than the value at which the free energy curves for the α - and the β - phases intersect and (ii) attains the Nb-content, corresponding to this matrix composition of (i), for which the driving force for nucleation is maximum. An assessment of X_m can be carried out, an example of which is shown in the G–X plot at 800 °C in Figure 4.17, by approximating the matrix composition to the intersection of the G^α and G^β curves i.e., X_0 and estimating the precipitate composition at which the driving force for nucleation is maximum. These compositions i.e., X_0 , X_m and also the equilibrium matrix and precipitate compositions (X_e^α , X_e^β) have been estimated at different temperatures viz., 675 °C, 800 °C, 825 °C, 832 °C and are presented in Table 4.2. The table clearly brings out that the composition corresponding to the maximum driving force is larger than the equilibrium values at all the temperatures of interest to the present study. Such exceeding of equilibrium composition requires high degree of diffusion and hence was observed predominantly in case of high temperature treated samples in the present study.

The same thermodynamic analysis also brings out the fact that a critical Nb-enrichment of the β -phase is required to be fulfilled for its nucleation from the α -matrix, which was found to be 3.8 wt.% of Nb at 675 °C, refer Figure 4.16. This explains the observation of a minimum of 4

wt.% of Nb in the β -precipitates in spite of comparatively higher diffusional constraints operating at 675 °C.

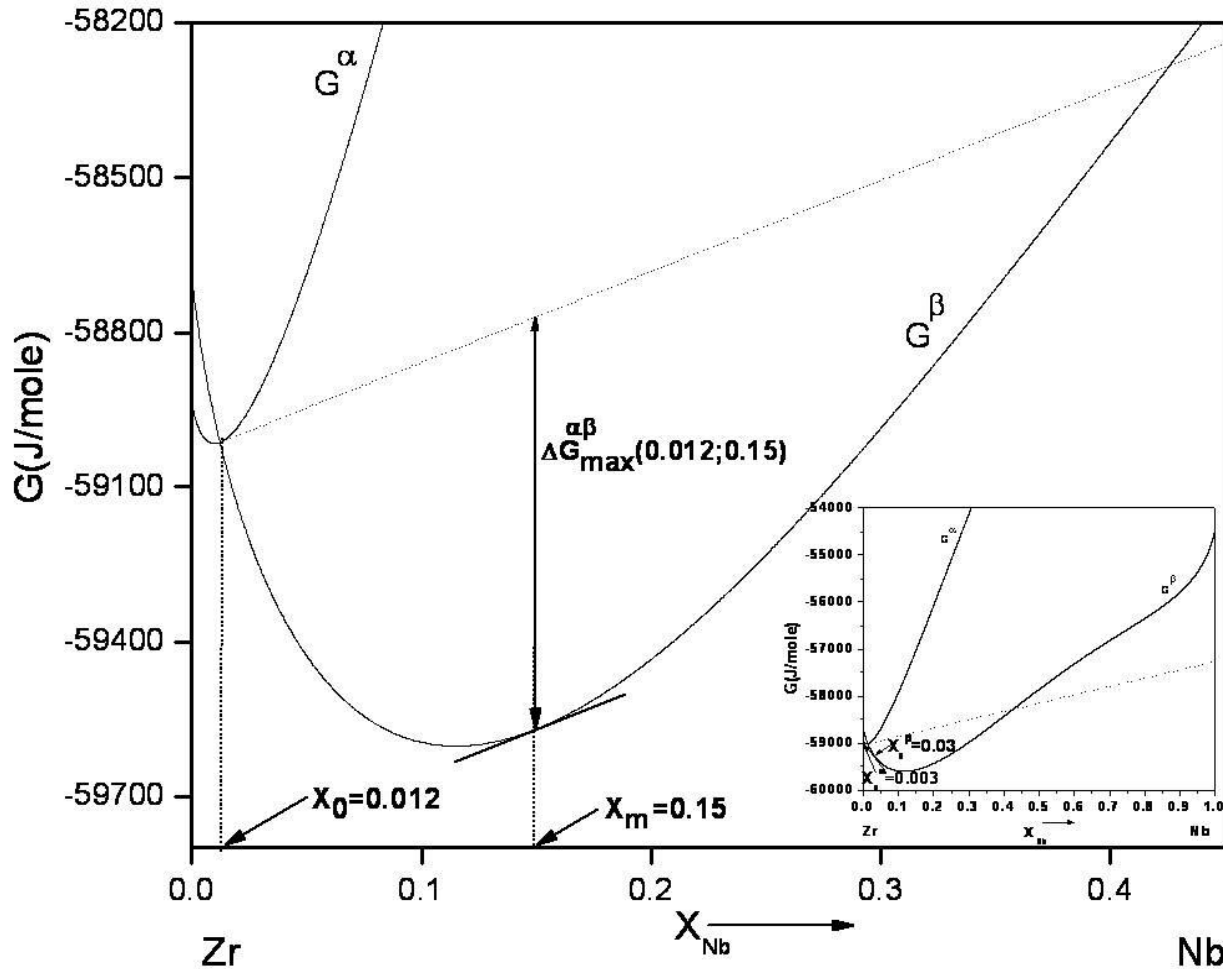


Figure 4.17 Free energy–composition diagram showing the variation of free energies of α - and the β - phases as a function of Nb-content in Zr–Nb system at 800 °C. The inset shows the same diagram for the entire Zr–Nb composition range. X_0 represents the composition at which the free energies of α - and β - phases are equal, and also the limiting composition of α -matrix for nucleation of β -precipitate. X_m represents the maximum Nb-content that a nucleated β -precipitate can achieve, and is obtained by maximizing the driving force of nucleation ($\Delta G_{\max}^{\alpha\beta} (0.012; 0.15)$) in respect of the tangent drawn to the free energy curve of the α -phase at X_0 .

Table 4.2 Nb contents of α - and β - phases in Zr–Nb system estimated from free energy–composition diagrams at 675 °C, 800 °C, 825 °C and 832 °C.

Temperature (°C)	X_e^α (wt. % Nb)	X_0 (wt. % Nb)	X_e^β (wt. % Nb)	X_m (wt. % Nb)
675	0.7	3.8	12	98
800	0.3	1.2	3	15
825	0.2	0.75	2	8
832	0.18	0.62	1.5	6

Elongated or needle like morphology of the β precipitates could be explained on the basis of the invariant line strain (ILS) model, as proposed by Dahmen [219]. According to this model because of the similarity in the atomic arrangements in the $(0001)_{\text{hcp}}$ and $(110)_{\text{bcc}}$ planes, many diffusional transformations in hcp-bcc systems involves the growth of the product phase as a lath or needle along an invariant line lying in $(0001)_{\text{hcp}}$. The needle morphology and invariant line minimizes the strains associated with the transformation. In the case of Zr–2.5 wt.% Nb alloy needle shaped Nb-rich β -precipitates have been observed in the α -matrix during tempering of β -quenched martensitic structures [59,209]. Luo and Weatherly [59] used the ILS model of Dahmen and predicted both the growth direction and crystallographic orientation of these precipitates; OR corresponded to that of Burgers [57] and the true growth direction was $\langle 7.09; 1.09; 6; 0 \rangle_{\text{hcp}}$ and $\langle 8; 1; 7; 0 \rangle_{\text{hcp}}$ lying on the $(0001)_{\text{hcp}}$ basal plane. The precipitates were also associated with strain field and showed Moire contrast under particular diffracting conditions. In the present work as well the obeying of Burgers OR by the β -precipitates and their growth directions making angles of 80° to 90° with $[0001]_{\text{hcp}}$ coupled with occurrence of strain field and Moire contrast (marked by an arrow in Figure 4.18) established similarities with the work of Luo and Weatherly [59] and suggested ILS to be the plausible mechanism responsible for the evolution of β -precipitates with needle morphology. The substantial increase in the sizes of the needles at higher temperatures was simply because of the higher diffusivities.

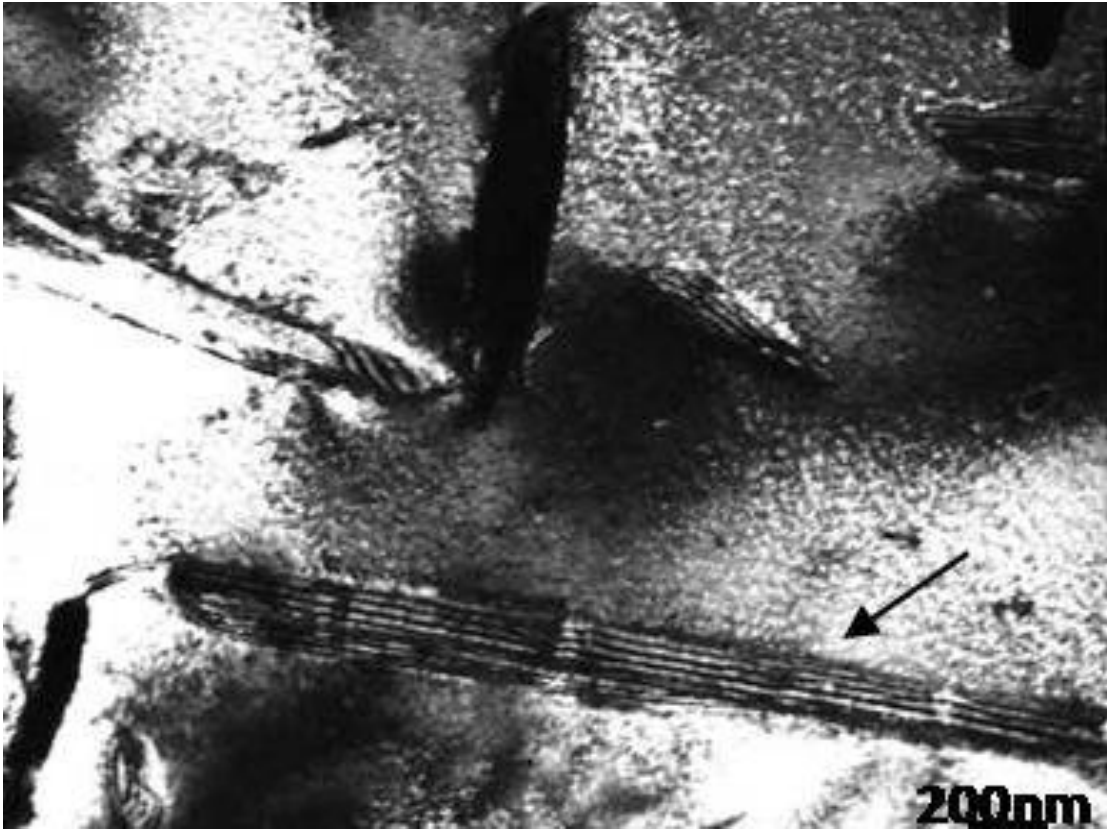


Figure 4.18 Bright-field TEM micrograph showing an elongated β -precipitate in Zr-1 wt.% Nb alloy (marked by an arrow) exhibiting Moiré contrast and strain field.

In an elongated precipitate, the broad faces are normally surrounded by low energy coherent/semi-coherent interfaces and the edges are made by incoherent interfaces. Mobility of coherent/semi-coherent interfaces requires the presence of growth steps or ledges and precipitate growth occurs by the volume diffusion controlled transport of solute to these steps. The thickening of the needles occurs by the lateral motion of the ledges. Generally for a volume diffusion controlled growth reaction it has been found that the half-thickness, a_x , and half-length, a_y , of the precipitates vary with the square root of the annealing time [220,221] as follows:

$$a_x=2(\beta Dt)^{1/2} \text{ and } a_y=2A(\beta Dt)^{1/2} \quad (4.8)$$

where A is the initial aspect ratio, D is the diffusion coefficient and β is a dimensionless growth parameter. A plot of the maximum half-length, corresponding to each annealing time at 800 °C, showed an increase against the square root of time (Figure 4.19). However, the maximum half width first decreased and then increased as is evident from Table 4.3. The observed thickening behavior as mentioned above could be explained on the basis of the interface nature of the broad

face of the precipitate as discussed above. The thickening reaction is not solely diffusion limited but it is partly interface limited as well because for a ledged interface, the interface velocity is limited by ledge density. The thickening velocity will not be maintained unless very rapid rates of ledge nucleation can occur. This may inhibit thickening leading to an increase in the aspect ratio. From Table 4.3 it could be seen that, in the early stages of heat treatment at 800 °C (upto 2 h) the thickening of the needle like precipitates was inhibited by interfacial processes, thus giving an increase in the aspect ratio. Subsequently thickening and lengthening occurred at diffusion-controlled rates with a constant aspect ratio ($A \sim 19$). It is proposed that the period of inhibited thickening, which increased the aspect ratio, ended when the longest precipitates intersected other precipitates, normally on different variants of the habit plane. The intersection points provided the growth ledges that were needed for thickening [222]. This also explained the observed decrease in the number of orientation variants of elongated β -precipitates with time.

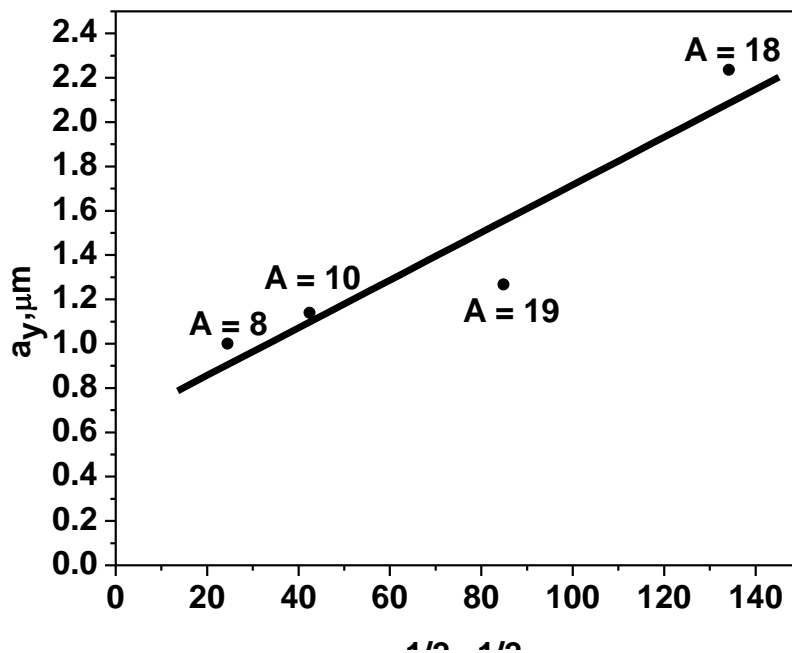


Figure 4.19 A plot of the maximum half-length of the precipitates against the square root of time at 800 °C in Zr–1 wt.% Nb alloy. The corresponding maximum aspect ratio (A) of the precipitates has been indicated in the plot.

Table 4.3 Morphological parameters of β -phase precipitates in 800 °C heat treated Zr-1 wt.% Nb alloy samples.

<i>Parameter</i>	<i>10 mins</i>	<i>30 mins</i>	<i>2 h</i>	<i>5 h</i>
Maximum length (nm)	2000	2278	2533	4472
Maximum width (nm)	380	267	179	389
Width corresponding to maximum length (nm)	250	222	133	250
Maximum aspect ratio	8	10	19	18

4.3.2 Size dependency of β -phase transformations

The present study has clearly brought out that having the suitable chemical composition is not sufficient enough to induce α' - or ω - transformations (Section 4.2.2). β -precipitates which are larger than a critical size (167 nm in the case of α' and 60 nm in the case of ω) have only undergone these transformations. This clearly brings out the importance of size effect in determining the feasibility of these transformations.

The present Section has made an attempt to rationalize the size dependency of feasibility of α' -transformation, the energetics involved in which have been evaluated as a function of the size of the β -phase. The fundamental governing equation expressing such energetics can be expressed as,

$$\Delta F = V(\Delta F_v^T + W^*) + AS \quad (4.9)$$

where, V = volume of α' -martensite, ΔF_v^T = free energy change per unit volume for bcc \rightarrow hcp transformation, W^* = strain energy density of α' per unit volume, S = interface energy per unit area between α' and β (taken to be 200 mJ/m², typical of semi-coherent interfaces), A = interface area between α' and β . ΔF_v^T was evaluated using regular solution thermodynamics model, as mentioned earlier. Eshelby micro-mechanical theory was used to estimate W^* [223], which relies on the following principle [224]:

- (i) Cutting and removal of the region to be transformed from the matrix (called as 'inclusion').
- (ii) Allowing the 'inclusion' to transform unconstrainedly.

(iii) Application of suitable surface tractions to restore the transformed ‘inclusion’ back to its original shape.

(iv) Putting the ‘inclusion’ back into the hole in the matrix and rejoining it across the cut. There is no change in the deformation fields in either the ‘inclusion’ or the matrix from step (iii).

(v) Removal of the applied surface traction, which have become as a built in layer of body force spread over the interface between the matrix and the ‘inclusion’, by applying a cancelling body force to the internal surface of the elastic body. The additional elastic field thus introduced is computed by integration from the expression for the elastic field of a point force.

The α' was assumed to be an ellipsoid cylinder, where its radii $a_1 = a_2 \ll a_3$. W^* , of a precipitate in a homogeneous matrix is given by

$$W^* = -\frac{1}{2} \sigma_{ij}^* \varepsilon_{ij}^p \quad (4.10)$$

where, σ_{ij}^* is the homogeneous internal stress in the transformed region (α'). This stress arises due to the presence of some uniform Eigen strain ε_{ij}^p in the transformed region. In this case, the Eigen strain is simply the Bain tensor [225]. The expression for σ_{ij}^* is given by the following relation [223]:

$$\sigma_{ij}^* = C_{ijkl}^* (S_{klmn} (\varepsilon_{mn}^* + \varepsilon_{mn}^{tr}) - \varepsilon_{kl}^{tr}) = C_{ijkl} (S_{klmn} (\varepsilon_{mn}^* + \varepsilon_{mn}^{tr}) - (\varepsilon_{kl}^* + \varepsilon_{kl}^{tr})) \quad (4.11)$$

where ε_{mn}^* is a fictitious eigen strain introduced to account for the differences in elastic properties of the matrix and precipitate. The quantities S_{klmn} (called Eshelby tensor) for an ellipsoidal precipitate are given in [223]. The elastic stiffnesses C_{ijkl}^* and C_{ijkl} describe the elasticity of the precipitate and the matrix, respectively. For estimation of the elastic strain energy, temperature-dependent elastic modulus data was used [226]. For calculation purpose the Nb-content in the β -phase was taken as 8 wt.%, the limiting Nb-content of the β -phase to show α' -transformation.

It is to be noted that in general α' -transformation involves formation of more than one variant of the α' -phase. A considerable reduction in the net strain energy is possible by suitable geometric arrangement of these variants. Previous works have shown that strain energy reduction to the extent of 90% is achievable in case of twin-related three-plate α' -clusters [60]. Figure 4.20

depicts the energetics involved in the formation of single α' -needle as a function of the extent of strain energy accommodation for various size of β -precipitates from which it is forming. In calculating this figure, the size of the β -precipitate was equated to the longest dimension of the α' -needle and aspect ratio of α' was taken to be 6 (as the smallest β -precipitate in which α' was observed in the present study had an aspect ratio of 6). This β -size actually corresponds to the smallest dimension of β that needs to be present in all the directions, for facilitating α' formation without any directional bias. In addition an undercooling of ΔM_s ($= T_o - M_s$, where T_o is the temperature at which the α - and β - phases of 8 wt.% Nb are in equilibrium and M_s is the martensite start temperature) of 50 °C was considered as per Kaufman's work [227].

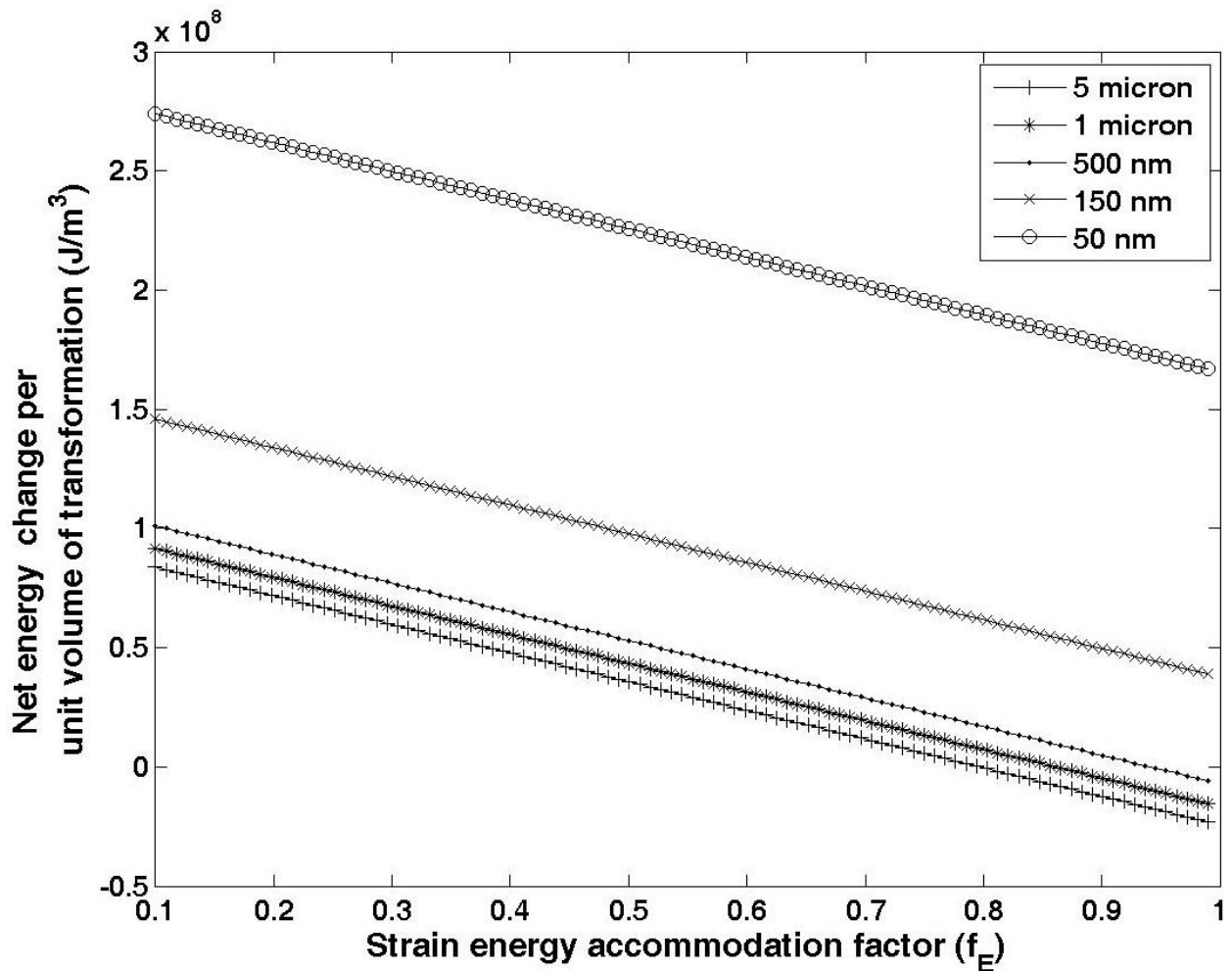


Figure 4.20 Effect of strain energy accommodation on the feasibility of martensite formation inside β -precipitate as a function of the size of the precipitate (assuming an undercooling of ΔM_s : 50 °C and precipitate composition of Zr–8 wt.% Nb).

It is clear from Figure 4.20 that to induce α' -transformation in β of size few microns, strain energy accommodation of more than 80% is required at an undercooling of 50 °C, which was shown to be practically feasible [60]. What is even more interesting is that, even with 100% strain energy relaxation, the calculations show that at this level of undercooling, α' formation in a particle of nano-dimension is not feasible, signifying the dominating role of interface energy at this size ranges. Practically there exists a very little scope of strain accommodation, by formation of α' in self-accommodating morphologies, in β in the nano-size domain due to constrained volume.

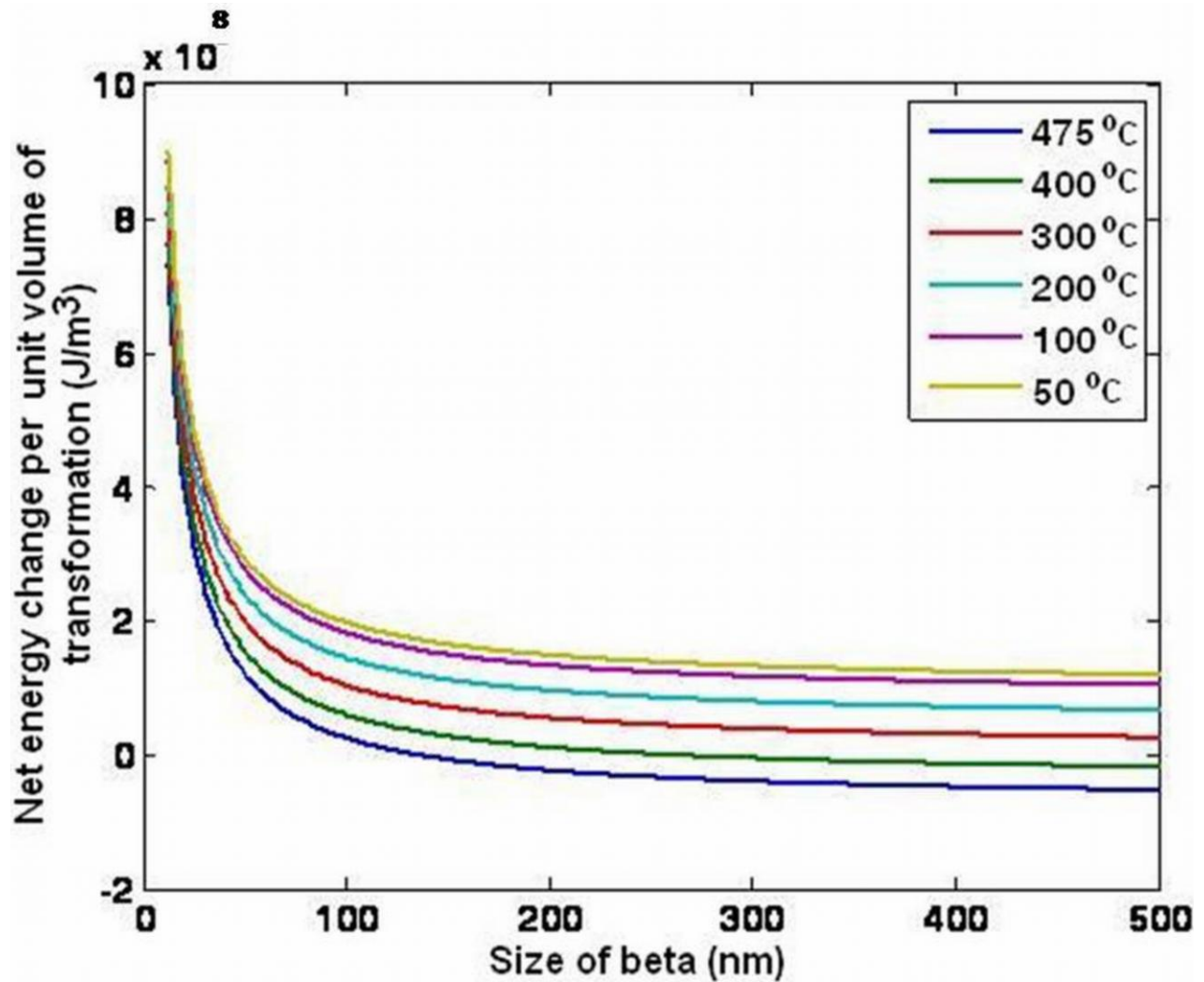


Figure 4.21 The net energy change associated with martensitic transformation against various assumed values of β -precipitate size and undercooling (ΔM_s) (assuming a precipitate composition of Zr-8 wt.% Nb).

Only other avenue by which transformation can be induced in such nano-size precipitates is by enhancing the driving force through increased undercooling. Such a possibility was also simulated (ignoring the strain energy accommodation) and presented in Figure 4.21, as a function of β -precipitate size (assuming a precipitate composition of Zr–8 wt.% Nb). Figure 4.21 clearly shows that the requirement of undercooling is of the extent of few hundred of degrees when the size of the β -precipitate is in nanometers. Further, it also shows that a critical size of 150 nm of β -precipitate is required in order to induce α' -formation at the maximum possible undercooling (corresponding to $T_o = 500$ °C and M_s as room temperature ~ 25 °C) which is in good agreement with the experimental observation of 167 nm and 1000 nm as the width and length of the smallest β -precipitate showing α' -transformation. This finding was further corroborated when a β -precipitate with length and width of 231 nm and 60 nm (note that critical dimension for α' -transformation is not exceeded in all directions), respectively, and having composition suitable for both α' - and ω - transformations showed only ω .

ω -transformation on the other hand has been found to occur in much finer precipitates as compared to α' -transformation. Diffraction analysis combined with HREM could detect ω in β -precipitates of sizes down to 60 nm (which is much lower than the smallest β -precipitate with α' -transformation). This is mainly because ω forms coherently within the β -phase [64,228] and hence the interfacial energy reduces substantially. Moreover, the misfit between the ω -particles and the parent β -phase becomes very low as the Nb-content of the ω -phase reaches around 10 wt.% [39]. This results in the reduction of the misfit strain energy. These two aspects (low interface energy and strain energy) gave rise to observed lower size dependency of ω -transformation in comparison to corresponding α' -transformation.

4.4 Summary

The morphological and compositional evolution of β -phase, as a function of heat treatment temperature and time in the ($\alpha + \beta_{Zr}$) phase-field, followed by its transformation into metastable phases on quenching has been assessed in the Zr–1Nb alloy. The salient findings of the investigation have been summarized in the following:

- Significant changes in the morphologies of the β -phase from spherical precipitates to irregular shaped patches and elongated needles were observed during heat treatment at various temperatures (675 °C, 800 °C, 825 °C and 832 °C) for different time durations.
- The growth of the β -precipitates in form of needles was found to follow the invariant line strain (ILS) criteria.
- The morphological changes of the β -phase were coupled with attainment of metastable compositions (higher than equilibrium), which could be rationalized thermodynamically by virtue of free energy–composition (G–X) diagrams.
- Transformation within the β -needle, upon quenching from the heat treatment temperature, was governed both by its composition and size.
- Thermodynamics and micromechanical modeling predicted the critical size of the β -precipitate to allow α' -transformation as 150 nm, which is in close agreement with the experimental observation of 167 nm.
- Though α' - and ω - phase transformations both showed limiting β -phase sizes for occurrence, the dependence of former on the size of the β -phase was more evident.

Study on γ -phase stability in U–9Mo alloy

5.1 Background

The irradiation stability of γ -phase U-alloys is linked to their ability to retain the isotropic bcc γ -phase in metastable state at the reactor operating temperature. In this context, the work highlighted in this chapter is focused on a U–9Mo alloy, wherein the stability of the γ -phase against different thermo-mechanical treatments has been investigated employing various microstructural characterization techniques. The stability of the γ -phase in as-cast, as-rolled, homogenized and aged conditions has been assessed. The homogenization of as-rolled samples, carried out in the γ -U phase-field at 1000 °C for 24 h, was aimed (i) to bring in complete chemical and microstructural uniformity in the as-rolled samples and (ii) to generate a different starting condition, apart from the as-rolled condition, for the subsequent ageing experimentations. Since the γ -phase in U–Mo alloys, containing Mo in the range of 8-10 wt.%, has been shown to decompose in a sluggish manner at lower temperatures [12], the ageing studies were conducted in the ($\alpha + \gamma'$) phase-field at temperatures closer to the eutectoid temperature, so as to make the decomposition kinetics faster. Moreover, since U–9Mo happens to be a hypo-eutectoid composition from literature [24,134-136], ageing was also carried out in the ($\alpha + \gamma$) phase-field lying above the eutectoid.

It is to be noted that in comparison of Zr–1Nb alloy, where heat treatments were carried out in the temperature range of 675 °C-832 °C, the maximum ageing temperature in the case of U–9Mo alloy for decomposition of the γ -phase was restricted to 575 °C. This is because the ($\alpha + \beta_{Zr}$) phase-field in the former, where changes in β -phase composition, morphology and volume fraction were noticed, existed over the temperature interval of 610 °C-840 °C, whereas, in the case of latter a further higher ageing temperature would take the alloy into the single γ -phase field thereby stabilizing the γ -phase further.

5.2 Experimental observations

Microstructural studies of as-cast, as-rolled, homogenized and aged samples of U–9Mo alloy using X-ray diffraction, optical microscopy, SEM and TEM have generated information with respect to the morphology, distribution and identity of the constituent phase(s).

The XRD patterns obtained from different samples were analyzed using the PowderCell Program [214]. The space group, Wyckoff notation, atomic position and lattice parameter data of the probable phases, needed for analysis, were collected from Pearson’s Handbook [215] (Table 5.1). In the case of γ' (U_2Mo)-intermetallic compound, the above data was obtained by consulting the work of Halteman [229] and the International Tables for Crystallography [230]. For quantitative phase (volume fraction) analysis using PowderCell Program, the standard powder patterns corresponding to each of the probable phases were first generated based on the abovementioned crystallographic inputs pertaining to each phase. A simultaneous fitting of the experimentally determined pattern with all of the generated standard patterns was then carried out in respect of position, intensity and line profile of individual peaks. In doing so, the technique of Rietveld refinement was employed using the pseudo-Voigt profile shape function. The volume fraction of individual phases was estimated by the ratios of relative intensities of respective lines of each phase in the experimental and the generated pattern.

Table 5.1 Space group, Wyckoff notation, atomic position and lattice parameter data of α -U, γ -U, γ' (U_2Mo), UO_2 and UO used for the analysis of X-ray diffraction patterns.

Phase	Space Group (Space Group No.)	Atom	Wyckoff Notation	Atomic Position			Lattice parameter (nm)		
				x	y	Z	a	b	C
α -U	$Cmcm$ (63)	U	4c	0	0.1034	0.25	0.285	0.587	0.495
γ -U	$Im\bar{3}m$ (229)	U	2a	0	0	0	0.353	0.353	0.353
γ' (U_2Mo)	$I4/mmm$ (139)	U	4e	0	0	0.328	0.343	0.343	0.983
		Mo	2a	0	0	0			
UO_2	$Fm\bar{3}m$ (225)	U	4a	0	0	0	0.547	0.547	0.547
		O	8c	0.25	0.25	0.25			
UO	$Fm\bar{3}m$ (225)	U	4b	0.5	0.5	0.5	0.492	0.492	0.492
		O	4a	0	0	0			

XRD pattern obtained from the as-cast sample is shown in Figure 5.1. Analysis of this pattern showed the retention of the high temperature γ -phase in a metastable state at room temperature, and the occurrence of UO and UO₂ inclusions. The total phase fraction of the inclusions was estimated to be around 12 vol.%, with UO being about 8 vol.%. The XRD patterns of the as-rolled and homogenized samples (Figure 5.2) were very similar to that of the as-cast sample and pointed towards the stabilization of the γ -phase as well. In fact, the as-rolled sample, furnace-cooled after being homogenized at 1000 °C for 24 h, also showed no signature of decomposition of the γ -phase, as may be seen in the XRD pattern of Figure 5.2. TEM analysis of this sample, through imaging and SAED, confirmed the stabilization of the γ -phase at room temperature. Typical bright-field TEM micrograph and SAED pattern are given in Figures 5.3 and 5.4, respectively.

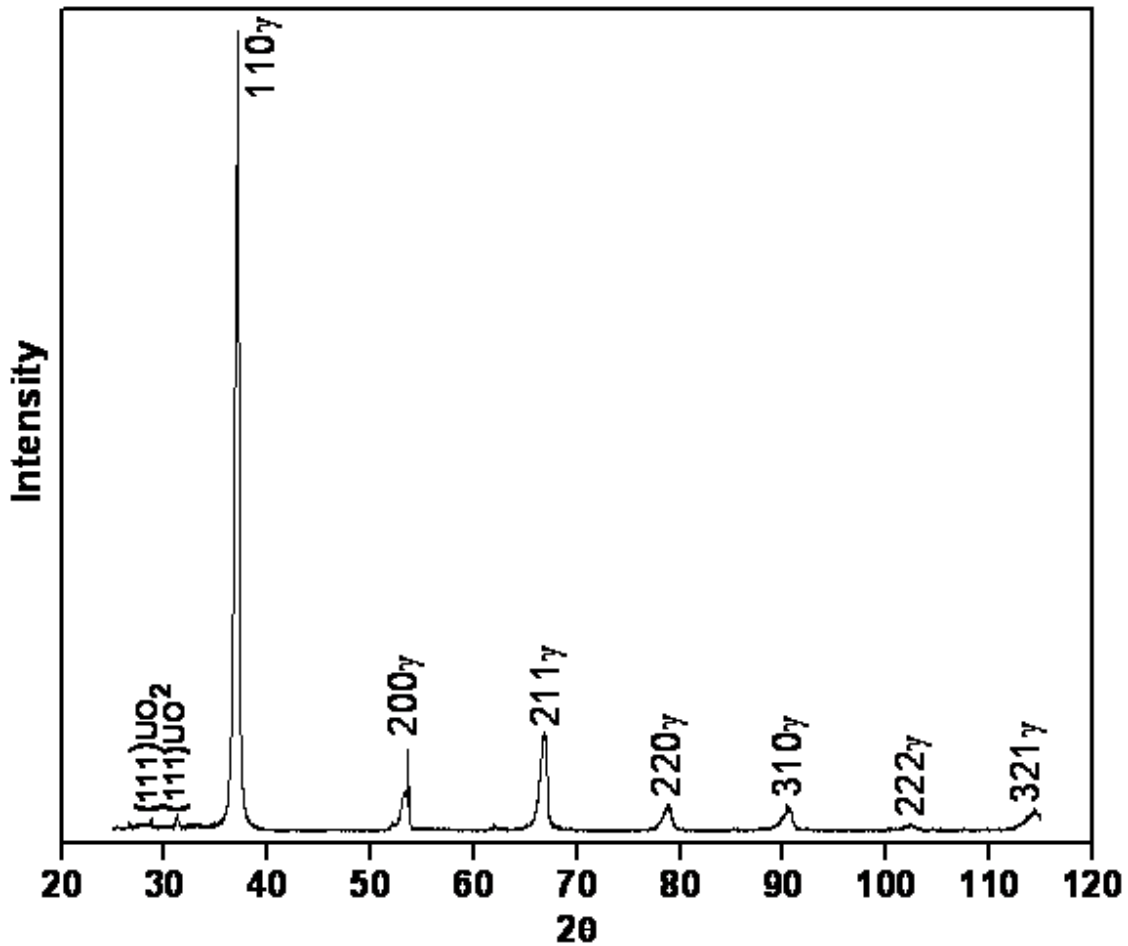


Figure 5.1 X-ray diffraction pattern obtained from the vacuum induction melted and cast U-9 wt.% Mo alloy.

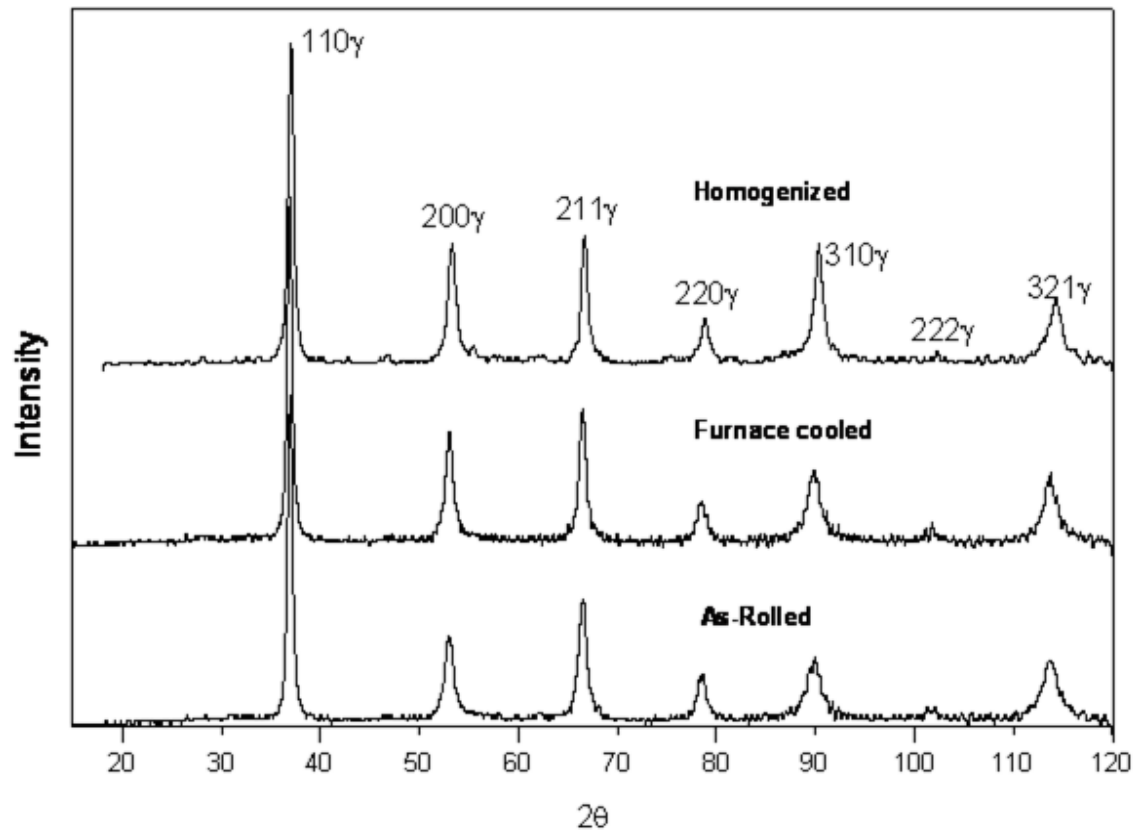


Figure 5.2 X-ray diffraction patterns obtained from the homogenized, furnace-cooled and as-rolled samples of U-9 wt.% Mo alloy.

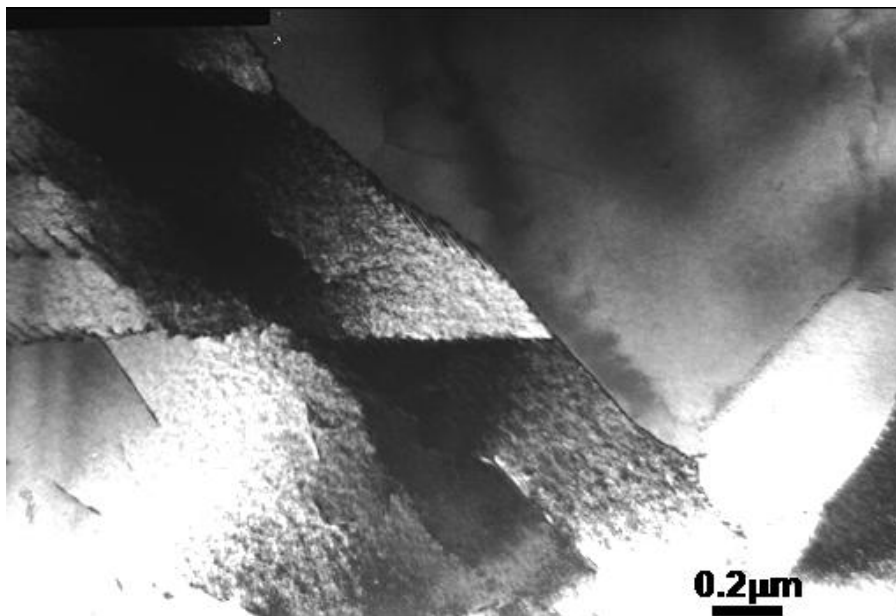


Figure 5.3 A typical bright-field TEM micrograph representing the microstructure of the as-rolled U-9 wt.% Mo alloy sample furnace-cooled after being homogenized at 1000 °C for 24 h.



Figure 5.4 A typical SAED pattern (Zone Axis = $[001]_{\gamma}$) obtained from the γ -phase present in the microstructure of the as-rolled U-9 wt.% Mo alloy sample furnace-cooled after being homogenized at 1000°C for 24 h.

Optical microscopy images of the as-cast, as-rolled and homogenized samples are presented in Figures 5.5, 5.6 and 5.7, respectively. Microstructure of the as-cast sample (Figure 5.5) very distinctly showed the presence of inclusions in particulate morphology at the grain boundaries and within the grains, which were identified as UO and UO_2 by XRD analysis. The average grain size in the cast state was estimated to be $\sim 74\ \mu\text{m}$. The as-rolled sample showed very small grains of the γ -phase, average size being of the order of $\sim 16\ \mu\text{m}$ (Figure 5.6). A considerable increase in grain size ($\sim 133\ \mu\text{m}$) occurred during homogenization (Figure 5.7). In addition, abnormal grain coarsening could also be noticed in this sample at many places (marked by boxes in Figure 5.7).

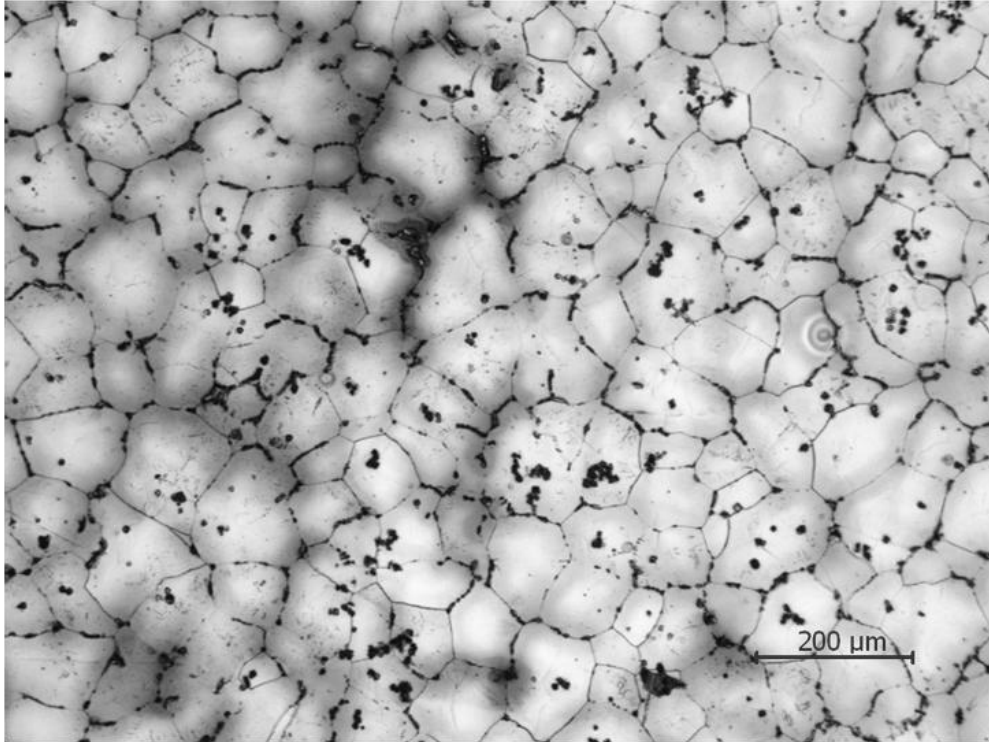


Figure 5.5 Optical micrograph showing the microstructure of vacuum induction melted and cast U-9 wt.% Mo alloy.

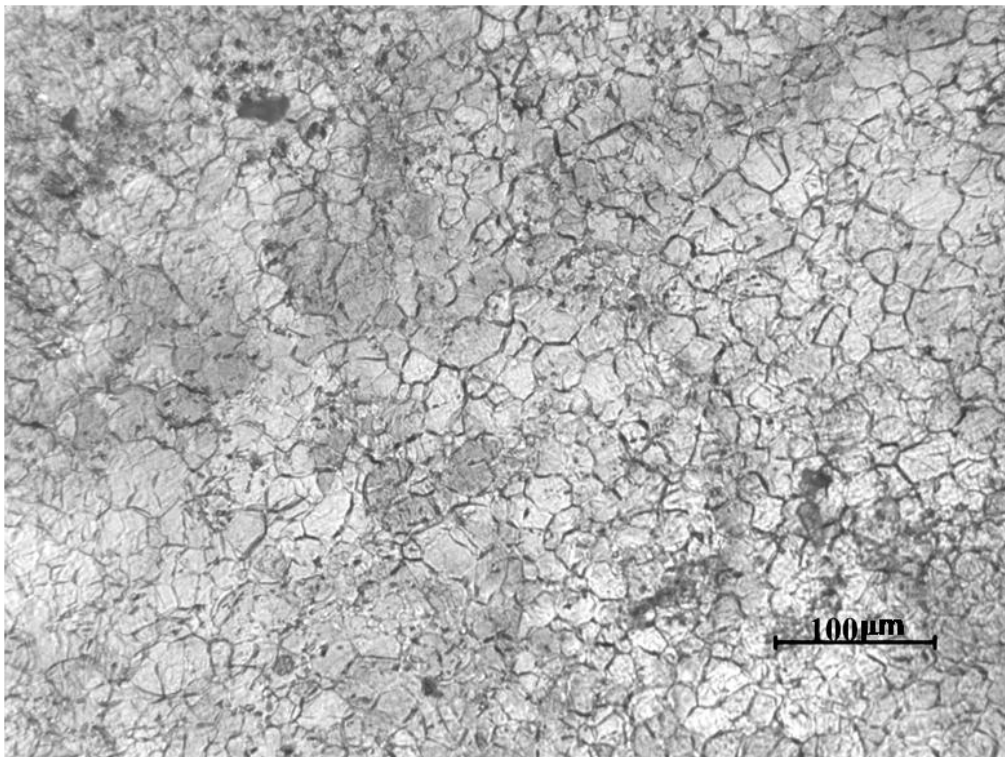


Figure 5.6 Optical micrograph showing the microstructure of as-rolled U-9 wt.% Mo alloy.

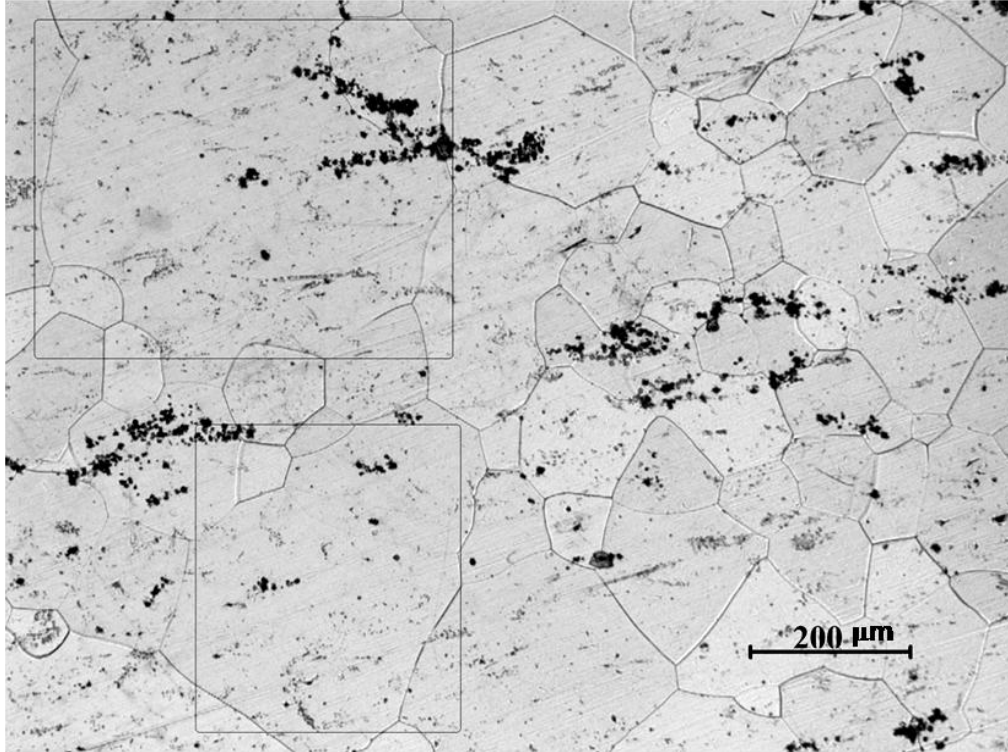


Figure 5.7 Optical micrograph showing the microstructure of homogenized U-9 wt.% Mo alloy. Boxes marked in the figure indicate abnormal grain coarsening noticed in the microstructure.

In order to investigate the effect of two different starting microstructures, viz., as-rolled vs. homogenized, on the stability of the metastable γ -phase or its decomposition into the stable phase(s) at higher temperatures, ageing heat treatments of as-rolled and homogenized samples were carried out at three different temperatures of 500 °C, 565 °C and 575 °C for different time periods. The ageing conditions have been elaborated in Table 5.2.

Table 5.2 Ageing schedule of U-9 wt.% Mo alloy.

<i>Initial state of sample</i>	<i>Ageing temperature (°C)</i>	<i>Ageing duration (days)</i>
As-rolled	500	5, 40
	565	7, 14
	575	14
Homogenized	500	5

Optical micrographs representative of overall microstructural characteristics of the samples aged at 500 °C are given in Figures 5.8 to 5.10.

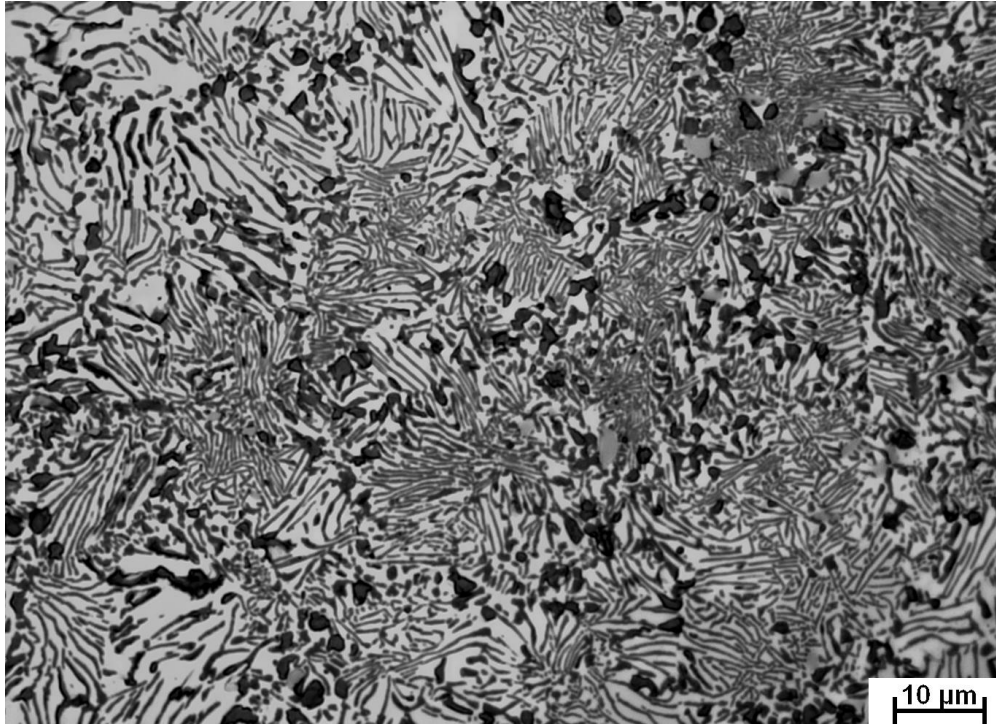


Figure 5.8 Optical micrograph of as-rolled U-9 wt.% Mo alloy after ageing at 500 °C for 5 days.

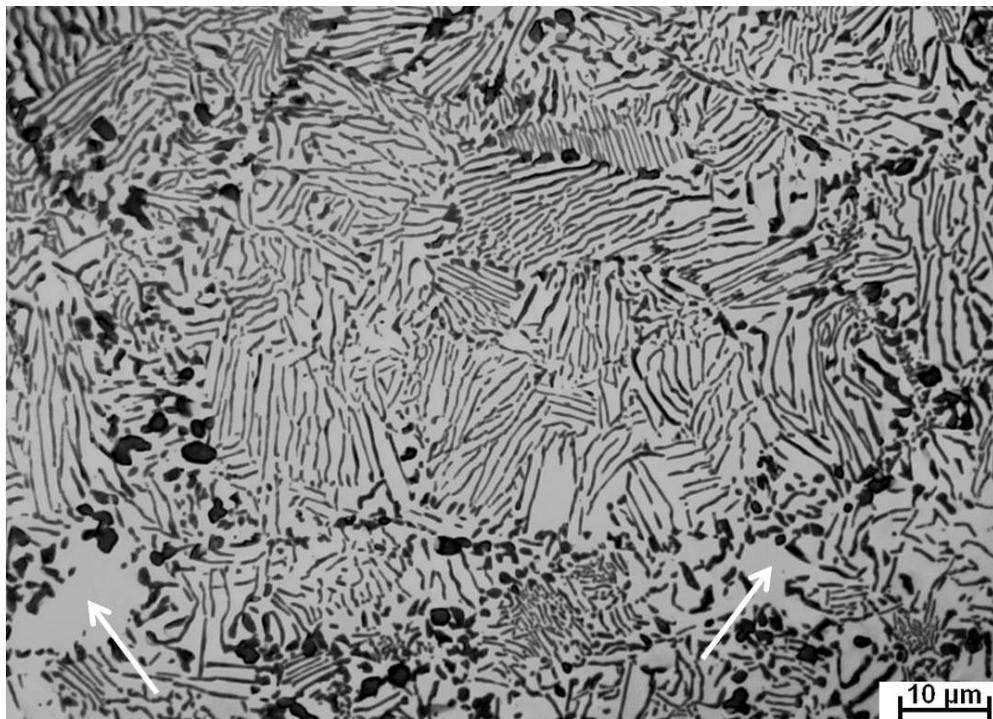


Figure 5.9 Optical micrograph of homogenized U-9 wt.% Mo alloy after ageing at 500 °C for 5 days. The regions marked by arrow indicate undecomposed γ -phase.

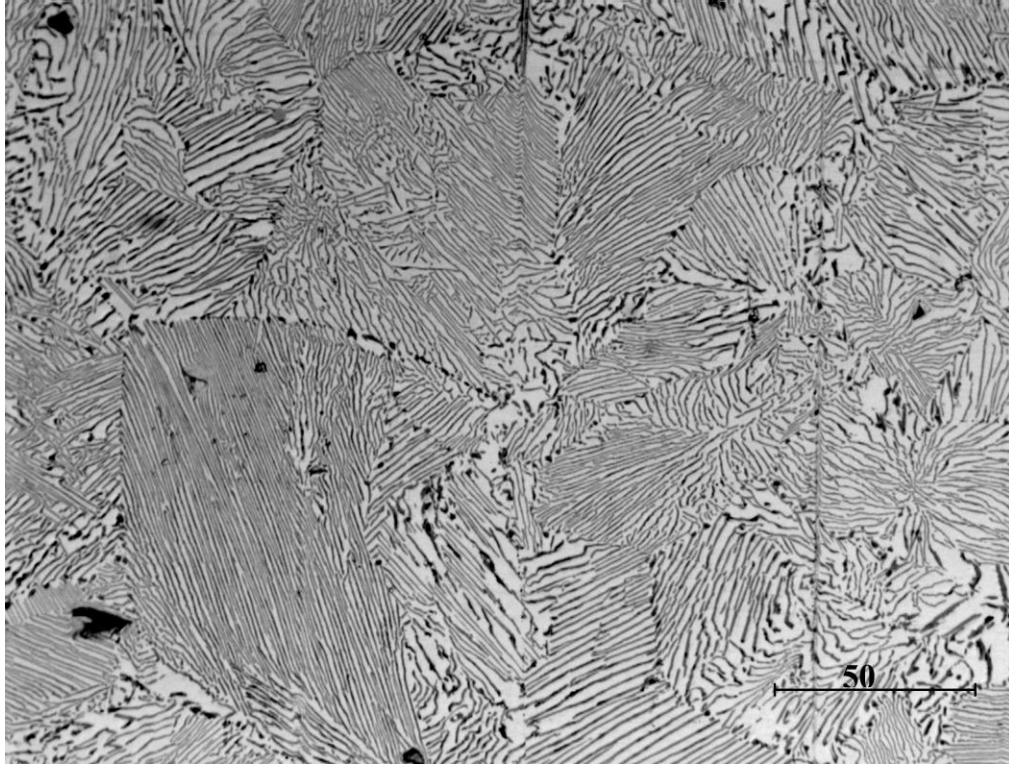


Figure 5.10 Optical micrograph of as-rolled U-9 wt.% Mo alloy after ageing at 500 °C for 40 days.

It could be seen from these micrographs that ageing of the metastable γ -phase at 500 °C has led to its decomposition, as lamellar features characteristic of a eutectoid decomposition reaction are visible in these micrographs. It also became visibly apparent that the extent of decomposition is higher in the case of as-rolled sample as compared to the homogenized sample for same ageing duration (5 days), as density of lamellar features was found to be more in the former and undecomposed γ -regions could be seen in the latter (as indicated by arrows in Figure 5.9). In addition, the decomposition event in the as-rolled sample for both the ageing durations viz., 5 and 40 days was found to be nearly complete, as lamellar features were present throughout the microstructure without any undecomposed γ -regions.

Optical micrographs representative of overall microstructural characteristics of the samples aged at 565 °C and 575 °C are given in Figures 5.11 to 5.13. It may be seen from the micrographs that ageing at 565 °C has as well led to the decomposition of the metastable γ -phase, as lamellar microstructures are visible in Figures 5.11 and 5.12. However, the decomposition event did not proceed to completion, as un-decomposed γ -grains could easily be noticed in these

micrographs. In the microstructure of the sample heat treated at 575 °C (Figure 5.13), small needle-like feature, as marked by arrows in Figure 5.13, could be found distributed in a non-random manner within many γ -grains.



Figure 5.11 Optical micrograph of as-rolled U-9 wt.% Mo alloy after ageing at 565 °C for 7 days.



Figure 5.12 Optical micrograph of as-rolled U-9 wt.% Mo alloy after ageing at 565 °C for 14 days.

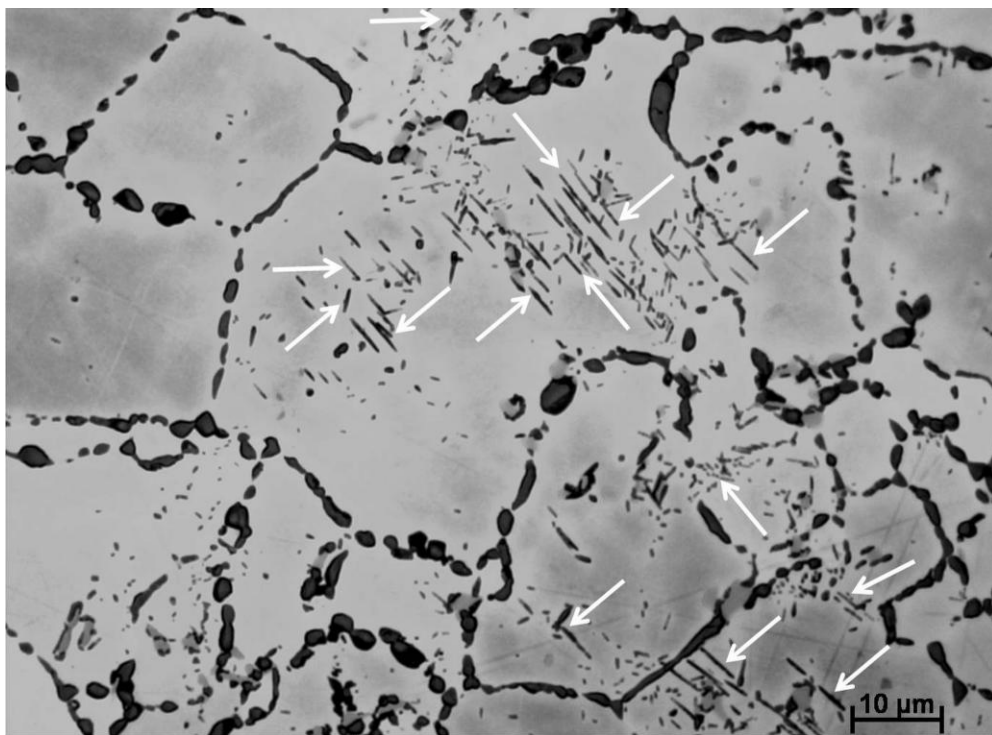


Figure 5.13 Optical micrograph of as-rolled U-9 wt.% Mo alloy after ageing at 575 °C for 14 days.

The XRD patterns obtained from all the aged samples, as shown in Figures 5.14 to 5.19, were analyzed to ascertain the structural identity of the decomposition products.

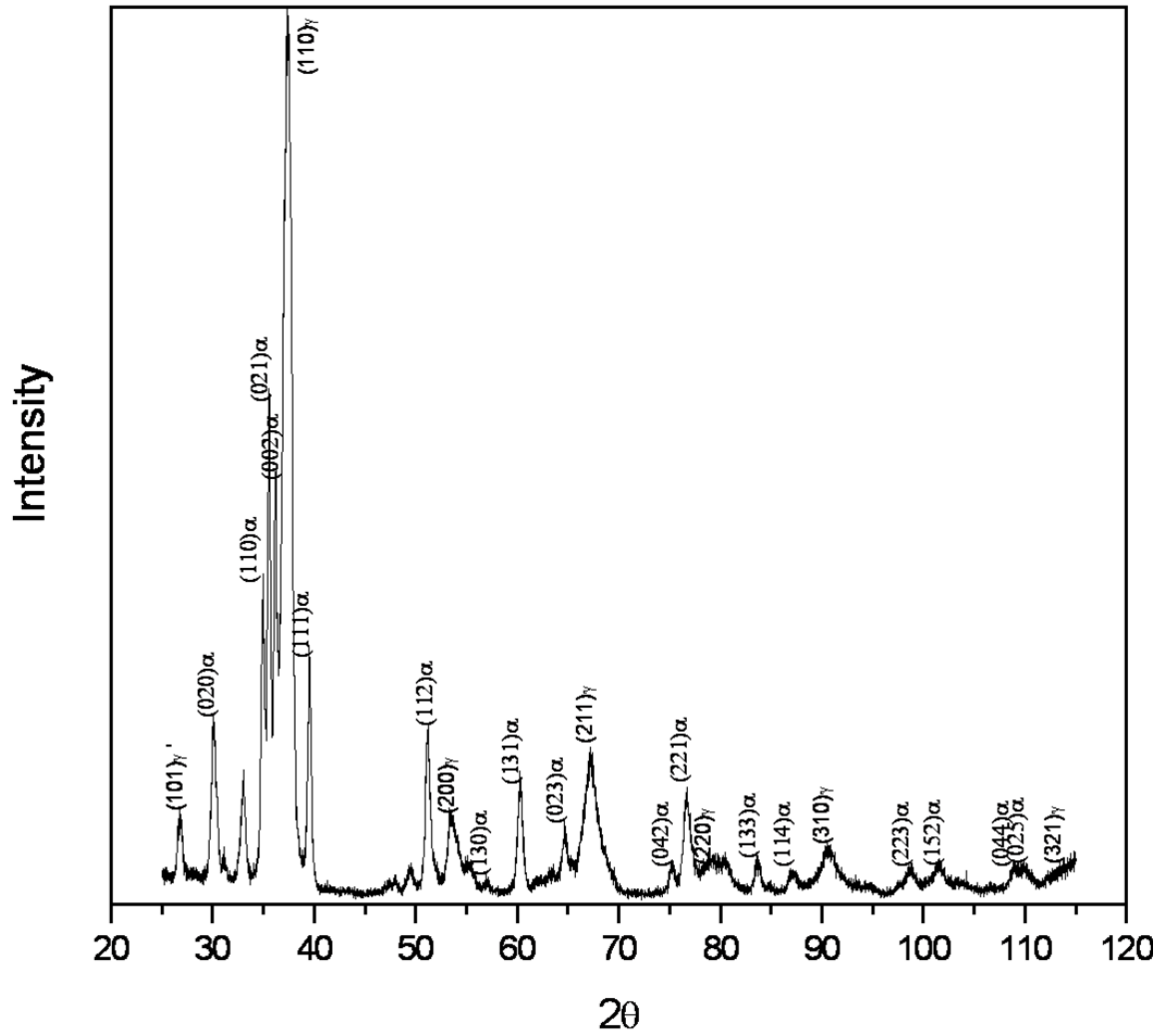


Figure 5.14 XRD pattern obtained from the as-rolled U-9 wt.% Mo alloy after ageing at 500 °C for 5 days.

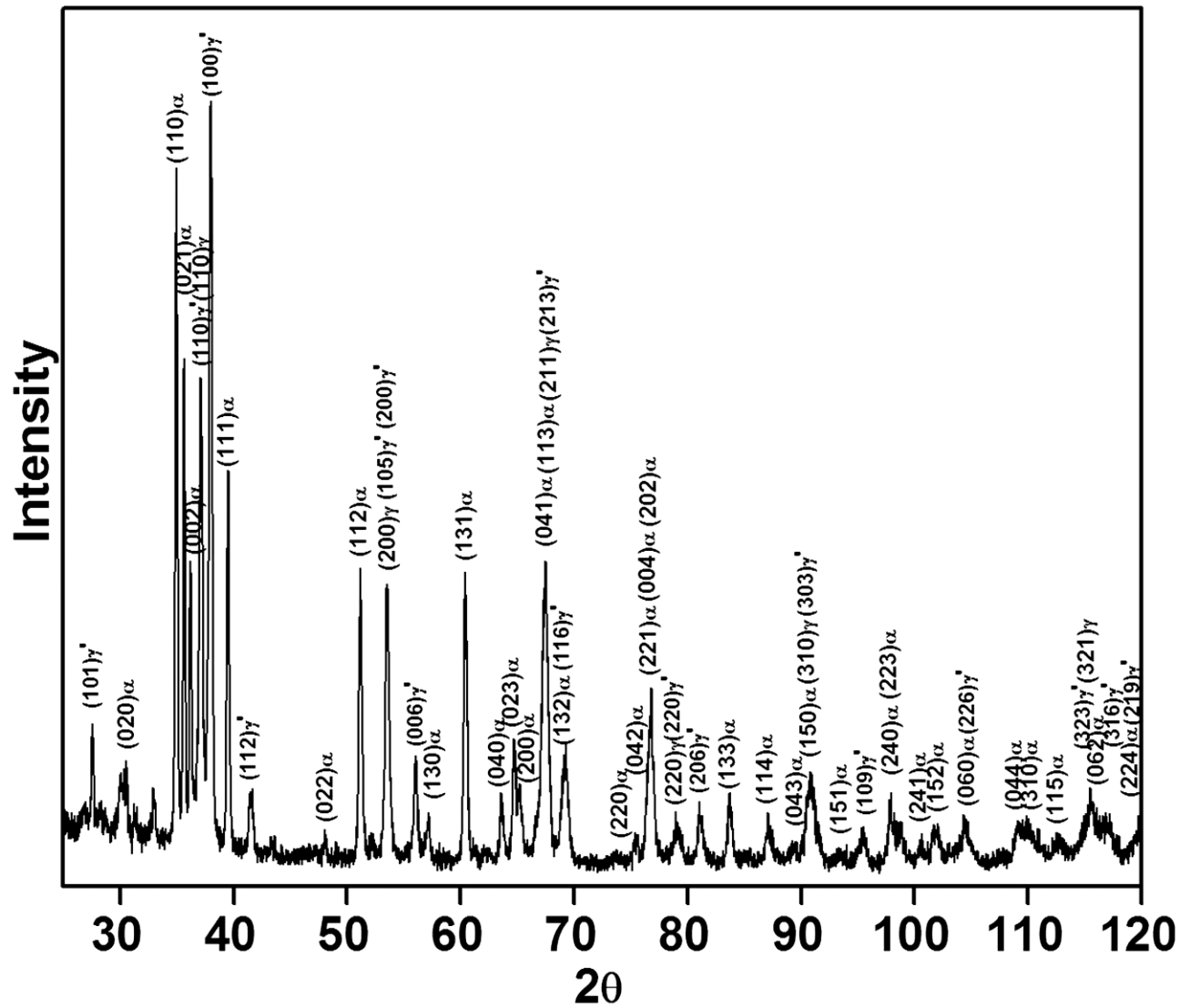


Figure 5.15 XRD pattern obtained from the as-rolled U-9 wt.% Mo alloy after ageing at 500 °C for 40 days.

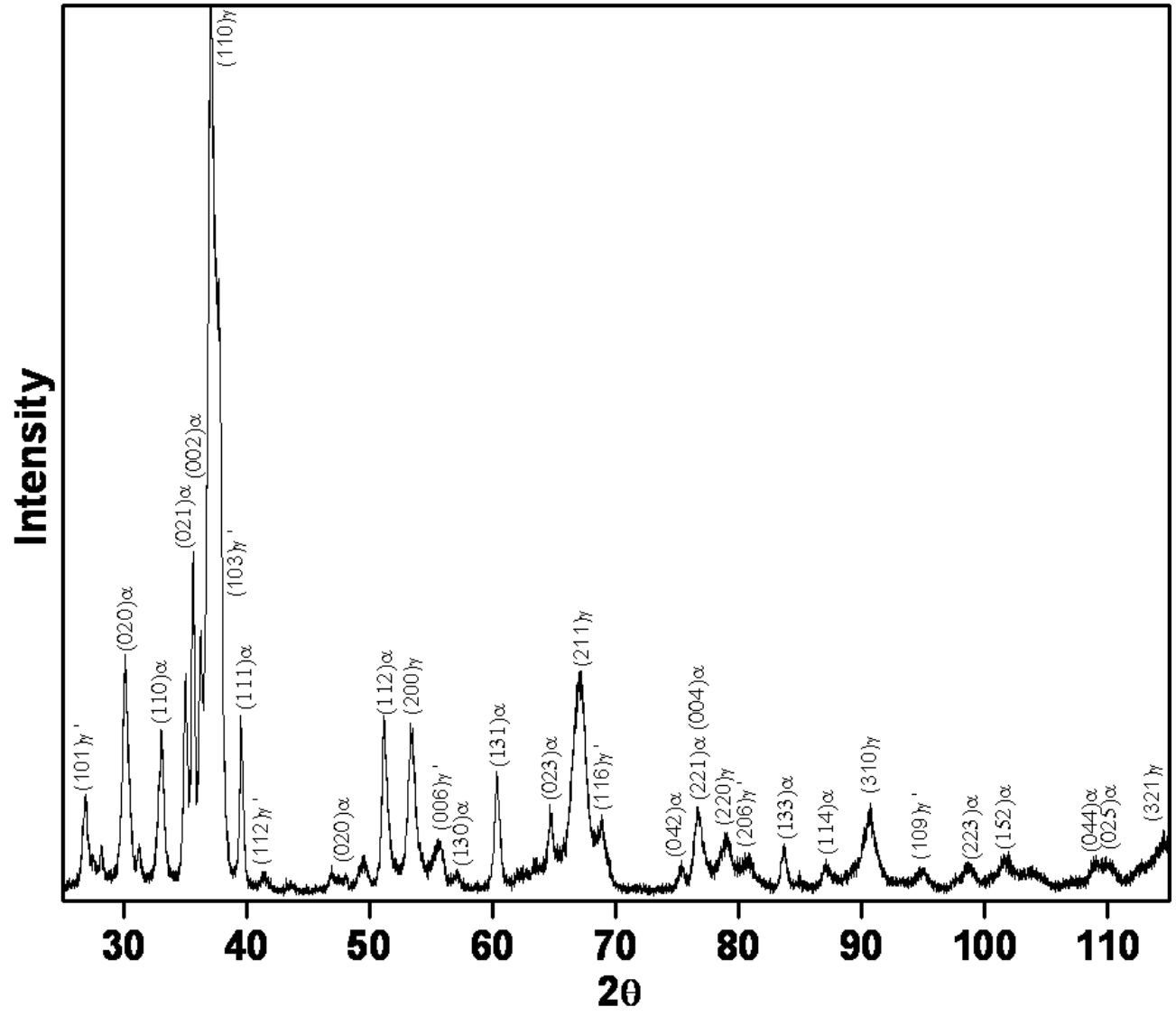


Figure 5.16 XRD pattern obtained from homogenized U-9 wt.% Mo alloy after ageing at 500 °C for 5 days.

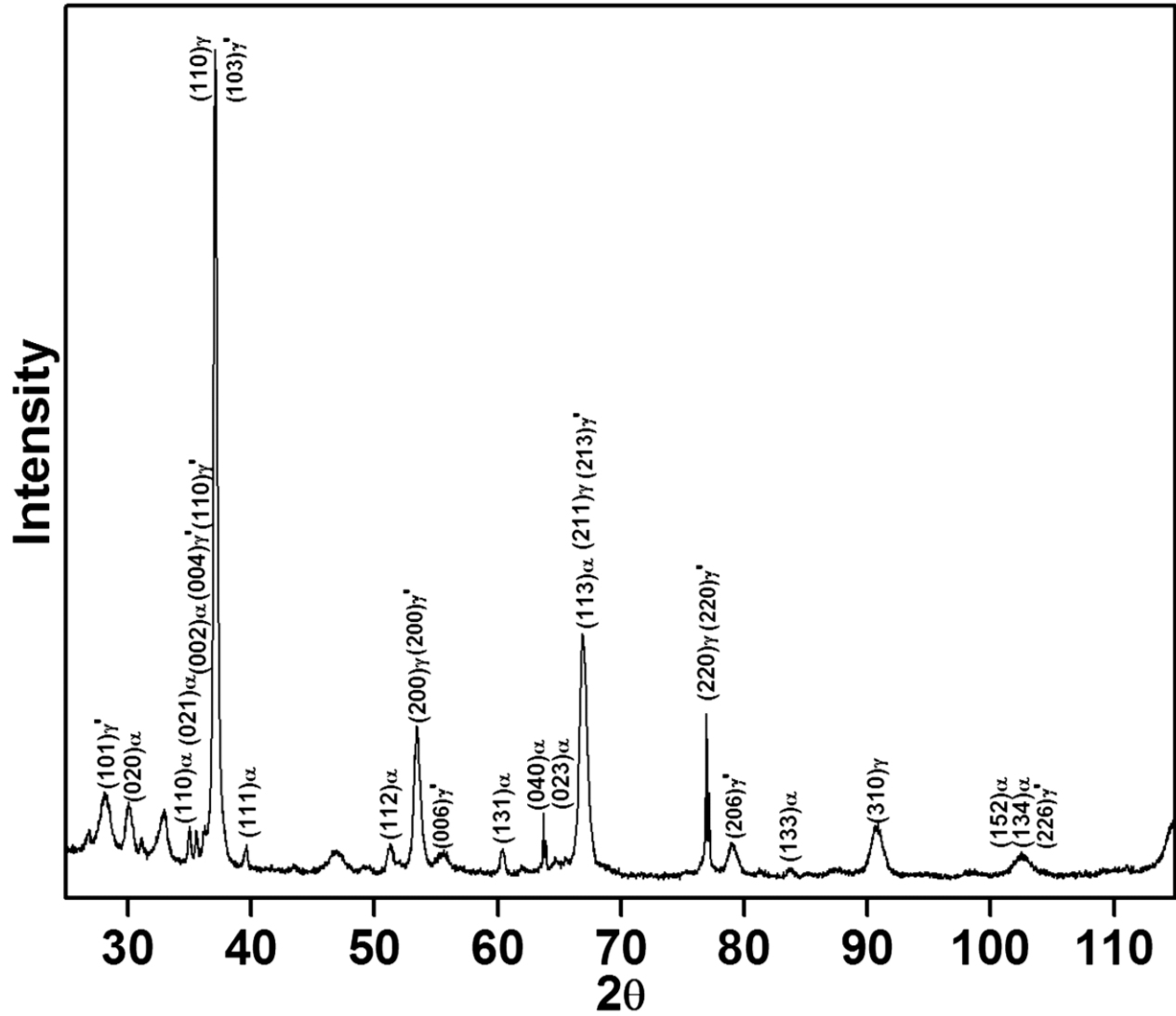


Figure 5.17 XRD pattern obtained from as-rolled U-9 wt.% Mo alloy after ageing at 565 °C for 7 days.

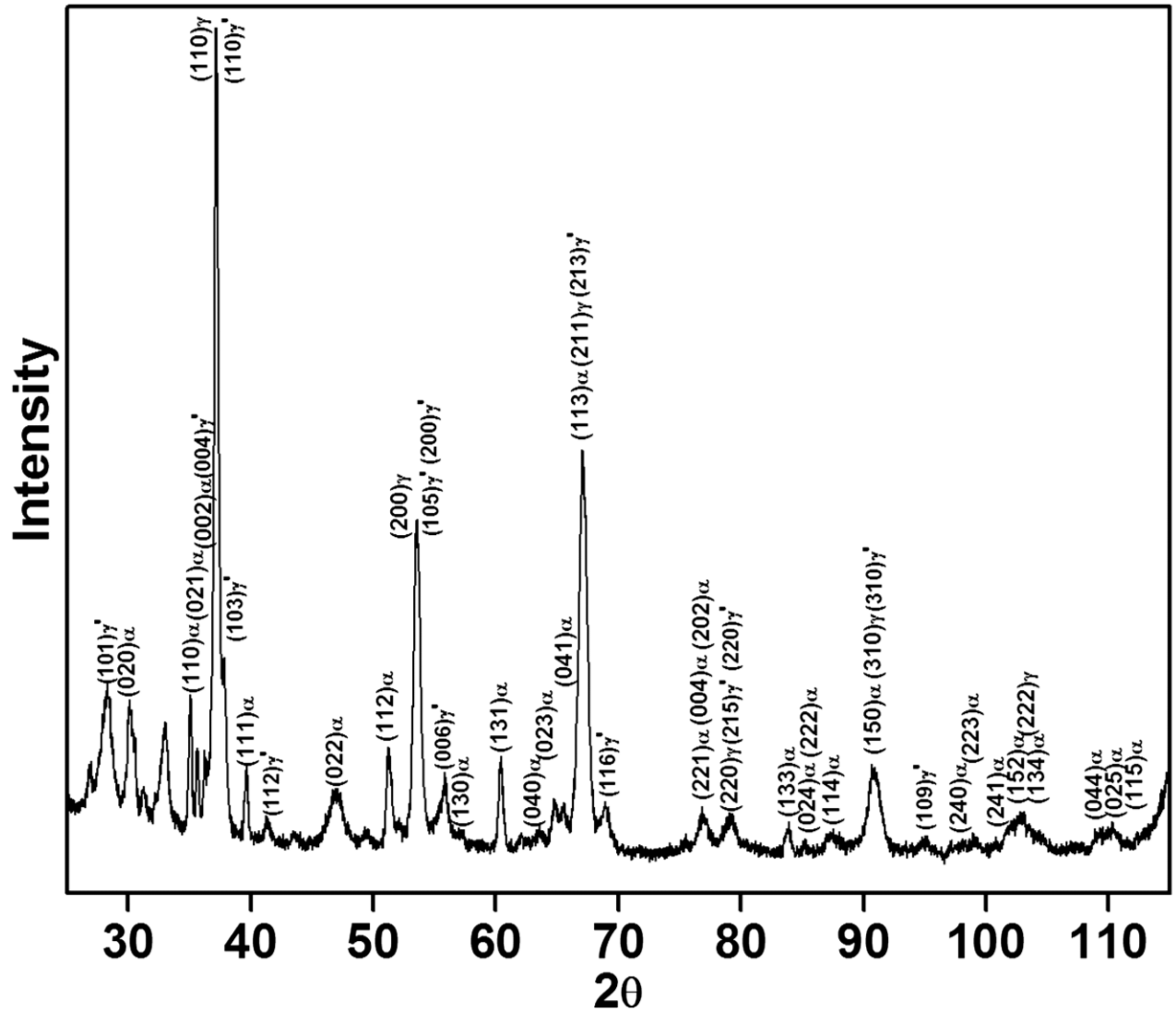


Figure 5.18 XRD pattern obtained from as-rolled U-9 wt.% Mo alloy after ageing at 565 °C for 14 days.

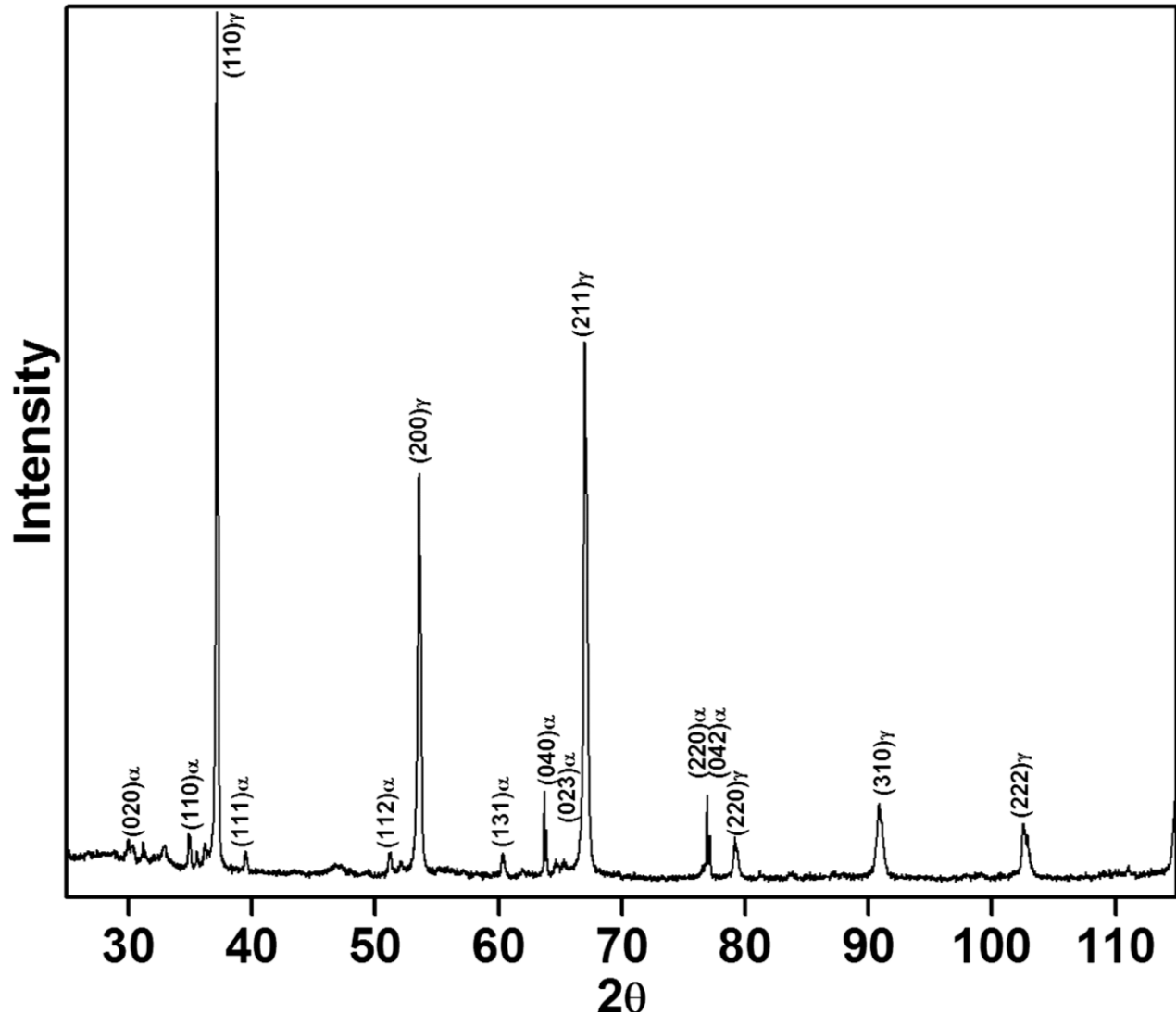


Figure 5.19 XRD pattern obtained from as-rolled U-9 wt.% Mo alloy after ageing at 575 °C for 14 days.

The decomposed microstructures of samples aged at 500 °C and 565 °C could be attributed to the formation of α - and γ' - phases in the γ -matrix, whereas, the needle-shaped feature present in the 575 °C aged sample was found to comprise of α -phase, as may be seen from the indexed XRD patterns. The results of quantitative phase (volume fraction) analysis carried out in all the heat treated samples, using the XRD patterns and the PowderCell Program [214], are presented in Table 5.3. A comparison of the observed phase fractions of α - and γ' - phases in the aged samples with the phase fractions expected has been brought out in Table 5.3, where the latter represent the phase fractions of α - and γ' - phases as per the lever rule after

normalization with respect to the decomposed fraction of the γ -phase (assuming a stoichiometric γ' -phase, Mo \approx 0 in α -U phase and U-9 wt.% Mo as the eutectoid composition).

Table 5.3 Volume fractions of γ -U, α -U and γ' (U_2Mo) phases present in the aged U-9 wt.% Mo alloy samples, as determined from XRD phase fraction analysis. For sake of comparison, expected equilibrium volume fractions of α - and γ' - phases, based on decomposed γ -phase fraction, have also been included in the table.

Ageing condition (initial state of sample)	Volume fractions (%) of phases present in the aged samples as per the XRD analysis			Expected volume fractions of α and γ' as per phase diagram [24] based on decomposed γ fraction	
	γ	α	γ'	α	γ'
500 °C / 5 days (as-rolled)	21	32	47	34	45
500 °C / 40 days (as-rolled)	06	48	46	40	54
500 °C / 5 days (homogenized)	52	20	28	21	27
565 °C / 7 days (as-rolled)	67	14	19	14	19
565 °C / 14 days (as-rolled)	64	17	19	15	21
575 °C / 14 days (as-rolled)	91	09	-	-	-

On correlating the results of phase fraction analysis of the aged samples, as listed in Table 5.3, with their microstructural details, as exhibited by the optical microscopy images, the following inconsistencies got featured up:

(i) The as-rolled samples aged at 500 °C for 5 and 40 days, the microstructures of which apparently suggested complete decomposition, have some fraction of γ -phase left undecomposed (especially the 5 days aged sample).

(ii) The estimated undecomposed γ -phase fraction left over in the homogenized sample after ageing at 500 °C for 5 days and in the as-rolled samples after ageing at 565 °C for 7 and 14 days was found to be higher against what could be inferred from their optical micrographs.

Thus, to resolve the above inconsistencies, the 565 °C aged samples (7 and 14 days) were examined in SEM with the objective of classifying the distribution of α - and γ' - phases in the partially decomposed lamellar microstructures. Figures 5.20 and 5.21 show the BSE images of the sample aged at 565 °C for 14 days.

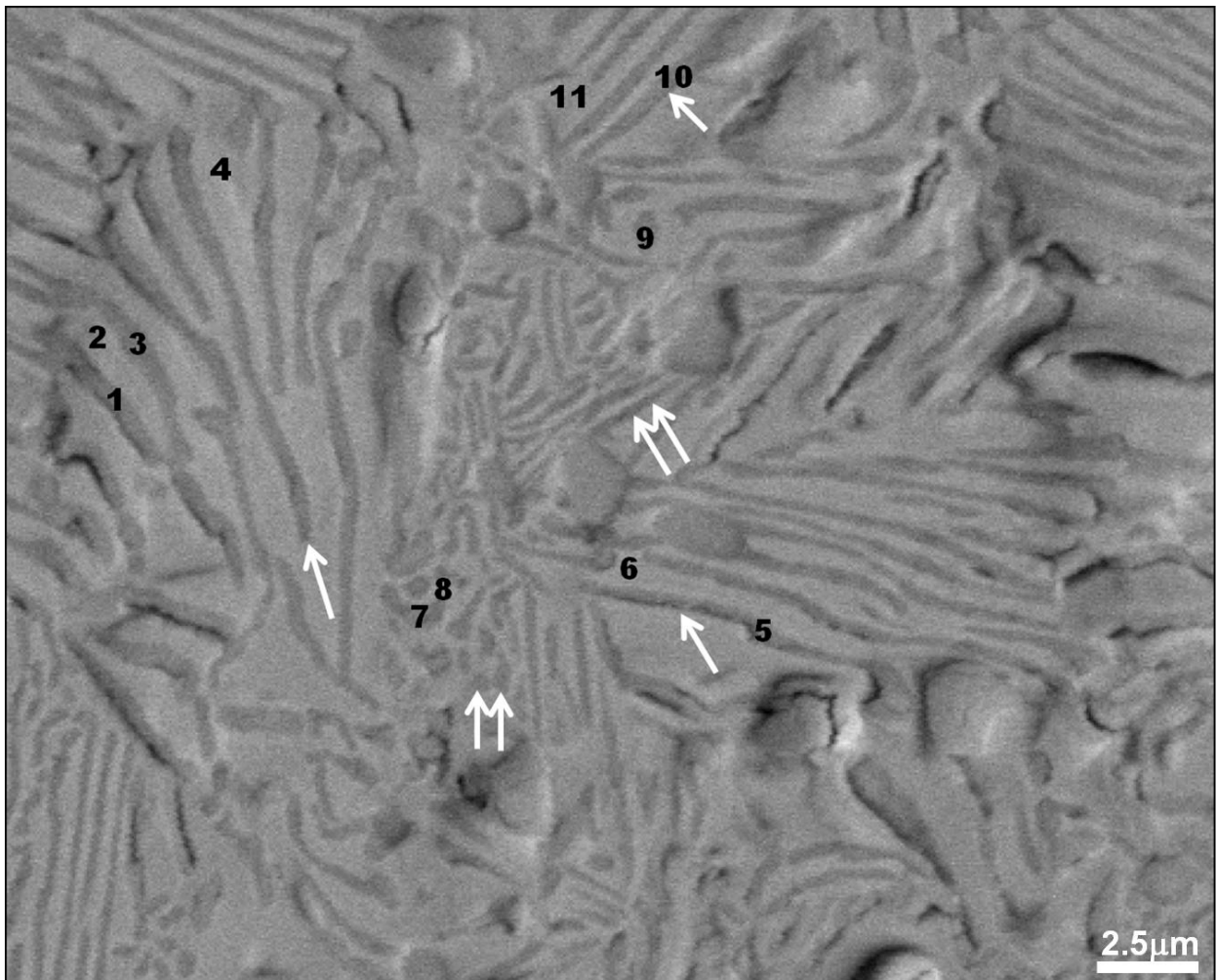


Figure 5.20 SEM micrograph showing BSE image of the U-9 wt.% Mo alloy sample aged at 565 °C for 14 days. The labels indicate the features from which EDS analysis was carried out. Single arrow and double arrows indicate long and short lamellae types, respectively.

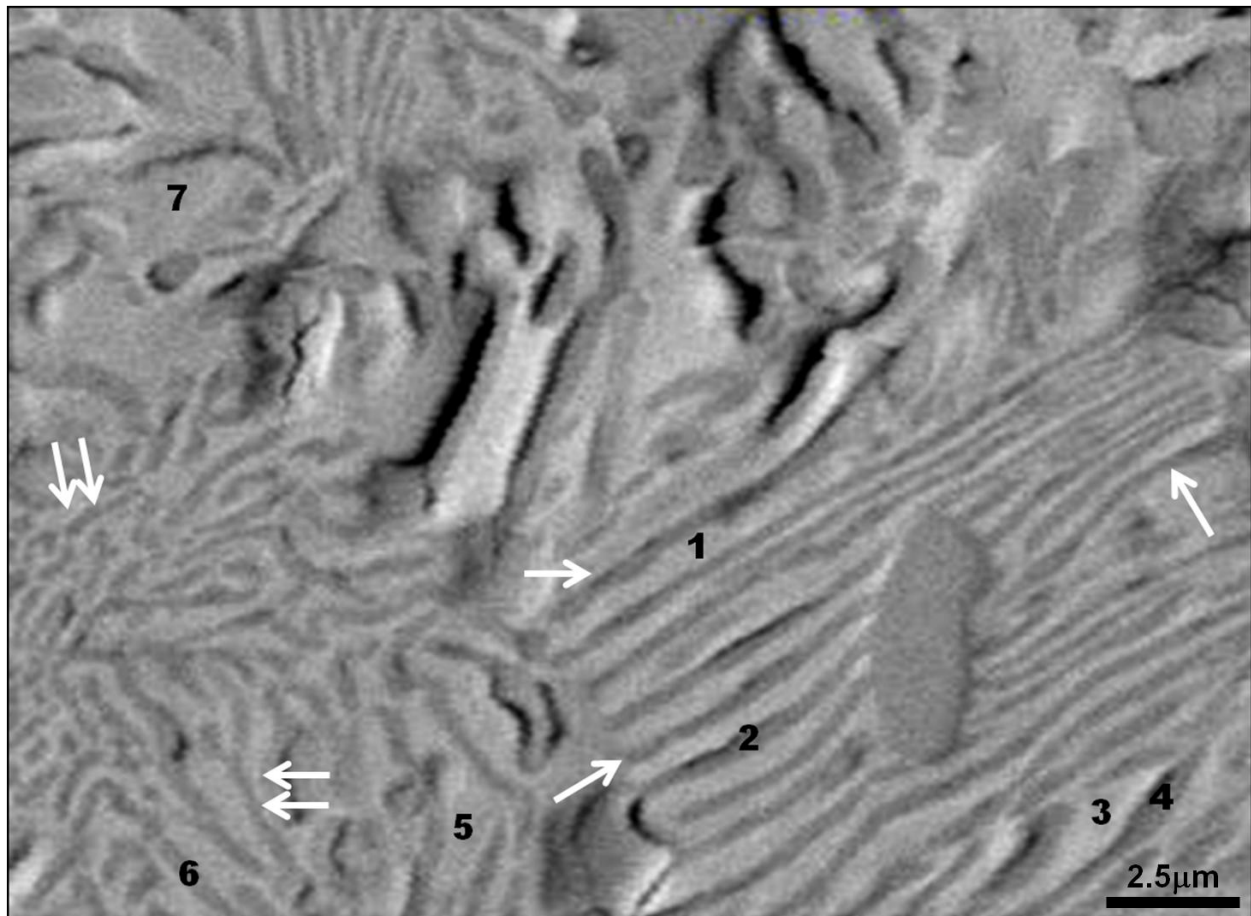


Figure 5.21 SEM micrograph showing BSE image of the U-9 wt.% Mo alloy sample aged at 565 °C for 14 days. The labels indicate the features from which EDS analysis was carried out. Single arrow and double arrows indicate long and short lamellae types, respectively.

Chemical analysis of the microstructural constituents was carried out in SEM using EDS, the results of which are presented in Tables 5.4 and 5.5.

Table 5.4 Chemical compositions of labeled regions in Figure 5.20, determined using SEM-EDS.

Element (wt.%)	Labels in Figure 5.20										
	1	2	3	4	5	6	7	8	9	10	11
U	95.6	89.7	93.4	90.3	92.1	91.8	89.8	93.0	91.4	95.0	92.5
Mo	04.4	10.3	06.6	09.7	07.9	08.2	10.2	07.0	08.6	05.0	07.5

Table 5.5 Chemical compositions of labeled regions in Figure 5.21, determined using SEM-EDS.

<i>Element</i> (wt.%)	<i>Labels in Figure 5.21</i>						
	<i>1</i>	<i>2</i>	<i>3</i>	<i>4</i>	<i>5</i>	<i>6</i>	<i>7</i>
U	93.9	90.4	94.6	92.2	94.8	89.8	94.1
Mo	06.1	09.6	05.4	07.8	05.2	10.2	05.9

The compositional values of the microstructural features labeled in Figures 5.20 and 5.21, reported in Tables 5.4 and 5.5, respectively, do not truly represent their absolute compositions. This is essentially because of the sampling volume, contributing to the characteristic X-ray signals actually used in SEM-EDS quantification, exceeding the thickness of an individual lamella or that of an interlamellar region in most of the cases. Thus, the elemental composition obtained from an individual lamella will always have some contribution in it from the adjacent interlamellar region, and vice versa. This, in effect, would lead to an averaging of the composition of the individual constituents with their adjacent features. Even then, the following general observations on the microstructural characteristics of the aged samples could be made based on the morphological and compositional attributes (relative Mo-content) of different constituent features:

(i) Presence of decomposed colonies of long lamellae (marked by single arrow in Figures 5.20 and 5.21) exhibiting either low-Mo or high-Mo in respect of interlamellar regions. Colonies comprising of low-Mo and high-Mo long lamellae will henceforth be referred as type-I and type-II colonies, respectively. Labels 1, 2, 3 and 4 in Figure 5.20 represent a type-I colony, whereas, a type-II colony is represented by the labels 1, 2, 3 and 4 in Figure 5.21. The average Mo-content of lamellae and the interlamellar regions was found to be 6 wt.% and 9 wt.%, respectively, in type-I colony and 9 wt.% and 6 wt.%, respectively, in type-II colony.

(ii) Presence of decomposed colonies of short irregular lamellae (marked by double arrows in Figures 5.20 and 5.21) containing Mo higher than the interlamellar regions, hereafter referred to as type-III colony. The average Mo-content of lamellae and the interlamellar regions was found to be 10 wt.% and 6 wt.%, respectively. Labels 7 and 8 in Figure 5.20 and 5 and 6 in Figure 5.21 represent type-III colonies.

To further establish the formation of different types of lamellar colonies, as was interpreted from the results of SEM-EDS investigation, an in-depth examination of all the aged samples (both 500 °C and 565 °C) was undertaken in TEM to obtain a detailed morphological and crystallographic description of the state of aggregation of the eutectoid decomposition products. Imaging and diffraction analyses of all the aged samples led to the identification of three distinct types of morphological features of the decomposition products:

- (i) Formation of α -lamellae alone in the γ -matrix (Figure 5.22).
- (ii) Presence of γ' -lamellae alone in the γ -matrix (Figure 5.23).
- (iii) Appearance of fragmented γ' -lamellae alone in the γ -matrix (Figure 5.24).

In all of the above cases, SAED combined with dark-field imaging, and micro-diffraction confirmed the identity of the respective phases. It can thus be affirmed that feature (i) representing partially transformed ($\gamma + \alpha$) lamellar colony is essentially the type-I colony, as interpreted from SEM-EDS investigation, where the low Mo-content lamellae are constituted of α -phase and the interlamellar regions, of relatively high Mo-content, of γ -phase. Similarly, features (ii) and (iii) representing partially transformed ($\gamma + \gamma'$) lamellar colonies correspond to type-II and type-III colonies, respectively, of SEM-EDS investigation, where the high Mo-content lamellae are constituted of γ' -phase and the interlamellar regions, of relatively low Mo-content, of γ -phase.

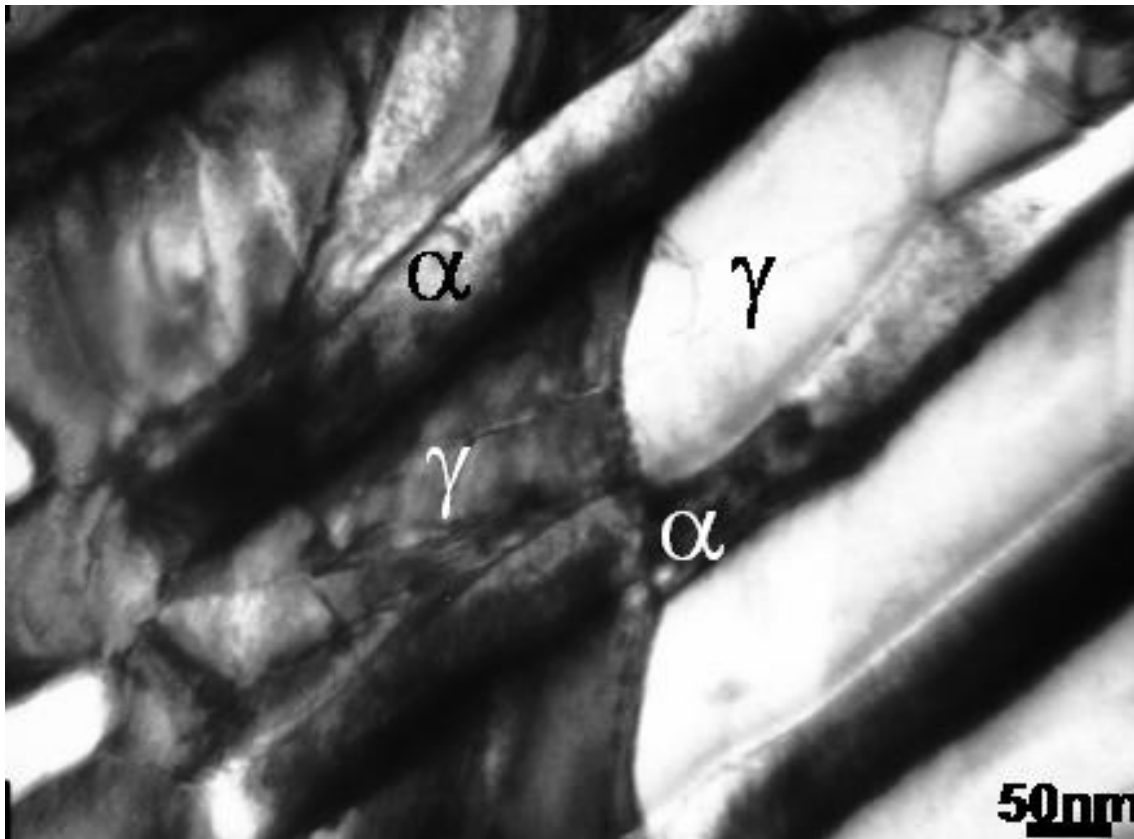


Figure 5.22 A typical bright-field TEM micrograph showing the partially decomposed type-I ($\gamma + \alpha$) lamellar colony comprising of long α -phase lamellae and γ -interlamellar regions in U-9 wt.% Mo alloy.

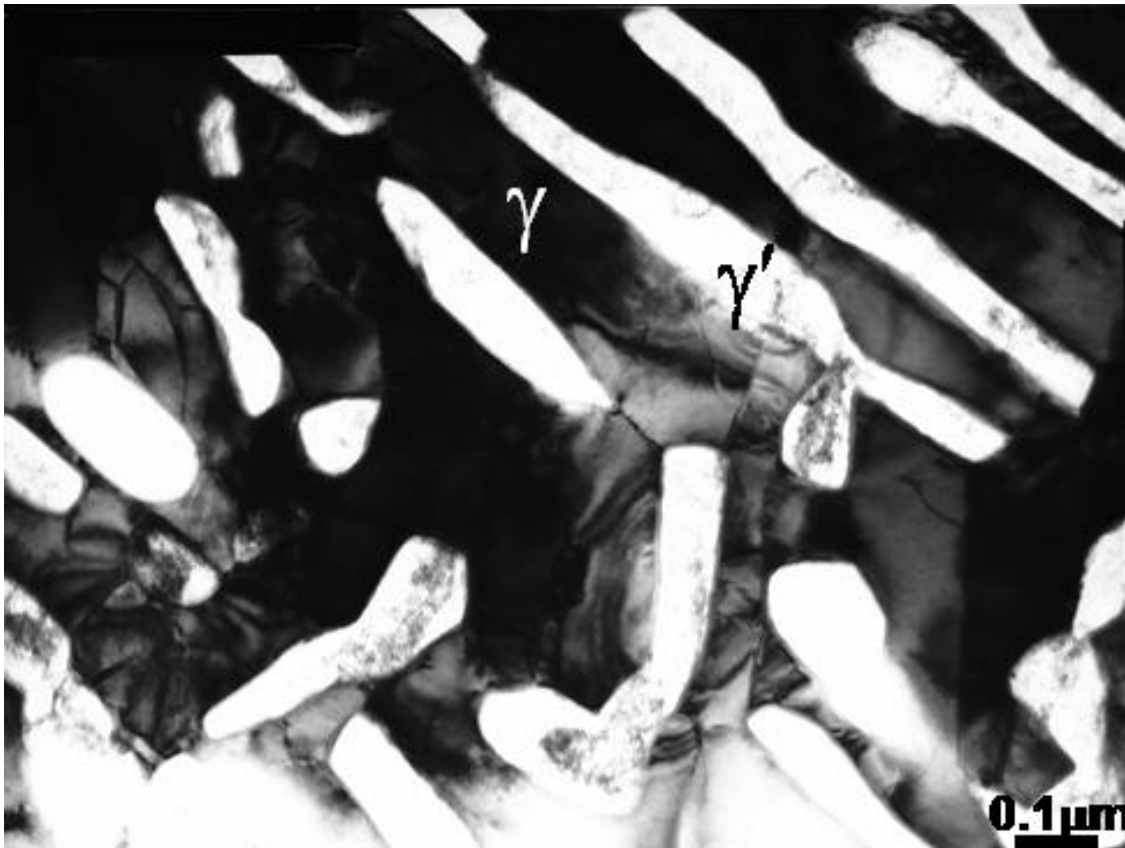


Figure 5.23 A typical bright-field TEM micrograph showing the partially decomposed type-II ($\gamma + \gamma'$) lamellar colony comprising of long γ' -phase lamellae and γ -interlamellar regions in U-9 wt.% Mo alloy.



Figure 5.24 A typical bright-field TEM micrograph showing the partially decomposed type-III ($\gamma + \gamma'$) lamellar colony comprising of short γ' -phase lamellae and γ -interlamellar regions in U-9 wt.% Mo alloy.

In addition to the above morphological types, another feature was also noticed occasionally in the 500 °C aged sample in TEM which was found to be an extension of type-I lamellar colony. Herein, γ' -phase in form of short lath was noticed in the γ -interlamellar region in between two α -lamellae with an orientation transverse to the α -lamellae (Figure 5.25). Typical micro-diffraction and SAED patterns corresponding to α -, γ - and γ' - phases are shown in Figures 5.26a to c and Figures 5.27a to c, respectively.

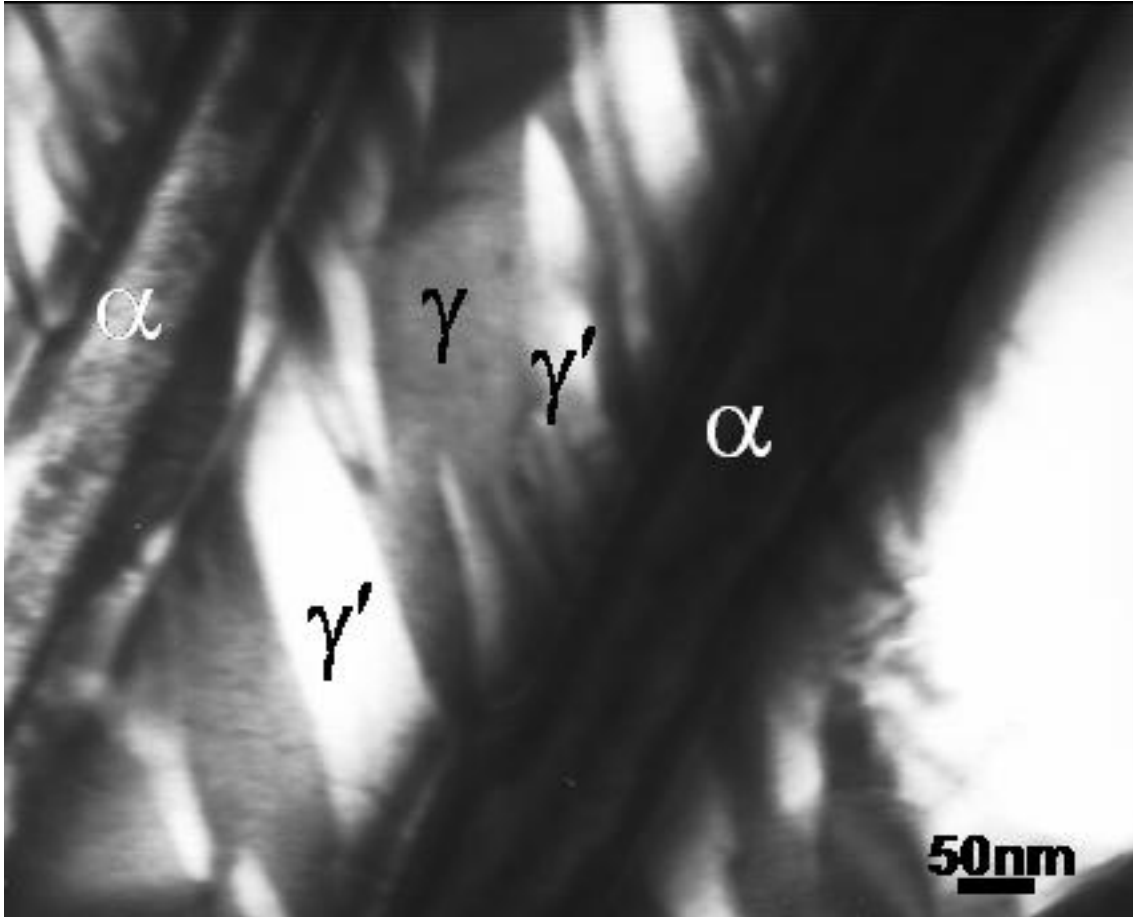


Figure 5.25 A typical bright-field TEM micrograph showing the occasional presence of the γ' -phase in the γ -interlamellar region between two α -phase lamellae in partially decomposed type-I ($\gamma + \alpha$) lamellar colony in U-9 wt.% Mo alloy.

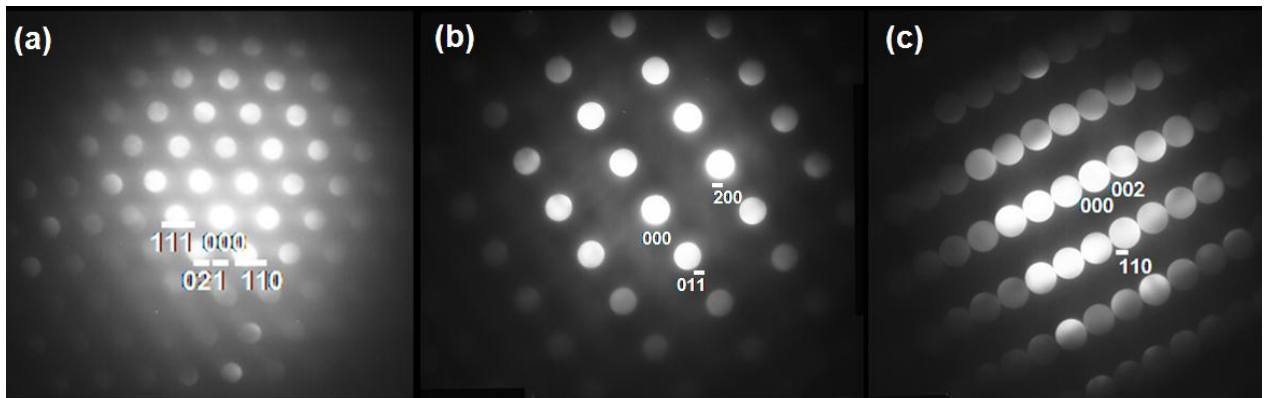


Figure 5.26 Typical micro-diffraction patterns of (a) α (Zone Axis = $[\bar{1}\bar{1}\bar{2}]_{\alpha}$), (b), γ (Zone Axis = $[011]_{\gamma}$) and (c) γ' (Zone Axis = $[110]_{\gamma}$) phases.

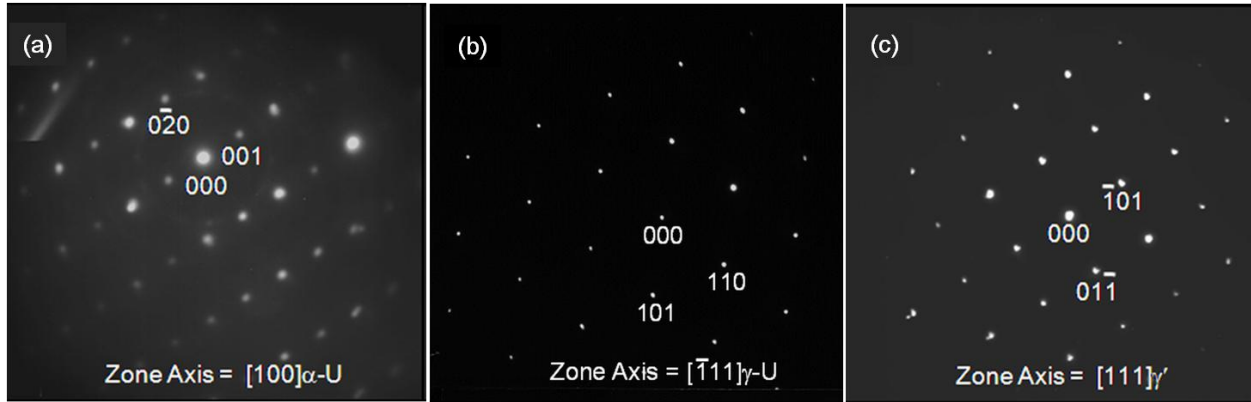


Figure 5.27 Typical SAED patterns of (a) α -U, (b) γ -U and (c) γ' phases.

The orientation relationships (OR) existing between γ - α , γ - γ' and α - γ' have been determined by detailed crystallographic analyses of composite SAED patterns containing reflections from the γ -, α - and γ' - phases. A typical composite SAED pattern containing reflections from all these phases is shown in Figure 5.28. The ORs worked out can be expressed as:

$$\gamma-\alpha: (0\bar{1}1)_{\gamma} // (110)_{\alpha}, [011]_{\gamma} // [001]_{\alpha}$$

$$\gamma-\gamma': (0\bar{1}1)_{\gamma} // (\bar{1}\bar{1}0)_{\gamma'}, [011]_{\gamma} // [110]_{\gamma'}$$

$$\alpha-\gamma': (110)_{\alpha} // (\bar{1}\bar{1}0)_{\gamma'}, [001]_{\alpha} // [110]_{\gamma'}$$

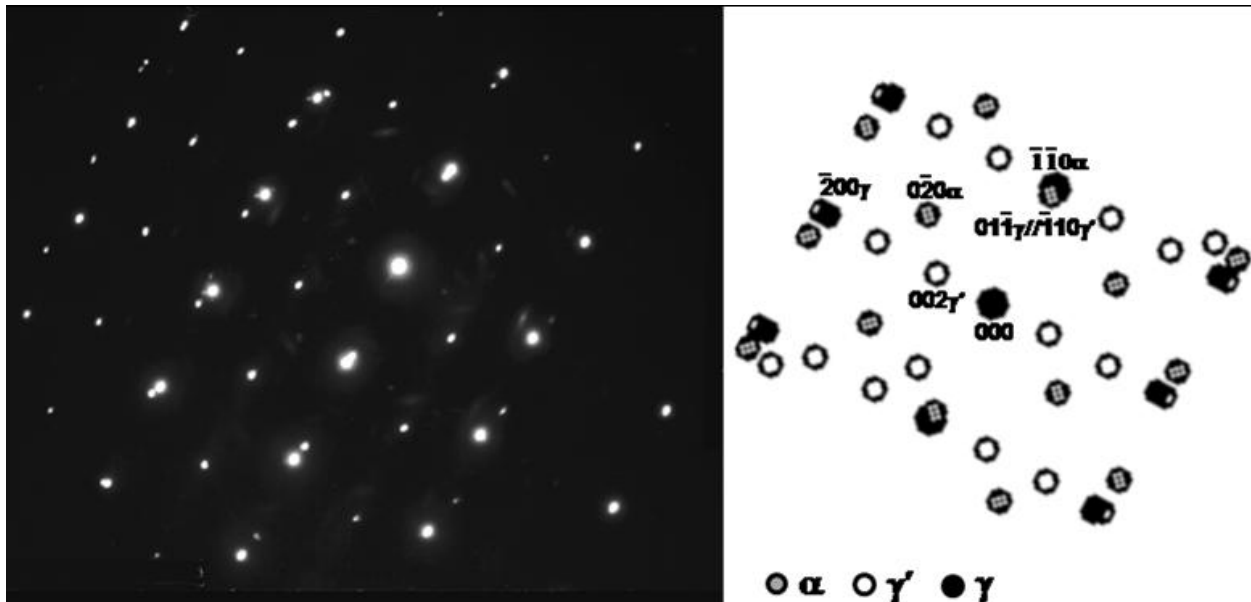


Figure 5.28 Composite SAED pattern (along with its key) showing reflections from the α -, γ - and γ' - phases. $[001]_{\alpha} // [011]_{\gamma} // [110]_{\gamma'}$; $(\bar{1}\bar{1}0)_{\alpha} // (0\bar{1}1)_{\gamma} // (\bar{1}\bar{1}0)_{\gamma'}$.

Microstructural analyses of 500 °C and 565 °C aged samples through XRD, optical microscopy, SEM and TEM thus brought out the following gross aspects of the decomposition of the metastable γ -phase viz., the absence of ($\alpha + \gamma'$) lamellar colonies, and the nonexistence of γ' - and α - within the partially transformed ($\gamma + \alpha$) and the ($\gamma + \gamma'$) lamellar colonies, respectively, except for the 500 °C aged samples where occasionally γ' -phase was noticed between α -phase lamellae. This also explains the inconsistency in the judgment of the decomposition fraction of the γ -phase from the optical microscopy images and its observed phase fraction in XRD analysis, as apart from the undecomposed γ -grains the interlamellar regions of all the lamellar colonies comprise mostly of γ -phase against what is being presumed as α - or γ' - phases in the optical micrographs. However, it is also imperative to mention at this juncture that on prolonged ageing, like the 500 °C/40 days heat treatment in the present study, the γ -phase in the partially transformed ($\gamma + \alpha$) and ($\gamma + \gamma'$) lamellar colonies transforms to γ' - and α - phases, respectively, thereby leading to the generation of ($\alpha + \gamma'$) lamellar microstructure. The presence of only 6 vol.% of γ -phase in the as-rolled sample aged at 500 °C for 40 days is testimony to this. It may be further noted that coarsening of the lamellar structure may occur during the course of the ageing process even before the decomposition of the metastable γ -phase into the equilibrium α - and γ' - phases is complete. Coarsening of the lamellar structure to some extent has been noticed in all the aged samples, as may be seen from the optical microscopy images given in Figures 5.8 to 5.12. The BSE-SEM image of the as-rolled 500 °C/40 days aged sample presented in Figure 5.29 shows the nature of the coarsening process in detail. A sudden increase in both the interlamellar spacing and width of lamellae could be noticed, which indicated the discontinuous nature of the coarsening process. The results of compositional analysis of coarsened regions through SEM-EDS, though limited in accuracy due to the size of the interaction volume exceeding those of the microstructural features, showed average Mo-contents of 4.8 wt.% and 9.6 wt.% in the lamellae and interlamellar regions, respectively. These results along with the findings of minimum 0.3 wt.% and maximum 14.7 wt.% of Mo-contents in the lamellae and interlamellar regions, respectively, indicated the lamellae to be comprised of α - and the interlamellar regions to be of γ' - phases.

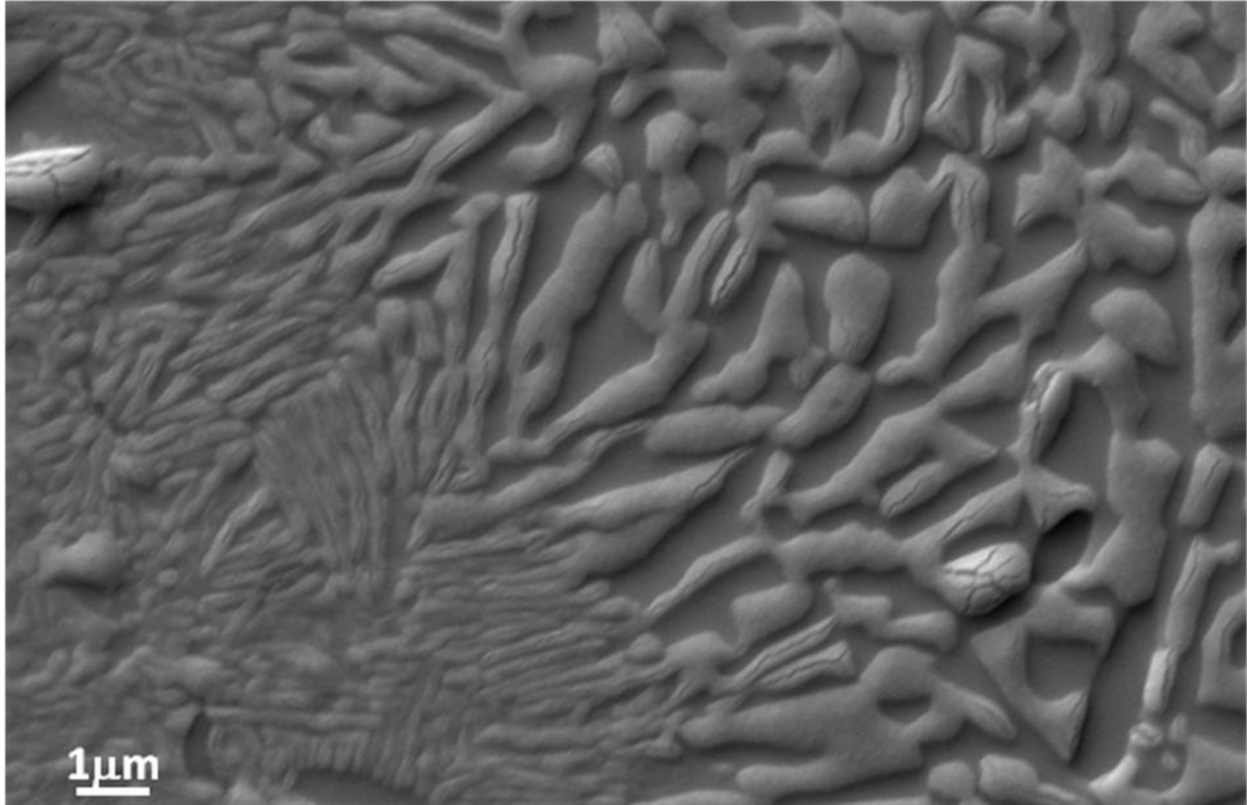


Figure 5.29 SEM micrograph showing the BSE image of the as-rolled U-9 wt.% Mo alloy sample aged at 500 °C for 40 days.

5.3 Discussion

The observation of γ -U phase in the XRD patterns of as-cast and the subsequently processed as-rolled and homogenized samples indicated the ability of 9 wt.% of Mo-addition in U in stabilizing the high temperature bcc γ -U allotrope at room temperature.

The retention of the γ -U phase, in a metastable state at room temperature, has already been reported earlier under conditions of rapid cooling [10,122]. Sinha et al. [115] however showed stabilization of the γ -phase under very slow cooling condition (furnace cooling) with minimum 8 wt.% addition of Mo in U. In the present work as well, even slow cooling rate during casting under vacuum did not led to the decomposition of the γ -phase into equilibrium α - and γ' -phases. These observations were in disagreement with the work of Eckelmeyer [231] who have shown U-10 wt.% Mo alloy, cooled slowly, to consist of α -U and γ' - phases with lamellar structure. In addition, ordering tendency of the γ -phase under slow cooling, as shown by Seong et al. [12] through neutron diffraction in U-10 wt.% Mo alloy furnace-cooled from γ , also could

not be witnessed in the as-cast sample of the present study. Hence, to resolve these issues one as-rolled sample was homogenized for 24 h at 1000 °C and then cooled in the furnace itself to achieve a very slow cooling rate. XRD pattern obtained from this sample (Figure 5.2) in fact indicated stabilization of the γ -phase. It may be noted that no lamellar structure, characteristic of the eutectoid decomposition of γ - into α - and γ' -, is visible in the TEM micrograph of this sample shown in Figure 5.3. Moreover, electron diffraction analyses of this furnace-cooled sample in TEM did not show the presence of any superlattice reflection, corresponding to ordering in the bcc structure of the γ -phase, as may be seen in the SAED pattern of Figure 5.4. The γ -phase is not expected to decompose in the as-rolled and homogenized samples when it had not undergone any decomposition during furnace cooling. The finer grain size of the as-rolled sample ($\sim 16 \mu\text{m}$), compared to the as-cast material ($\sim 74 \mu\text{m}$), indicated dynamic recrystallization during the rolling operation at 550 °C. The increase in grain size in the homogenized sample ($\sim 133 \mu\text{m}$) was because of the high homogenization temperature.

The microstructural analyses of 500 °C and 565 °C aged samples through optical microscopy revealed the decomposition of the metastable γ -phase while ageing at these temperatures. The further details of the decomposition microstructure with respect to the identity and volume fraction of the constituent phase(s), however, got revealed only on carrying out the indexing and the phase fraction analysis of the XRD patterns obtained from these samples. The difference in the extent of decomposition of the γ -phase in the as-rolled and homogenized samples aged for the same duration of 5 days at 500 °C, with the γ -phase decomposing more in the former, could be explained on the basis of the size of the γ -grains in these two samples. Any eutectoid decomposition reaction nucleates primarily at the grain boundaries of the parent phase. The grain size of the homogenized sample was almost an order of magnitude higher as compared to the as-rolled sample. This, in effect, led to a substantial decrease in grain boundary area in the former thereby lowering the $\gamma \rightarrow \alpha + \gamma'$ transformation. Retardation of the decomposition process, as a result of grain coarsening during homogenization, has also been reported by Lee et al [232]. In addition, the eutectoid decomposition of the γ -phase would necessitate partitioning of Mo atoms within the metastable γ -phase thereby leading to the formation of Mo-lean and Mo-rich regions which would transform subsequently to α - and γ' - phases, respectively. The process of partitioning of Mo atoms, being diffusion controlled, must involve interdiffusion of U and Mo

atoms. Huang et al. have found the tracer diffusion coefficient of Mo in γ -U to be smaller than that of U in pure γ -U [233]. In addition, Adda and Kirianenko have observed a decrease in the tracer diffusion coefficient of U in γ -U with the addition of Mo [234]. Although, U was found to intrinsically diffuse much faster than Mo [233], the intrinsic diffusion coefficient of Mo and the U–Mo interdiffusion coefficient were found to decrease in bcc γ U–Mo alloys with an increase in Mo-concentration along with a corresponding increase in the activation energy for interdiffusion [13,200,231,233,234]. In general, in a binary solid solution if the melting point increases with the addition of an alloying element, like the increase in γ -U solidus and liquidus with the addition of Mo in U (Figure AI.2), the interdiffusion coefficient tends to decrease on increasing the alloying content [235]. Hence, from the perspective of diffusion it may be inferred that presence of 9 wt.% of Mo in the γ -U matrix makes it inherently stable against decomposition, as the γ -phase remained undecomposed even in the homogenized-furnace cooled sample. In addition, an increase in grain size can lead to its further stabilization against ageing.

It may be further seen from the results of fraction phase analysis (Table 5.3) that ageing at a higher temperature of 565 °C has, in fact, reduced the fraction of the decomposed γ -phase as compared to 500 °C, even in as-rolled samples. The higher retention of the γ -phase, or, a reduced kinetics of its eutectoid decomposition at 565 °C is understandable in view of the fact that the ‘nose’ of the C-curve, signifying the fastest decomposition kinetics, is close to 500 °C for the 9 wt.% Mo γ -phase in the T–T–T diagram, as mentioned in Section 2.5.1. Thus, the decomposition of the γ -phase at any temperature higher or lower than 500 °C would proceed with a reduced kinetics as compared to 500 °C. An increase in the ageing time, however, has enhanced the decomposition of the γ -phase at both 500 °C and 565 °C, as may be seen from Table 5.3. The decomposition of the γ -phase during ageing at 500 °C and 565 °C has led to the generation of partially transformed ($\gamma + \alpha$) and ($\gamma + \gamma'$) lamellar colonies in contrast to ($\alpha + \gamma'$) pearlitic-type lamellar eutectoid colonies. These colonies were later on found to adopt a ($\alpha + \gamma'$) structure on ageing for a prolonged duration. The course or mechanism of such decomposition of the metastable γ -phase has been elaborated in the next chapter with due substantiation from thermodynamic analysis.

The coarsening of lamellar structure, as observed in all the aged samples to some extent, can be attributed to a discontinuous coarsening (DC) reaction noticed commonly in systems where a two-phase lamellar product aggregate has been generated by discontinuous precipitation, eutectoid transformation or eutectic solidification reactions [236,237]. In this coarsening process a finer distribution of the lamellar products is converted into a coarser distribution of the same, either at the reaction temperature itself or at some different temperature, across a migrating boundary acting as a short-circuit conduit for diffusion. A discontinuous change in the composition and orientation of the microstructural constituents across the moving boundary characterizes such a reaction. The reduction in interfacial free energy on account of coarsening is not the only factor that drives a DC reaction. A DC reaction also draws its driving free energy from the reduction in the supersaturation left over in the lamellar products on account of their compositions not corresponding to the equilibrium compositions dictated by phase diagram. Thus, the synergy of interfacial and chemical free energy changes not only leads to a coarsening of the lamellar structure but also helps the products therein to achieve their equilibrium compositions. In the context of the present study it may thus be conjectured that the supersaturation existing in the partially transformed ($\gamma + \alpha$) or ($\gamma + \gamma'$) lamellar colonies, owing to their constitution not corresponding to the equilibrium ($\alpha + \gamma'$) phases, might also assist in their transformation to the ($\alpha + \gamma'$) configuration by means of a DC reaction. The discontinuously coarsened ($\alpha + \gamma'$) lamellar colonies noticed in the aged samples could be a result of occurrence of either of the following events or the both:

(i) DC of partially transformed ($\gamma + \alpha$) and ($\gamma + \gamma'$) lamellar colonies facilitating the process of their transformation into the equilibrium ($\alpha + \gamma'$) configuration as mentioned above.

(ii) DC of lamellar colonies already existing in ($\alpha + \gamma'$) configuration thereby leading to the attainment of further equilibrium compositions by the α - and γ' - phases.

If the former event is primarily held responsible for the occurrence of the DC colonies then the presumption that the DC reaction only extends support to the process of attainment of equilibrium ($\alpha + \gamma'$) configuration by the partially transformed ($\gamma + \alpha$) and ($\gamma + \gamma'$) colonies, and is not the sole mechanism behind it, gets corroborated in the observation of limited DC colonies in all the aged samples, especially in the 500 °C/ 40 days aged as-rolled sample where the γ -phase decomposition was nearly complete. In the likelihood of appearances of DC colonies

through the second event, their scant occurrences could be a result of the ageing time not being adequate enough to generate an appreciable fraction of it. This is due to the fact that a DC reaction, in normal circumstances, is known to initiate only after the completion of the primary reaction generating the two-phase lamellar microstructure thus calling for a prolonged heat treatment duration. In none of the ageing heat treatments of the present study the decomposition of the γ -phase into the α - and γ' - phases was found to be over (Table 5.3). In addition, several other factors which govern a DC-reaction, as listed in references [236,237], could be equally responsible for the meager occurrences of DC colonies formed through any or both of the above-mentioned events.

The microstructure of the as-rolled sample aged at 575 °C, comprising of a distribution of needle-shaped α -phase in γ -phase matrix, could be an outcome of the ageing temperature being lying above the invariant eutectoid temperature thereby resulting in a generation of a two-phase ($\alpha + \gamma$) structure. This aspect of the decomposition of the γ -phase has been detailed in the next chapter.

5.4 Summary

The phase stability of isotropic bcc γ -phase has been investigated in the present study in U–9Mo alloy, a candidate for high uranium density nuclear fuel. The salient findings, obtained through detailed microstructural characterization employing X-ray diffraction, optical microscopy, SEM and TEM, could be summarized as follows:

(i) U–Mo alloy containing 9 wt.% of Mo can be considered as a “sluggish” eutectoid system, where the eutectoid decomposition of the γ -phase is slow and it is possible to retain this phase metastably at low temperatures even without rapid cooling.

(ii) Homogenization at 1000 °C for 24 h, aimed to ensure chemical and microstructural homogeneity, influences the eutectoid decomposition of the metastable γ -phase into α - and γ' -phases. The extent of the decomposition process is less in homogenized condition on account of higher grain size. Thus, a direct increase in the homogenization temperature or time, leading to a further increase in the grain size of the γ -phase, could enhance its stabilization.

(iii) The kinetics of decomposition of the γ -phase has been found to follow an ‘inverse-C’ variation with temperature like any other diffusion controlled nucleation and growth process.

(iv) In contrast to a two-phase ($\alpha + \gamma'$) lamellar pearlitic-type eutectoid decomposition microstructure, ageing of the metastable γ -phase at 500 °C and 565 °C resulted in the generation of partially decomposed ($\gamma + \alpha$) and ($\gamma + \gamma'$) lamellar colonies. In the 500 °C aged samples occasional presence of γ' -phase could be noticed in the γ -interlamellar region between two α -phase lamellae. Ageing for a longer duration, however, resulted in formation of ($\alpha + \gamma'$) lamellar colonies, as was observed in the as-rolled sample after ageing at 500 °C for 40 days.

(v) All the aged samples showed coarsening of the lamellar structures to a certain extent, which could be attributed to a discontinuous coarsening reaction driven by a reduction in the interfacial free energy and the supersaturation remaining in the lamellar decomposition products.

(vi) Ageing at 575 °C resulted in the generation of a two-phase non-lamellar ($\alpha + \gamma$) structure, wherein α -phase in form of needles was found to be distributed within the grains of the γ -phase.

Decomposition pathway of the metastable γ -phase in U–9Mo alloy

6.1 Background

The Mo–U binary phase diagram given in Figure A1.2 shows a eutectoid decomposition of the γ -phase into the orthorhombic α -U and the tetragonal γ' (U_2Mo) phases. The Mo-content of the γ -phase at the invariant eutectoid point has been reported to vary between 9.7 to 11.1 wt.% [24,134-136]. Since the γ -phase with Mo \geq 8 wt.% does not decompose even on furnace cooling, the formation of a eutectoidally decomposed microstructure in alloys with either hypoeutectoid, hypereutectoid or eutectoid compositions is ruled out in the course of continuous cooling from the γ -phase field. In such a scenario the decomposition of the γ -phase can be set in by ageing of the metastable γ -phase. Experimental observations pertaining to ageing characteristics of the metastable γ -phase in U–9Mo alloy at 500 °C and 565 °C in the ($\alpha + \gamma'$) phase-field and at 575 °C in the ($\gamma + \alpha$) phase-field have been discussed in the previous chapter.

It must be realized that deciphering the mechanism by which an alloy undergoes eutectoid decomposition reaction is a potential phase transformation research topic. The different reaction mechanisms operative in ferrous systems encompassing the eutectoid composition and temperature, exhibiting decomposed microstructures ranging from lamellar to non-lamellar two-phase mixtures, have been accounted very well in literature [238-244]. Therein, the competition existing amongst the different product phases with respect to their sequence of formation in the decomposition event, and the corresponding morphological attributes, have remained the central investigating issues [238-240,245-247]. In similar lines, the present chapter has made an attempt to delineate the mechanism of decomposition of the γ -phase in U–9Mo alloy from its ageing characteristics. A rationalization of the same has been made by invoking a detailed thermodynamic assessment of the U–Mo system involving free energy–composition (G–X) diagrams at different ageing temperatures.

6.2 Thermodynamic evaluation of γ -phase decomposition

In order to rationalize the observed decomposition behavior of the metastable γ -phase reported in the preceding chapter, a thermodynamic assessment of the U–Mo system has been carried out at the different ageing temperatures of 500 °C, 565 °C and 575 °C employing free energy–composition (G–X) diagrams. The regular solution thermodynamics model was applied to estimate the free energies of the solid solution γ - and α - phases by making use of expressions similar to Equations 2.6 to 2.9.

The $G\text{-H}_{\text{SER}}$ expression for G_{Mo}^{α} , the Gibbs free energy of Mo in the orthorhombic structural state, being unavailable in the reference of Dinsdale [207] was estimated using the following expressions from the works of Zhang et al. [135] and Berche et al. [136], respectively:

$$G_{\text{Mo}}^{\alpha} = G_{\text{Mo}}^{\gamma} + 21482.5454 \quad (6.1)$$

$$G_{\text{Mo}}^{\alpha} = G_{\text{Mo}}^{\gamma} + 20000 \quad (6.2)$$

The expressions for G_{U}^{α} , used to calculate the free energy of the α -phase, and for G_{U}^{γ} and G_{Mo}^{γ} , used to calculate the free energy of the γ -phase, in the temperature range investigated, are obtained from reference [207]:

$$G_{\text{U}}^{\alpha} = -8407.734 + 130.955151T - 26.9182T\ln(T) + 1.25156E-3T^2 - 4.42605E-6T^3 + 38568T^{-1} \quad (6.3)$$

$$G_{\text{U}}^{\gamma} = -752.767 + 131.5381T - 27.5152T\ln(T) - 8.35595E-3T^2 + 0.967907E-6T^3 + 204611T^{-1} \quad (6.4)$$

$$G_{\text{Mo}}^{\gamma} = -7746.302 + 131.9197T - 23.56414T\ln(T) - 3.443396E-3T^2 + 0.566283E-6T^3 + 65812T^{-1} - 0.130927E-9T^4 \quad (6.5)$$

The interaction parameter data between Mo and U in the γ - and α - phases have been obtained as well from the works of Zhang et al. [135] and Berche et al [136].

Interaction parameter between Mo and U in the γ -phase from [135]:

$$^{(0)}L_{\text{Mo},\text{U}}^{\gamma} = 28739.2 - 217.1736T + 27.7696T\ln T + 6.8435E-3T^2 - 785719.805T^{-1} \quad (6.6)$$

$$^{(1)}L_{\text{Mo},\text{U}}^{\gamma} = 27365.2138 - 5.7719T \quad (6.7)$$

$$^{(2)}L_{\text{Mo},\text{U}}^{\gamma} = 20317.698 - 3.1805T \quad (6.8)$$

Interaction parameter between Mo and U in the γ -phase from [136]:

$${}^{(0)}L_{Mo,U}^{\gamma} = 26180 - 9.2T \quad (6.9)$$

$${}^{(1)}L_{Mo,U}^{\gamma} = 28370 + 2.2T \quad (6.10)$$

$${}^{(2)}L_{Mo,U}^{\gamma} = 47200 - 25T \quad (6.11)$$

Interaction parameter between Mo and U in the α -phase from [135]:

$${}^{(0)}L_{Mo,U}^{\alpha} = -33595.3252 + 28.2996T \quad (6.12)$$

Interaction parameter between Mo and U in the α -phase from [136]:

$$L_{Mo,U}^{\alpha} = L_{Mo,U}^{\gamma} + 8000 \quad (6.13)$$

The γ' (U_2Mo) phase, being an intermetallic compound, forms only within the narrow compositional domain of U-(32.5-34.1) at.% Mo [24]. In the present thermodynamic analysis the γ' -phase has been assumed to be of stoichiometric composition i.e., U-33.3 at.% Mo, for which the Gibbs energy has been referred to the stable states of the constituting elements as per the Kopp-Neumann rule i.e.,

$$G_{U_2Mo} = 0.667 G_U^{\alpha} + 0.333 G_{Mo}^{\gamma} + A + BT + CT \ln T \quad (6.14)$$

The 'A', 'B' and 'C' parameters have been obtained as well from the works of Zhang et al. ($A = -6351.66$, $B = 9.3906$, $C = -0.9$) [135] and Berche et al. ($A = -20000$, $B = 20$, $C = 0$) [136]. Thus, in contrast to the G^{α} - and G^{γ} -curves representing the free energies of α - and γ - phases, respectively, over the entire U-Mo composition range, the free energy of the γ' -phase has been represented in the G-X diagrams only for the stoichiometric U_2Mo composition. All thermodynamic data have been expressed in terms of $Jmol^{-1}$.

The selection of thermodynamic parameters for the construction of G-X diagrams at the different ageing temperatures was carried out in such a manner that thermodynamic and experimental findings agree with each other. As outlined in the following, the G-X diagrams constructed using the thermodynamic parameters of Berche et al. [136] could corroborate the experimental observations made at 500 °C and 565 °C, whereas, those obtained at 575 °C could be substantiated by the G-X diagram constructed with the thermodynamic parameters of Zhang et al

[135]. The G–X diagrams at 500 °C, 565 °C and 575 °C are shown in Figures 6.1 to 6.3, respectively (where X represents the atom fraction of Mo).

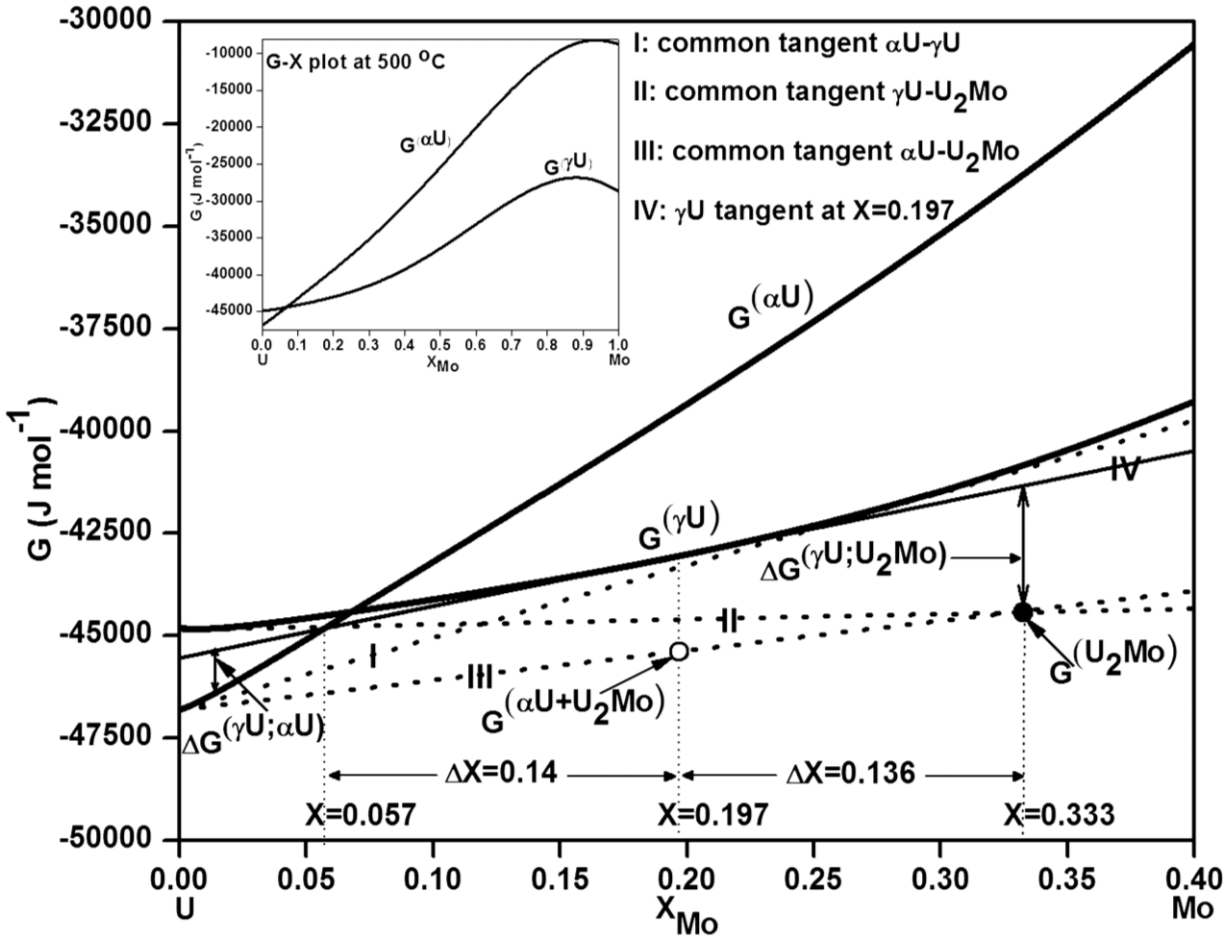


Figure 6.1 Free energy–composition diagram at 500 °C showing the variation of free energies of α -U and γ -U phases as a function of Mo-content in U–Mo system. The inset shows the same diagram for the entire U–Mo composition range. The free energy of the stoichiometric γ' (U_2Mo) phase of 33.3 at.% Mo (G^{U_2Mo}) is marked in the diagram by the filled circle. The free energy of the U-19.7 at.% Mo alloy existing as a mixture of α -U phase, of equilibrium composition, and stoichiometric γ' phase ($G^{\alpha U+U_2Mo}$) is indicated in the diagram by the open circle on tangent-III. $\Delta X = 0.14$ (or 14 at.% Mo) represents the minimum amount of Mo-depletion required in the 19.7 at.% Mo γ -matrix to nucleate the α -U phase, whereas, $\Delta X = 0.136$ (or 13.6 at.% Mo) represents the minimum amount of Mo-enrichment required in the same γ -matrix to nucleate the γ' phase. $X = 0.057$ (or 5.7 at.% Mo) represents the maximum Mo-content with which the α -U phase can nucleate, and is given by the intersection of tangent-IV and free energy curve of α -U phase.

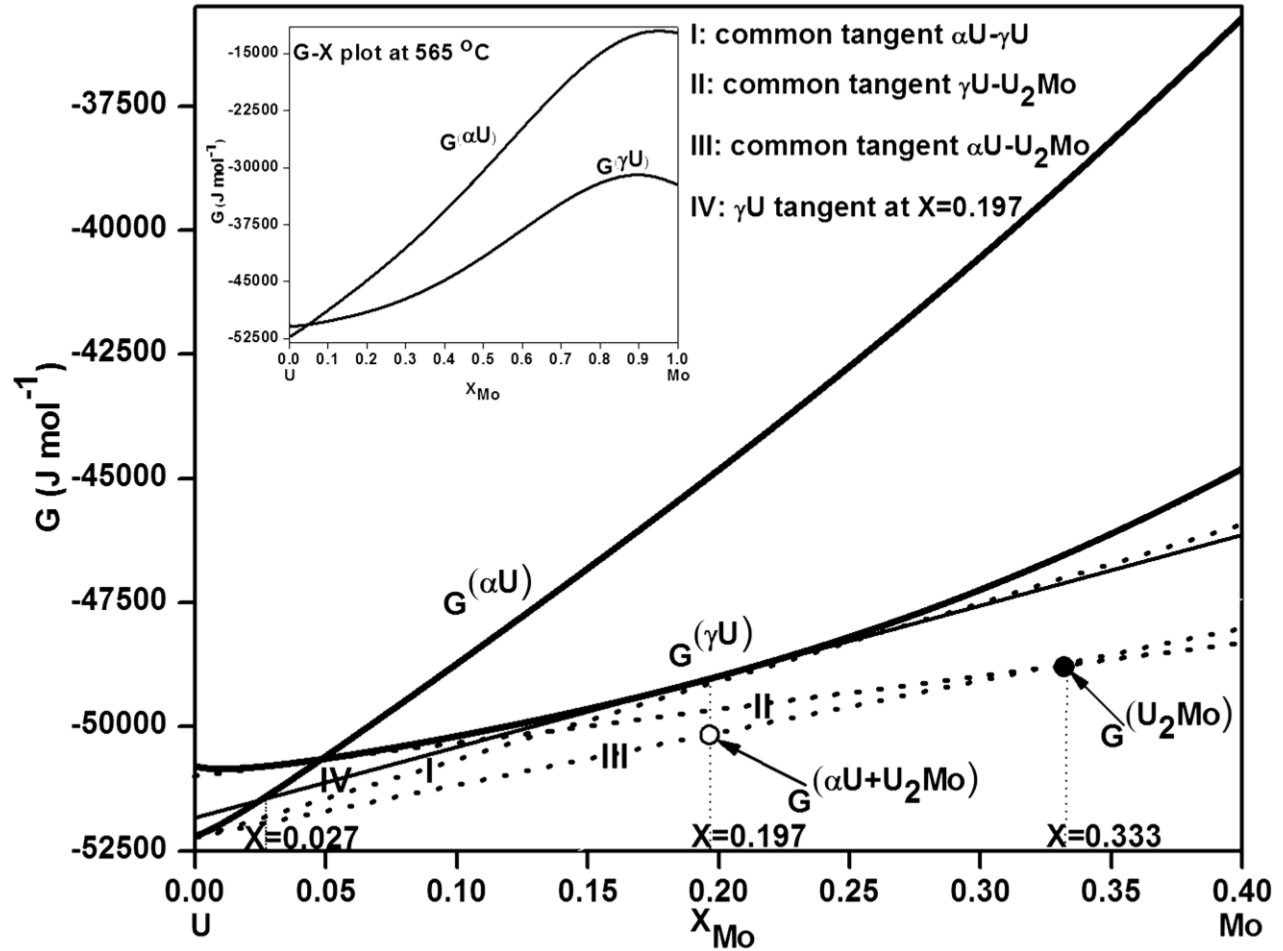


Figure 6.2 Free energy–composition diagram at 565 °C showing the variation of free energies of $\alpha\text{-U}$ and $\gamma\text{-U}$ phases as a function of Mo-content in U–Mo system. The inset shows the same diagram for the entire U–Mo composition range. The free energy of the stoichiometric γ' (U_2Mo) phase of 33.3 at.% Mo ($G^{\text{U}_2\text{Mo}}$) is marked in the diagram by the filled circle. The free energy of the U-19.7 at.% Mo alloy existing as a mixture of $\alpha\text{-U}$ phase, of equilibrium composition, and stoichiometric γ' phase ($G^{\alpha\text{U}+\text{U}_2\text{Mo}}$) is indicated in the diagram by the open circle on tangent-III. $X = 0.027$ (or 2.7 at.% Mo) represents the maximum Mo-content with which the $\alpha\text{-U}$ phase can nucleate, and is given by the intersection of tangent-IV and free energy curve of $\alpha\text{-U}$ phase.

As shown in the G–X diagrams at 500 °C and 565 °C, three common tangents could be constructed encompassing the γ -matrix containing 9 wt.% (19.7 at.%) of Mo. These are tangent-I between the free energy curves of α - and γ -, tangent-II between the free energy curve of γ - and the free energy of the stoichiometric γ' -phase, and tangent-III between the free energy curve of α - and the free energy of the stoichiometric γ' -phase. The first two tangents signified that the γ -matrix is capable of nucleating both α - and γ' - phases at these temperatures, whereas, the last one represented the minimum energy ($\alpha + \gamma'$) configuration attainable on decomposition of the γ -matrix.

The thermodynamics of nucleation of α - and γ' - phases in the γ -matrix, in terms of phase composition and the chemical free energy change associated with nucleation, has been discussed below in the general context of nucleation of a second phase in a parent matrix [23,248-251]. The G–X diagrams of Figures 6.1 and 6.2 can be referred in the perspective of nucleation of α - and γ' - phases in the γ -matrix. The nucleation of a second phase, compositionally and structurally distinct from the parent matrix, involves development of atomic clusters of second phase composition within the matrix followed by their crystallographic transformation into the crystal structure of the second phase. Likewise, nucleation of α - and γ' - phases will involve depletion and accumulation of Mo-atoms in the γ -matrix to form Mo-lean and Mo-rich matrix clusters followed by their transformations into the orthorhombic and the tetragonal crystal structures, respectively. The free energy of a matrix cluster (like the Mo-lean and the Mo-rich clusters) can be estimated as a function of its composition from the tangent drawn to the free energy curve of the matrix phase at the matrix composition (like tangent-IV drawn to the γ -matrix at 19.7 at.% Mo in Figures 6.1 and 6.2). In a G–X diagram if G_c represents the free energy of a cluster of composition of X_c , G_m represents the free energy of the matrix of composition X_m , and the derivative of the matrix free energy at X_m represents the slope of the tangent drawn to the matrix free energy curve at X_m , then

$$G_c = G_m + \left(\frac{dG^{matrix}}{dX} \right)_{X=X_m} * (X_c - X_m) \quad (6.15)$$

The point of intersection of the above tangent with the free energy curve of the second phase then represents the limiting composition (X_l) at which the free energies of the cluster and the

second phase become equal. It is only beyond this composition where the free energy of the second phase being lower than the cluster drives the transformation of the cluster into the second phase. The chemical driving force or the free energy released per mole of the second phase nucleated is given by the difference in free energies of the second phase and the cluster, as represented in Figure 6.1 by $\Delta G^{(\gamma U; \alpha U)}$ and $\Delta G^{(\gamma U; U2Mo)}$ for nucleation of α - and stoichiometric γ' -phases, respectively.

It may thus be seen from the G–X diagrams of Figures 6.1 and 6.2 that for a Mo-lean cluster to have a finite driving force for α -phase formation at 500 °C and 565 °C, the Mo-content of it should be less than ~ 5.7 at.% and 2.7 at.%, respectively. In other words, a minimum ~ 14 at.% and 17 at.% of Mo-depletion is required in the 19.7 at.% Mo γ -matrix to nucleate the α -phase at 500 °C and 565 °C, respectively. It may also be comprehended from Figures 6.1 and 6.2 that the driving force would be maximum for a α -phase nucleating with Mo-content ≈ 0 , in which case the Mo-lean clusters must be completely devoid of Mo. The diffusion of Mo-atoms in the γ -matrix, required to form the clusters, is kinetically sluggish [13,200,231,233-235]. Hence, it might be favorable for the α -phase to nucleate with a Mo-content just lower than the limiting composition, in spite of a lower driving force, and then to reduce its Mo-content gradually to the equilibrium value. Infact, α -phase with Mo-contents of 2.2 and 2.6 at.% has been shown to form upon annealing a γ -phase U–5.4 wt.% Mo alloy at 400 °C and 500 °C, respectively [147]. In the case of nucleation of γ' -phase, a likewise assertion of the limiting composition from the intersection of the matrix tangent with the free energy curve of the γ' -phase could not be made due to the representation of only the free energy of the stoichiometric γ' -phase in the G–X diagrams. Even then, the minimum Mo-content for γ' -nucleation can be considered to be 32.5 at.% Mo, as the γ' -phase can only form with compositions lying within its stability range. In the present case, the assumption of a stoichiometric γ' -phase formation would then necessitate a 13.6 at.% of Mo-enrichment of the γ -matrix. This would also maximize its driving force for nucleation due to a minimum in the free energy of the γ' -phase at this composition. A similar observation related to the Mo-enrichment of the γ -matrix prior to γ' -formation was made by May [252]. Although, in the G–X diagrams of Figures 6.1 and 6.2 the driving force for the nucleation of stoichiometric γ' -phase was found to be higher than that of the α -phase of any Mo-content, it must be realized that the nucleation of γ' -

phase is associated with a free energy barrier in contrast to that of the α -phase. This barrier will arise on account of the accumulation of Mo-atoms in the γ -matrix prior to the nucleation of γ' -phase, as the γ -phase shows a gradual rise in its free energy with increasing Mo-content in the compositional range of the γ' -phase. These subtle differences in the thermodynamics of nucleation of α - and γ' - phases did not get reflected in their observed phase fractions at 500 °C and 565 °C, when compared with the expected lever rule phase fractions (Table 5.3), except for the 500 °C/40 days aged as-rolled sample where a little lower γ' - and a correspondingly higher α -phase fractions could be noticed in comparison of equilibrium phase fractions. Pedrosa et al., however, have indicated an increased precipitation of the γ' -phase on ageing a U-10 wt.% Mo alloy at 500 °C [170]. The formation of α - necessitating a higher Mo-depletion, and a noticeable drop in the driving force for nucleation of both α - and γ' - phases at 565 °C, evident in the G-X diagram of Figure 6.2, would slow down the decomposition of the γ -phase at 565 °C compared to 500 °C. This is apparent from the results of the phase fraction analysis of as-rolled samples aged at 500 °C and 565 °C (Table 5.3). Such an observation is understandable in view of the fact that the ‘nose’ of the C-curve, signifying the fastest decomposition kinetics, is close to 500 °C for the 9 wt.% Mo γ -phase in the T-T-T diagram, as mentioned in Section 2.5.1. Decomposition kinetics at any temperature higher than 500 °C would then be limited by a reduction in the chemical driving force as opposed to an increase owing to enhanced diffusion.

The G-X diagram in Figure 6.3 showed that at 575 °C a common tangent can only be constructed between the free energy curves of α - and γ - phases encompassing the 19.7 at.% Mo γ -matrix. Thus, ageing at 575 °C should result in a generation of a two-phase ($\alpha + \gamma$) structure, as was observed experimentally.

It is imperative to mention at this juncture that G-X diagram constructed at 500 °C (Figure AII.1) using the thermodynamic parameters of Zhang et al. [135] predicted the nucleation of the α -phase with a limiting Mo-content of 13.6 at.%, which was too high an estimation. In addition, the G-X diagram at 565 °C (Figure AII.2) constructed using the same thermodynamic parameters predicted the formation of only α -phase in the 19.7 at.% Mo γ -matrix in contrast to the experimentally observed both α - and γ' - phases. Hence, G-X diagrams at 500 °C and 565 °C constructed with the parameters of Zhang et al. [135] were not used for the thermodynamic

analyses. Similarly, the G–X diagram at 575 °C (Figure AII.3) constructed using the parameters of Berche et al. [136] predicted the formation of both α - and γ' - phases in the 19.7 at.% Mo γ -matrix as against the experimental observation only α -phase, and hence was not considered for the analysis.

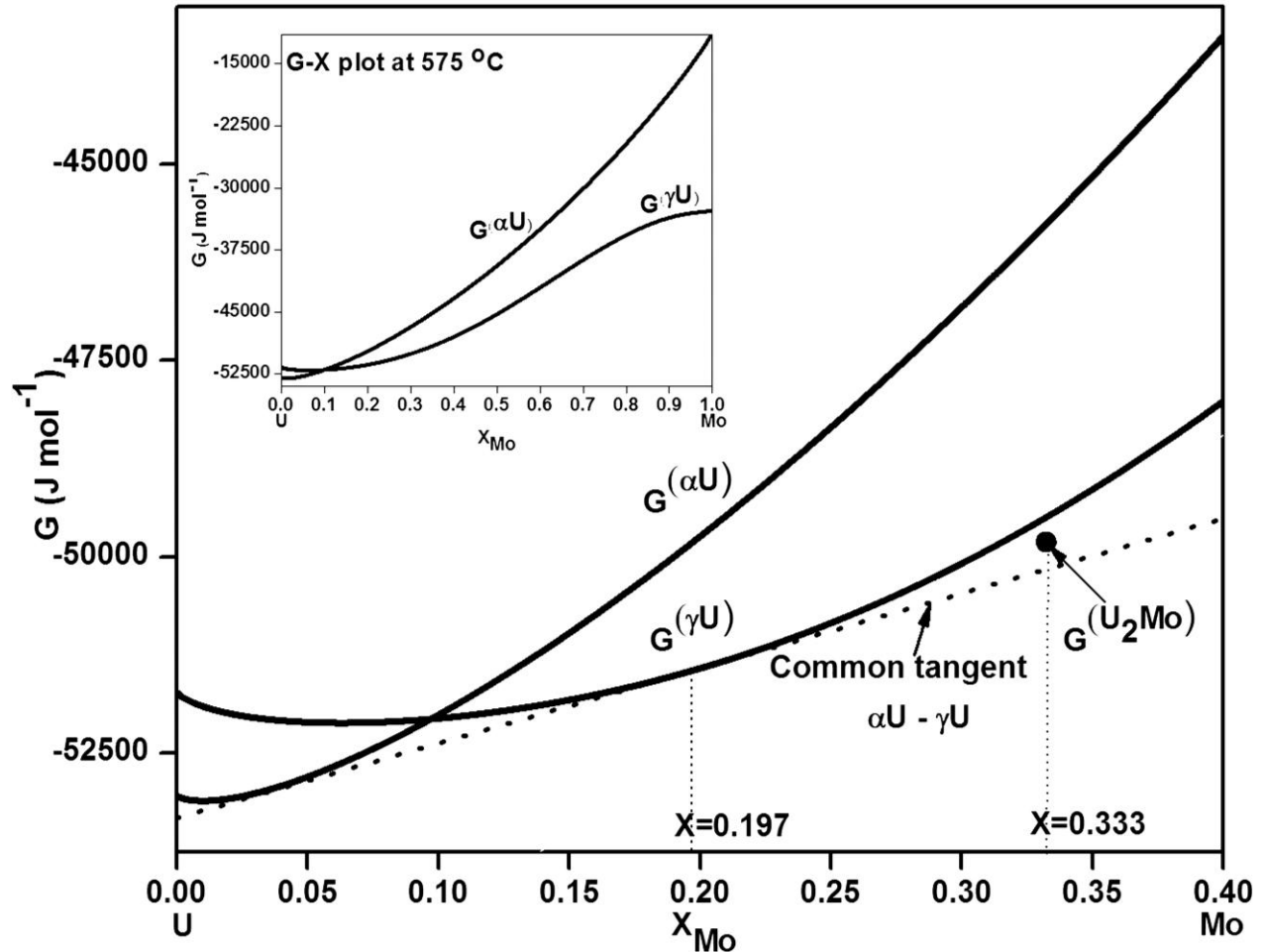


Figure 6.3 Free energy–composition diagram at 575 °C showing the variation of free energies of α -U and γ -U phases as a function of Mo-content in U–Mo system. The inset shows the same diagram for the entire U–Mo composition range. The free energy of the stoichiometric γ' (U_2Mo) phase of 33.3 at.% Mo (G^{U_2Mo}) is marked in the diagram by the filled circle.

6.3 Discussion

In general, eutectoid decomposition leading to a lamellar product morphology establishes a cooperative growth of the product phases, wherein, growth of one of the phases makes its vicinity conducive for the growth of the other phase due to a difference in their compositions

[23,241,243,248-251,253]. The thermodynamic criterion which governs the co-occurrence of the product phases in the decomposed structure is the simultaneous supersaturation of the parent matrix with respect to each of these phases [23,248-251,253]. Apart from the eutectoid composition at the eutectoid temperature, the compositional range of the matrix phase exhibiting such a behavior at any temperature below the eutectoid is estimated by constructing common tangents between the free energy curves of the matrix and the product phases. The composition of the matrix phase defined by the tangent drawn between the matrix and the solute-lean product phase (tangent-I in Figures 6.1 and 6.2) sets the upper limit of the above range, whereas, the lower limit is decided by the tangent drawn with respect to the solute-rich product phase (tangent-II in Figures 6.1 and 6.2). In the light of thermodynamics of nucleation, it may then be said that the tangent drawn to the matrix free energy curve at a composition exhibiting simultaneous supersaturation with respect to each of the product phases (like tangent-IV to the γ -phase at 19.7 at.% Mo in Figures 6.1 and 6.2) will intersect the free energy curves of the product phases. These intersections ensure the concurrent availability of the driving force required for the nucleation of the product phases and determine their limiting compositions.

The decomposition of the 9 wt.% Mo γ -matrix, exhibiting a eutectoid transformation, is thus expected to commence by nucleation of one of the product phases (either the α - or the γ' -) at the matrix grain boundaries, and proceed in a cooperative manner.

In the event of the decomposition of the γ -matrix at 500 °C and 565 °C, if α - happens to be phase nucleating first at a matrix grain boundary then the region adjoining it would become enriched with Mo. The migration of Mo-atoms to this effect can occur through the lattice of the γ -matrix, along the α - γ interface and along the γ - γ grain boundary. Once the γ -matrix adjacent to the α -phase attains a Mo-content of 33.3 at.% it is expected to transform to γ' . TEM examination of samples aged at 500 °C could show the presence of γ' -phase in between the α -phase lamellae, but occasionally, in form of short lath oriented transversely to the α -lamellae (Figure 5.25). It appeared that the interfaces of α -lamellae with γ -interlamellar regions are the sites for the nucleation of the γ' -phase. Moreover, the morphology of the γ' -phase suggested its interface with the α -phase to consist of a low energy coherent facet of lower mobility, which restricted its growth in the direction of the lamellae, and an incoherent interface with the γ -phase promoting its growth in the γ interlamellar region transverse to the α -lamellae. A partially decomposed ($\gamma +$

α) lamellar colony of this nature was labeled as type-I lamellar colony during SEM-EDS investigation. Compositional analysis in TEM showed the Mo-content in the γ -matrix and the γ' -phase to vary between 25.5-32.2 at.% and 32.8-34.9 at.%, respectively. The α -phase was found to be devoid of Mo. The infrequent occurrence of the γ' -phase between the α -phase lamellae could be because of the gradual nature of the Mo-enrichment of γ interlamellar regions. In contrast to 500 °C, TEM analyses of type-I colony in 565 °C aged samples showed an absence of the γ' -phase in the γ interlamellar regions containing 24.2–31.1 at.% Mo. This could be an effect of the low driving force for the nucleation of the γ' -phase at 565 °C failing to account for the interfacial energy (after what is being gained on account of heterogeneous nucleation) and the strain energy associated with its formation.

In the decomposition of the γ -matrix, the choice of γ' - to be the phase nucleating first at a matrix grain boundary will lead to a depletion of Mo-atoms adjacent to it, thereby prompting the nucleation of α -phase in these regions. TEM examination of aged microstructures, however, did not reveal the existence of α -phase between γ' -lamellae at both 500 °C and 565 °C. This kind of partially transformed ($\gamma + \gamma'$) lamellar colonies was labeled as type-II and type-III colonies based on the long and the short morphologies of the γ' -lamellae, respectively, during SEM-EDS investigation. The absence of α -phase in the γ interlamellar regions of these colonies could be an effect of the limited Mo-depletion (13.6 at.%) achieved out of γ' -formation as against the depletion required for α -nucleation (a minimum of ~ 14 at.% and ~ 17 at.% at 500 °C and 565 °C, respectively).

It may be noted that the occurrence of γ' -phase in between the α -lamellae of ($\gamma + \alpha$) colony and the development of partially decomposed colonies of short irregular γ' -lamellae could also be noticed in the work of Pedrosa et al. upon critically examining the electrostatic force microscopy contrast exhibited by the lamellar microstructure of 500 °C aged U–10 wt.% Mo alloy [170]. This sort of decomposition of the γ -matrix, initiating at the grain boundaries and forming a cellular microstructure with one of the product phases as the lamellae and a compositionally different matrix phase constituting the interlamellar region, falls under the category of discontinuous precipitation (DP) reaction (or the cellular reaction). Although, eutectoid decomposition and DP share an identical product morphology and reaction mechanism,

they differ in the constitution of the interlamellar region where it is composed of a product phase in the former as compared to a compositionally different matrix phase in the latter [237,242,244,246]. The further transformation of the metastable γ -phase within $(\gamma + \alpha)$ and $(\gamma + \gamma')$ colonies, to attain the equilibrium $(\alpha + \gamma')$ configuration, was noticed partially within the $(\gamma + \alpha)$ colonies in the samples aged at 500 °C. This kind of sequential precipitation during ageing is similar to the in-situ transformation of a metastable phase mixture to a more stable one, as observed in some ferrous alloys [254]. This in-situ transformation is expected to convert the partially transformed $(\gamma + \alpha)$ and $(\gamma + \gamma')$ lamellar colonies to lamellar $(\alpha + \gamma')$ colonies and bring in the complete decomposition of the metastable γ -phase upon prolonged ageing, like in the as-rolled sample aged for 40 days at 500 °C. The incidence of this event is driven by the maximum reduction in free energy obtainable on forming an equilibrium mixture of α - and γ' - phases, the free energy of which ($G^{\alpha+U_2Mo}$) is marked by a point on tangent-III in the G–X diagrams of Figures 6.1 and 6.2. The occurrence of DP leading to the formation of a lamellar structure followed by its in-situ transformation into a more stable form has been noticed before in U–Mo system, but in a different context, wherein the lamellae of discontinuously precipitated γ -phase, formed in α -phase matrix upon annealing a orthorhombic U–5 at.% Mo martensitic phase at 550 °C, transformed to γ' -phase at a later stage [252].

At this juncture it becomes imperative to recognize the factors which have been responsible for the nucleation of α -phase prior to the γ' -phase and vice versa at the grain boundaries of the γ -matrix, as the cellular colonies were found to evolve based on it. If the driving force for nucleation is considered to be the governing factor, which has a profound influence in deciding the phase to be nucleated first in a eutectoid decomposition, then under the present scenario the decomposition of the γ -matrix would have resulted in primarily $(\gamma + \gamma')$ colonies owing to the higher driving force of the γ' -phase. However, the presence of $(\gamma + \alpha)$ colonies envisaged the dominance of some other factors over the driving force in the nucleation of α -phase prior to the γ' -phase at the grain boundaries. In DP reactions, the heterogeneous nucleation of the product phase at the grain boundaries of the parent phase has been found to depend markedly on the orientation relationship (OR) existing between the plane of the grain boundary and the precipitate habit planes [237]. It may thus be conjectured that the

exhibition of such an OR preferring the formation of α -phase by the matrix grain boundaries has led to the development of $(\gamma + \alpha)$ colonies. In fact, at 500 °C the formation of γ' -phase within the Mo-enriched interlamellar regions of $(\gamma + \alpha)$ colonies by nucleating heterogeneously at the α -phase lamellae, and not at the original γ - γ grain boundaries, upholds the proposition that such grain boundaries favored the formation of α -phase.

The observed morphological attributes of the α -phase present in the γ -matrix of the 575 °C aged sample suggested its formation plausibly following the different variants of the orientation relationship existing between it and the γ -phase. Many diffusional solid-state precipitation reactions, where a lattice shear is known to take part in the overall transformation mechanism, generate second phase precipitates in needle-like morphology which maintain strict orientation relationship and habit plane with the parent matrix [23]. The needle shape of the α -phase could be a consequence of strain energy minimization [250], as the chemical free energy change driving its formation is quite small at 575 °C (Figure 6.3).

6.4 Summary

The ageing response of the metastable bcc γ -phase in U-9Mo alloy, with respect to the extent of decomposition and the nature, state of aggregation, relative fractions of the aged products, has been rationalized by thermodynamic analyses in this chapter as a function of ageing temperature. The salient findings, based on the observed attributes of γ -phase decomposition and the analyses of free energy–composition diagrams constructed at the different ageing temperatures, could be summarized as follows:

(i) The decomposition characteristics at 500 °C and 565 °C could be associated to the extent of Mo-segregation required in the γ -matrix for the nucleation of α - and γ' - phases and the chemical free energy change associated with their nucleation.

(ii) A discontinuous precipitation (or cellular) reaction, leading to the generation of partially transformed cellular colonies with lamellae comprising of either the α -phase or the γ' -phase with a compositionally different γ -phase as the interlamellar region, was found to be the mechanism operative behind the decomposition of the metastable γ -phase to the α - and γ' -phases at 500 °C and 565 °C.

(iii) The in-situ transformation of γ interlamellar regions to α - or γ' - phases, noticed occasionally within the ($\gamma + \alpha$) lamellar colonies in form of lath-shaped γ' -phase in the sample aged at 500 °C, was driven by the reduction in free energy available on forming an equilibrium mixture of α - and γ' - phases.

(iv) Ageing at 575 °C, being carried out above the eutectoid temperature, resulted in generation of α -phase in γ -phase matrix. The needle-like morphology of the α -phase could be a result of its formation following an orientation relationship with the γ -matrix coupled with strain energy minimization.

Interaction between U–9Mo fuel alloy and Zr–1Nb cladding alloy

7.1 Background

Chemical interaction occurring due to the interdiffusion of the constituent elements of fuel and clad, while in contact, has been a major cause of fuel failures, as mentioned in Section 2.6. Further, it has been highlighted in Section 2.6 that Zr can act as a diffusion barrier in circumventing the metallurgical interaction between U-based metallic fuel alloys, such as U–Mo, and Al-based fuel-meat matrix or cladding alloys. In this pretext, the use of Zr-based alloys as clad in case of monolithic fuels will not only reduce processing steps related to fabrication of Zr-barrier layer but will also eliminate the plausible deleterious effect of the phases formed due to the diffusional interaction between Zr-barrier layer and Al-alloy clad. Although Zr-based alloys are being considered as clad material for monolithic fuels based on U–Mo system [255,256], their chemical interactions with the fuel would require further evaluation before successful implementation.

It is worthwhile to mention here that out-of-pile diffusion bonding studies between fuel and fuel-matrix or fuel-cladding materials have come a long way in elucidating the mechanism of evolution of the interdiffusion zone developing at the interfaces of these materials while in contact [127,128,177-179,184,191,257-259]. Such investigations, apart from predicting the behavior of the fuel assembly during fabrication and in-pile operation, envisage precautionary measures to mitigate the deleterious effect of these interactions. Therefore, employing this principle, the work reported in this chapter is focused on ascertaining the metallurgical interaction between U–9Mo fuel alloy and Zr–1Nb cladding alloy by forming solid-to-solid interdiffusion couple. An elevated temperature of 800 °C was selected for the diffusion bonding operation in view of the following points:

- (i) Employment of, in general, higher temperatures (~ 650 °C) during fabrication of monolithic fuel plates [176].
- (ii) Possibility of transient temperature excursions well above the operating temperature domain in the reactor.

(iii) Decomposition of the γ -phase being prerequisite for the fuel-clad interaction (Section 2.6), a higher temperature would enhance the decomposition of the γ -phase which is otherwise sluggish at lower temperatures [12].

7.2 Experimental observations

The microstructures of Zr-1Nb and U-9Mo alloy samples used for diffusion bonding experiment comprised of α -Zr grains with intra and intergranular distribution of Nb-rich β -phase precipitates in the case of former and grains of the γ -phase in the case of latter.

The optical micrograph of the cross-section of the as-bonded sample is shown in Figure 7.1. A further examination of it was undertaken in SEM to reveal the finer microstructural details of the interdiffusion zone or the interaction layer (IL). Figure 7.2 shows the micrograph obtained in SEM using the BSE mode.

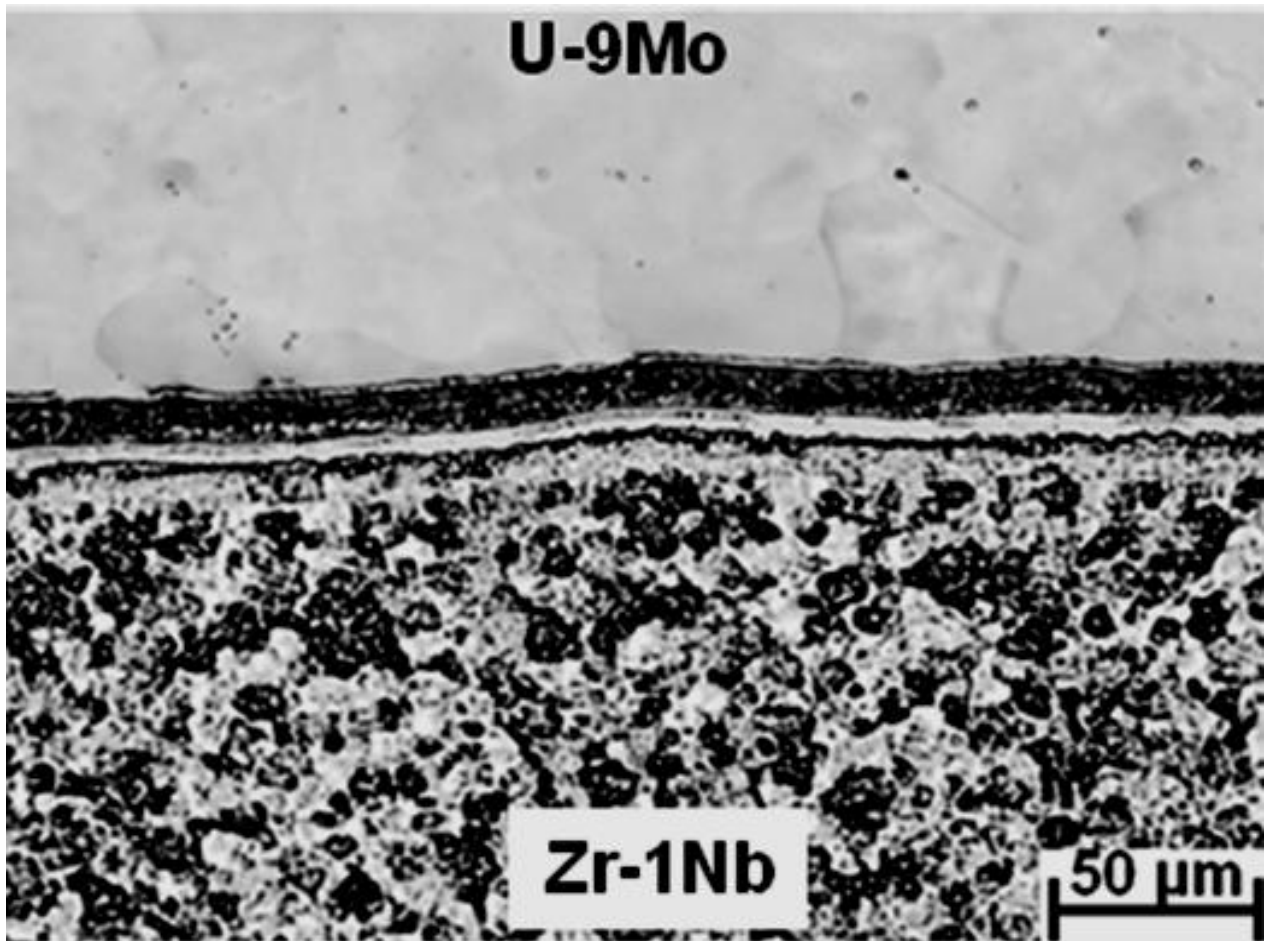


Figure 7.1 Optical micrograph depicting the microstructure of the cross-section of as-bonded U-9Mo/Zr-1Nb sample.

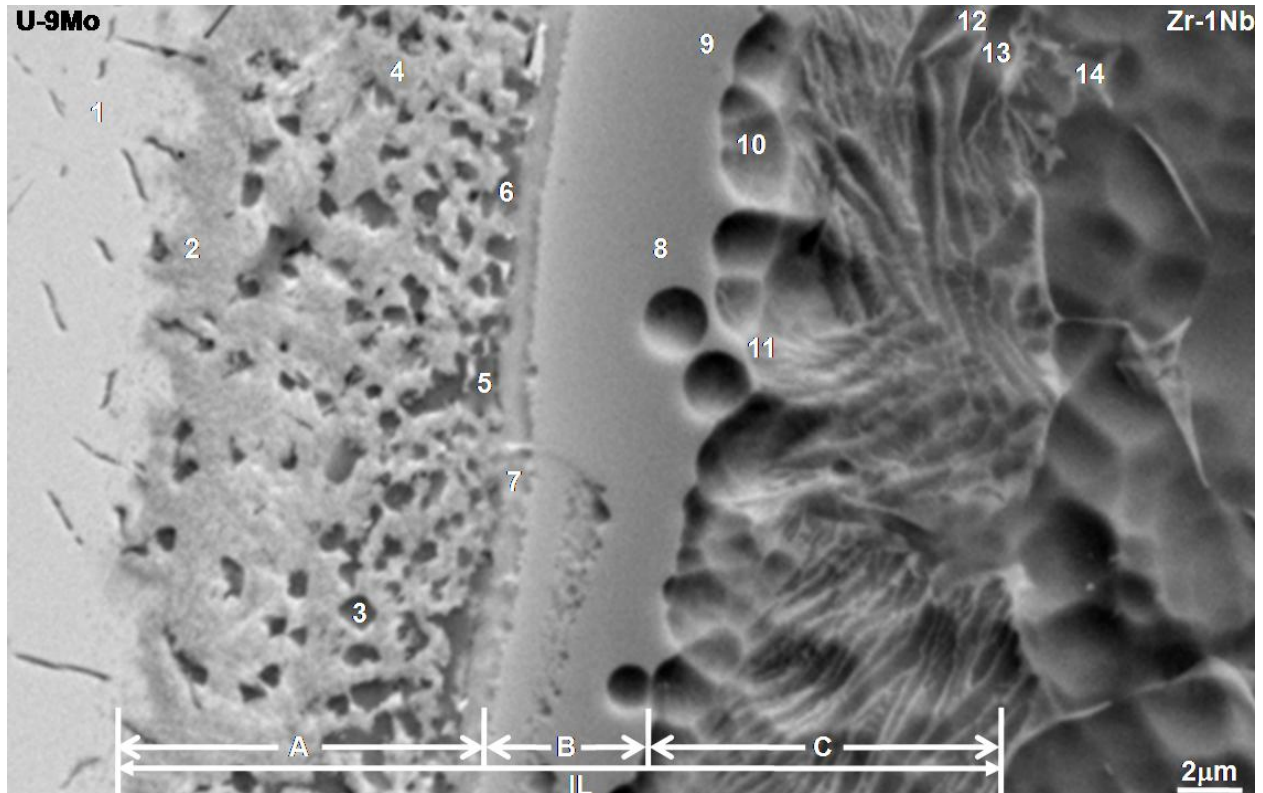


Figure 7.2 Back scattered electron image of the interaction layer (IL) formed between U-9Mo and Zr-1Nb alloys during the diffusion bonding operation at 800 °C. The compositions at regions labeled 1, 2, 3, ..., 14 are given in Table 7.1. The interaction layer could be divided into three distinct regions as marked by A, B and C in the figure. Labels 3, 5 and 6 correspond to the Mo_2Zr phase present in region-A as dispersoids. Labels 12 and 13 in region-C correspond to $\beta\text{-Zr(U)}$ and $\alpha\text{-Zr}$ phases, respectively.

The chemical composition at different regions of IL, labeled as 1, 2, 3, ..., 14 in Figure 7.2, are presented in Table 7.1. The concentration profiles of U, Mo and Zr across the IL are shown in Figure 7.3.

Table 7.1 Chemical compositions of different regions, as labeled in Figure 7.2, within the interaction layer (IL) formed between U–9Mo and Zr–1Nb alloys during the diffusion bonding operation at 800 °C, determined using EDS in SEM.

Label in Figure 7.2	U	Mo	Zr	
	(at. %)			
1	79.7	20.3	00.0	U–9Mo
2	84.3	11.1	04.6	Region A
3	09.4	57.3	33.3	
4	86.0	08.6	05.4	
5	22.5	45.5	32.0	
6	21.3	45.6	33.1	
7	53.2	12.0	34.8	
8	22.9	06.3	70.8	Region B
9	15.6	03.4	81.0	B
10	09.6	00.0	90.4	Region C
11	08.1	00.0	91.9	
12	10.4	00.0	89.6	
13	03.5	00.0	96.5	
14	00.4	00.0	99.6	Zr–1Nb

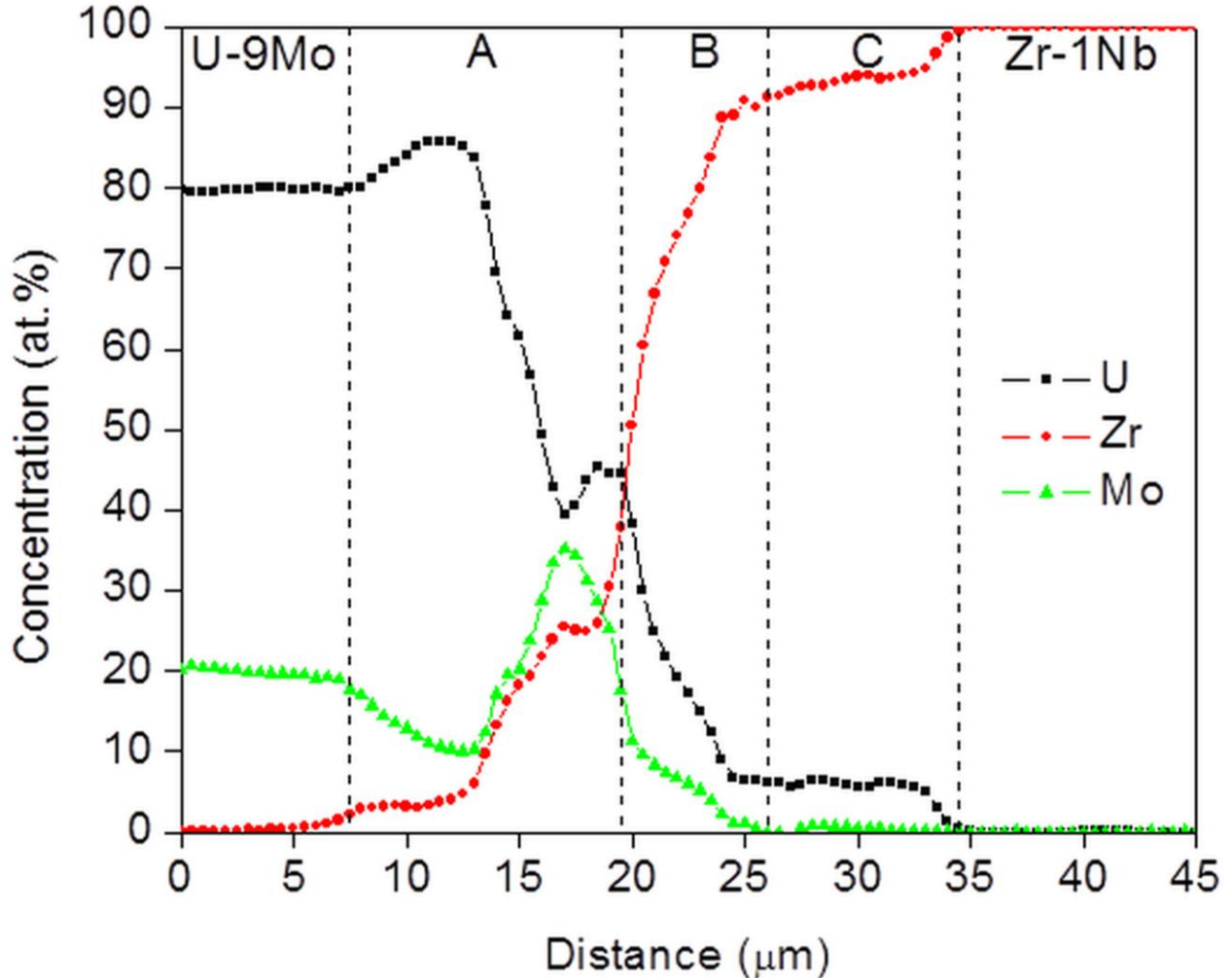


Figure 7.3 Concentration-distance profiles of U, Mo and Zr across the interaction layer (IL) formed between U-9Mo and Zr-1Nb alloys during the diffusion bonding operation at 800 °C, as determined by EPMA. The profiles have been divided into three zones viz., A, B and C (as marked in the figure) in accordance with the classification of the interaction layer (IL) carried out on the basis of microstructural features (Figure 7.2) and EDS analysis (Table 7.1).

The diffusion of Nb across the interface was found to be negligible, essentially due to its presence in small quantity (1 wt.%). A similar finding, with respect to insignificant diffusion of Nb across the interface of a co-extruded U-80 at.% Zr/Zr-1 at.% Nb rod during heat treatment, has been reported by Lee et al [260].

The phase-constituents of various parts of IL were determined by their chemical compositions and TEM analysis, in consultation with the Mo-U, U-Zr and Mo-Zr binary phase

diagrams (Figures AI.2, AI.5 and AI.6, respectively). Thus the entire IL of 27 μm width was classified into three distinct regions labeled A, B and C in Figure 7.2 and Table 7.1.

A few noteworthy observations were made from the microstructure (Figure 7.2) and the chemistry of IL across regions A, B and C (Table 7.1 and Figure 7.3). The concentration of U (C_U) rose upto 86 at.%, with a simultaneous drop in concentration of Mo (C_{Mo}) to 10 at.%, over a small area of about 5 μm adjacent to the U–9Mo/IL interface in region-A. On entering deeper into region-A, from this U-enriched area, C_U was found to decrease to about 39 at.%, along with a rise in C_{Mo} to 35 at.%, over a zone of width 5 μm . The intermetallic compound Mo_2Zr with diamond cubic structure was found to have formed in the region-A as dispersoids with varying shape and size, and their density was observed to increase progressively on moving towards region-B. The BSE contrast across regions B and C in Figure 7.2 indicated their existence as single-phase and two-phase structure, respectively.

A detailed TEM examination of region-A revealed that besides Mo_2Zr and $\gamma\text{-U}(\text{Mo},\text{Zr})$, hcp $\alpha\text{-Zr}$ and orthorhombic $\alpha\text{-U}$ phases also existed at room temperature. The microdiffraction patterns of $\alpha\text{-Zr}$, Mo_2Zr , $\gamma\text{-U}(\text{Mo},\text{Zr})$ and $\alpha\text{-U}$ are shown in Figures 7.4a to d, respectively, and the orientation relationships (ORs) amongst these phases, determined using composite SAED patterns, such as shown in Figures 7.5a and b, are listed in Table 7.2.

The TEM micrograph given in Figure 7.6a represents the microstructure of region-A near the U–9Mo/IL interface, where large Mo_2Zr precipitates were found to be present in the matrix. The micrograph in Figure 7.6b was obtained from the region-A, near its interface with region-B.

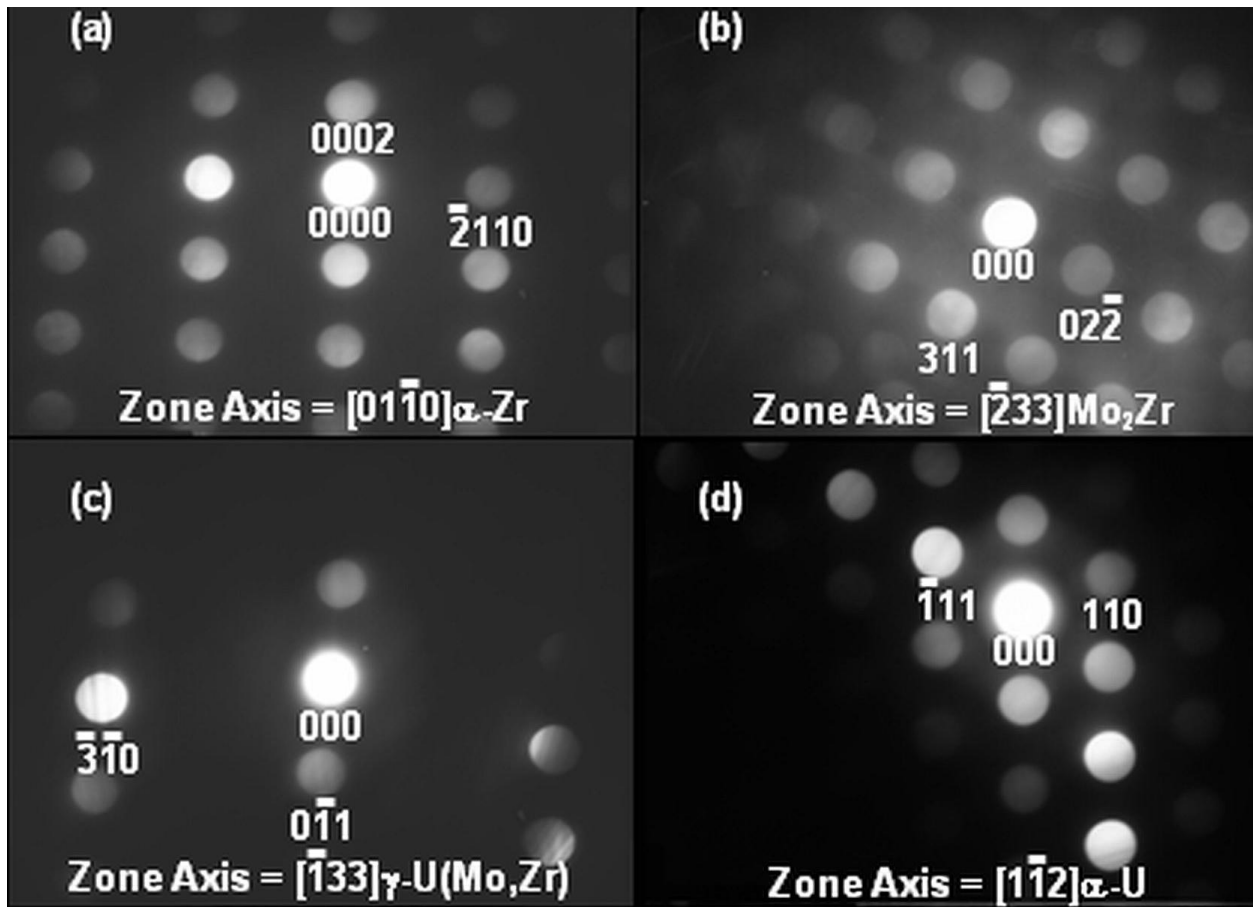


Figure 7.4(a-d) Typical microdiffraction patterns of $\alpha\text{-Zr}$, Mo_2Zr , $\gamma\text{-U(Mo,Zr)}$ and $\alpha\text{-U}$ phases present in the interdiffusion zone of the as-bonded U-9Mo/Zr-1Nb sample.

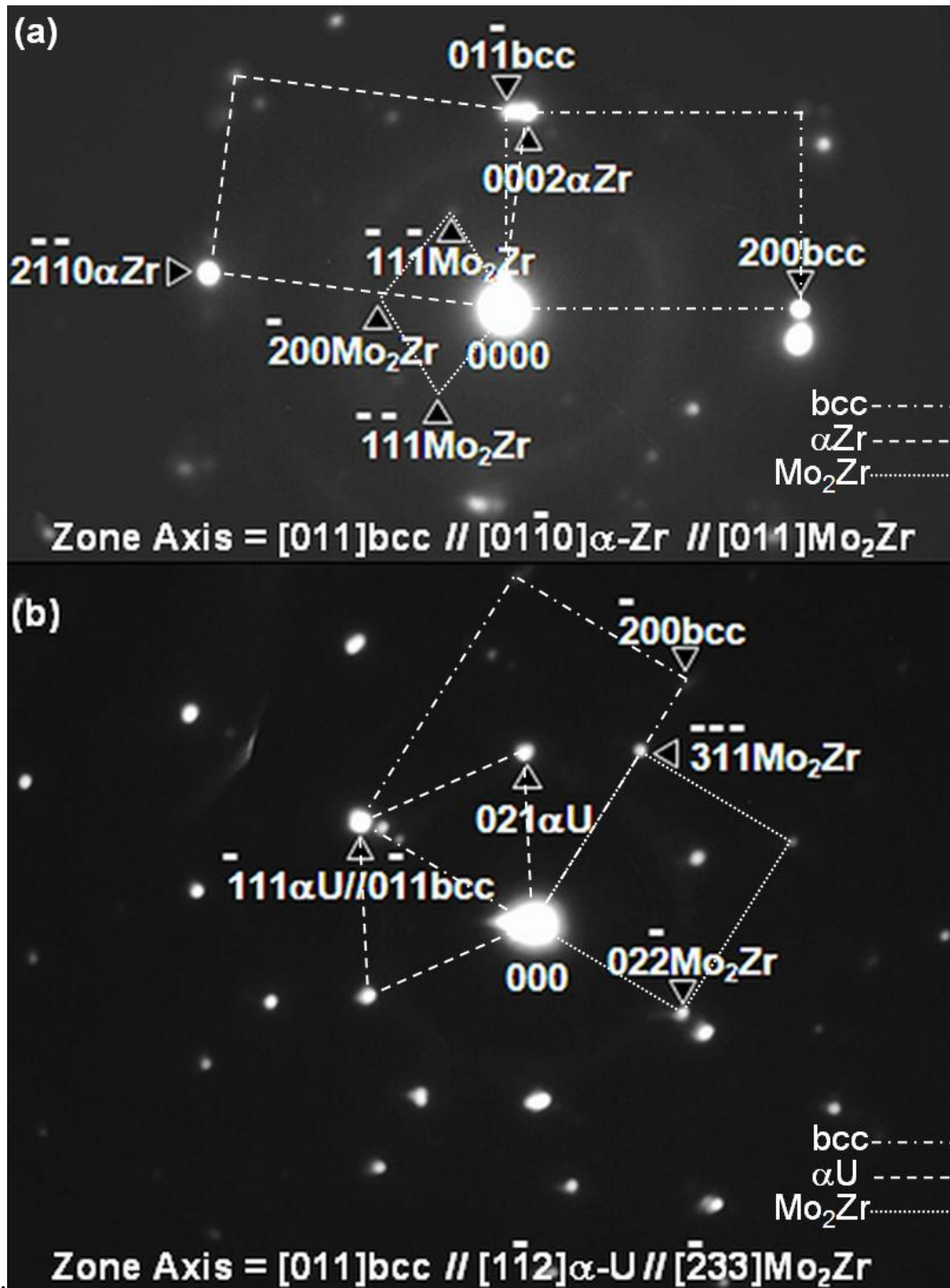


Figure 7.5 Typical composite SAED patterns showing reflections from (a) γ -U(Mo,Zr), α -Zr and Mo_2Zr phases, (b) γ -U(Mo,Zr), α -U and Mo_2Zr phases present in the interdiffusion zone of the as-bonded U-9Mo/Zr-1Nb sample. Cells constituting of diffracting planes for each of the phases have been outlined in the patterns.

Table 7.2 Orientation relationships between different phases present in the interdiffusion zone of the as-bonded U–9Mo/Zr–1Nb sample.

Phases	Orientation relationship
bcc– α -U	$(0\bar{1}1)\text{bcc} // (\bar{1}11)\alpha\text{-U}$ $[011]\text{bcc} // [\bar{1}\bar{1}2]\alpha\text{-U}$
bcc– α -Zr	$(0\bar{1}\bar{1})\text{bcc} \angle 5^\circ (0002)\alpha\text{-Zr}$ $[011]\text{bcc} // [0\bar{1}\bar{1}0]\alpha\text{-Zr}$
bcc–Mo ₂ Zr	$(3\bar{1}2)\text{bcc} // (110)\text{Mo}_2\text{Zr}$ $[\bar{1}33]\text{bcc} // [\bar{1}\bar{1}2]\text{Mo}_2\text{Zr}$
	$(100)\text{bcc} // (311)\text{Mo}_2\text{Zr}$ $[011]\text{bcc} // [\bar{2}33]\text{Mo}_2\text{Zr}$
α -U–Mo ₂ Zr	$(1\bar{1}\bar{1})\alpha\text{-U} // (3\bar{1}\bar{1})\text{Mo}_2\text{Zr}$ $[\bar{1}\bar{1}2]\alpha\text{-U} // [\bar{1}\bar{1}4]\text{Mo}_2\text{Zr}$
	$(1\bar{1}\bar{1})\alpha\text{-U} // (02\bar{2})\text{Mo}_2\text{Zr}$ $[\bar{1}\bar{1}2]\alpha\text{-U} // [\bar{2}33]\text{Mo}_2\text{Zr}$
α -Zr–Mo ₂ Zr	$(\bar{2}1\bar{1}2)\alpha\text{-Zr} // (3\bar{1}\bar{1})\text{Mo}_2\text{Zr}$ $[0\bar{1}\bar{1}0]\alpha\text{-Zr} // [011]\text{Mo}_2\text{Zr}$

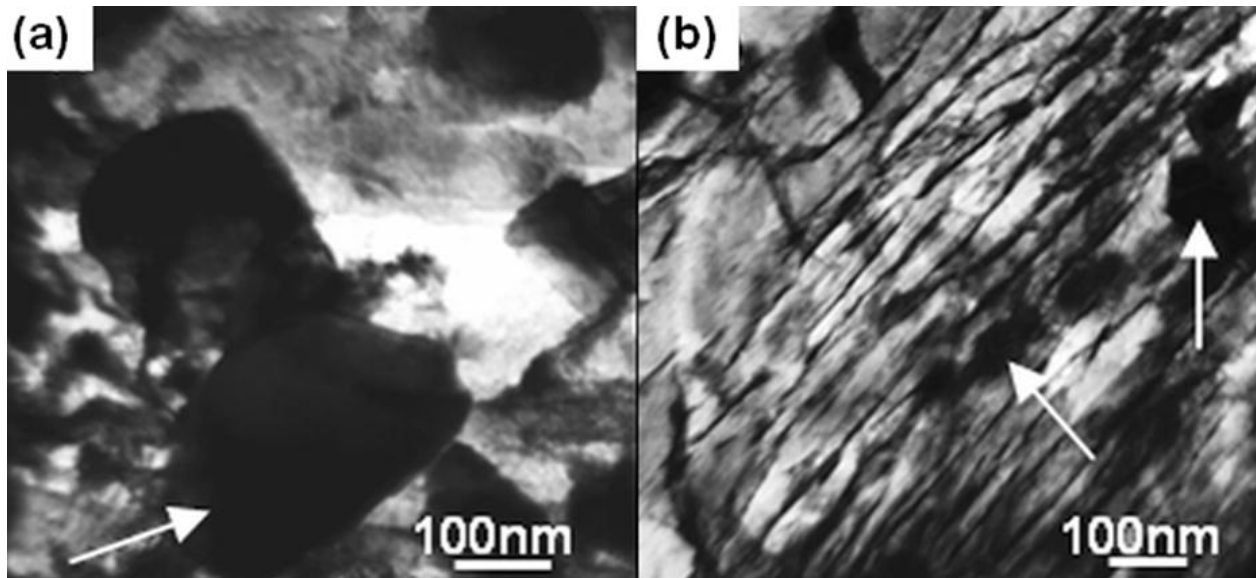


Figure 7.6 Typical bright-field TEM micrographs representing the microstructure of (a) region-A near the U-9Mo/IL interface and (b) region-A near the interface with region-B in the interdiffusion zone of the as-bonded U-9Mo/Zr-1Nb sample. Mo₂Zr precipitates are indicated by arrows in the micrographs.

7.3 Discussion

It may be assumed that at 800 °C, the interdiffusion of U, Zr and Mo across the interface led to the formation of a single bcc solid solution across IL, initially with a chemical composition exhibiting a gradual decrease in the concentration of U and Mo and an increase in the concentration of Zr across all of the regions of A, B and C from U-9Mo side to Zr-1Nb side. Concomitantly, diffusion of Zr into the U-rich region-A led to the formation of Mo₂Zr phase. The presence of Mo₂Zr only in the bcc γ -U(Mo,Zr) matrix of region-A is due to the prominence of Mo in this region, coupled with sluggish diffusion of Mo in the β -Zr(U) phase [4] of Zr-rich regions B and C. The increasing demand for Mo atoms to continue the precipitation process led to the formation of a Mo-depleted zone ($C_{Mo} \sim 10$ at.%) in region-A near the U-9Mo/IL interface as mentioned earlier. This process, in turn, prompted an enrichment of U in this layer, against the concentration gradient. Recently, Huang et al. [4] have also observed a similar up-hill diffusion of U atoms in a related study. Therefore, it may be argued that the expected down-the-concentration gradient composition profiles of especially U and Mo were locally altered in

region-A due to the formation of the Mo_2Zr phase thereby resulting in up-hill diffusion and peaking in the concentration profiles of U and Mo, respectively.

Mo is known to be a stronger stabilizer of $\gamma\text{-U}$ as compared to Zr [261], and a minimum 17.7 at.% of Mo is required to stabilize this phase during slow cooling [115]. Since $(C_{\text{Mo}} + C_{\text{Zr}}) < 17.7$ at.% in Mo-depleted matrix of region-A (Table 7.1), $\gamma\text{-U}(\text{Mo,Zr})$ would tend to transform to $\alpha\text{-U}$ during cooling of the couple. The solubility of Mo and Zr in $\alpha\text{-U}$ being negligible [24], such a transformation would lead to an enrichment of the remaining $\gamma\text{-U}(\text{Mo,Zr})$ phase with Mo and Zr, and thereby will enhance its stability. A partial transformation of $\gamma\text{-U}(\text{Mo,Zr})$ to $\alpha\text{-U}$ is experimentally evidenced by the presence of an OR between the two (Table 7.2). The Zr-content of the matrix of region-A reached to about 35 at.% near its interface with region-B. The U–Zr phase diagram shows the presence of a miscibility gap in the range $20 \text{ at.\%} < C_{\text{Zr}} < 45 \text{ at.\%}$, hence while cooling, the $\gamma\text{-U}(\text{Mo,Zr})$ matrix within this composition domain is expected to decompose into U-rich and Zr-rich fractions, which would eventually transform to $\alpha\text{-U}$ and $\alpha\text{-Zr}$, respectively. The presence of $\alpha\text{-Zr}$, confirmed by microdiffraction (Figure 7.4a), and its OR with $\gamma\text{-U}(\text{Mo,Zr})$ (Table 7.2) convincingly points out such a scheme of phase transformation. Existence of Zr-rich phase in the interdiffusion zone of U–Mo–Zr system was also indicated by other workers recently [4,176]. The OR between the retained $\gamma\text{-U}(\text{Mo,Zr})$ and Mo_2Zr suggested precipitation of the latter phase from the former matrix. In addition, the existence of ORs between Mo_2Zr and both $\alpha\text{-U}$ and $\alpha\text{-Zr}$ phases (Table 7.2) endorsed the phase separation of $\gamma\text{-U}(\text{Mo,Zr})$ matrix adjoining the Mo_2Zr precipitates. The diffraction contrast exhibited in the TEM micrograph (Figure 7.6b) obtained from the region-A, near the interface with region-B, could possibly be a result of occurrence of the reaction phenomena described above.

The chemical composition of region-B as determined through SEM-EDS and EPMA are presented in Table 7.1 and Figure 7.3, respectively. Composition profiles obtained through EPMA, across region-B, showed gradual variation in the concentrations of Zr from ~ 40 at.% to 90 at.% and that of U from ~ 45 at.% to 5 at.%. The diffusion of Mo was found to cease at the end of region-B, starting from a concentration of ~ 15 at.%. According to binary U–Zr phase diagram, region-B exhibiting this sort of compositional variation is expected to exist as a single bcc solid solution phase at 800°C during the diffusion bonding experiment. The U–Zr phase diagram primarily suggests a transformation of this bcc phase to hexagonal $\delta\text{-UZr}_2$ phase below

~ 620 °C during cooling of the couple, especially in the composition range of 66.5-80.2 at.% Zr. Nevertheless, U–Zr alloys of these compositions once cooled at a moderate rate from the high temperature bcc γ -phase do not show any transformation to δ -phase. This is essentially because the transformation from γ - to δ - follows the mechanism of omega-phase transformation and requires either rapidly cooling of the bcc structure or ageing of the metastable bcc structure [24,262-265]. Hence, during cooling of the diffusion couple, region B undergoing cooling as well at a slow rate is expected to retain its bcc crystal structure without undergoing any further decomposition and remain as a single phase at room temperature.

It can be seen at the Zr-rich end of the U–Zr phase diagram that β -Zr transforms to α -Zr when cooled below 862 °C. The β -Zr(U) phase in region-C, while cooling, invoked the formation of α -Zr in Widmanstätten morphology. The low solubility of U in α -Zr resulted in U-enrichment of the untransformed β -Zr(U) matrix. Even though EPMA analysis estimated an almost flat composition profile for both U and Zr within region-C, local compositional variation in it could be brought out from SEM-EDS analysis which indeed highlighted higher U-content of β -Zr matrix in respect of α -Zr plates (labels 12 and 13, respectively, in Figure 7.2 and Table 7.1). This corroborated the BSE contrast exhibited by the α -Zr + β -Zr(U) two-phase mixture.

7.4 Summary

Metallurgical interaction occurring between U–9Mo fuel alloy and Zr–1Nb cladding alloy has been assessed by forming diffusion couple between the two. The interaction of these alloys during the bonding operation at 800 °C and during subsequent cooling of the diffusion couple led to the formation of a complex layered microstructure in the interdiffusion zone. The salient features of the interdiffusion zone have been summarized below:

(i) The diffusion reaction in the U-rich part of the zone was dominated by the formation of Mo_2Zr phase in form of spheroids, which promoted instability and hence phase separation to occur in the γ -U(Mo,Zr) matrix during cooling. This led to the appearances of α -U and α -Zr phases in this part of the interdiffusion zone, which could be brought out only by an in-depth TEM analysis of the interaction zone.

(ii) A two-phase (α + β)-Zr layer in Widmanstätten morphology was formed on the Zr-rich side of the couple.

(iii) The in-between region of the interdiffusion zone was found to exist as a single bcc solid solution phase.

(iv) The presence of 1 wt.% of Nb in the cladding alloy was found to have an insignificant influence on the microstructural evolution of the interdiffusion zone, which adds to the advantage of using Zr-1Nb as clad.

Assessment of U–9Mo/Zr–1Nb interdiffusion zone stability

8.1 Background

A detailed overview of the evolution of the interdiffusion zone during diffusion bonding of U–9Mo fuel alloy with Zr–1Nb cladding alloy was presented in the previous chapter. In the present chapter annealing studies undertaken to investigate the stability of this interdiffusion zone, in terms of further growth and plausible microstructural modifications, have been reported. Since the bonding operation was carried out at 800 °C itself, annealing temperatures of 800 °C, 900 °C and 1000 °C were selected. These elevated temperature annealings would facilitate to assess the behavior of the interdiffusion zone under probable in-reactor temperature excursions. Moreover, annealing experiments at these different temperatures would also aid in evaluating the kinetic growth parameters of the interdiffusion zone which would (i) help to estimate its growth rate at any other temperature of interest and (ii) enable a comparison to be made with the growth rates observed in couples formed between U–Mo and Al or Al–Si alloys or pure-Zr. Such comparisons together with stability assessment of interdiffusion zone are essential to establish Zr–1Nb alloy as a cladding material for monolithic fuels against the existing Al or Al-based alloys and to eliminate the use of Zr diffusion barrier layer.

8.2 Experimental observations

The as-bonded U–9Mo/Zr–1Nb diffusion couple was subjected to annealing heat treatments as per the schedule given in Table 8.1 followed by microstructural characterization of the cross-sections employing optical microscopy, EPMA, SEM and TEM.

Table 8.1 Annealing schedule of U–9Mo/Zr–1Nb as-bonded diffusion couple.

<i>Temperature (°C)</i>	<i>Duration (cooling condition)</i>
800	10 days (water-quenched)
	10 days (furnace-cooled)
900	10 days, 12 days (furnace-cooled)
1000	10 days (furnace-cooled)

A detailed examination of the interdiffusion zone of all the annealed samples in optical microscopy, SEM and EPMA revealed three distinct microstructural features, as mentioned below in the order of their appearances from the Zr–1Nb side of the couple:

(a) An interwoven structure of parallelly stacked group of laths resembling the “basket weave” microstructure, except for the sample water-quenched after annealing at 800 °C.

(b) (i) The presence of an almost continuous layer of Mo₂Zr phase running parallel to the interface near the U–9Mo side of the interdiffusion zone, accompanied by Mo₂Zr phase with a ‘massive’ morphological feature in the vicinity.

(ii) The presence of a ‘halo’, with a lamellar microstructure within, in the neighborhood of the Mo₂Zr phase, except for the sample water-quenched after annealing at 800 °C.

(c) The presence of Zr-rich precipitates further deep into the U–9Mo side of the interdiffusion zone.

The optical micrograph given in Figure 8.1 typically represents the overall microstructural characteristics of the interdiffusion zones formed during the different annealing heat treatments of the as-bonded sample.

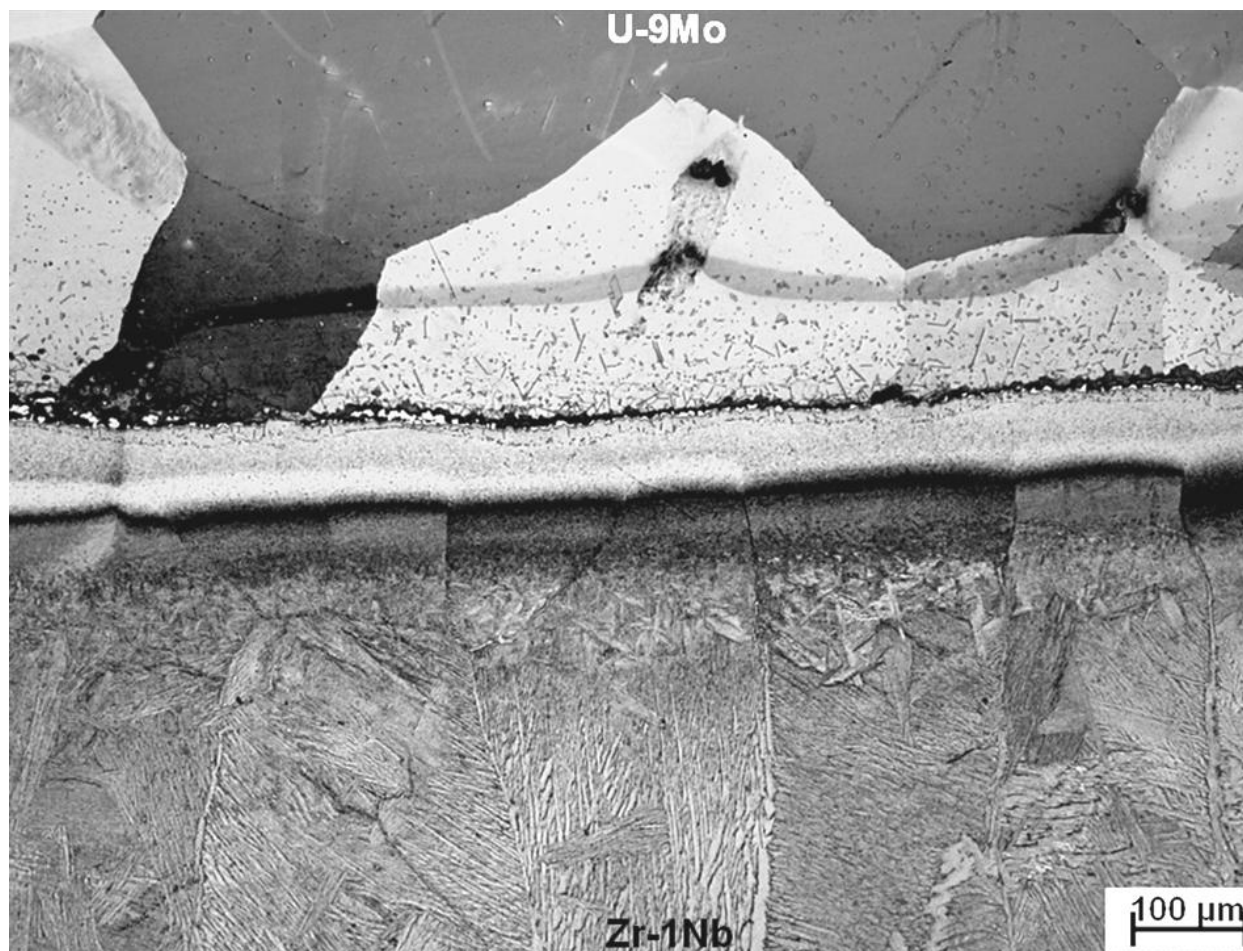


Figure 8.1 A typical optical microscopy image representing the overall microstructural features of the interdiffusion zones of all the annealed U-9Mo/Zr-1Nb bonded samples.

The identity of the Mo_2Zr phase and those of the Zr-rich precipitates was established through compositional analyses in SEM using EDS and in EPMA using WDS.

A few representative BSE-SEM images of the interdiffusion zones of the annealed samples are presented in Figures 8.2 to 8.9. Site-specific composition analysis of the features of the interdiffusion zone has been accomplished using EDS, some of the results of which are presented in Table 8.2 corresponding to the labels marked in Figures 8.2 to 8.9.

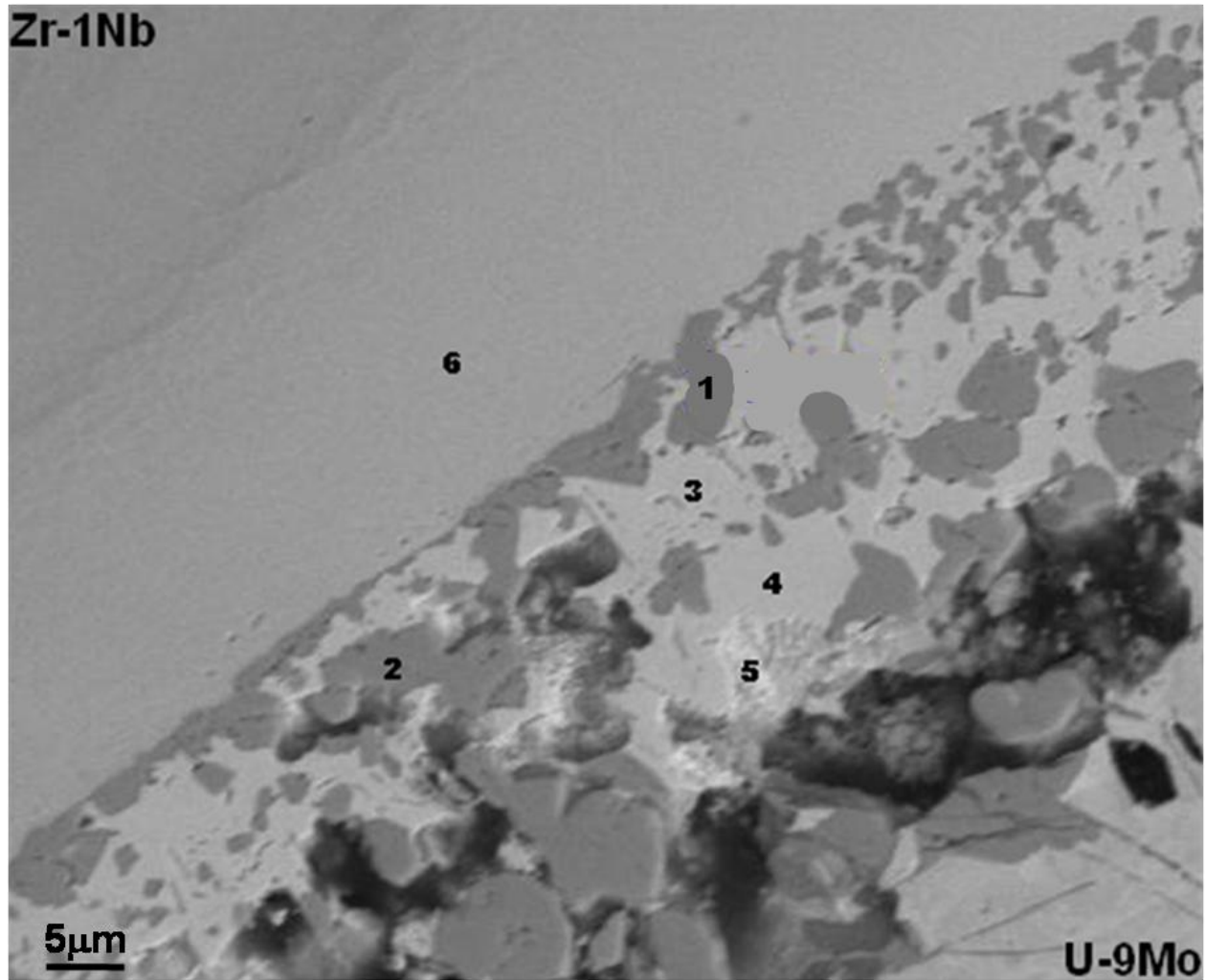


Figure 8.2 Backscattered electron image of the interdiffusion zone of U-9Mo/Zr-1Nb bonded sample annealed at 800 °C for 10 days followed by water quenching. Labels 1 and 2 represent the ‘massive’ morphological feature of the Mo₂Zr phase.

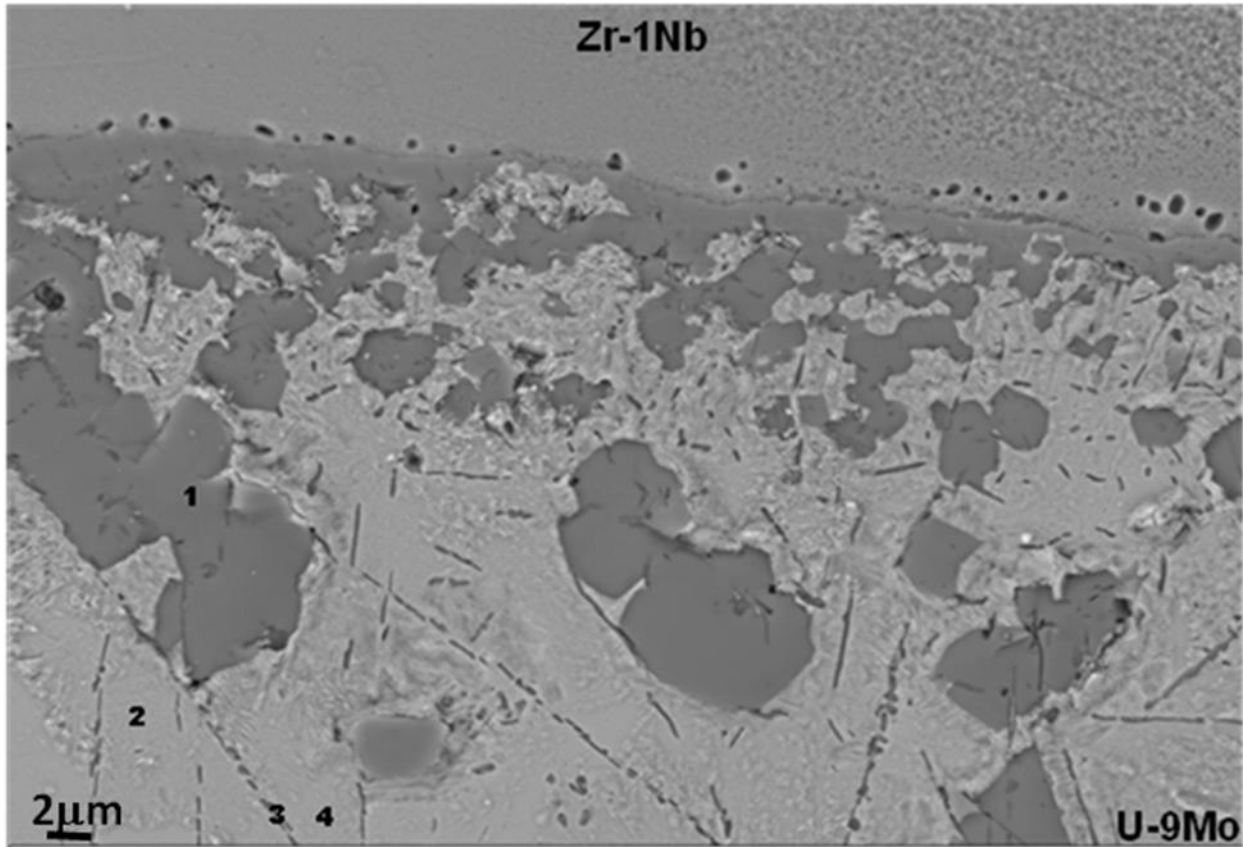


Figure 8.3 Backscattered electron image of the interdiffusion zone of U-9Mo/Zr-1Nb bonded sample annealed at 800 °C for 10 days followed by furnace cooling. Label 1 represents the 'massive' morphological feature of the Mo₂Zr phase. Label 3 represents the Zr-rich precipitate phase.

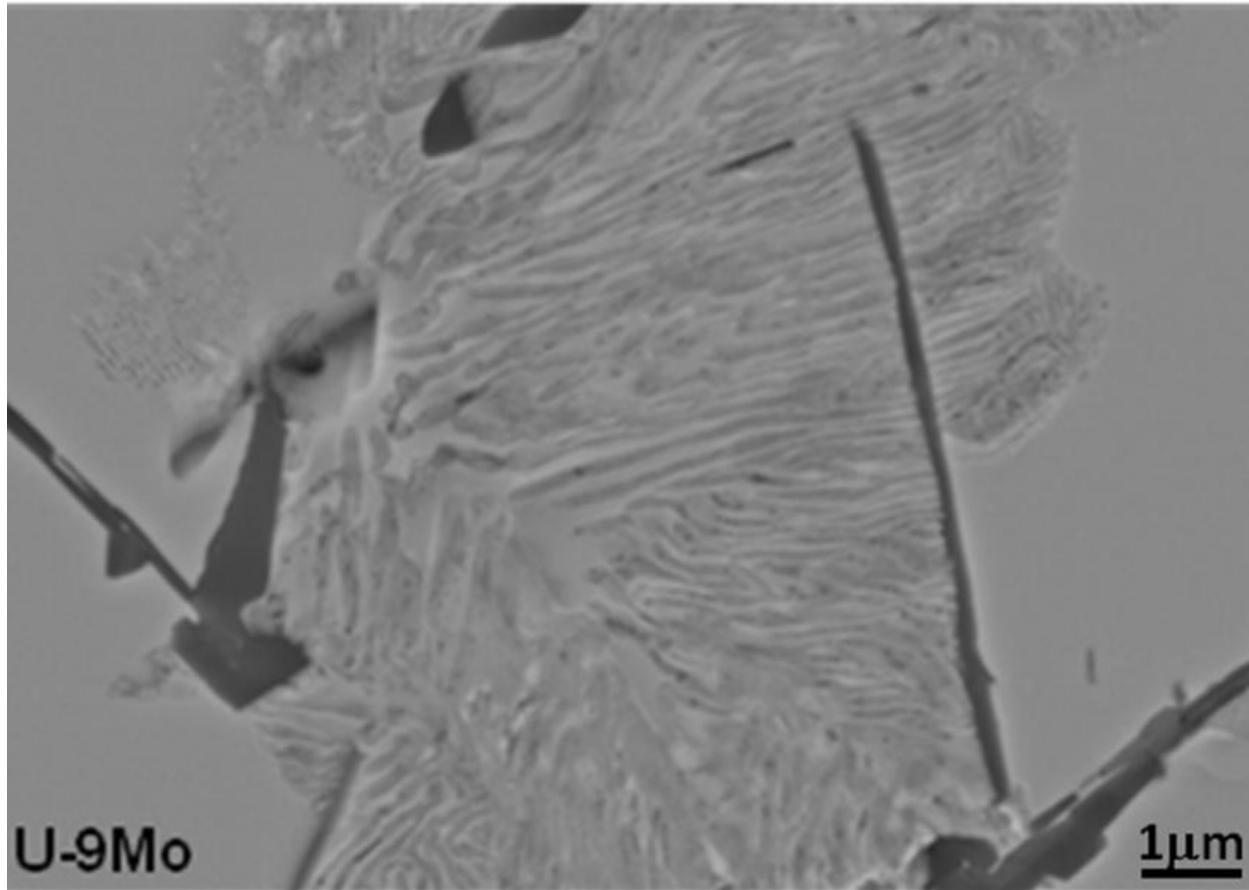


Figure 8.4 Backscattered electron image of the interdiffusion zone of U-9Mo/Zr-1Nb bonded sample annealed at 800 °C for 10 days followed by furnace cooling depicting the lamellar 'halo' region adjoining the Mo_2Zr phase.

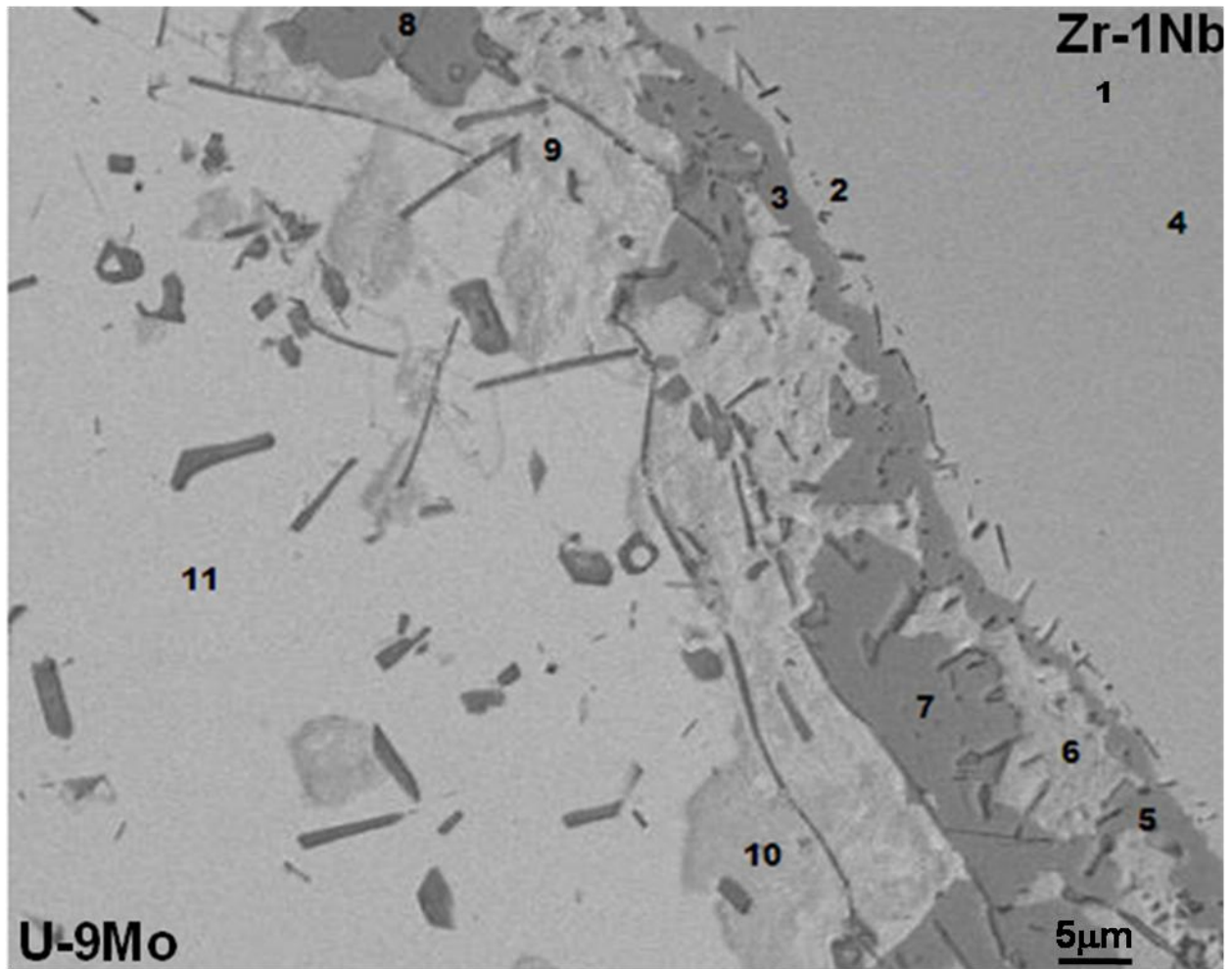


Figure 8.5 Backscattered electron image of the interdiffusion zone of U-9Mo/Zr-1Nb bonded sample annealed at 900 °C for 10 days followed by furnace cooling. Labels 3 and 5 represent the continuous layer of Mo_2Zr phase running parallel to the as-bonded interface. Labels 7 and 8 represent the ‘massive’ morphological feature of the Mo_2Zr phase. Labels 6, 9 and 10 represent the ‘halo’ region adjoining the Mo_2Zr phase.

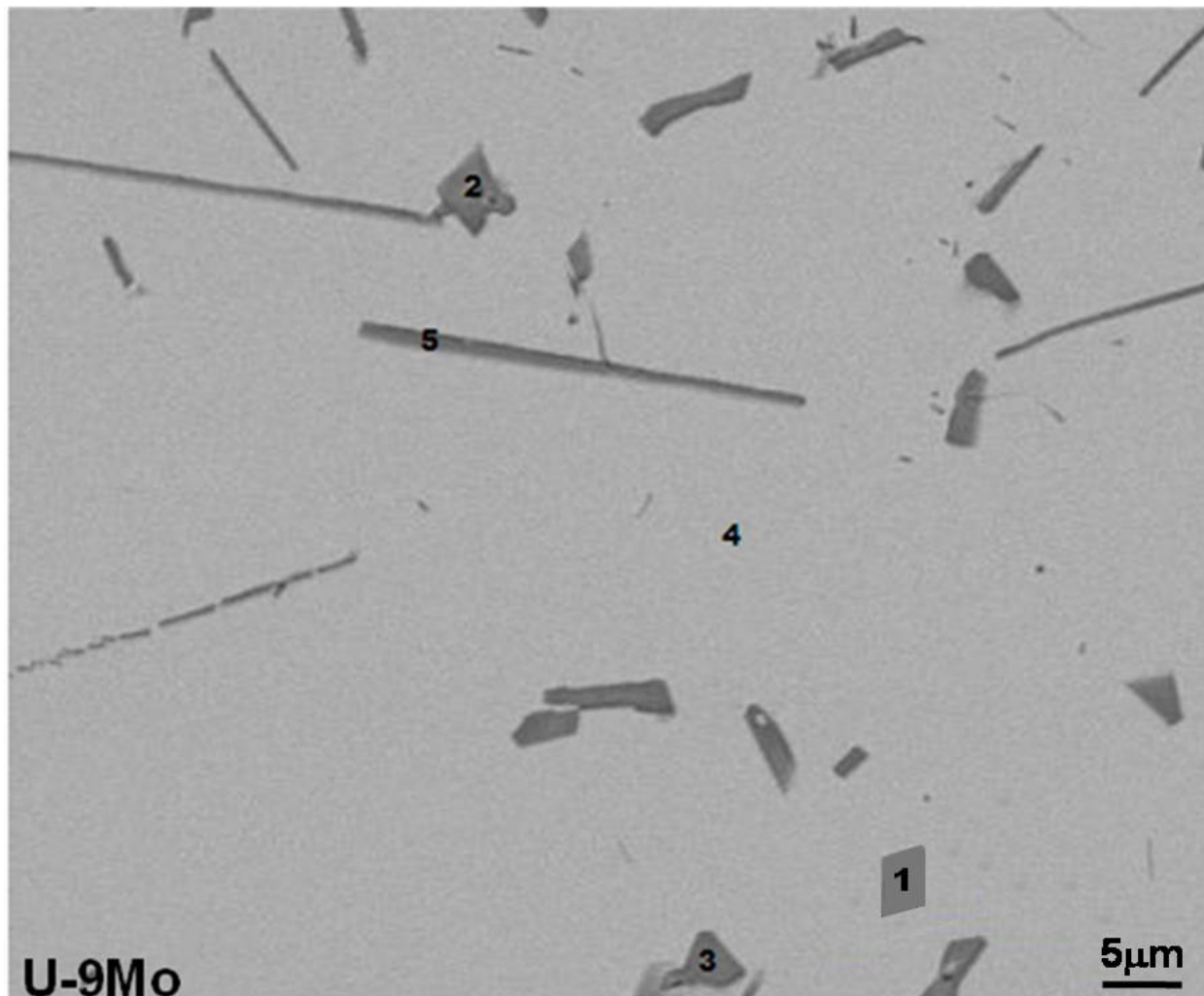


Figure 8.6 Backscattered electron image of the interdiffusion zone further deep into the U-9Mo side of U-9Mo/Zr-1Nb bonded sample annealed at 900 °C for 10 days followed by furnace cooling. Labels 1, 2, 3 and 5 represent the Zr-rich precipitate phase.

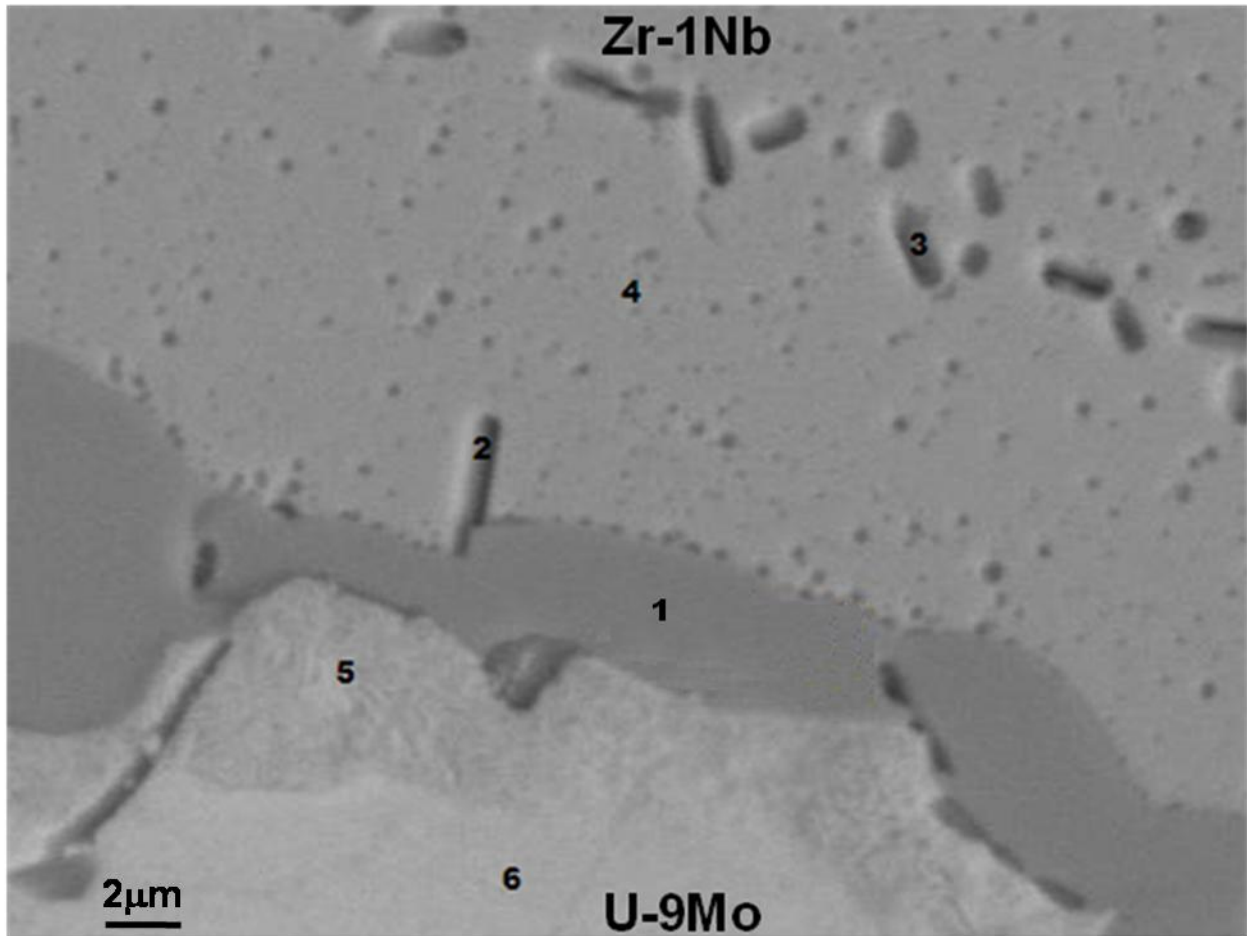


Figure 8.7 Backscattered electron image of the interdiffusion zone of U-9Mo/Zr-1Nb bonded sample annealed at 900 °C for 12 days followed by furnace cooling. Label 1 represents the continuous layer of Mo₂Zr phase running parallel to the as-bonded interface. Labels 5 represents the 'halo' region adjoining the Mo₂Zr phase.

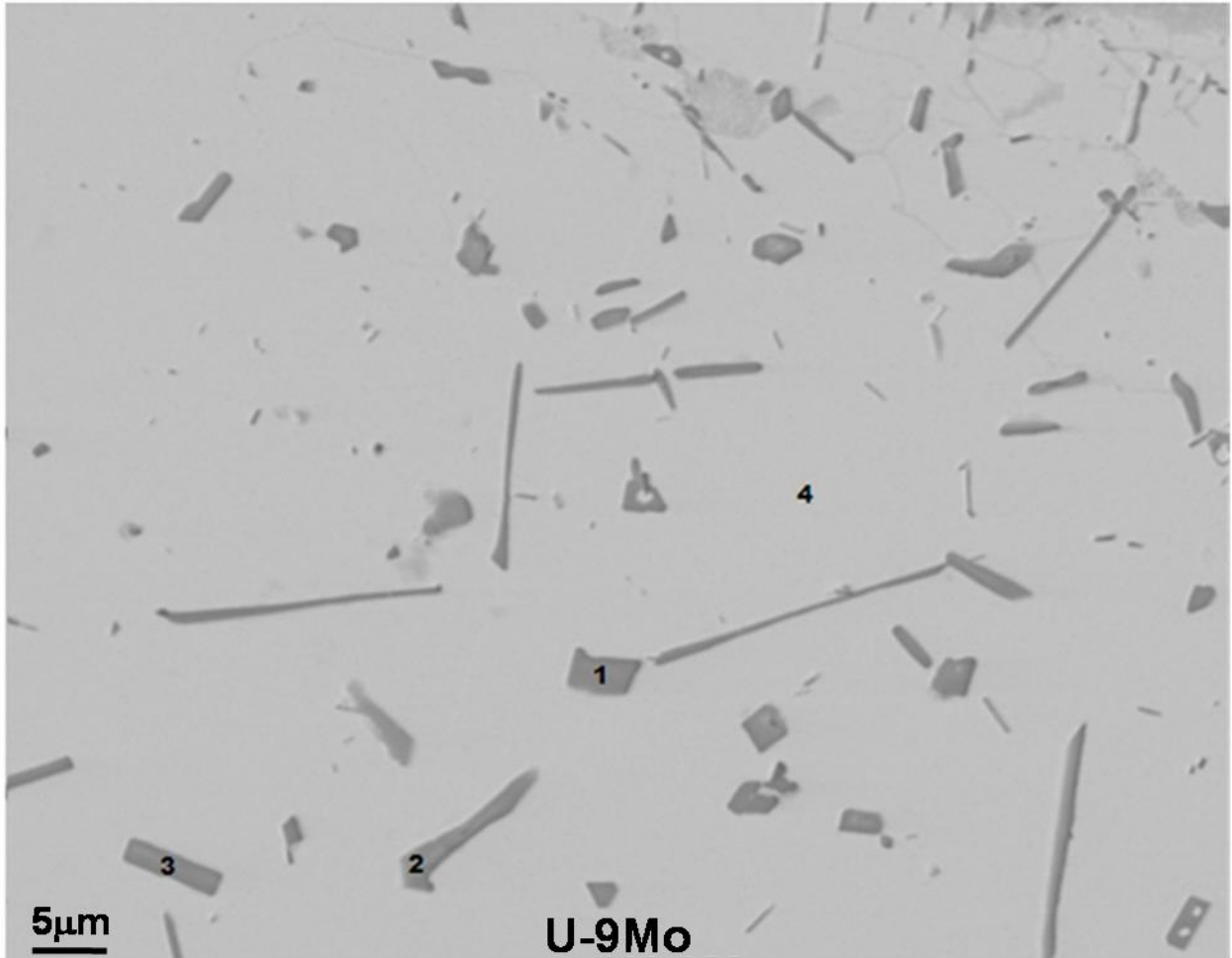


Figure 8.8 Backscattered electron image of the interdiffusion zone further deep into the U-9Mo side of U-9Mo/Zr-1Nb bonded sample annealed at 900 °C for 12 days followed by furnace cooling. Labels 1, 2 and 3 represent the Zr-rich precipitate phase.

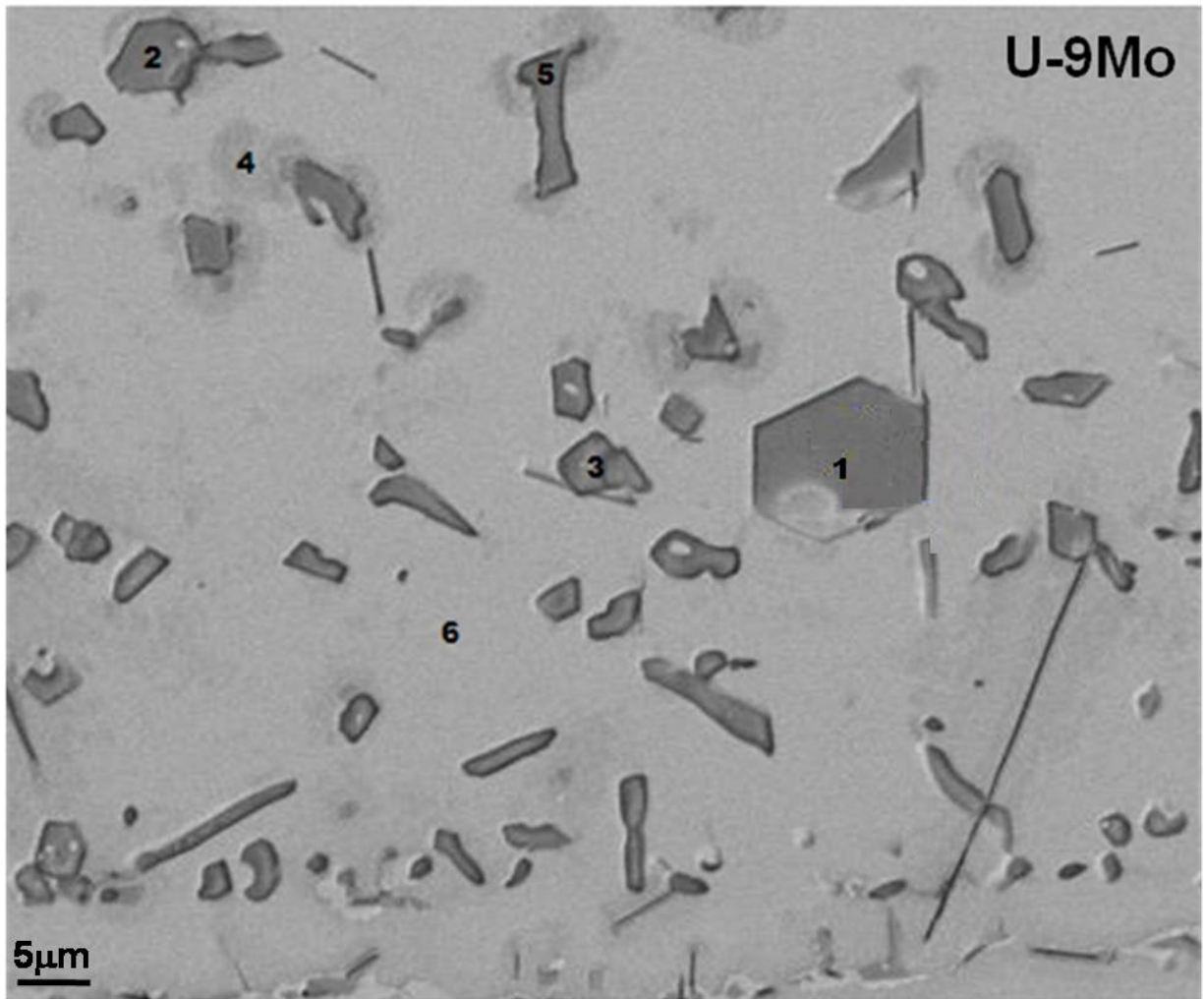


Figure 8.9 Backscattered electron image of the interdiffusion zone of U-9Mo/Zr-1Nb bonded sample annealed at 1000 °C for 10 days followed by furnace cooling. Labels 1, 2, 3 and 5 represent the Zr-rich precipitate phase.

Table 8.2 Chemical compositions at different regions within the interdiffusion zone of the annealed U–9Mo/Zr–1Nb bonded samples as labeled in Figures 8.2 to 8.9, determined using EDS in SEM.

<i>Sample Details</i>	<i>Figure No.</i>	<i>Label</i>	<i>U (at.%)</i>	<i>Mo (at.%)</i>	<i>Zr (at.%)</i>
800 °C/ 10 days/ water-quenched	8.2	1	01.1	63.5	35.4
		2	00.4	64.4	35.2
		3	74.6	08.5	16.9
		4	77.2	09.0	13.8
		5	74.6	10.2	15.2
		6	40.1	10.2	49.7
800 °C/ 10 days/ furnace-cooled	8.3	1	01.0	64.8	34.2
		2	86.6	11.7	01.7
		3	56.0	08.5	35.5
		4	85.7	12.0	02.3
900 °C/ 10 days/ furnace-cooled	8.5	1	25.4	11.9	62.7
		2	31.5	13.8	54.7
		3	22.1	29.7	48.2
		4	28.5	11.5	60.0
		5	02.1	62.7	35.2
		6	75.9	08.2	15.9
		7	00.5	62.9	36.6
		8	00.5	63.9	35.6
		9	85.0	10.4	04.6
		10	79.6	14.7	05.7
		11	80.9	14.6	04.5
	8.6	1	13.5	01.6	84.9
		2	14.2	03.5	82.3
		3	07.2	00.0	92.8
		4	80.5	16.4	03.1

Table 8.2 (continued)

		5	23.3	05.0	71.7
900 °C/ 12 days/ furnace-cooled	8.7	1	00.4	65.0	34.6
		2	18.0	12.2	69.8
		3	18.5	11.5	70.0
		4	18.2	11.8	70.0
		5	80.5	16.9	02.6
		6	79.1	17.1	03.8
	8.8	1	04.7	00.0	95.3
		2	06.4	00.0	93.6
		3	06.1	00.0	93.9
		4	79.4	16.1	04.5
1000 °C/ 10 days/ furnace-cooled	8.9	1	07.8	00.0	92.2
		2	11.0	00.0	89.0
		3	04.8	00.0	95.2
		4	75.6	11.3	13.1
		5	02.8	00.0	97.2
		6	59.2	17.0	23.8

The Mo₂Zr phase present in form of a continuous layer, running parallel to the interface, and also in a ‘massive’ morphology could be easily identified in the interdiffusion zone of all the diffusion annealed samples through EDS analysis. The average composition of the matrix phase present adjacent to the Mo₂Zr phase was estimated to be U–11Mo–9Zr (at.%) from the EDS analysis of all the annealed samples. The thin needle-like morphology of the Zr-rich precipitates in the 800 °C annealed samples made it difficult to ascertain their composition precisely due to a higher X-ray sampling volume as compared to the thickness of individual precipitates. The fact that the precipitates are rich in Zr, however, could firmly be established by carrying out X-ray line profile and area mapping analyses using SEM-EDS, as shown in Figure 8.10. In fact, the presence of the Mo₂Zr phase in ‘massive’ morphological form could also be evidently brought out in these analyses as shown in Figure 8.10. The EDS scan obtained across the line marked in

Figure 8.10a is shown in Figure 8.10b. The X-ray profile for the initial portion of the line falling within the 'massive' Mo₂Zr phase showed higher Mo-count as compared to Zr, with negligible U-count. This signified formation of the Mo₂Zr phase. A steep rise in the U-count accompanied by a sharp drop in both the Mo- and Zr- counts could be noticed in the profile as the line entered the matrix part, after which the counts of U, Mo and Zr remained steady. At the end of the profile where the line encountered an elongated Zr-rich precipitate, a peak was observed in the Zr-count together with a dip in both the U- and Mo- counts. X-ray maps of the entire microstructure, depicted in Figure 8.10a, are shown in Figures 8.10c-e. The presence or absence of any element within any microstructural feature can be established if the feature concerned exhibits a bright or a dark contrast, respectively, in the X-ray map corresponding to that element. Amongst the microstructural constituents of Figure 8.10a, the presence of U could be detected within the matrix phase and to some extent within the elongated Zr-rich precipitates but not within the 'massive' Mo₂Zr phase. This is on account of the exhibition of a complete dark contrast by the Mo₂Zr phase in the UM_{α1} X-ray map as opposed to less dark contrast and bright contrast by the Zr-rich precipitates and the matrix phase, respectively. The Mo₂Zr phase showed bright contrast in both MoL_{α1} and ZrL_{α1} X-ray maps, whereas, the Zr-rich precipitates showed bright contrast only in the ZrL_{α1} X-ray map. The fact that the matrix phase has both Mo and Zr within it to some extent is highlighted by the display of a very faint mottled-type of contrast by the matrix in both the MoL_{α1} and ZrL_{α1} X-ray maps.

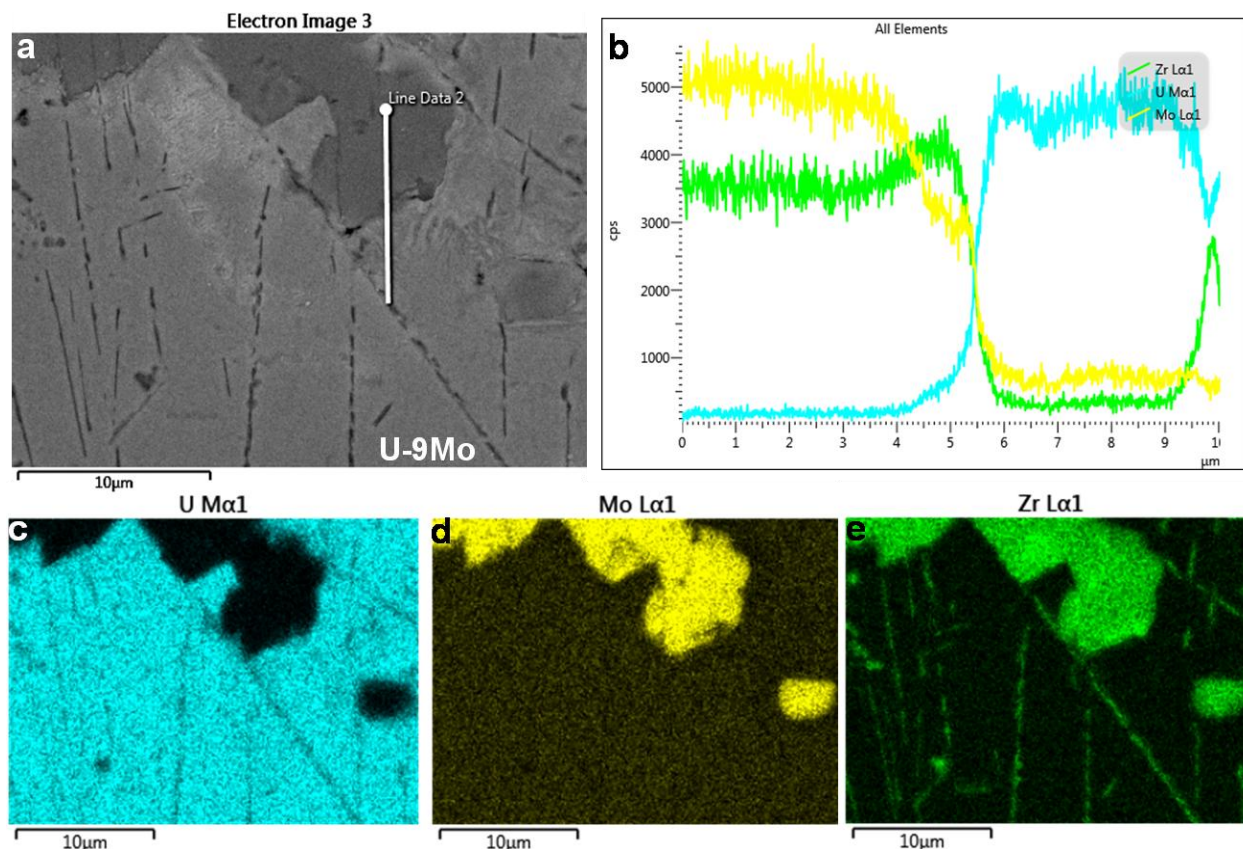


Figure 8.10 (a) BSE-SEM image of the interdiffusion zone close to the U-9Mo side of U-9Mo/Zr-1Nb bonded sample annealed at 800 °C for 10 days followed by furnace cooling. Mo₂Zr phase of ‘massive’ morphological feature and Zr-rich precipitates could be seen in this image, (b) qualitative U, Mo and Zr elemental concentration profiles across the line marked in (a), (c-e) elemental maps of (a) obtained with UMa₁, MoLa₁ and ZrLa₁ characteristic X-ray signals, respectively.

The presence of Mo₂Zr phase, in both morphological forms, and the formation of Zr-rich precipitates in the interdiffusion zone of all the annealed samples were reaffirmed through site-specific WDS compositional analysis in EPMA. The concentration-distance profiles of U, Mo and Zr across the interface of all the annealed samples were evaluated using EPMA, and are shown in Figures 8.11 to 8.15. An estimation of the width of the interdiffusion zone in all the cases was made from the respective elemental profiles of U and Zr and is presented in Table 8.3. The diffusional distance across the interface corresponding to $C_U \approx 0$ at.% on the Zr-side and $C_{Zr} \approx 0$ at.% on the U-side of the couple was approximated to be the width of the interdiffusion zone. The concentration-distance profile of Mo was not accounted for in the width calculation, as

diffusion of Mo in the Zr-side was found to cease much ahead of U. Along the interdiffusion zone where peaks in the Mo- and Zr- concentration profiles and troughs in the U-profile were found to superimpose illustrated the formation of the Mo_2Zr phase. On the other hand, peaks in the Zr-profile alone with simultaneous dips in the U-profile near the U–Mo side of the interdiffusion zone signified the formation of the Zr-rich precipitate phase.

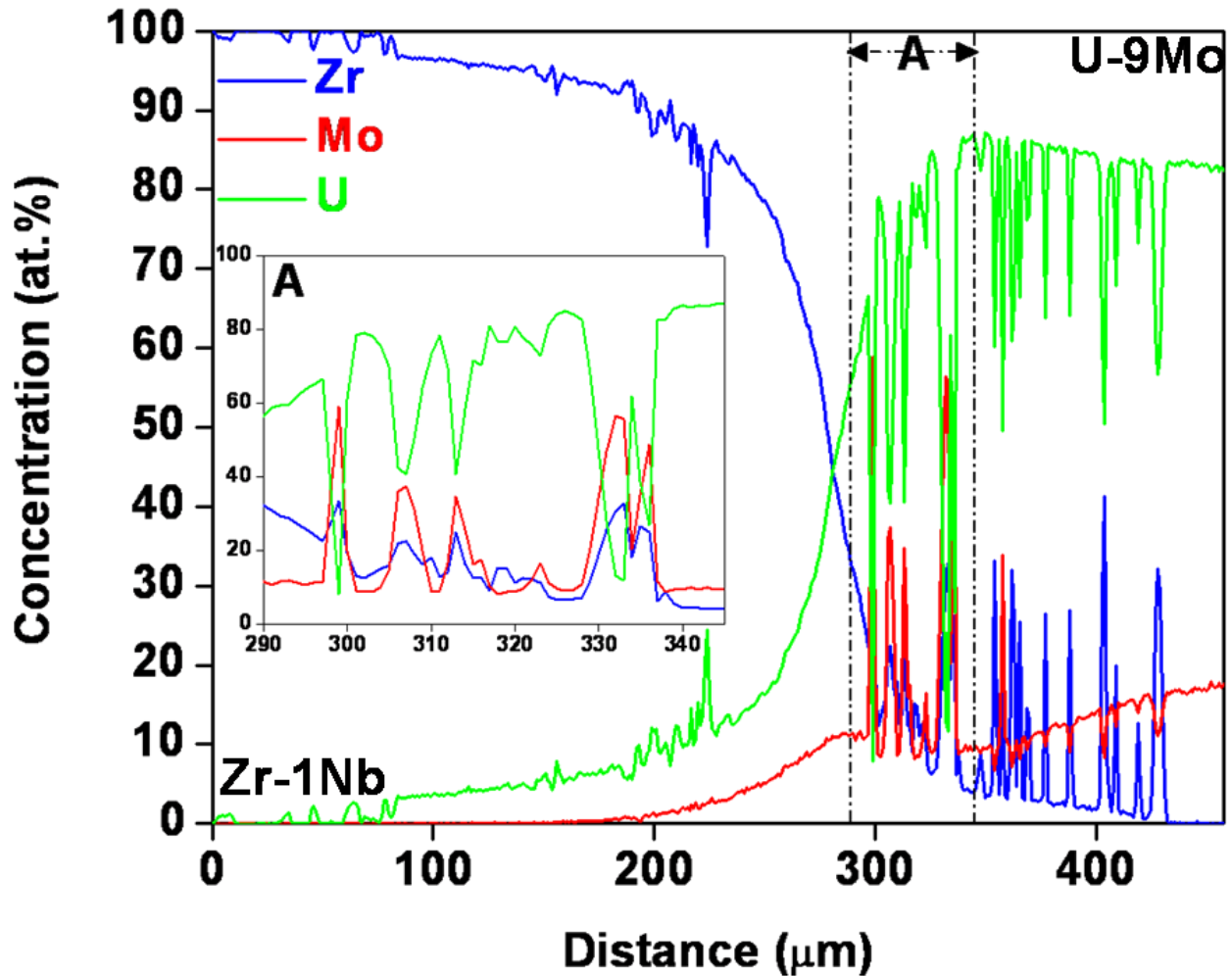


Figure 8.11 Concentration-distance profiles of U, Mo and Zr across the interdiffusion zone of U–9Mo/Zr–1Nb bonded sample annealed at 800 °C for 10 days followed by water quenching, as determined by EPMA. The inset shows an enlarged view of the profiles corresponding to the zone marked as A.

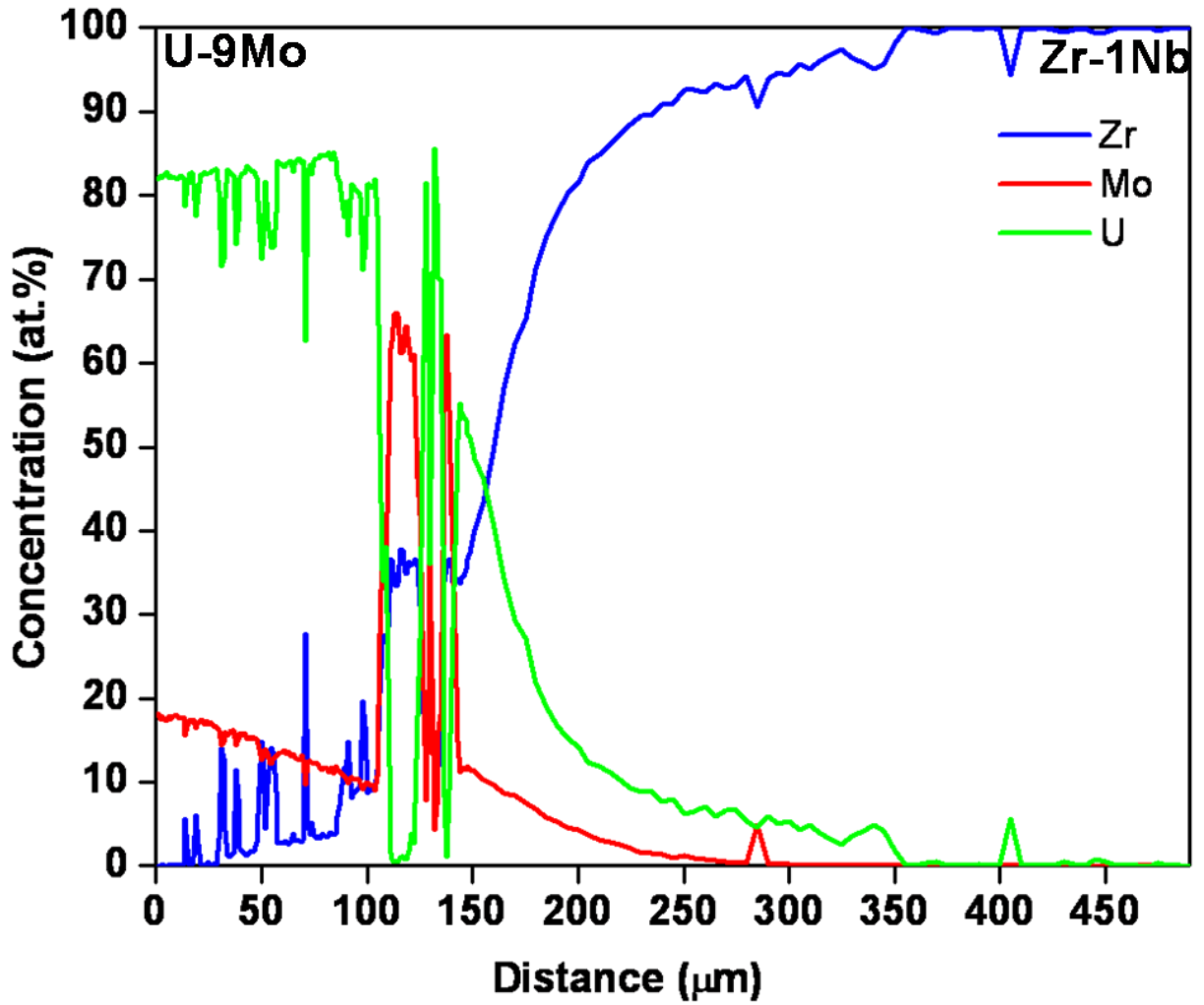


Figure 8.12 Concentration-distance profiles of U, Mo and Zr across the interdiffusion zone of U-9Mo/Zr-1Nb bonded sample annealed at 800 °C for 10 days followed by furnace cooling, as determined by EPMA.

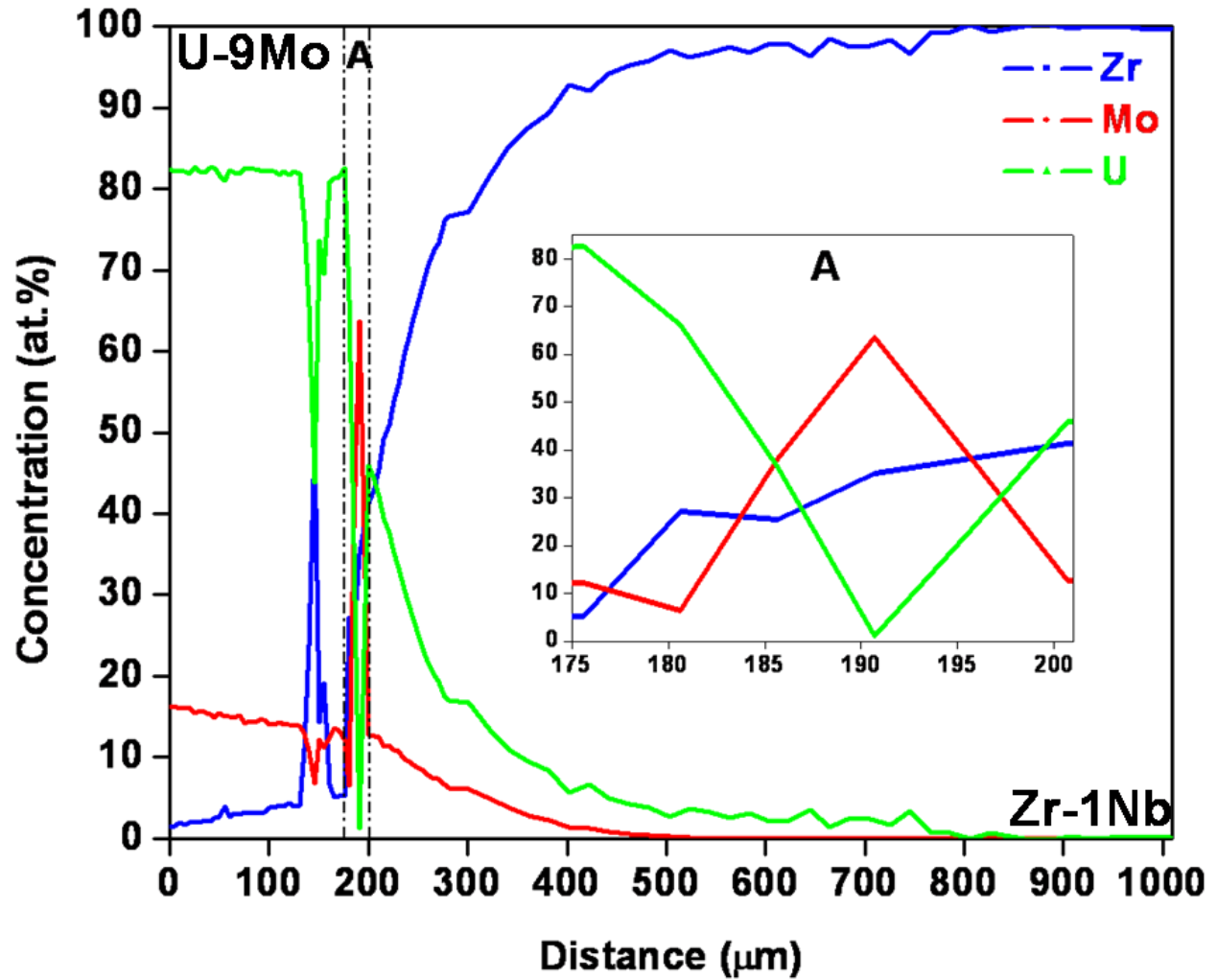


Figure 8.13 Concentration-distance profiles of U, Mo and Zr across the interdiffusion zone of U-9Mo/Zr-1Nb bonded sample annealed at 900 °C for 10 days followed by furnace cooling, as determined by EPMA. The inset shows an enlarged view of the profiles corresponding to the zone marked as A.

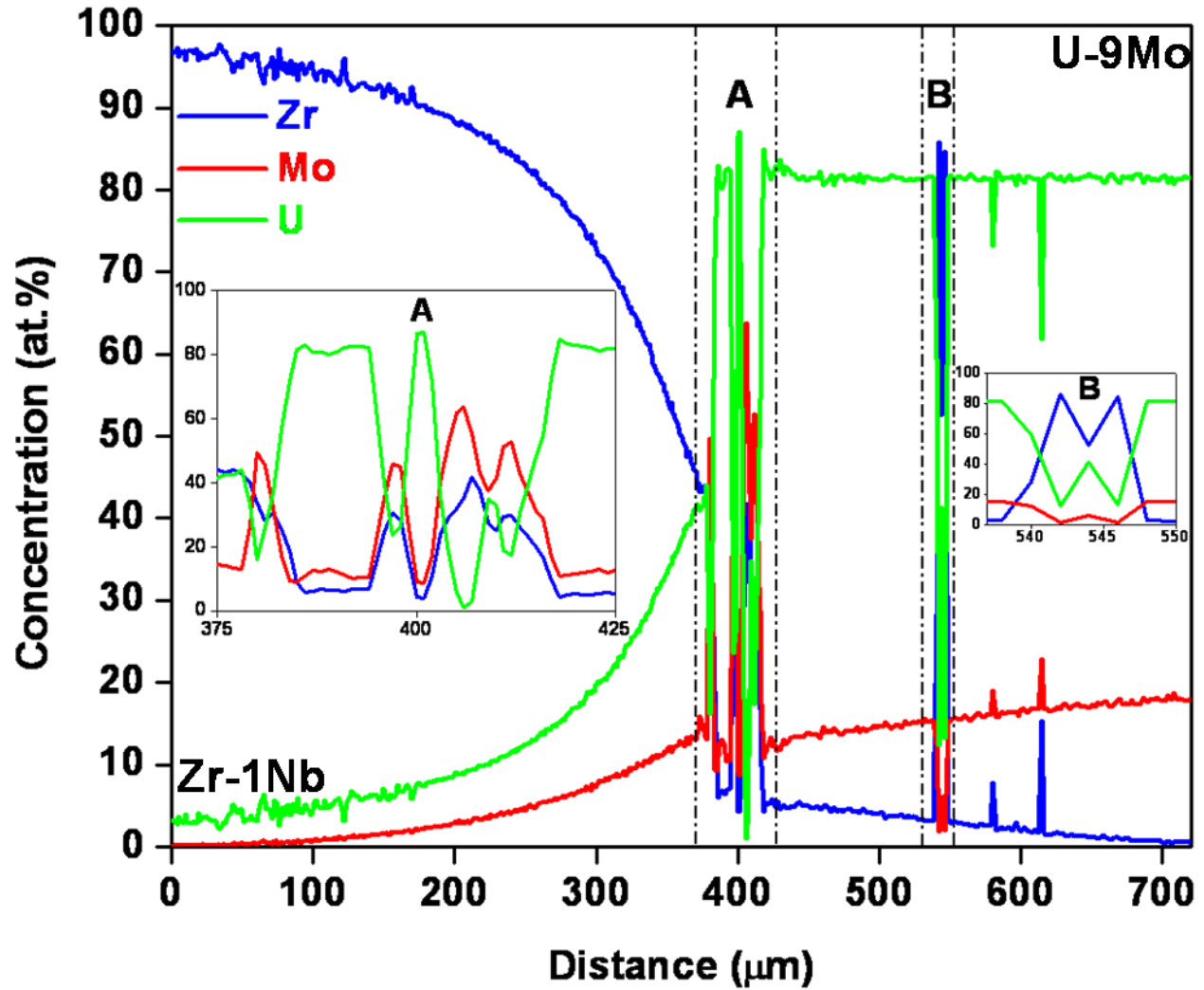


Figure 8.14 Concentration-distance profiles of U, Mo and Zr across the interdiffusion zone of U-9Mo/Zr-1Nb bonded sample annealed at 900 °C for 12 days followed by furnace cooling, as determined by EPMA. The insets show an enlarged view of the profiles corresponding to the zones marked as A and B.

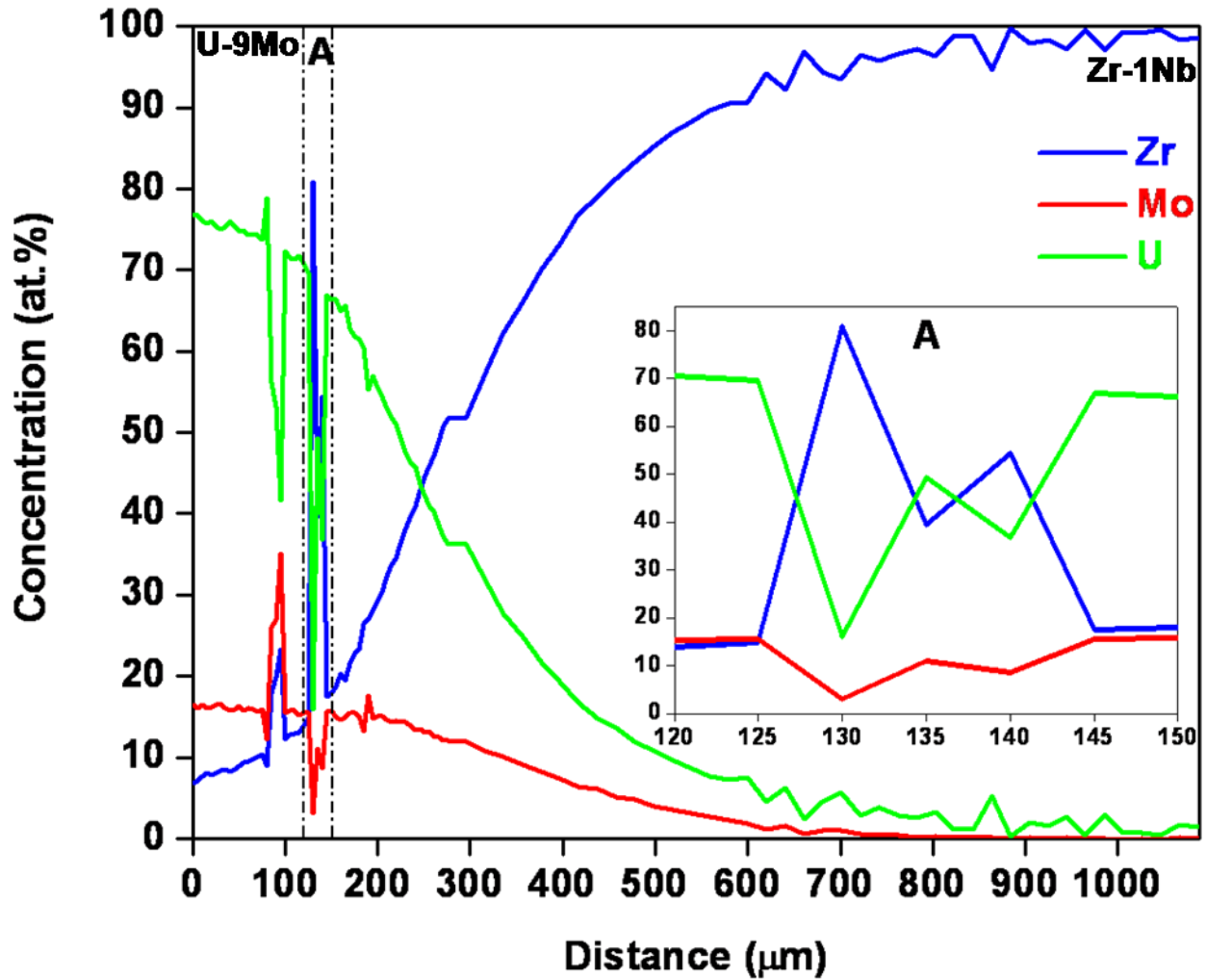


Figure 8.15 Concentration-distance profiles of U, Mo and Zr across the interdiffusion zone of U-9Mo/Zr-1Nb bonded sample annealed at 1000 °C for 10 days followed by furnace cooling, as determined by EPMA. The inset shows an enlarged view of the profiles corresponding to the zone marked as A.

Table 8.3 Interdiffusion zone width of annealed U–9Mo/Zr–1Nb bonded samples, as measured from the concentration-distance profiles determined by EPMA. For the sake of comparison, the width of the interdiffusion zone in the as-bonded sample is also included.

<i>Annealing condition</i>	<i>Measured interdiffusion zone width (μm)</i>
As-bonded condition (without annealing)	27
800 °C for 10 days followed by water quenching	402
800 °C for 10 days followed by furnace cooling	398
900 °C for 10 days followed by furnace cooling	913
900 °C for 12 days followed by furnace cooling	962
1000 °C for 10 days followed by furnace cooling	1421

The lamellar microstructural feature adjoining the Mo₂Zr phase, termed as ‘halo’, could be resolved clearly in the BSE mode of SEM, as shown in Figure 8.4. An attempt was made in SEM to ascertain the phase constitution of lamellae and interlamellar regions through composition analysis. SEM-EDS analyses of the lamellar ‘halo’ regions were carried out in point mode, line-scan mode and X-ray area mapping mode. In all these modes of analyses, the lamellae, exhibiting dark contrast in the SEM images, were found to show less Mo in comparison of the bright interlamellar regions. The average variation in Mo-content between the lamellae and the interlamellar regions was estimated to be only 3 at.% in the point analysis mode, which could be an effect of the larger electron interaction volume in comparison of the width of lamellae and interlamellar regions. This small variation, however, could be picked up in both EDS line scan and X-ray area mapping analyses as shown in Figure 8.16. The MoL_{α1} X-ray map in Figure 8.16b corresponding to the lamellar region in Figure 8.16a clearly shows higher Mo-content of the interlamellar regions discernible by the brighter contrast in comparison of the darker contrast exhibited by the lamellae. Similarly, the qualitative EDS line scan result given in Figure 8.16e shows the variation in Mo-content across the the white line in Figure 8.16c traversing through lamellae and interlamellar regions. Figure 8.16d shows a magnified view of the same line and the features across it for a better correlation of the line scan results with the microstructural features. It may be seen from Figure 8.16d and e that the dark lamellae are

associated with dips in Mo-count in contrast to appearances of Mo-peaks in the interlamellar regions. The Zr-content across the lamellae and the interlamellar regions was found to follow the variation in Mo-content, as shown in Figure 8.16e. The variation in U-content is not shown intentionally in Figure 8.16e alongside Mo and Zr, since the small variations in Mo- and Zr-contents would not become prominent in its presence with U being the major constituent.

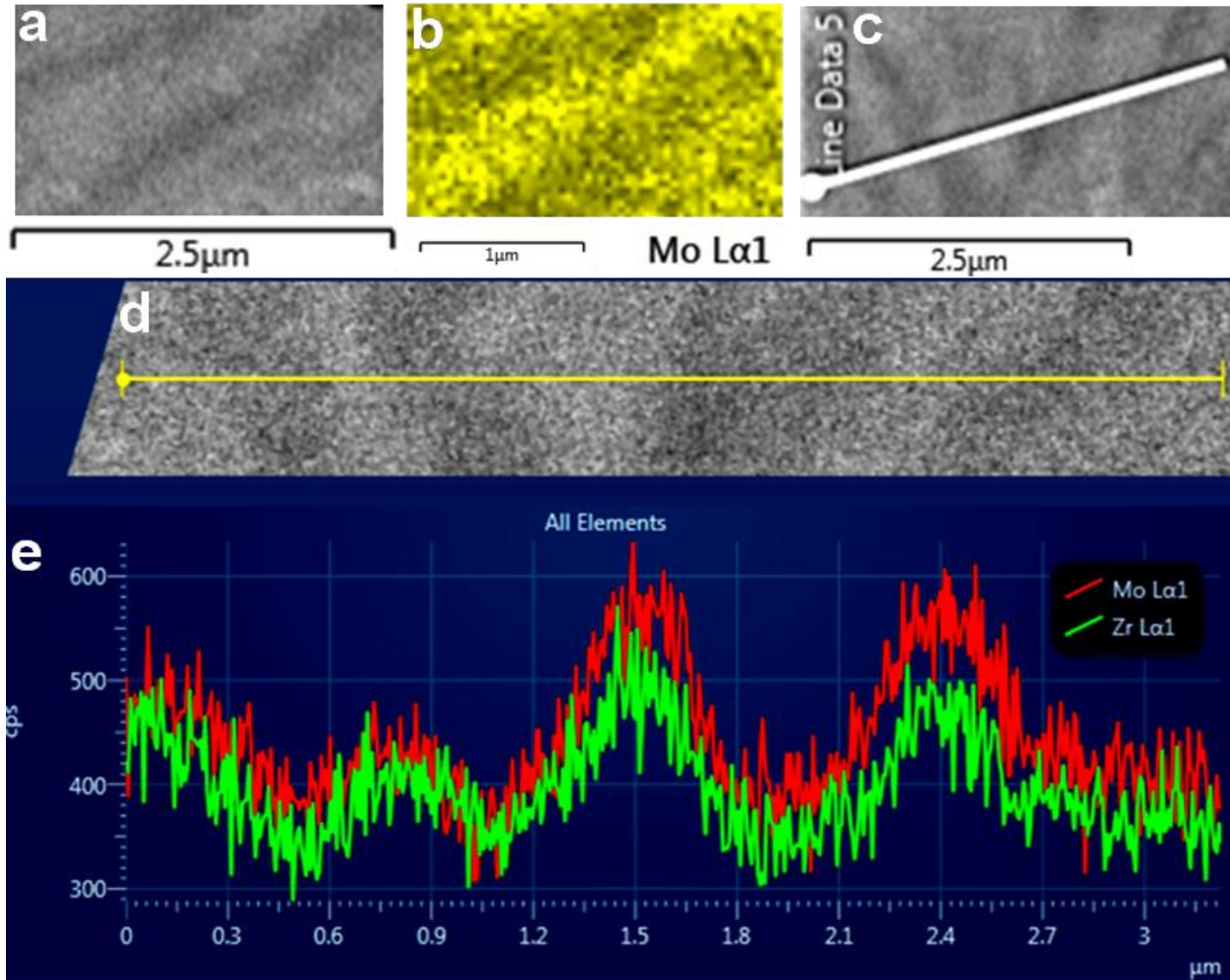


Figure 8.16 (a,c) Typical SEM images of lamellar ‘halo’ regions noticed adjacent to the ‘massive’ Mo_2Zr phase in the interdiffusion zone of the annealed U-9Mo/Zr-1Nb bonded samples, (b) X-ray map of (a) using $\text{MoL}\alpha_1$ characteristic radiation, (d) magnified view of the white line, and its associated features, marked in (c), (e) X-ray profiles of Mo and Zr across the line marked in (c).

The polarized light optical microscopy images given in Figures 8.17a and b represent the microstructural feature observed in all the annealed samples near the Zr-1Nb side of the

interdiffusion zone, except for the sample water-quenched after annealing at 800 °C. The “basket weave” arrangement of differently aligned parallelly stacked acicular lath groupings could easily be noticed in the micrographs.

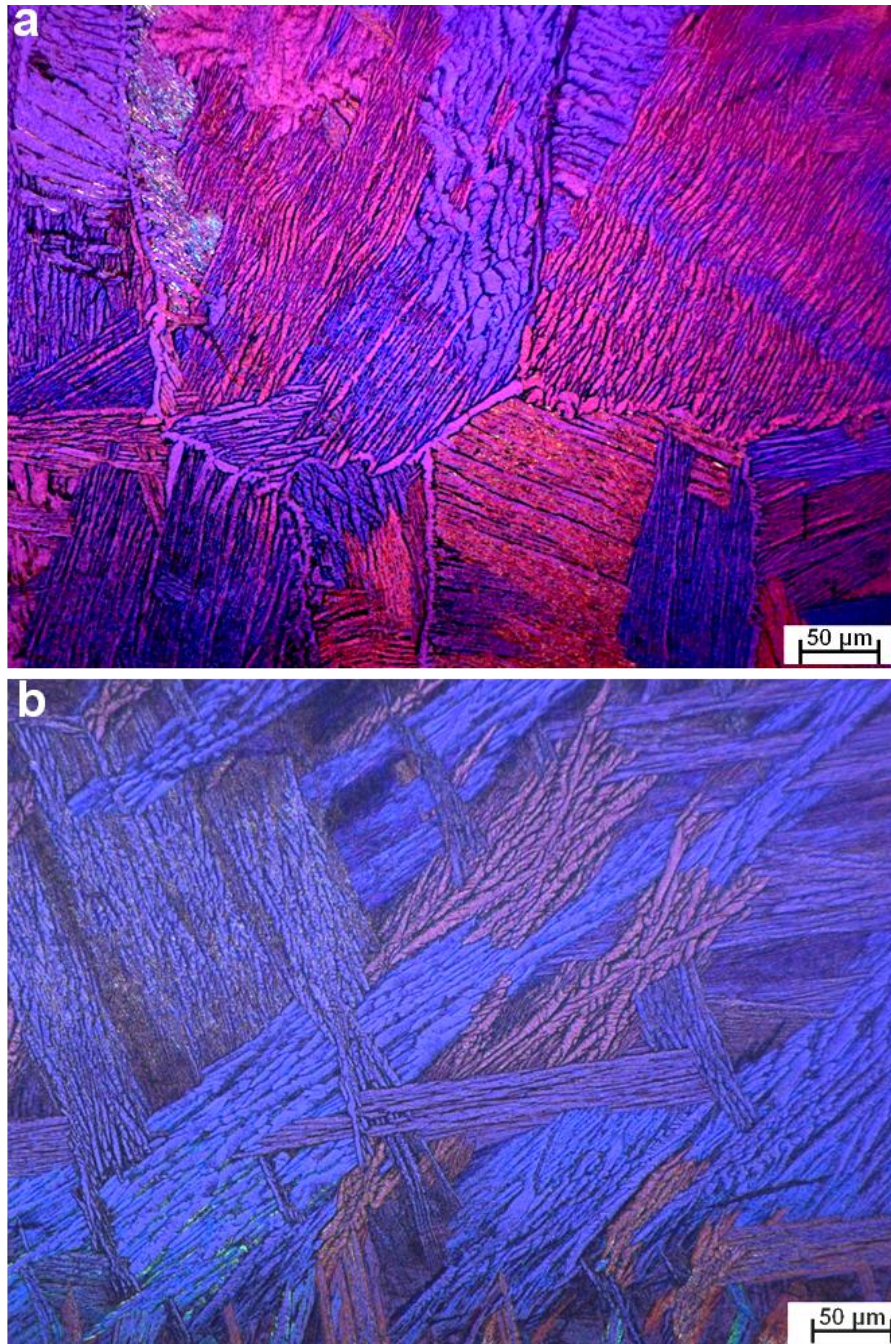


Figure 8.17 (a,b) Typical polarized light optical microscopy images depicting the “basket weave” microstructure noticed near the Zr–INb side of the interdiffusion zone of the annealed U–9Mo/Zr–1Nb bonded samples.

A detailed analysis of the “basket weave” microstructure has been carried out in TEM. The bright-field TEM micrographs of Figure 8.18a and b present an overview of the typical lath grouping mentioned above. The thick interlath boundaries pointed towards the presence of a second phase within it. The crystallographic identities of laths and interlath regions were ascertained through electron diffraction analyses, as shown in Figure 8.19a and b, respectively. The laths were found to comprise of hcp α -Zr phase and the interlath regions of bcc β -Zr phase.

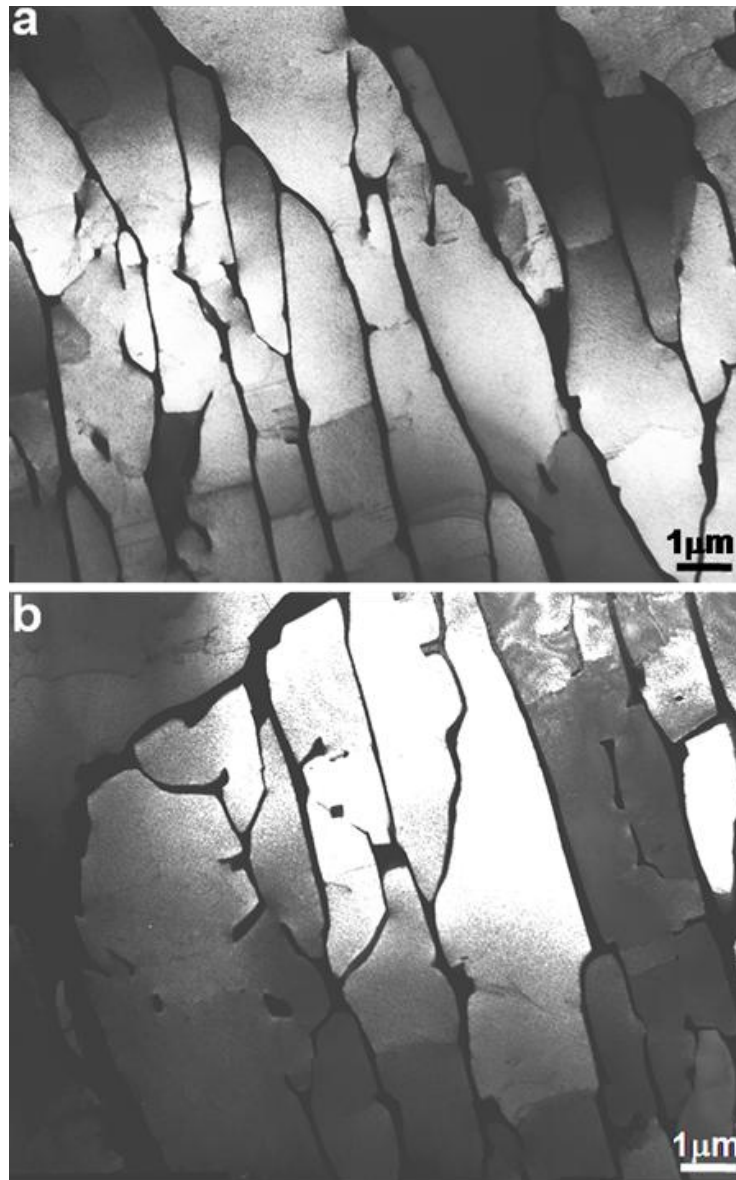


Figure 8.18 (a,b) Typical bright-field TEM micrographs showing the arrangement of laths in the “basket weave” microstructure, noticed near the Zr–INb side of the interdiffusion zone of the annealed U–9Mo/Zr–INb bonded samples.

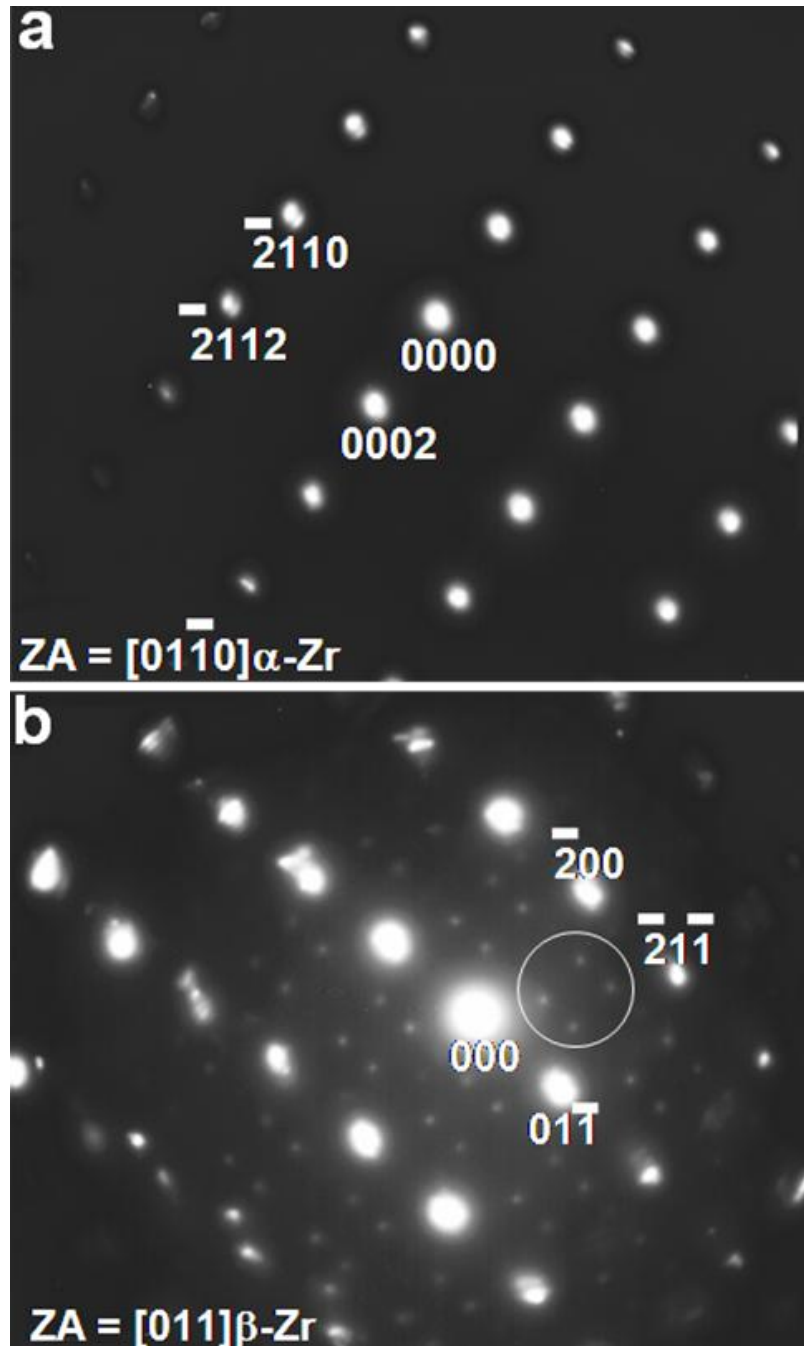


Figure 8.19 Typical SAED patterns corresponding to (a) α -Zr phase obtained from the intralath regions and (b) β -Zr phase obtained from the interlath regions of the “basket weave” microstructure noticed near the Zr–INb side of the interdiffusion zone of the annealed U–9Mo/Zr–INb bonded samples. The circle in (b) shows the omega-type reflections, similar to Figure 2.10b, corresponding to the second phase present within the β -phase interlath boundaries.

A careful examination of all the SAED patterns corresponding to the different crystallographic zone axes of the β -phase revealed the coexistence of reflections pertaining to a second phase within them, as can be seen encircled in Figure 8.19b. Interestingly, the reflections due to this second phase were found to superimpose the β -reflections in patterns commonly observed in the bcc β to hexagonal omega (ω) phase transformation [74]. The microdiffraction pattern presented in Figure 8.20 clearly shows the presence of omega-type reflections, marked by black dots, amidst the β -phase reflections.

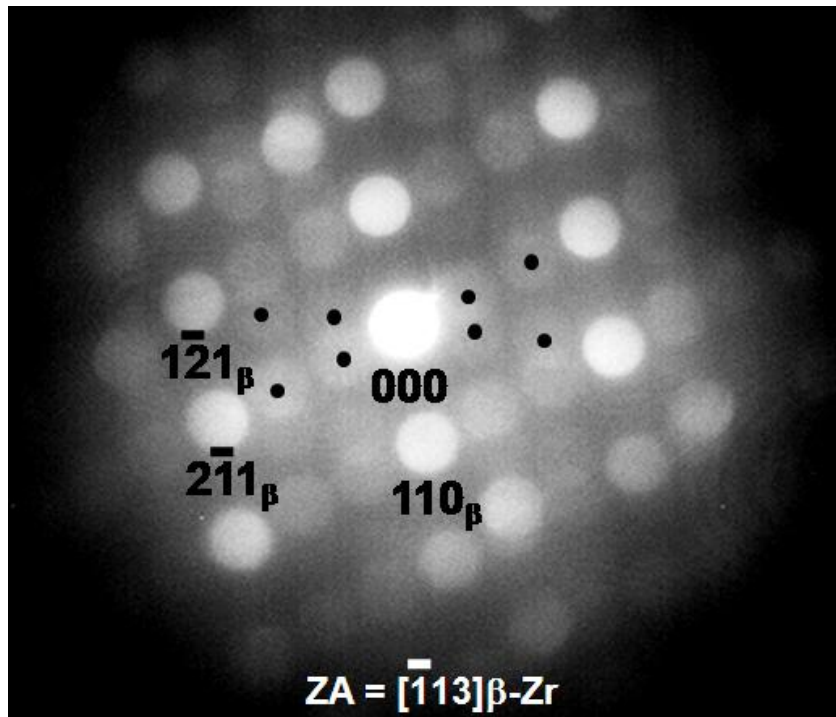


Figure 8.20 Microdiffraction pattern obtained from the β -phase present in the interlath regions of the “basket weave” microstructure noticed near the Zr–INb side of the interdiffusion zone of the annealed U–9Mo/Zr–INb bonded samples. The black dots represent the omega-type reflections, similar to Figure 2.10f, corresponding to the second phase present within the β -phase interlath boundaries.

Composition analysis of intralath and interlath regions were carried out using EDS in TEM, and the results are presented in Table 8.4. Nb and U enrichment of the β -phase, present at the interlath boundaries, could be seen in contrast to a negligible presence of these elements within the α -Zr laths.

Table 8.4 Chemical compositions of intralath and interlath regions of “basket weave” microstructure noticed near the Zr–1Nb side of the interdiffusion zone of the annealed U–9Mo/Zr–1Nb bonded samples, determined using EDS in TEM.

Region	Zr (at.%)	Nb (at.%)	U (at.%)
Intralath	99.5	00.0	00.5
	99.1	00.5	00.4
Interlath	76.5	09.5	14.0
	74.7	11.2	14.1
	75.6	11.0	13.4
	77.5	09.2	13.3

8.3 Discussion

The metallurgical interaction occurring between U–9Mo fuel alloy and Zr–1Nb cladding alloy, both during the bonding operation at 800 °C and subsequent cooling of the diffusion couple, resulted in the formation of a layered interdiffusion zone, as detailed in Chapter 7. On comparing the microstructural features of the interdiffusion zone of the as-bonded sample to those of the annealed samples, the following few observations clearly emerged out:

(i) An increase in the volume fraction of the Mo₂Zr phase in the annealed samples compared to the as-bonded sample, as could be seen from its existence both in form of a continuous layer and a ‘massive’ morphological feature in the former over predominantly dispersoids in the latter. The only exception to this was the 1000 °C annealed sample where a fragmented network of the Mo₂Zr phase was mostly noticed at the interface without much of the ‘massive’ type.

(ii) The presence of a lamellar microstructure, termed as ‘halo’, immediately adjacent to the Mo₂Zr phase in the annealed samples in comparison of the as-bonded sample, except for the couple water-quenched after annealing at 800 °C.

(iii) An evolution of the two-phase Widmanstätten ($\alpha + \beta$)-Zr layer, formed near the Zr–1Nb side of the interdiffusion zone in the as-bonded couple, into a much wider “basket weave” microstructural zone with α -Zr laths and β -Zr(Nb,U) interlath regions in the annealed samples. A β - to ω - transformation was also observed within the interlath regions. An exception

to this was the 800 °C annealed and water-quenched sample where the “basket weave” structure was found to be replaced by a martensitic microstructure.

(iv) The presence of a considerable fraction of Zr-rich precipitates in the U–9Mo side of the interdiffusion zone of the annealed samples, which were barely present in the as-bonded sample.

(v) A considerable increase in the overall width of the interdiffusion zone of the annealed samples (Table 8.3).

Each of the above observations has been rationalized in the following sections. It is to be noted that interdiffusion studies between U–10 wt.% Mo alloy and pure-Zr at 800 °C, 900 °C and 1000 °C have been carried out by Huang et al. [4], wherein the couples were water-quenched from the annealing temperature against that of furnace cooling in the present case. The formation of Mo₂Zr phase and Zr-rich precipitate phase were also observed by them in the interdiffusion zone. The Zr-rich precipitates were, however, found to be present throughout the interdiffusion zone in their study in contrast to their presence being mostly confined near the U-rich side of the couple in the present work. Another difference, which could be noticed with their work, is the presence of a β-Zr layer next to pure-Zr in the couple annealed at 800 °C in their work in contrast to the presence of a α-Zr + β-Zr(Nb,U) two-phase “basket weave” microstructure next to the Zr–1Nb base alloy at all the annealing temperatures in the present work.

8.3.1 Morphological evolution of the Mo₂Zr phase

The first observation with regard to an in-general increase in the volume fraction of the Mo₂Zr phase in the annealed samples can be explained on the basis of its continued formation on account of interdiffusional interaction between Mo and Zr atoms during the annealing heat treatments, as Mo₂Zr can form or remain stable till a temperature of 1880 °C [24]. The absence of Mo₂Zr dispersoids in the annealed samples could be a result of the growth of the pre-existing dispersoids of the as-bonded sample followed by their coarsening during the annealing heat treatments, which might have resulted in their evolution in a ‘massive’ morphological form. The formation of the Mo₂Zr phase in the as-bonded as well as the annealed samples has not occurred within the U–9Mo matrix of the couple having the highest source of Mo, but away from it within the interdiffusion zone. This signified not only the requirement of diffusion of Mo atoms besides that of Zr in the formation of the Mo₂Zr phase but also that of the interdiffusional interaction

between these atoms behind its formation. In respect of the relatively lower volume fraction of the Mo_2Zr phase in the 1000 °C annealed sample as compared to 800 °C or 900 °C, it may be conjectured that the relatively higher diffusivities of Mo and Zr atoms at 1000 °C on account of higher temperature might not have offered sufficient interaction time to these atoms in their diffusion path. The process of coarsening of the Mo_2Zr dispersoids of the as-bonded sample during annealing involves diffusion controlled growth of the larger dispersoids at the expense of the smaller ones. Owing to the high diffusivity values at 1000 °C, the Mo and Zr atoms from the smaller dispersoids in the course of their dissolution are swept away down the respective concentration gradients before getting associated with a larger dispersoid. This explains the absence of ‘massive’ type of Mo_2Zr in the interdiffusion zone of the 1000 °C annealed sample. The increased width of the interdiffusion zone at 1000 °C compared to 800 °C and 900 °C for the same annealing duration of 10 days bears testimony to the increased diffusivities of Mo, Zr and U atoms at 1000 °C. The SEM observation pertaining to the inadequate presence of the Mo_2Zr phase in the 1000 °C annealed sample gets corroborated with the absence of prominent peaks in the concentration–distance profiles of Mo and Zr, as shown in Figure 8.15. The matrix adjoining the Mo_2Zr phase with an average composition of U–11Mo–9Zr (at.%) existed as a single bcc solid solution phase at the annealing temperatures, as may be seen from the respective U–Mo–Zr isotherms given in references [4,14]. The experimental observation of reduced Mo_2Zr volume fraction at 1000 °C is consistent with the reduced ($\text{Mo}_2\text{Zr} + \text{bcc U–Mo–Zr}$) two-phase field in the U–Mo–Zr isotherm at 1000 °C in comparison of 800 °C and 900 °C [4,14].

8.3.2 Genesis of the lamellar ‘halo’ structure

The lamellar structure adjacent to the Mo_2Zr phase is a result of the decomposition of the $\gamma\text{-U}(\text{Mo,Zr})$ matrix initially present in these regions at the annealing temperatures with an average composition of U–11Mo–9Zr (at.%). As mentioned previously, a minimum 17.7 at.% of Mo is required to retain the high temperature $\gamma\text{-U}(\text{Mo})$ phase at room temperature during slow cooling [115]. The formation of the Mo_2Zr phase led to a lowering of the Mo-content below this limit in the adjacent regions, as may be seen from the average composition, and triggered the decomposition of the $\gamma\text{-U}(\text{Mo,Zr})$ phase during the furnace cooling of the samples after the annealing heat treatments. The presence of 9 at.% of Zr, also a $\gamma\text{-U}$ stabilizer, in the adjoining matrix was not found effective in compensating for the Mo-depletion on account of being not as

strong a γ -U stabilizer as that of Mo [261]. The couple water-quenched from 800 °C in the present work, and also those in the work of Huang et al. [4], did not exhibit the lamellar ‘halo’ structure. This is due to the stabilization of the γ -U(Mo,Zr) matrix adjoining the Mo_2Zr phase on account of fast cooling despite of having an almost similar (Mo + Zr)-content as those of the furnace cooled samples. The phase identities of lamellae and interlamellar regions could not be ascertained through composition analysis in SEM and EPMA owing to their fine structures. However, it could be firmly established that the interlamellar regions contain more Mo in comparison of the lamellae. If Mo–U phase diagram is considered (Figure AI.2), the decomposition of γ -U(Mo) matrix of Mo content < 17.7 at.% on continuous cooling will proceed by the formation of proeutectoid α -U phase in γ -U(Mo) matrix followed by an eutectoid decomposition of the remaining γ -U(Mo) phase to α -U and γ' (U_2Mo) phases on attaining the composition and temperature corresponding to those of the invariant eutectoid reaction. As mentioned earlier, the interdiffusion of Mo and U atoms in the U–Mo matrix becomes more and more sluggish as the Mo-content of the matrix increases [13,200,231,234], and thus a U–Mo matrix of eutectoid composition does not decomposes (refer to Chapter 5). Hence, it may be conjectured that the decomposition of γ -U(Mo) matrix of Mo content < 17.7 at.% into the α -U and γ' phases of equilibrium compositions and phase fractions would happen in the following manner without invoking the eutectoid reaction. The Mo atoms rejected on account of formation of the α -U phase would continuously enrich the remaining γ -U(Mo) phase with Mo, thereby transforming it to γ' -phase in-situ. The decomposition products, however, could still appear in a lamellar morphology even without the occurrence of the eutectoid reaction. This is due to the fact that the γ -U(Mo) phase can decompose by a cellular type of reaction generating lamellar decomposed microstructures, as discussed in Chapter 6. The α -U phase can precipitate out as lamellae within the γ -U(Mo) matrix, and the γ -U(Mo) interlamellar regions can eventually transform to γ' -phase. In the present context, it may thus be presumed that the γ -U(Mo,Zr) matrix present adjacent to the Mo_2Zr phase decomposed in a similar manner during the cooling of the samples. The lamellae in the ‘halo’ regions comprised of α -U and the interlamellar regions of γ -U(Mo,Zr) instead of γ' . This is because had the interlamellar regions been comprised of γ' -phase a much higher difference in the Mo-content of lamellae and interlamellar regions (much more

than the estimated 3 at.%) would have been observed. The absence of γ' -phase in the interlamellar regions can be explained on the basis of slow Mo-enrichment kinetics of the γ -U(Mo,Zr) phase considering the sluggish U–Mo interdiffusion.

8.3.3 Evolution of the “basket weave” microstructural zone

The appearance of “basket weave” microstructural zone comprising of α -Zr laths and β -Zr(Nb,U) interlath boundaries, near the Zr–1Nb side of the annealed couples, is due to the transformation of the Zr-rich β -Zr(Nb,U) phase, present at the annealing temperatures in this zone, during the cooling of the couples from the annealing temperatures. The formation of the Widmanstätten ($\alpha + \beta$)-Zr layer near the Zr–1Nb side of the interdiffusion zone of the as-bonded couple has already been highlighted in Chapter 7. The “basket weave” microstructural zone is an extension of this layer. The exhibition of different colour contrast by the differently aligned lath groupings, under polarized light, pointed towards their different crystallographic orientations (Figure 8.17). This can be explained by the emergence of the constituting laths of different groupings from the parent matrix following the different variants of the orientation relationship (OR) existing between the matrix-phase and the lath-phase. In general, a Burgers OR [57] is expected to be obeyed in the bcc $\beta_{Zr} \rightarrow$ hcp α_{Zr} transformation and, accordingly, the α -Zr laths would form following the six distinct variants of this OR from the high temperature β -Zr(Nb,U) phase. The increased diffusion length of U within the Zr–1Nb base material on annealing played an important role in the evolution of the “basket weave” microstructural zone in the 800 °C annealed and furnace-cooled sample. The presence of U, a β -stabilizer, resulted in the transformation of the Zr–1Nb alloy completely into the high temperature β -phase or rather the β -Zr(Nb,U) phase at 800 °C by lowering the ($\alpha + \beta$)/ β transus temperature. This was substantiated by the observation of a partially transformed microstructure, comprising of Widmanstätten α -Zr laths at the α -Zr grain boundaries, in the Zr–1Nb base material starting from the point where the diffusion of U atoms was found to cease i.e., from the end of the interdiffusion zone (Figure 8.21). This indicated cooling from the ($\alpha + \beta$)-Zr two phase region, wherein, the β -Zr phase formed at the α -Zr grain boundaries transformed to α -Zr Widmanstätten laths during cooling. The presence of a martensitic microstructure in the 800 °C annealed and water-quenched sample, instead of “basket weave”, was attributed to the transformation of the β -Zr(Nb,U) phase to

martensite on quenching. In the case of 900 °C and 1000 °C annealed samples the presence of U was not indispensable for the formation of the “basket weave” microstructural zone as these temperatures were above the $(\alpha + \beta)/\beta$ transus.

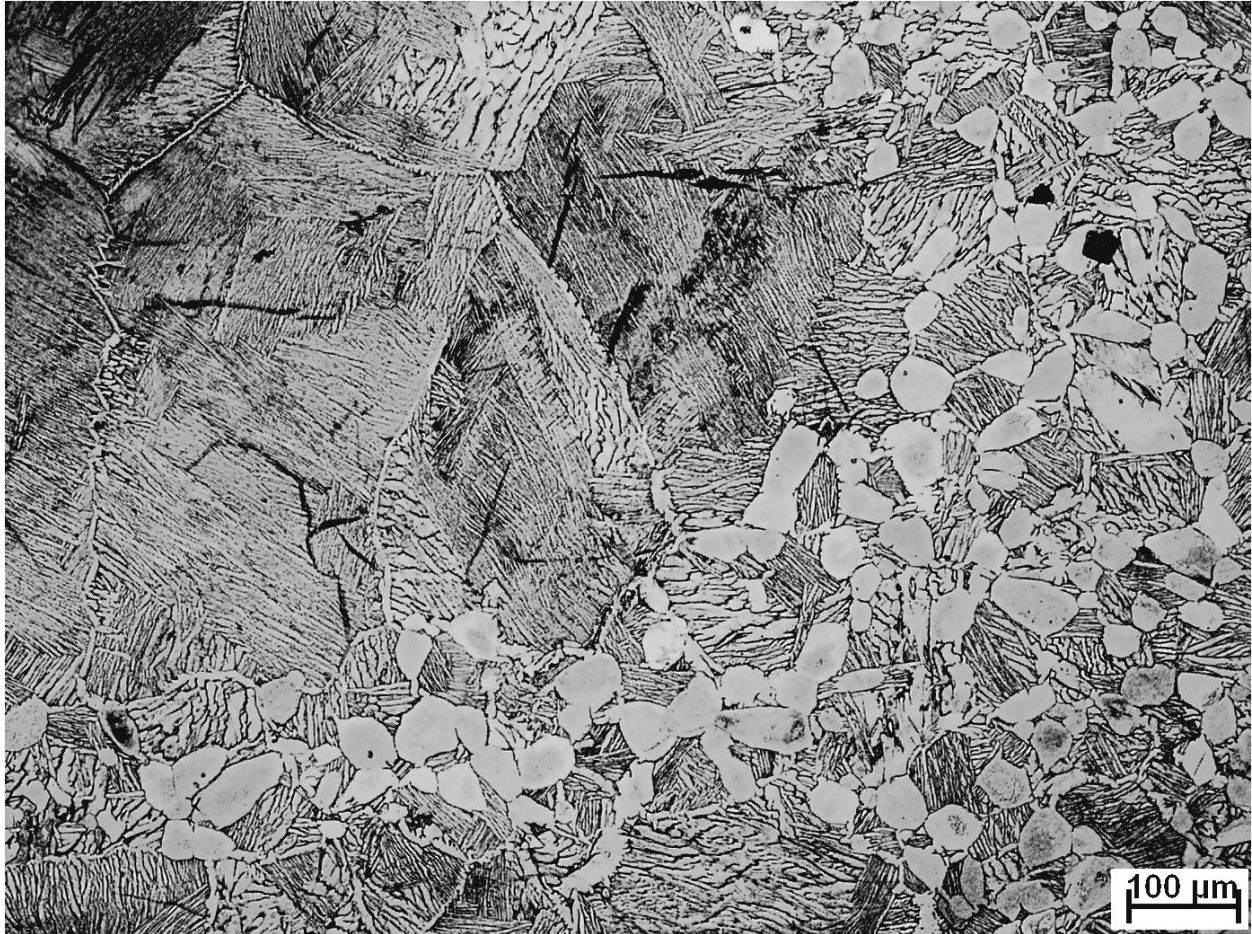


Figure 8.21 Optical microscopy image depicting the simultaneous formation of “basket weave” structure and Widmanstatten α -Zr laths at the α -Zr grain boundaries in the U-9Mo/Zr-1Nb bonded sample furnace-cooled after annealing at 800 °C.

The average composition of the interlath boundaries of the “basket weave” microstructural zone was estimated to be Zr-13.7U-10.2Nb (at.%). If concentrations of U and Nb, both of which are β -stabilizer, are added up and expressed in terms of U-equivalent then the average composition turns out to be Zr-23.9 at.% U-equivalent. On examining the binary U-Zr phase diagram (Figure A1.5) it may be seen that the high temperature bcc β -Zr(γ -U) phase with U in the range of 22 to 37 at.% transforms to the hexagonal δ -phase below 617 °C. This transformation has been found to proceed via the mechanism of omega phase transformation

[262-265]. Thus, a bcc β -phase present in the interlath boundaries with the abovementioned average composition is expected to transform to the δ -phase during the cooling of the couples from the annealing temperatures. This explains the superimposition of omega-type reflections of the δ -phase with the β -phase reflections in the electron diffraction patterns (Figures 8.19b and 8.20).

8.3.4 Precipitation of the Zr-rich phase in the U–9Mo side of the interdiffusion zone

On moving further deep into the U–9Mo side of the interdiffusion zone, Zr-rich precipitates with varying morphologies were observed in the U-rich matrix phase. Compositional analysis through SEM-EDS was performed on some morphologically larger precipitates so that the error arising out of the interaction volume effect could be minimized. These are reported in Table 8.5 along with some compositions of the matrix phase adjacent of these precipitates. As mentioned earlier, the thin needle-shaped morphology of the precipitates in the 800 °C annealed samples (both water-quenched and furnace-cooled ones) could not allow an accurate determination of their compositions, and hence are not included in Table 8.5.

Table 8.5 Chemical compositions of Zr-rich precipitates along with adjacent matrices noticed in the U-rich side of the interdiffusion zone of the annealed U–9Mo/Zr–1Nb bonded samples, determined using EDS in SEM.

<i>Sample</i>	<i>Phase</i>	<i>U (at. %)</i>	<i>Mo (at. %)</i>	<i>Zr (at. %)</i>
900 °C/ 10 days/ furnace-cooled	Matrix	80.7	16.2	03.1
	Matrix	80.5	16.4	03.1
	Matrix	79.2	15.4	05.4
	Precipitate	21.9	00.0	78.1
	Precipitate	18.7	00.0	81.3
	Precipitate	13.2	00.0	86.8
	Precipitate	10.4	00.0	89.6
	Precipitate	10.2	00.0	89.8
	Precipitate	07.5	00.0	92.5
	Precipitate	05.2	00.0	94.8
	Precipitate	05.0	00.0	95.0

Table 8.5 (continued)

900 °C/ 12 days/ furnace-cooled	Matrix	81.2	16.2	02.6
	Matrix	79.4	16.1	04.5
	Matrix	79.0	16.4	04.6
	Precipitate	06.4	00.0	93.6
	Precipitate	06.1	00.0	93.9
	Precipitate	04.7	00.0	95.3
1000 °C/ 10 days/ furnace-cooled	Matrix	79.7	09.5	10.8
	Matrix	78.4	8.3	13.3
	Matrix	75.6	11.3	13.1
	Matrix	68.2	17.2	14.6
	Matrix	59.6	15.4	25.0
	Matrix	59.2	17.0	23.8
	Matrix	55.1	16.5	28.4
	Precipitate	17.3	00.0	82.7
	Precipitate	13.9	00.0	86.1
	Precipitate	12.1	00.0	87.9
	Precipitate	10.3	00.0	89.7
	Precipitate	10.1	00.0	89.9
	Precipitate	10.0	00.0	90.0
	Precipitate	09.0	00.0	91.0
	Precipitate	07.3	00.0	92.7
	Precipitate	07.1	00.0	92.9
	Precipitate	05.9	00.0	94.1
	Precipitate	05.8	00.0	94.2
Precipitate	05.6	00.0	94.4	
Precipitate	04.2	00.0	95.8	

The EDS analyses showed a Zr-content of 78 at.% to 96 at.% within the precipitates. This scatter could be an effect of the size of the interaction volume, in comparison of the size of the

precipitates, on the analysis. The Mo-content of the precipitates was found to be negligible. The crystallographic phase of these precipitates at room temperature is expected to be hcp α -Zr(U) in consideration of their very high Zr-content. It could be noticed from Table 8.5 that in the sample annealed at 1000 °C, the matrices adjoining the Zr-rich precipitates have relatively higher Zr-content in comparison of the 900 °C annealed ones. This could be an effect of the increased diffusion of Zr on to the U-rich side of the couple owing to the higher diffusivity at 1000 °C. The matrix and the precipitate compositions (at.%) on averaging turned out to be U-16Mo-4Zr and Zr-10U, respectively, in the case of the 900 °C annealed samples. The same in the case of the 1000 °C annealed sample were U-14Mo-18Zr and Zr-9U, respectively. The average matrix composition of the 900 °C and the 1000 °C annealed samples once plotted on the respective ternary U-Mo-Zr isothermal section [4,14] showed the existence of the matrix phase in the bcc crystallographic form at both the temperatures.

In similar lines to the nucleation of a second phase in a parent matrix, the following two-step mechanism can be put forward to explain the formation of the Zr-rich precipitates keeping in mind the above-mentioned facts:

(i) A continuing segregation of Zr atoms within the bcc U-Mo-Zr matrix at the annealing temperatures thereby leading to the generation of Zr-rich clusters inheriting the same bcc crystallographic form of the matrix phase.

(ii) A changeover of bcc crystal structure of these clusters to hcp, provided (a) the Zr-content of the clusters lie within the compositional stability range of the hcp α -Zr(U) phase and (b) the annealing temperature falls within the thermal stability domain of the α -Zr(U) phase. It is this step which brings in the transformation of the clusters into the precipitates.

In justification of the first step of the above mechanism, the following reasoning can be offered based on the observed attributes of the precipitation of the α -Zr(U) phase. Firstly, the presence of precipitates in the sample water quenched from 800 °C bears testimony to the fact that cluster formation does take place during the annealing operation. This is because the fast cooling during water quenching would not lead to their formation in the course of the cooling process owing to the gradual nature of the clustering event. At the same time, almost similar number density of precipitates in samples water-quenched and furnace-cooled from 800 °C ruled out the possibility of cluster formation during the slow process of furnace cooling. A further experimental evidence of

cluster formation at the time of annealing comes from the observation of α -Zr(U) precipitates by Huang et al. in U–10 wt.% Mo vs. pure-Zr diffusion couples quenched after annealing at 900 °C and 1000 °C [4].

Thus, it may be argued that formation of Zr-rich clusters occurred during the annealing operation in all the annealed samples. However, in contrast to their transformation into the α -Zr(U) precipitates during the annealing operation at 800 °C, their transformation in the samples annealed at 900 °C and 1000 °C occurred once the temperature of these samples in the cooling process became lower than 862 °C corresponding to the bcc $\beta \rightarrow$ hcp α transition in unalloyed-Zr [24].

Thermodynamically, the clustering process taking place within the U–Mo–Zr matrix at all the annealing temperatures could be a result of the phase separation instability or the cluster formation tendency of the ternary U–Mo–Zr bcc phase. In this regard, it is to be noted that both the U–Zr and the U–Mo binary systems exhibit strong phase separation tendencies [24,261].

The effect of annealing temperature on cluster formation, and hence precipitation, got clearly revealed on comparing the morphology of the precipitates in the 800 °C, 900 °C and 1000 °C annealed samples. A change in the morphology from thin needle-like to irregular shaped voluminous particulates on going from 800 °C to 1000 °C evidently brought out the role of temperature in making the diffusion controlled segregation process kinetically faster at higher temperatures.

8.3.5 Growth rate of the interdiffusion zone

A substantial increase in the interdiffusion of U, Mo and Zr atoms across the U–9Mo/Zr–1Nb interface on increasing the annealing temperature resulted in increased interdiffusion zone width, as presented in Table 8.3. The following inferences could be drawn on comparing the width of the interdiffusion zone of the different annealed samples:

(i) Growth of the interdiffusion zone has not occurred during the cooling of the samples from the annealing temperatures, as the interdiffusion zone was almost of same width in samples furnace-cooled and water-quenched from 800 °C.

(ii) Dominance of annealing temperature over time in increasing the width of the interdiffusion zone.

The growth of the interdiffusion zone, being a diffusion controlled process, is expected to show a parabolic dependence of the growth rate on the annealing duration, with the rate gradually

falling of with time at any particular annealing temperature. Whereas, due to the exponential dependence of diffusion coefficients on temperature, an increase in the annealing temperature is expected to make the interdiffusion zone grow at a faster rate. The parabolic growth rate, K_p , of the interdiffusion zone was calculated at the annealing temperatures of 800 °C, 900 °C and 1000 °C. The width of the interdiffusion zone developed only during the annealing operation was used for the calculation purpose. This was obtained by subtracting the width of the interdiffusion zone of the as-bonded sample (27 μm) from the ones measured in the annealed samples (presented in Table 8.6). For the sake of uniformity, calculation of K_p at 800 °C was carried out by considering the width of the interdiffusion zone of the furnace-cooled sample, as in the case of the other two temperatures the samples were only furnace-cooled after the annealing operation. Growth rate of the interdiffusion zone was calculated from the following relation:

$$K_p = (\Delta x)^2/2t \quad (8.1)$$

where, Δx is the width of the interdiffusion zone and t is the annealing time. The values of K_p at the different annealing temperatures for a fixed annealing duration of 10 days are reported in Table 8.6.

Table 8.6 Width of interdiffusion zone, developed during annealing of U-9Mo/Zr-1Nb bonded sample, and its growth rate as a function of annealing temperature together with pre-exponential factor and activation energy for growth.

Annealing temperature, °C	Annealing time, days	Width of interdiffusion zone developed during annealing, μm	Growth rate (K_p), m^2/s	Pre-exponential factor (K_0), m^2/s	Activation energy (Q_K), KJ/mol
800	10	371	7.96×10^{-14}	2.03×10^{-6}	151
900		886	4.54×10^{-13}		
1000		1394	1.12×10^{-12}		

Assuming an Arrhenius relation between the growth rate and the annealing temperature i.e., $K_p = K_0 \cdot \exp(-Q_K/RT)$ in the temperature range of 800 °C to 1000 °C, the activation energy (Q_K) and the pre-exponential factor (K_0) were estimated from the plot shown in Figure 8.22 and

are reported in Table 8.6. It may be seen from Table 8.6 that for every 100 °C rise in annealing temperature the growth rate has increased by almost an order of magnitude. This once again signified the dominance of annealing temperature over time in increasing the width of the interdiffusion zone.

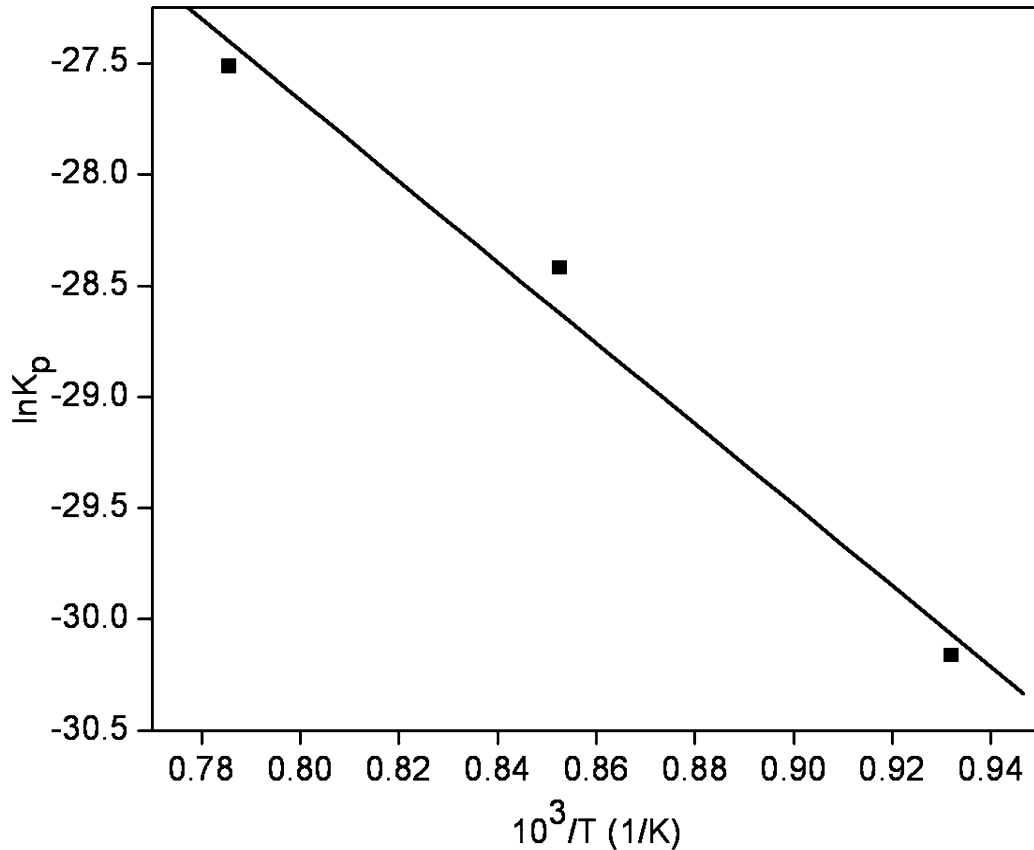


Figure 8.22 Plot showing the Arrhenius temperature dependence of the growth rate of the interdiffusion zone in U–9Mo/Zr–1Nb bonded sample annealed at 800 °C, 900 °C and 1000 °C for 10 days followed by furnace cooling.

As mentioned in Section 7.1, the diffusion bonding study between U–9Mo and Zr–1Nb alloys originated from the idea of using the latter as a cladding material against a fuel of the former. This required not only an in-depth evaluation of the microstructure of the interdiffusion zone forming between these alloys but also an assessment of the extent of the metallurgical interaction between them. Thus, different parameters which reflect the interdiffusion zone growth characteristics were evaluated (Table 8.6). It also becomes imperative to draw a comparison with the interdiffusion zone growth rates recorded between U–Mo and the currently used Al or Al–Si

cladding alloys, if Zr–1Nb is to be conceived as an alternative. Since the growth rate data between U–Mo and Al [177] or Al–Si alloys [266] is available only at 550 °C and 600 °C in the literature, the U–9Mo/Zr–1Nb interdiffusion zone growth rates at these temperatures were determined by Arrhenius extrapolation using the values of Q_K and K_0 listed in Table 8.6. A comparison of the growth rates of the diffusion couples of U–Mo alloys of different Mo-content vs. Al or Al–Si alloys with those of the U–9Mo/Zr–1Nb diffusion couple, extrapolated at 550 °C and 600 °C, are presented in Table 8.7. It may be seen from Table 8.7 that the growth rates of the interdiffusion zone between U–9Mo and Zr–1Nb are almost 2-3 orders of magnitude lower than those between U–(7-12)Mo and Al or Al–(2-5)Si alloys. Thus, a direct advantage in terms of reduced fuel–clad chemical interaction can be envisaged upon using Zr–1Nb alloy as clad in place of Al or Al–Si alloys.

Table 8.7 A comparison of the growth rates of the interdiffusion zone in U–Mo vs. Al and U–Mo vs. Al–Si diffusion couples with those of the U–9Mo vs. Zr–1Nb diffusion couple.

Annealing temperature, °C	Diffusion couple	Growth rate (K_p), m^2/s
550	U–10 wt.% Mo vs. Al–2 wt.% Si [266]	1.45×10^{-14}
	U–10 wt.% Mo vs. Al–5 wt.% Si [266]	1.62×10^{-14}
	U–9 wt.% Mo vs. Zr–1 wt.% Nb	5.06×10^{-16}
600	U–7 wt.% Mo vs. Al [177]	4.05×10^{-13}
	U–10 wt.% Mo vs. Al [177]	1.69×10^{-12}
	U–12 wt.% Mo vs. Al [177]	7.20×10^{-13}
	U–9 wt.% Mo vs. Zr–1 wt.% Nb	1.79×10^{-15}

As elaborated in Section 2.6, pure-Zr is being contemplated as a diffusion barrier liner material between U–Mo alloy monolithic fuel and Al or Al–Si alloy clad to restrict the interdiffusion of the constituent elements of fuel and clad. Hence, interdiffusion studies between U–Mo alloy and pure-Zr in the form of diffusion couple are reported in literature [4,203]. The interdiffusion zone growth rates of the U–9Mo vs. Zr–1Nb diffusion couple of this work were compared with those of the U–Mo vs. pure-Zr diffusion couple reported in literature [4]. An

almost similar growth rate could be observed in both the cases at the same temperature of annealing, as listed in Table 8.8. This clearly brought out the insignificant role of 1 wt.% of Nb present in the Zr–1Nb alloy in the development of the interdiffusion zone.

Table 8.8 A comparison of the growth rates of the interdiffusion zone in U–10 wt.% Mo vs. pure-Zr diffusion couple with those of the U–9 wt.% Mo vs. Zr–1 wt.% Nb diffusion couple.

<i>Annealing temperature, °C</i>	<i>Growth rate (K_p), m^2/s</i>	
	<i>U–10 wt.% Mo vs. pure- Zr [4]</i>	<i>U–9 wt.% Mo vs. Zr–1 wt.% Nb</i>
800	1.22×10^{-13}	7.96×10^{-14}
900	5.67×10^{-13}	4.54×10^{-13}
1000	1.85×10^{-12}	1.12×10^{-12}

8.4 Summary

The as-bonded U–9Mo/Zr–1Nb couple was annealed at different temperatures under different conditions to ascertain the stability of the interdiffusion zone developed during the diffusion bonding operation. At first, annealing was carried out at 800 °C, 900 °C and 1000 °C for a fixed duration of 10 days followed by furnace cooling to investigate the effect of temperature. Then, the effect of annealing duration was examined by carrying out annealing for 12 days at 900 °C followed by furnace cooling. Finally, the effect of the rate of cooling from the annealing temperature was looked at by carrying out water-quenching after annealing at 800 °C for 10 days. The salient findings of the in-depth microstructural characterization of the interdiffusion zone of the annealed samples have been summarized in the following:

(a) The microstructure of the interdiffusion zone was layered-type, similar to the as-bonded couple, with distinctly different microstructural features of each layer as mentioned below:

(i) An interwoven structure of differently oriented acicular lath groupings resembling the “basket weave” morphology near the Zr–1Nb side of the couple. The laths were found to comprise of hcp α -Zr phase, whereas, the presence of bcc β -Zr(Nb,U) phase coexistent with hexagonal δ -phase could be noticed within the interlath regions.

(ii) The precipitation of hcp α -Zr(U) phase in bcc U–Mo–Zr matrix near the U–9Mo side of the couple. The clustering tendency of the bcc matrix prompted the formation of Zr-rich clusters within the matrix followed by their transformation into the α -Zr(U) precipitates.

(iii) The interdiffusion zone in-between was characterized by the presence of Mo_2Zr phase within the bcc U–Mo–Zr matrix. The Mo_2Zr phase was present both in form of a continuous layer, running parallel to the interface, and in a ‘massive’ morphology. The formation of the Mo_2Zr phase depleted the Mo-content of the surrounding matrix and thus instigated its decomposition by lowering the stability. The decomposition proceeded in a manner similar to the discontinuous precipitation reaction forming lamellar α -U phase within the γ -U(Mo,Zr) matrix.

(b) An increase in the annealing temperature resulted in a change in the morphology of the α -Zr(U) precipitates from thin needle-like at 800 °C to voluminous particulates at 1000 °C.

(c) An increase in the annealing duration led to no observable difference in the microstructure of the interdiffusion zone.

(d) Different rates of cooling after the annealing heat treatments, viz., furnace cooled vs. water quenched, were not found to modify the microstructure of the interdiffusion zone further, and hence its width.

(e) A significant increase in the width of the interdiffusion zone of the as-bonded couple was observed upon annealing, with the width increasing exponentially with temperature. Dominance of temperature over time was observed in increasing the width of the zone.

(f) The growth rate of the interdiffusion zone, calculated assuming a diffusion controlled parabolic growth, showed Arrhenius temperature dependence. The growth rates at different temperatures were found to be orders of magnitude lower when compared with those between the U–10 wt.% Mo and Al or Al–Si alloys. In addition, the growth rates were also found to be comparable with those between the U–10 wt.% Mo and pure-Zr. Thus, both the barrier characteristics of Zr–1Nb alloy and a lower fuel–clad chemical interaction upon using it as a clad became evident.

Conclusions

The studies performed on U–9 wt.% Mo and Zr–1 wt.% Nb alloys under the present research work, aiming to assess the microstructural stabilities of these alloys and their interaction under different heat treatment conditions, was driven by the objective of using them as a plausible fuel–clad combination in nuclear research and test reactors. The heat treatment parameters were chosen in such a manner that they incorporate the off-normal scenarios of temperature excursions and rapid cooling which can make the phase constituent(s) of these alloys undergo solid-state stable/metastable phase transformation(s) in the reactor. In addition, the metallurgical interaction likely to occur between these alloys in contact has also been evaluated, without which the objective of the current research work would be incomplete.

The β -phase present in the starting microstructure of Zr–1Nb alloy, in form of spherical β_{Nb} -precipitates, was found to evolve both morphologically and compositionally during heat treatment in the $(\alpha + \beta_{\text{Zr}})$ phase-field. This evolution of the β -phase was driven by a need to reduce its Nb-content accompanied by a corresponding increase in the volume fraction. The reduction in the Nb-content of the β_{Nb} -precipitates ultimately led to their dissolution into the α -phase matrix which, in turn, prompted the nucleation of fresh β -phase in form of intergranular patches and intragranular precipitates. The nucleated β -precipitates exhibited a needle-shaped morphology which could be attributed to their growth following the invariant line strain (ILS) criteria. The dissolution of the β -phase followed by its re-precipitation and growth, being diffusion-controlled, showed significant dependence on the heat treatment temperature. An increase in the size of the β - needles and patches together with a decrease in the number density of the original β_{Nb} -precipitates were noticed as a function of temperature. The morphological change of the β -phase was found to be associated with attainment of intermediate metastable compositions (higher than equilibrium) during the initial stages of heat treatment at higher temperatures. This was rationalized thermodynamically on the basis of maximization of driving force for nucleation using free energy–composition (G–X) diagrams. Such a compositional evolution of the β -phase got reflected in its transformation to metastable phases like α' - or ω - in

the course of quenching of the alloy after the heat treatment. While the β -phase in samples heat treated for a shorter duration showed only ω , a longer duration heat treatment resulted in the formation of α' too. This indicated a shift in the composition of the β -phase towards equilibrium with heat treatment duration. Transformation within the β -needles, as compared to patches, was found to be governed by their sizes as well. Thermodynamics and micromechanical modeling established the dominant role of interfacial energy in it. In addition, the modeling could predict the requirement of a critical dimension of 150 nm in all the directions of a β -precipitate to allow martensitic transformation at the maximum possible undercooling, which was in close agreement with the experimental findings. The ω -transformation, on the other hand, showed less size-dependency as compared to α' -transformation.

The γ -phase in U-9Mo alloy was found to be retained in a metastable state even in the as-cast condition by suppressing the equilibrium eutectoid decomposition into α and γ' (U_2Mo) phases. This retention of the γ -phase was attributed to the sluggish interdiffusion of U and Mo atoms in the γ -phase with increased Mo-addition. The decomposition of the metastable γ -phase could only be set in by ageing and was found to depend on the grain size owing to the preferential nucleation of the decomposition reaction at the grain boundaries. A larger grain size in the 1000 °C/24 h homogenized samples resulted in lesser decomposition in comparison to the fine-grained as-rolled material. The extent of the decomposition reaction was again found to depend on the temperature of ageing which could be explained on the basis of free energy–composition (G–X) diagrams. A reduction in the decomposed γ -phase fraction at 565 °C in comparison of 500 °C could be associated to the extent of Mo-segregation required in the γ -matrix for the nucleation of α - and γ' - phases and the chemical free energy change associated with their nucleation. The same thermodynamic analyses could also corroborate the observed microstructural features of the 500 °C and 565 °C aged samples. The γ -phase was found to decompose by the mechanism of discontinuous precipitation (or cellular) reaction which led to the generation of partially transformed cellular colonies with either the α -phase or the γ' -phase as lamellae and a compositionally different γ -phase as interlamellar region. In the 500 °C aged samples, occasional presence of γ' -phase resulting from the in-situ transformation of γ interlamellar region, could be noticed between two α -phase lamellae in ($\gamma + \alpha$) colonies. Such a

transformation was driven by the reduction in free energy on forming an equilibrium mixture of α - and γ' -phases and resulted in the development of ($\alpha + \gamma'$) lamellar colonies upon prolonged ageing, like the one observed in the 500 °C/40 days aged sample. Discontinuous coarsening of the lamellar colonies to some extent was noticed in all the aged samples which was driven by the reduction in both the interfacial free energy and the supersaturation remaining in the lamellar decomposition products. Ageing at 575 °C resulted in a two-phase non-lamellar ($\alpha + \gamma$) structure, wherein α -phase needles were found to be distributed within the γ -matrix. The needle-like morphology of the α -phase was attributed to its formation following an orientation relationship with the γ -matrix coupled with strain energy minimization.

The interaction of U–9Mo and Zr–1Nb alloys during diffusion bonding at 800 °C led to the development of a layered interdiffusion zone at the joint interface. The expected “down-the-gradient” concentration profiles of U, Mo and Zr across the bonded interface got modified near the U–9Mo side of the couple due to the formation of Mo_2Zr spheroids in the γ -U(Mo,Zr) matrix. The depletion of Mo and Zr on account of formation of the Mo_2Zr phase promoted instability in the γ -U(Mo,Zr) matrix, and got it partially transformed to α -U phase during the cooling of the couple. A phase separation of the γ -U(Mo,Zr) phase to α -U and α -Zr phases was also noticed in this part of the interdiffusion zone. On annealing the as-bonded couple at 800 °C, 900 °C and 1000 °C, the Mo_2Zr phase was found to evolve in form of a continuous layer and also in a ‘massive’ morphology. A discontinuous precipitation reaction in the matrix adjoining the Mo_2Zr phase, instigated by Mo-depletion, led to the formation of lamellar α -U phase within the γ -U(Mo,Zr) matrix in the annealed samples. Precipitation of α -Zr(U) phase in U–Mo–Zr matrix was observed in the annealed samples towards the U–9Mo side end of the interdiffusion zone. The morphology of the α -Zr(U) precipitates changed from thin needle-like to voluminous particulates with the increase in the annealing temperature. A two-phase ($\alpha + \beta$)-Zr layer in Widmanstätten morphology was formed near the Zr–1Nb side of the interdiffusion zone in the as-bonded couple. This layer became much wider during annealing, engulfing most of the Zr–1Nb base material, and exhibited a “basket weave” microstructure with α -Zr laths and β -Zr(Nb,U) interlath regions. A β - to ω -transformation was also observed within the interlath regions. The mid-section of the interdiffusion zone in both as-bonded as well as annealed

couples was found to exist as a single bcc solid solution phase. The parabolic growth rates of the interdiffusion zone, determined at different temperatures, were orders of magnitude lower than those between the similar U–10 wt.% Mo and Al or Al–Si alloys, reported earlier [177,266]. On the other hand, the growth rates were found to be comparable with those reported between U–10 wt.% Mo and pure-Zr [4]. These observations established that Zr–1Nb alloy provides a lower fuel–clad chemical interaction with U–9Mo by being an efficient diffusion barrier.

On the basis of the above summarization it can be further concluded that U–9Mo and Zr–1Nb alloys when put together in form of fuel and clad, respectively, would respond differently to different thermal conditions in the reactor, as shown schematically in Figure 9.1. Temperature excursions of upto 575 °C would set off the decomposition of the metastable γ -phase in U–9Mo alloy, whereas, morphological evolution of the β -phase in Zr–1Nb alloy, accompanied by compositional changes, would occur only above a temperature of 610 °C. In the case of U–9Mo alloy stabilization of the γ -phase would occur once the temperature exceeds 575 °C, whereas, in Zr–1Nb alloy the evolution of the β -phase would continue to occur till 840 °C corresponding to the $(\alpha + \beta)/\beta$ transus temperature. Moreover, in comparison of U–9Mo alloy where the microstructural constituents at any temperature do not undergo any further modification on cooling, the morphologically and compositionally evolved β -phase in Zr–1Nb alloy would undergo transformations into α' - and/or ω - phases on being cooled rapidly. The formation of these metastable phases can cause mechanical instability in the alloy. In each of these alloys, however, the time duration for which the temperature excursion is being experienced will decide the degree of microstructural modification. For example, in Zr–1Nb alloy changes in respect of the β -phase can be brought about in a span of few mins depending on the temperature, whereas, a few days time would be required in U–9Mo to have an appreciable decomposed fraction of the γ -phase even at the temperature of fastest decomposition. In respect of the metallurgical interaction of U–9Mo and Zr–1Nb alloys, appreciable interdiffusion of the constituent elements of the two would occur at a temperature of 800 °C and above, if adequate time is provided for the interdiffusion of the species into each other. The interaction products, however, would not degrade the fuel performance, as these are known to remain stable under irradiation [196]. With regard to the extent of interaction below 800 °C, in the absence of experimental data, it can only be predicted that the interaction will

increase with temperature and time, as shown in Figure 9.1, on the basis of the results of the interdiffusion studies between U-10 wt.% Mo and pure-Zr in the temperature range of 600 °C to 700 °C [4,14,203].

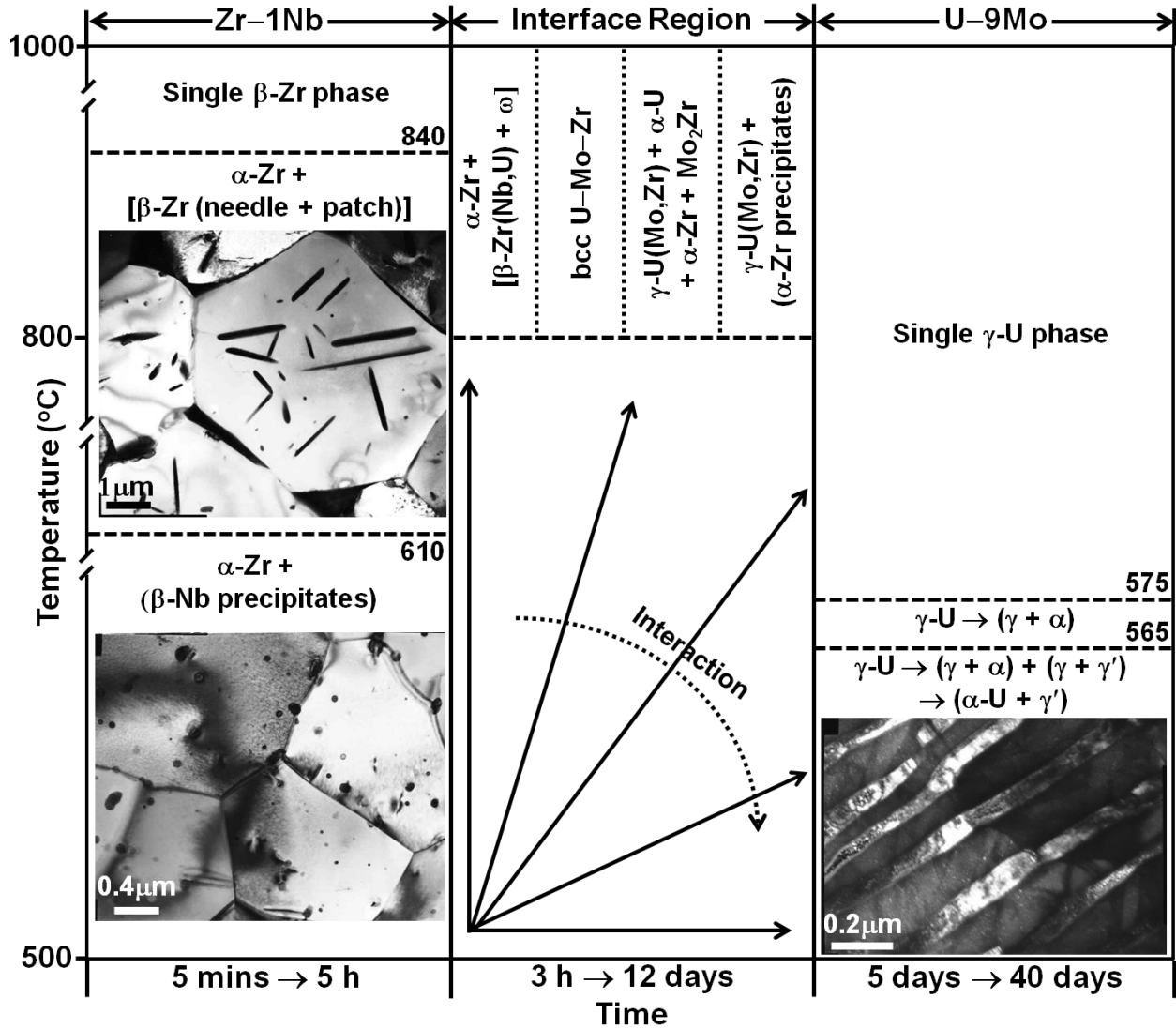


Figure 9.1 A schematic representation of different reaction sequences exhibited by Zr-1 wt.% Nb and U-9 wt.% Mo alloys over different temperature ranges, and their metallurgical interaction, in the present work. The β -Zr needle/patch in the Zr-1Nb alloy would transform to α' - and/or ω -metastable phases depending on the composition and size.

References

- [1] “Limiting the use of highly enriched uranium in domestically licensed research and test reactors”, *U. S. Nuclear Regulatory Commission 10 CFR Part 50, Federal Register (Rules and Regulations)*, **1986**, 51 (37). Available at <http://www.rertr.anl.gov/REFDOCS/NRCRULE.pdf>
- [2] “Development of very-high-density low-enriched-uranium fuels”, J. L. Snelgrove, G. L. Hofman, M. K. Meyer, C. L. Trybus and T. C. Wiencek, *Nucl. Eng. Des.*, **1997**, 178, 119-126.
- [3] “Development status of metallic, dispersion and non-oxide advanced and alternative fuels for power and research reactors”, *IAEA-TECDOC-1374*, International Atomic Energy Agency, Vienna, **2003**.
- [4] “Interdiffusion between Zr diffusion barrier and U–Mo alloy”, K. Huang, Y. Park, D. D. Keiser Jr. and Y. H. Sohn, *J. Phase Equilib. Diffus.*, **2012**, 33, 443-449.
- [5] “Irradiation behavior of high uranium-density alloys in the plate fuels”, M. Ugajin, A. Itoh, M. Akabori, N. Ooka and Y. Nakakura, *J. Nucl. Mater.*, **1998**, 254, 78-83.
- [6] “Irradiation behavior of U₆Mn–Al dispersion fuel elements”, M. K. Meyer, T. C. Wiencek, S. L. Hayes and G. L. Hofman, *J. Nucl. Mater.*, **2000**, 278, 358-363.
- [7] “Irradiation behavior of low-enriched U₆Fe–Al dispersion fuel elements”, G. L. Hofman, R. F. Domagala and G. L. Copeland, *J. Nucl. Mater.*, **1987**, 150, 238-243.
- [8] A. N. Holden, *Physical Metallurgy of Uranium*, Addison-Wesley Publishing Co. Inc., Massachusetts, USA, **1958**.
- [9] “Low-temperature irradiation behavior of uranium–molybdenum alloy dispersion fuel”, M. K. Meyer, G. L. Hofman, S. L. Hayes, C. R. Clark, T. C. Wiencek, J. L. Snelgrove, R. V. Strain and K. H. Kim, *J. Nucl. Mater.*, **2002**, 304, 221-236.
- [10] “Development of Uranium-Silicide and U–Mo alloy fuels by centrifugal atomization, Studies on Fuels with Low Fission Gas Release”, K. Kim, D. B. Lee, C. K. Kim, I. H. Kuk and K. W. Baek, *IAEA-TECDOC-970*, Vienna, **1997**, 77-86. Available at http://www-pub.iaea.org/MTCD/publications/PDF/te_970_prn.pdf
- [11] “Fission product induced swelling of U–Mo alloy fuel”, Y. S. Kim and G. L. Hofman, *J. Nucl. Mater.*, **2011**, 419, 291-301.

- [12] “Neutron diffraction study of U–10 wt.% Mo alloy”, B. S. Seong, C. H. Lee, J. S. Lee, H. S. Shim, J. H. Lee, K. H. Kim, C. K. Kim and V. Em, *J. Nucl. Mater.*, **2000**, 277, 274-279.
- [13] “Interdiffusion Between Potential Diffusion Barrier Mo and U–Mo Metallic Fuel Alloy for RERTR Applications”, K. Huang, Y. Park, D. D. Keiser Jr. and Y. H. Sohn, *J. Phase Equilib. Diff.*, **2013**, 34, 307-312.
- [14] “Diffusion barrier selection from refractory metals (Zr, Mo and Nb) via interdiffusion investigation for U–Mo RERTR fuel alloy”, K. Huang, C. C. Kammerer, D. D. Keiser Jr. and Y. H. Sohn, *J. Phase Equilib. Diff.*, **2014**, 35, 146-156.
- [15] “Solid-State Phase Transformation in Diffusion Couples of U–Mo/Nb”, P. Xiaoxuan, L. Tingting, Y. Changgeng and S. Changlong, *Rare Metal Mat. Eng.*, **2011**, 40, 1718-1720.
- [16] “Irradiation performance of U–Mo–Ti and U–Mo–Zr dispersion fuels in Al–Si matrixes”, Y. S. Kim, G. L. Hofman, A. B. Robinson, D. M. Wachs, H. J. Ryu, J. M. Park and J. H. Yang, *J. Nucl. Mater.*, **2012**, 427, 233-238.
- [17] “Fuel-Matrix Chemical Interaction Between U–7 wt.% Mo Alloy and Mg”, K. Huang, H. Heinrich, D. D. Keiser Jr. and Y.H. Sohn, *Defect Diffus. Forum*, **2013**, 333, 199-206.
- [18] “Swift heavy ion irradiation induced interactions in the UMo/X/Al trilayer system (X = Ti, Zr, Nb, and Mo): RBS and μ -XRD studies”, H. Y. Chiang, S. H. Park, M. Mayer, K. Schmid, M. Balden, U. Boesenberg, R. Jungwirth, G. Falkenberg, T. Zweifel and W. Petry, *J. Alloys Comp.*, **2015**, 626, 381-390.
- [19] “Development of a Cladding Alloy for High Burnup”, G. P. Sabol, G. R. Kilp, M. G. Balfour and E. Roberts, *ASTM STP 1023*, Zirconium in the Nuclear Industry: Eighth International Symposium, L. F. P. Van Swam and C. M. Eucken (Eds.), ASTM, Philadelphia, PA, **1989**, 227-244.
- [20] “Improved PWR Fuel Cladding”, G. P. Sabol, G. Schoenberger and M. G. Balfour, *IAEA-TECDOC-665*, Proceedings of IAEA Technical Committee Meeting on Materials for Advanced Water Cooled Reactors, International Atomic Energy Agency, Vienna, **1992**.
- [21] “Zirconium alloys in nuclear applications”, C. Lemaignan and A. T. Motta, *Nuclear Materials II, Materials Science and Technology, A Comprehensive Treatment, 10B*, in: R. W. Cahn, P. Hassen and E. J. Kramer (Eds.), VCH, **1994**, 1-51.

- [22] “Transformations in zirconium-niobium alloys”, R. F. Hehemann, *Can. Metall. Q.*, **1972**, *11*, 201-211.
- [23] S. Banerjee and P. Mukhopadhyay, *Phase transformations: examples from titanium and zirconium alloys*, Pergamon Press, Oxford, **2004**.
- [24] T. B. Massalski, H. Okamoto, P. R. Subramanian and L. Kacprzak, *Binary Alloy Phase Diagrams*, 2nd ed., ASM International, Materials Park, OH, **1990**.
- [25] “Influence of some factors upon hydriding and variation properties of zirconium alloy with 1% Nb used for fuel element cladding in water-moderated water-cooled power reactors”, A. D. Amaev, R. S. Ambartsumyan, A. A. Kiselev, S. T. Konobeevskiy, J. A. Anisomova, A. M. Glukhov, L. M. Lebedev, V. A. Myshkin, V. V. Goncharov, E. G. Ivanov, M. S. Orlov, P. F. Pravdyuk, E. P. Ryazantsev and V. V. Skvortsov, *Proc. 3rd U.N. Int. Conf. on Peaceful Uses of Atomic Energy*, Geneva, CH, A/Conf.28/P/342, **1964**.
- [26] “Mechanical properties and corrosion resistance of zirconium and its alloys in water, steam and gases at elevated temperature”, R. S. Ambartsumyan, A. A. Kiselev, R. V. Grebennikov, V. A. Myshkin, L. J. Tsuprun, A. V. Nikulina, *Proc. 2nd U.N. Int. Conf. on Peaceful Uses of Atomic Energy*, Geneva, CH, A/Conf.15/P/2044, **1958**.
- [27] “Zr-Alloys, the Nuclear Material for Water Reactor Fuel. A Survey and Update with Focus on Fuel for Pressurized Water Reactor Systems”, H. G. Weidinger, *7th International Conference on WWER Fuel Performance, Modelling and Experimental Support*, Albena, Bulgaria, **2007**. Available at http://www.iaea.org/inis/collection/NCLCollectionStore/_Public/39/079/39079704.pdf
- [28] “Influence of Structure Changes in E110 Alloy Claddings on Ductility Loss Under LOCA Conditions”, S. Nikulin, A. Rozhnov, V. Belov, N. Lyaschenko, A. Nikulina and A. Malgin, *Journal of ASTM International*, **2008**, *5(8)*, 1-16. Available at <http://dx.doi.org/10.1520/JAI101148>. ISSN 1546-962X
- [29] “Structure-Phase State, Corrosion and Irradiation Properties of Zr-Nb-Fe-Sn System Alloys”, V. Shishov, M. Peregud, A. Nikulina, V. Konkov, V. Novikov, V. Markelov, T. Khokhunova, G. Kobylansky, A. Novoselov, Z. Ostrovsky and A. Obukhov, *Journal of ASTM International*, **2008**, *5(3)*, 1-18. Available at <http://dx.doi.org/10.1520/JAI101127>. ISSN 1546-962X.

- [30] “Characteristics and Properties of Cladding Tubes for VVER-1000 Higher Uranium Content Fuel Rods”, M. M. Peregud, V. A. Markelov, V. V. Novikov, A. Y. Gusev and V. F. Konkov, *8th International conference on WVER fuel performance, modeling and experimental support*, Bulgaria, **2009**. Available at http://www.iaea.org/inis/collection/NCLCollectionStore/_Public/41/081/41081138.pdf
- [31] “ASTM manual on Zirconium and Hafnium”, J. H. Schemel, *ASTM STP 639*, American Society for Testing and Materials, **1977**.
- [32] “Westinghouse Fuel Operating Experience at High Burn-up and with Advanced Fuel Features”, M. G. Balfour, D. L. Burman, R. S. Miller, J. E. Moon, P. A. Pritchett, R. N. Stanutz, R. A. Weiner and H. W. Wilson, *Proceedings, American Nuclear Society, European Nuclear Society, ANS/ENS Fuel for the 90’s: International Topical Meeting on Light Water Reactor Fuel Performance*, Avignon, France, **1991**, 104-112.
- [33] “Corrosion Experience with Zircaloy and ZIRLOTM in Operating PWRs”, G. R. Kilp, M. G. Balfour, R. N. Stanutz, K. R. McAtee, R. S. Miller, L. H. Boman, N. P. Wolfhope, O. Ozer, R. L. Yang, *Proceedings, International Topical Meeting on Light Water Reactor Fuel Performance-Fuel for the 90’s, American and European Nuclear Societies*, Avignon, France, **1991**, 2, 730-741.
- [34] “Development of new Zr alloys for PWR fuel rod cladding”, J. P. Mardon, D. Charquet and J. Senevat, *Proc. ANS Int. Topical Meeting on LWR Fuel Performance*, West Palm Beach, Florida, **1994**, 643-649.
- [35] “PWR Zr Alloy Cladding Water Side Corrosion - State of Knowledge on In-PWR Corrosion Analysis Methods of Measured Oxide Data and Oxide Thickness Prediction”, F. Garzarolli and M. Garzarolli, *Advanced Nuclear Technology International*, P. Rudling (Ed.), Mölnlycke, Sweden, **2012**. Available at https://www.antinternational.com/fileadmin/Products_and_handbooks/PZAC/pzac_sample/files/assets/basic-html/toc.html
- [36] “Application of free energy-composition diagrams in predicting the sequences of phase transformations in Zr-Nb alloys”, S. K. Menon, S. Banerjee and R. Krishnan, *Metall. Trans. A*, **1978**, 9A, 1213-1220.

- [37] “Structural Properties and Stability of the BCC and Omega Phases in the Zr-Nb System: II. Composition Dependence of the Lattice Parameters”, G. B. Grad, A. F. Guillermet, J. J. Pieres and G. J. Cuello, *Z. Metallkd.*, **1996**, 87, 721-725.
- [38] “Structural properties and stability of metastable phases in the Zr-Nb system: Part I. Systematics of quenching-and-aging experiments”, G. Aurelio, A. F. Guillermet, G. J. Cuello and J. Campo, *Metall. Trans. A*, **2001**, 32, 1903-1910.
- [39] “Structural properties of metastable phases in Zr–Nb alloys: III. The athermal Ω phase”, G. Aurelio, A. F. Guillermet, G. J. Cuello and J. Campo, *J. Alloys Comp.*, **2002**, 335, 132-138.
- [40] “Corrosion and microstructural characteristics of Zr–Nb alloys with different Nb contents”, H. G. Kim, S. Y. Park, M. H. Lee, Y. H. Jeong and S. D. Kim, *J. Nucl. Mater.*, **2008**, 373, 429-432.
- [41] “Effect of isothermal annealing on the corrosion behavior of Zr–xNb alloys”, H. G. Kim, Y. H. Jeong and T. H. Kim, *J. Nucl. Mater.*, **2004**, 326, 125-131.
- [42] “Correlation between microstructure and corrosion behavior of Zr–Nb binary alloy”, Y. H. Jeong, K. O. Lee and H. G. Kim, *J. Nucl. Mater.*, **2002**, 302, 9-19.
- [43] “Corrosion behavior of Zr alloys with a high Nb content”, J. Y. Park, B. K. Choi, Y. H. Jeong and Y. H. Jung, *J. Nucl. Mater.*, **2005**, 340, 237-246.
- [44] “Effect of β phase, precipitate and Nb-concentration inmatrix on corrosion and oxide characteristics of Zr–xNb alloys”, Y. H. Jeong, H. G. Kim and T. H. Kim, *J. Nucl. Mater.*, **2003**, 317, 1-12.
- [45] “Microstructural Evolution in Zr-1Nb and Zr-1Nb-1Sn-0.1Fe Alloys”, S. Neogy, D. Srivastava, J. K. Chakravarty, G. K. Dey and S. Banerjee, *Metall. Mater. Trans. A*, **2007**, 38A, 485-498.
- [46] “Recrystallization Behavior of Zr-xNb Alloys”, Y. S. Lim, H. G. Kim and Y. H. Jeong, *Mater. Trans.*, **2008**, 49, 1702-1705.
- [47] “Recrystallization behavior of cold-rolled Zr–1Nb alloy”, H. Tian, X. Wang, W. Gong, J. Zhou and H. Zhang, *J. Nucl. Mater.*, **2015**, 456, 321-328.
- [48] M. J. Buerger, *Crystallographic aspects of phase transformations*, in: *Phase Transformations in Solids*, W. A. Weyl (Ed.), John Wiley and Sons, New York, **1951**, 183-211.
- [49] C. N. R. Rao and K. G. Rao, *Phase Transitions in Solids*, McGraw Hill, New York, **1978**.
- [50] “The influence of stress on martensite-start temperatures in Fe-Ni-C alloys”, G. F. Bolling and R. H. Richman, *Scr. Metall.*, **1970**, 4, 539-543.

- [51] “The plastic deformation-transformation of paramagnetic f.c.c. Fe-Ni-C alloys”, G. F. Bolling and R. H. Richman, *Acta Metall.*, **1970**, *18*, 673-681.
- [52] “A mechanism for the strain-induced nucleation of martensitic transformations”, G. B. Olson and M. Cohen, *J. Less-Common Metals*, **1972**, *28*, 107-118.
- [53] “The nature of martensite”, E. C. Bain and N. Y. Dunkirk, *Trans. Am. Inst. Min. Metall. Eng.*, **1924**, *70*, 25-47.
- [54] “The crystallography of martensite transformations I”, J. S. Bowles and J. K. Mackenzie, *Acta Metall.*, **1954**, *2*, 129-137.
- [55] “On the theory of the formation of martensite”, M. S. Wechsler, D. S. Lieberman and T. A. Read, *Trans. AIME J. Metals*, **1953**, *197*, 1503-1515.
- [56] “Beta Phase Transformations in Zirconium base Alloys”, D. Srivastava, *Ph.D. Thesis*, Indian Institute of Science, Bangalore, India, **1996**.
- [57] “On the process of transition of the cubic-body-centered modification into the hexagonal-close-packed modification of zirconium”, W. G. Burgers, *Physica*, **1934**, *1*, 561-586.
- [58] A. Kelly and G. W. Groves, *Crystallography and Crystal defects*, Longman, London, **1970**.
- [59] “The precipitation behavior of a Zr-2.5 wt pct Nb alloy”, C. P. Luo and G. C. Weatherly, *Metall. Mater. Trans. A*, **1988**, *19*, 1153-1162.
- [60] “Self accommodation morphology of martensite variants in Zr-2.5 wt.% Nb alloy”, D. Srivastava, K. Madangopal, S. Banerjee and S. Ranganathan, *Acta Metall. Mater.*, **1993**, *41*, 3445-3454.
- [61] “Morphology and substructure of lath martensites in dilute Zr-Nb alloys”, D. Srivastava, P. Mukhopadhyay, S. Banerjee and S. Ranganathan, *Mater. Sci. Eng. A*, **2000**, *288*, 101-110.
- [62] “Isothermal Transformation of Titanium-Chromium Alloys”, P. D. Frost, W. M. Parris, L. L. Hirsch, J. R. Doig and C. M. Schwartz, *Trans. Am. Soc. Metals*, **1954**, *46*, 231-256.
- [63] “Crystal Structures of Titanium, Zirconium, and Hafnium at High Pressures”, J. C. Jamieson, *Science*, **1963**, *140*, 72-73.
- [64] “Omega phase in materials”, S. K. Sikka, Y. K. Vohra and R. Chidambaram, *Prog. Mat. Sci.*, **1982**, *27*, 245-310.
- [65] “Omega phase transformation – morphologies and mechanisms”, S. Banerjee, R. Tewari and G. K. Dey, *Int. J. Mat. Res.*, **2006**, *97*, 963-977.

- [66] “Evolution of ordered ω phases in (Zr_3Al) -Nb alloys”, R. Tewari, P. Mukhopadhyay, S. Banerjee and L. A. Bendersky, *Acta Mater.*, **1999**, *47*, 1307-1323.
- [67] “The Mechanism of Phase Transformations in Metals”, J. M. Silcock, M. H. Davies and H. K. Hardy, *Institute of Metals*, London, **1955**, *Monograph No. 18*, 93-104.
- [68] “About the crystal structure and nature of the ω -phase in alloys of titanium with chromium”, Y. A. Bagaryatskii, G. I. Nosova and T. V. Tagunova, *Dokl. Akad. Nauk SSSR*, **1955**, *105*, 1225-1228.
- [69] “Structural Properties and Stability of the Bcc and Omega phases in the Zr-Nb System: Part III. Analysis of Interatomic Distances and Chemical Bonding Effects”, G. B. Grad, A. F. Guillermet and J. R. Granada, *Z. Metallkd.*, **1996**, *87*, 726-731.
- [70] “Structural properties and stability of the bcc and omega phases in the Zr-Nb system. I. Neutron diffraction study of a quenched and aged Zr-10 wt.% Nb alloy”, G. J. Cuello, A. F. Guillermet, G. B. Grad, R. E. Mayer and J. R. Granada, *J. Nucl. Mater.*, **1995**, *218*, 236-246.
- [71] “Systematics of lattice parameters and bonding distances of the omega phase in Zr-Nb alloys”, G. B. Grad, J. J. Pieres, A. F. Guillermet, G. J. Cuello, J. R. Granada and R. E. Mayer, *Physica B*, **1995**, *213–214*, 433-435.
- [72] “Mechanical instabilities in the b.c.c. lattice and the beta to omega phase transformation”, D. de Fontaine, *Acta Metall.*, **1970**, *18*, 275-279.
- [73] “On the nature of the omega transformation”, H. E. Cook, *Acta Metall.*, **1973**, *21*, 1445-1449.
- [74] “Zr-Al based intermetallics: processing, microstructure evolution and indentation creep”, R. Tewari, *Ph.D. Thesis*, Indian Institute of Technology, Bombay, India, **2000**.
- [75] “Martensitic transformation in zirconium-niobium alloys”, S. Banerjee and R. Krishnan, *Acta Metall.*, **1971**, *19*, 1317-1326.
- [76] “Martensitic Transformation in Zr-Ti Alloys”, S. Banerjee and R. Krishnan, *Metall. Trans. A*, **1973**, *4*, 1811-1819.
- [77] “The crystallography of martensite transformations—IV body-centred cubic to orthorhombic transformations”, J. K. Mackenzie and J. S. Bowles, *Acta Metall.*, **1957**, *5*, 137-149.

- [78] “The crystallography of the β - α transformation in titanium”, A. J. Williams, R. W. Cahn and C. S. Barrett, *Acta Metall.*, **1954**, 2, 117-128.
- [79] “The cubic-hexagonal transformation in single crystals of cobalt and cobalt-nickel alloys”, P. Gaunt and J. W. Christian, *Acta Metall.*, **1959**, 7, 529-533.
- [80] “Characteristics of lath martensite: Part II. The martensite-austenite interface”, B. P. J. Sandvik and C. M. Wayman, *Metall. Trans. A*, **1983**, 14, 823-834.
- [81] “Characteristics of lath martensite: Part III. Some theoretical considerations”, B. P. J. Sandvik and C. M. Wayman, *Metall. Trans. A*, **1983**, 14, 835-844.
- [82] “The morphology of martensite in iron alloys”, G. Krauss and A. R. Marder, *Metall. Trans. A*, **1971**, 2, 2343-2357.
- [83] “The ω -phase in zirconium base alloys”, B. A. Hatt and J. A. Roberts, *Acta Metall.*, **1960**, 8, 575-584.
- [84] “The β -phase transformation of some zirconium-thorium alloys”, C. G. Hanson, V. G. Rivlin and B. A. Hatt, *J. Nucl. Mater.*, **1964**, 12, 83-93.
- [85] “High-speed thermal analysis of Zr-Nb alloys”, D. Stewart, B. A. Hatt and J. A. Roberts, *Brit. J. Appl. Phys.*, **1965**, 16, 1081-1088.
- [86] “The ω phase in a Zr-25 at.% Ti alloy”, S. L. Sass, *Acta Metall.*, **1969**, 17, 813-820.
- [87] “Standard single-crystal electron-diffraction patterns of the hexagonal phases α' and Ω in zirconium alloys”, M. Chaturvedi and R. N. Singh, *J. Less-Common Metals*, **1969**, 18, 71-77.
- [88] “The formation of omega phase in titanium and zirconium alloys: A review”, B. S. Hickman, *J. Mater. Sci.*, **1969**, 4, 554-563.
- [89] “Omega Phase Precipitation in Alloys of Titanium with Transition Metals”, B. S. Hickman, *Trans. AIME.*, **1969**, 245, 1329-1335.
- [90] “The as-quenched form of the omega phase in Zr-Nb alloys”, C. W. Dawson and S. L. Sass, *Metall. Trans. A*, **1970**, 1, 2225-2233.
- [91] “Ultrasonic study of the beta \rightarrow omega phase transformation in Zr-Nb alloys”, C. Goasdoue, P. S. Ho and S. L. Sass, *Acta Metall.*, **1972**, 20, 725-733.
- [92] “The structure and decomposition of Zr and Ti b.c.c. solid solutions”, S. L. Sass, *J. Less-Common Metals*, **1972**, 28, 157-173.

- [93] J. C. Williams, *Titanium Science and Technology*, R. I. Jaffee and H. M. Burte (Eds.), Plenum Press, New York, **1973**, 3, 1433-1494.
- [94] “A theory of the omega transformation”, H. E. Cook, *Acta. Metall.*, **1974**, 22, 239-247.
- [95] “Simple models for the omega phase transformation”, D. de Fontaine, *Metall. Trans. A*, **1988**, 19, 169-175.
- [96] “Unusual morphology of the omega phase in a Zr-1.75 at. Pct Ni alloy”, D. Srivastava, P. Mukhopadhyay, E. Ramadasan and S. Banerjee, *Metall. Trans. A*, **1993**, 4, 495-501.
- [97] “Thermodynamic Analysis of Stable Phases in the Zr-Nb System and Calculation of the Phase Diagram”, A. F. Guillermet, *Z. Metallkd.*, **1991**, 82, 478-487.
- [98] “First-Principles Bond-Length Correlation for the Omega Structure of the 4d-Transition Elements”, J. E. Garces, G. B. Grad, A. F. Guillermet and S. J. Sferco, *J. Alloys Comp.*, **1999**, 287, 6-11.
- [99] “Theoretical Study of the Structural Properties and Thermodynamic Stability of the Omega Phase in the 4d-Transition Series”, J. E. Garces, G. B. Grad, A. F. Guillermet and S. J. Sferco, *J. Alloys Comp.*, **1999**, 289, 1-10.
- [100] “Interatomic Distances in the Stable and Metastable Bcc and Omega Structures of the Transition Metals: Analysis of Experimental and Theoretical Trends and Correlations with Pauling's Bond-Lengths”, G. Aurelio and A. F. Guillermet, *J. Alloys Comp.*, **1999**, 292, 31-37.
- [101] “Assessment of the Structural Relations between the Bcc and Omega Phases of Ti, Zr, Hf and other Transition Metals”, G. Aurelio and A. F. Guillermet, *Z. Metallkd.*, **2000**, 91, 35-42.
- [102] “Phenomenological Bond Length-Bond Number Correlations for Ti, Zr and Hf: Assessment and Applications to Metastable Structures”, G. Aurelio and A. F. Guillermet, *J. Alloys Comp.*, **2000**, 298, 30-39.
- [103] “Structural Properties of Metastable Phases in Zr-Nb Alloys. I. Neutron Diffraction Study and Analysis of Lattice Parameters”, G. M. Benites, A. F. Guillermet, G. J. Cuello and J. Campo, *J. Alloys Comp.*, **2000**, 299, 183-188.
- [104] “Structural Properties of Metastable Phases in Zr-Nb Alloys. II. Systematics of Atomic Volumes and Interatomic Distances”, G. M. Benites and A. F. Guillermet, *J. Alloys Comp.*, **2000**, 302, 192-198.

- [105] “Nucleation of martensite in small particles”, K. E. Easterling and P. R. Swann, *Acta Metall.*, **1971**, *19*, 117-121.
- [106] “The martensitic transformation of iron precipitates in a copper matrix”, K. E. Easterling and H. M. Miettinen-Oja, *Acta Metall.*, **1967**, *15*, 1133-1141.
- [107] “On the nucleation of martensite in iron precipitates”, K. E. Easterling and G. C. Weatherly, *Acta Metall.*, **1969**, *17*, 845-852.
- [108] “Structure of martensite in very small iron-rich precipitates”, K. R. Kinsman, J. W. Sprys and R. J. Asaro, *Acta Metall.*, **1975**, *23*, 1431-1442.
- [109] “U-Si and U-Si-Ai Dispersion Fuel Alloy Development for Research and Test Reactors”, R. F. Domagala, T. C. Wiecek and H. R. Thresh, *Nucl. Technol.*, **1983**, *62*, 353-360.
- [110] “Reduced Enrichment for Research and Test Reactors (RERTR)”. Available at <http://www.rertr.anl.gov>
- [111] “LEU fuel development at CERCA: Status as of October 1993”, J. P. Durand and Y. Fanjas, *Proceedings of the 16th International Meeting on Reduced Enrichment for Research and Test Reactors*, 1993, Oarai, Japan, JAERI-M 94-02, **1994**, 71-78.
- [112] “Preliminary Developments of MTR Plates with Uranium Nitride”, J. P. Durand, P. Laudamy and K. Richter, *Proceedings of the 1994 International Meeting on Reduced Enrichment for Research and Test Reactors*, Williamsburg, Virginia, ANL/RERTR/TM-20 (CONF-9409107), **1994**, 191-203. Available at http://www.iaea.org/inis/collection/NCLCollectionStore/_Public/29/036/29036183.pdf
- [113] “LEU fuel DEVELOPMENT at CERCA, status as of October 1997, preliminary developments of MTR plates with UMo fuel”, J. P. Durand, Y. Lavastre and M. Grasse, *Proceedings of the 20th International Meeting on Reduced Enrichment for Research and Test Reactors*, Argonne National Laboratory Report ANL/TD/TM99-06, **1997**.
- [114] “Coextrusion of 60 to 80 wt.% U₃O₈ Nuclear Fuel Elements”, H. B. Peacock, International meeting on development, fabrication, and application of reduced-enrichment fuels for research and test reactors, Argonne, IL, USA, 13-14 Nov. **1980**, CONF-801144-1, DPST-80-447. Available from NTIS., PC A02/MF A01, Report Number DP-MS-80-114.
- [115] “Effect of molybdenum addition on metastability of cubic γ -uranium”, V. P. Sinha, P. V. Hegde, G. J. Prasad, G. K. Dey and H. S. Kamath, *J. Alloys Comp.*, **2010**, *491*, 753-760.

- [116] “Performance of low enrichment U_3Si_2 -aluminium dispersion fuel elements in the Oak Ridge Research Reactor”, G. L. Copeland, R. W. Hobbs, G. L. Hofman and J. L. Snelgrove, *Argonne National Laboratory Report*, ANL/RERTR/TM-10, **1987**. Available at http://www.iaea.org/inis/collection/NCLCollectionStore/_Public/19/073/19073235.pdf
- [117] “Post-irradiation examination of AlFeNi clad U₃Si₂ fuel plates irradiated under severe conditions”, A. Leenaers, E. Koonen, Y. Parthoens, P. Lemoine and S. Van den Berghe, *J. Nucl. Mater.*, **2008**, 375, 243-251.
- [118] “Research and Test Reactor Fuel Reprocessing at the AREVA NC La Hague”, E. Helaine, P. Bernard, D. Leach, J. L. Emin and F. Gouyau, *Proceedings of the European Nuclear Society 10th International Topical Meeting on Research Reactor Fuel Management*, Sofia, Bulgaria, **2006**, 172-177. Available at <https://www.euronuclear.org/meetings/rrfm2006/pdf/RRFM%202006,Transactions.pdf>
- [119] “Properties and Selection: Non Ferrous Alloys and Special Purpose Materials”, *ASM Handbook*, ASM International, **1990**, Vol. 2.
- [120] “Nuclear Materials”, G. L. Hofman and L. C. Walters, *Materials Science and Technology*, B. R. T. Frost (Ed.), VCH Publishers, N.Y., **1994**, Vol. 10A.
- [121] “Design of γ -Phase High-Density Uranium Alloys for LEU Dispersion Fuel Applications”, G. L. Hofman, M. K. Meyer and A. E. Ray, *Proceedings of the 21st International Meeting on Reduced Enrichment for Research and Test Reactors*, São Paulo, 18-23 October **1998**. Available at <http://www.rertr.anl.gov/Fuels98/GHofman.pdf>
- [122] “Characterization of U-2 wt.% Mo and U-10 wt.% Mo alloy powders prepared by centrifugal atomization”, K. H. Kim, D. B. Lee, C. K. Kim, G. E. Hofman and K. W. Paik, *J. Nucl. Mater.*, **1997**, 245, 179-184.
- [123] “Development of high density uranium molybdenum alloys by powder metallurgy route for dispersion fuel application in research and test reactors”, V. P. Sinha, P. V. Hegde, G. J. Prasad and H. S. Kamath, *17th Plansee Seminar*, Reutte, Austria, RM 78/1-16, **2009**, Vol. 1.
- [124] “Physical properties of monolithic U-8 wt.% Mo”, R. M. Hengstler, L. Beck, H. Breikreutz, C. Jarousse, R. Jungwirth, W. Petry, W. Schmid, J. Schneider and N. Wieschalla, *J. Nucl. Mater.*, **2010**, 402, 74-80.

- [125] “UMo full size plate irradiation experiment IRIS-TUM—a progress report”, W. Petry, A. Röhrmoser, J. L. Falgoux, C. Jarousse, P. Boulcourt, A. Chabre, S. Dubois, P. Lemoine, S. Van den Berghe and A. Leenaers, *ENS-RRFM*, **2008**, 89-98. Available at <https://www.euronuclear.org/meetings/rrfm2008/transactions/rrfm2008-transactions.pdf>
- [126] “Reduced Enrichment Program for FRM II, Actual Status and a Principal Study of Monolithic Fuel for FRM II”, A. Röhrmoser and W. Petry, *European Nuclear Society 10th International Topical Meeting on Research Reactor Fuel Management*, **2006**, 237-241. Available at <https://www.euronuclear.org/meetings/rrfm2006/pdf/RRFM%202006,Transactions.pdf>
- [127] “Effect of Si and Zr on the interdiffusion of U–Mo alloy and Al”, J. M. Park, H. J. Ryu, S. J. Oh, D. B. Lee, C. K. Kim and Y. S. Kim, *J. Nucl. Mater.*, **2008**, 374, 422-430.
- [128] “Characterization of the reaction layer in U–7wt%Mo/Al diffusion couples”, M. I. Mirandou, S. N. Balart, M. Ortiz and M. S. Granovsky, *J. Nucl. Mater.*, **2003**, 323, 29-35.
- [129] “History of fast reactor fuel development”, J. H. Kittel, B. R. T. Frost, J. P. Mustelier, K. Q. Bagley, G. C. Crittenden and J. Van Dievoet, *J. Nucl. Mater.*, **1993**, 204, 1-13.
- [130] “High-Density, Low-Enriched Uranium Fuels for Nuclear Research Reactors,” D. D. Keiser, S. L. Hayes, M. K. Meyer and C. R. Clark, *JOM—Journal of the Minerals, Metals & Materials Society*, **2003**, 55, 55-58.
- [131] “Progress in development of low-enriched U–Mo dispersion fuels”, G. L. Hofman, J. L. Snelgrove, S. L. Hayes and M. K. Meyer, *6th International Topical Meeting on Research Reactor Fuel Management (RRFM 2002)*, *European Nuclear Society*, Ghent, Belgium, **2002**, 50-58. Available at <http://www.euronuclear.org/meetings/rrfm/pdf/RRFM%202002.pdf>
- [132] “Phase transformation of metastable cubic γ -phase in U–Mo alloys”, V. P. Sinha, P. V. Hegde, G. J. Prasad, G. K. Dey and H. S. Kamath, *J. Alloys Comp.*, **2010**, 506, 253-262.
- [133] “Microstructural Characterization of U-Nb-Zr, U-Mo-Nb, and U-Mo-Ti Alloys via Electron Microscopy”, A. Ewh, E. Perez, D. D. Keiser Jr. and Y. H. Sohn, *J. Phase Equilib. Diffus.*, **2010**, 31, 216-222.
- [134] “The uranium-molybdenum equilibrium diagram below 900 °C”, A. E. Dwight, *J. Nucl. Mater.*, **1960**, 2, 81-87.

- [135] “Thermodynamic assessment of the U–Mo–Al system”, X. Zhang, Y. F. Cui, G. L. Xu, W. J. Zhu, H. S. Liu, B. Y. Yin and Z. P. Jin, *J. Nucl. Mater.*, **2010**, *402*, 15-24.
- [136] “Calphad thermodynamic description of some binary systems involving U”, A. Berche, N. Dupin, C. Guéneau, C. Rado, B. Sundman and J. C. Dumas, *J. Nucl. Mater.*, **2011**, *411*, 131-143.
- [137] “Metastable phases in the uranium molybdenum system and their origin”, K. Tangri and G. I. Williams, *J. Nucl. Mater.*, **1961**, *4*, 226-233.
- [138] “Proposed nomenclature for phases in uranium alloys”, M. J. Lehmann and R. F. Hills, *J. Nucl. Mater.*, **1960**, *2*, 261-268.
- [139] “The Effect of the Rate of Cooling on the Allotropic Transformation Temperatures of Uranium”, P. Duwez, *J. Appl. Phys.*, **1953**, *24*, 152-156.
- [140] “A study of the effect of cooling rate on the decomposition of the γ -phase in uranium-low molybdenum alloys”, R. F. Hills, B. R. Butcher and J. A. Heywood, *J. Less-Common Metals*, **1961**, *3*, 155-169.
- [141] “Further studies on the decomposition of the γ phase in uranium-low molybdenum alloys”, R. F. Hills, B. W. Howlett and B. R. Butcher, *J. Less-Common Metals*, **1963**, *5*, 369-373.
- [142] “Phases monocliniques dans les alliages uranium-molybdene”, M. J. Lehmann, *J. Nucl. Mater.*, **1961**, *4*, 218-225.
- [143] “The structure and occurrence of the metastable monoclinic phase, α''_b , in uranium-molybdenum alloys”, D. Stewart and G. I. Williams, *J. Nucl. Mater.*, **1966**, *20*, 262-268.
- [144] “Phase equilibria in uranium-rich binary alloys containing molybdenum and zirconium and the effect of ternary additions of carbon”, R. L. Craik, D. Birch, C. Fizzotti and F. Saraceno, *J. Nucl. Mater.*, **1962**, *6*, 13-25.
- [145] “Selection and Microstructures of High Density Uranium Alloys”, M. K. Meyer, C. L. Trybus, G. L. Hofman, S. M. Frank and T. C. Wiencek, *Proceedings of the 20th International Meeting on Reduced Enrichment for Research and Test Reactors*, Argonne National Laboratory Report ANL/ED/CP-94693 (CONF-9710102), **1997**. Available at <http://www.osti.gov/scitech/servlets/purl/554785-IdMDqx/webviewable/>
- [146] “Design and Fabrication of High Density Uranium Dispersion Fuels”, C. L. Trybus, T. C. Wiencek, M. K. Meyer, D. J. McGann and C. R. Clark, *Proceedings of the 20th International Meeting on Reduced Enrichment for Research and Test Reactors*, Argonne National Laboratory

Report ANL/ED/CP-94337, **1997**. Available at <http://www.osti.gov/scitech/servlets/purl/8122-AZnvsB/webviewable/>

[147] “Neutron diffraction study of U–5.4 wt.% Mo alloy”, J. S. Lee, C. H. Lee, K. H. Kim and V. Em, *J. Nucl. Mater.*, **2000**, *280*, 116-119.

[148] “A study of the shear transformations from the gamma-phase in uranium-molybdenum alloys containing 6.0–12.5 at % molybdenum”, B. W. Howlett, *J. Nucl. Mater.*, **1970**, *35*, 278-292.

[149] “Hall effect, resistivity and superconductivity of some metastable uranium-rich alloys”, T. G. Berlincourt, *J. Phys. Chem. Solids*, **1959**, *11*, 12-17.

[150] “High-density U-Mo fuel for research reactors”, A. V. Vatulin, A. V. Morozov, V. B. Suprun, Y. I. Petrov and Y. I. Trifonov, *Met. Sci. Heat Treat.*, **2004**, *46*, 484-489.

[151] “Beta-phase retention in uranium alloys”, K. H. Eckelmeyer, M. O. Eatough and M. E. McAllaster, *J. Nucl. Mater.*, **1990**, *170*, 157-163.

[152] “Metallographic study of the transformation of γ phase into ($\alpha + \gamma'$) phases in a U-1.6 wt.% Mo alloy”, G. Östberg, M. Möller and B. Schönntng-Christiansson, *J. Nucl. Mater.*, **1963**, *10*, 329-338.

[153] “Processus des transformations dans les alliages uranium molybdene de faibles teneurs en molybdene”, M. J. Lehmann, *J. Nucl. Mater.*, **1960**, *2*, 152-168.

[154] “The kinetics of the isothermal decomposition of a gamma-phase uranium - 6 atomic % molybdenum alloy”, B. W. Howlett, A. J. Eycott, I. K. Kang and D. R. F. West, *J. Nucl. Mater.*, **1963**, *9*, 143-154.

[155] “Transformation Kinetics of Uranium-Molybdenum Alloys”, R. J. Van Thyne and D. J. McPherson, *Trans. Am. Soc. Met.*, **1957**, *49*, 598-621.

[156] “Isothermal transformation of U–14 and U–16 wt.% Mo alloys at 550 °C”, W. A. Holland, *Report NAA-SR-6125*, **1961**. Available at <http://www.osti.gov/scitech/servlets/purl/4825994>

[157] “The decomposition of the γ -uranium base solid solutions as revealed by X-ray investigations”, O. S. Ivanov and Y. S. Virgiliev, *J. Nucl. Mater.*, **1962**, *6*, 199-202.

[158] “Transformation characteristics of three uranium base alloys”, P. E. Repas, R. H. Goodenow and R. F. Hehemann, *Technical Report AMRA CR 63-02/ 1F*, **1963**. Available at <http://www.dtic.mil/dtic/tr/fulltext/u2/403776.pdf>

- [159] “The effect of irradiation temperature and fission rate on the radiation stability of the Uranium–10 wt.% Molybdenum alloy”, A. A. Shoudy, W. E. McHugh and M. A. Silliman, *Radiation damage in reactor materials*, IAEA–Vienna, **1963**, 133-162.
- [160] “Isothermal Transformation Study of Some Uranium-Base Alloys”, C. A. W. Peterson, W. J. Steele and S. L. DiGiallonardo, *Report: UCRL-7824, Metals, Ceramics, and Materials, UC-25, TID-4500 (34th Ed.)*, Lawrence Radiation Laboratory, Livermore, California, August, **1964**. Available at <http://www.osti.gov/scitech/servlets/purl/4672623>
- [161] “A Review of X-ray Diffraction Studies in Uranium Alloys”, H. L. Yakel, *Proceedings of the Physical Metallurgy of Uranium Alloys Conference Sponsored by the AEC*, Army Material and Mechanical Research Center, Vail, Colorado, Report No. CONF.740205-9, **1974**. Available at <http://www.osti.gov/scitech/servlets/purl/4306144-KNHJN1/>
- [162] “Uranium Alloys”, A. Bar-Or, G. Hirsch, I. Goldstein and P. Wynblatt, *Proceedings of the Third United Nations International Conference on the Peaceful Uses of Atomic Energy*, Nuclear Fuels II, Types and Economics, New York, United Nations, **1965**, Vol. 11, 177-182.
- [163] “Decomposition Kinetics of Gamma Phase Uranium Alloys Containing 8, 10.8, and 14.3 wt% Molybdenum”, Y. Goldstein and A. Bar-Or, *J. Inst. Metals*, **1967**, 95, 17-21.
- [164] “Transformation Characteristics of U-Mo and U-Mo-Ti Alloys”, P. E. Repas, R. H. Goodenow and R. F. Hehemann, *Trans. ASM.*, **1964**, 57, 150-163.
- [165] “On the gamma to gamma prime transformation in uranium—33 at% molybdenum”, C. G. Rhodes and D. Kramer, *J. Nucl. Mater.*, **1963**, 9, 114-115.
- [166] “Crystallographic study of Si and ZrN coated U–Mo atomised particles and of their interaction with Al under thermal annealing”, T. Zweifel, H. Palancher, A. Leenaers, A. Bonnin, V. Honkimäki, R. Tucoulou, S. Van Den Berghe, R. Jungwirth, F. Charollais and W. Petry, *J. Nucl. Mater.*, **2013**, 442, 124-132.
- [167] “Quantitative crystallographic analysis of as-fabricated full size U–Mo/Al(Si) nuclear fuel plates”, H. Palancher, A. Bonnin, V. Honkimäki, T. Buslaps, M. Grasse, B. Stepnik and T. Zweifel, *J. Alloys Comp.*, **2012**, 527, 53-65.
- [168] “Development of characterisation methods on U(Mo) powders for material testing reactors (MTRs)”, G. Champion, R. Belin, H. Palancher, X. Iltis, H. Rouquette, M. Pasturel, V. Demange, P. Castany, V. Dorcet and O. Tougait, *Powder Technol.*, **2014**, 255, 29-35.

- [169] “Study of decomposition and stabilization of splat-cooled cubic γ -phase U–Mo alloys”, N. T. H. Kim-Ngan, I. Tkach, S. Mašková, A. P. Gonçalves and L. Havela, *J. Alloys Compd.*, **2013**, 580, 223-231.
- [170] “Phase transitions during artificial ageing of segregated as-cast U–Mo alloys”, T. A. Pedrosa, A. M. M. dos Santos, F. S. Lameiras, P. R. Cetlin and W. B. Ferraz, *J. Nucl. Mater.*, **2015**, 457, 100-117.
- [171] “Phase Changes in Pile-Irradiated Uranium-Base Alloys”, M. L. Bleiberg, L. J. Jones and B. Lustman, *J. Appl. Phys.*, **1956**, 27, 1270-1282.
- [172] “Effect of fission rate and lamella spacing upon the irradiation-induced phase transformation of U-9 wt.% Mo alloy”, M. L. Bleiberg, *J. Nucl. Mater.*, **1959**, 1, 182-190.
- [173] “Post-irradiation examination of uranium–7 wt% molybdenum atomized dispersion fuel”, A. Leenaers, S. Van den Berghe, E. Koonen, C. Jarousse, F. Huet, M. Trotabas, M. Boyard, S. Guillot, L. Sannen and M. Verwerft, *J. Nucl. Mater.*, **2004**, 335, 39-47.
- [174] “Radiation induced recrystallization of UMo fuel particles and radiation induced amorphisation of interaction products in UMo/Al dispersion fuel”, H. J. Ryu, Y. S. Kim, G. Hofman, J. Rest, J. M. Park and C. K. Kim, *Mater. Sci. Forum*, **2007**, 558-559, 319-322.
- [175] “Transmission electron microscopy investigation of irradiated U–7 wt.% Mo dispersion fuel”, S. Van den Berghe, W. Van Renterghem and A. Leenaers, *J. Nucl. Mater.*, **2008**, 375, 340-346.
- [176] “Microstructural analysis of as-processed U–10 wt.% Mo monolithic fuel plate in AA6061 matrix with Zr diffusion barrier”, E. Perez, B. Yao, D. D. Keiser Jr. and Y. H. Sohn, *J. Nucl. Mater.*, **2010**, 402, 8-14.
- [177] “Phase Constituents and Microstructure of Interaction Layer Formed in U-Mo Alloys vs Al Diffusion Couples Annealed at 873 K (600 °C)”, E. Perez, D. D. Keiser Jr. and Y. H. Sohn, *Metall. Mater. Trans. A*, **2011**, 42, 3071-3083.
- [178] “Characterization of Interaction Layer in U-Mo-X (X= Nb, Zr) and U-Nb-Zr vs. Al Diffusion Couples Annealed at 600° C for 10 Hours”, A. Ewh, E. Perez, D. D. Keiser Jr. and Y. H. Sohn, *Diffus. Defect Data Part. A*, **2011**, 312-315, 1055-1062.

- [179] “Evidence of amorphous interdiffusion layer in heavy ion irradiated U–8wt%Mo/Al interfaces”, H. Y. Chiang, T. Zweifel, H. Palancher, A. Bonnin, L. Beck, P. Weiser, M. Döblinger, C. Sabathier, R. Jungwirth and W. Petry, *J. Nucl. Mater.*, **2013**, *440*, 117-123.
- [180] “Diffusion reaction behaviors of U-Mo/Al dispersion fuel”, H. J. Ryu, J. M. Park, C. K. Kim, Y. S. Kim and G. L. Hofman, *J. Phase Equilib. Diffus.*, **2006**, *27*, 651-658.
- [181] “Microstructural characterization of U-7Mo/Al-Si alloy matrix dispersion fuel plates fabricated at 500 C”, D. D. Keiser, J. F. Jue, B. Yao, E. Perez, Y. H. Sohn and C. R. Clark, *J. Nucl. Mater.*, **2011**, *412*, 90-99.
- [182] “Microstructure Characterization of As-Fabricated and 475 C Annealed U-7 wt.% Mo Dispersion Fuel in Al-Si Alloy Matrix”, B. Yao, E. Perez, D. D. Keiser Jr., J. F. Jue, C. R. Clark, N. Woolstenhulme and Y. H. Sohn, *J. Alloys Comp.*, **2011**, *509*, 9487-9496.
- [183] “Further Insight into Mechanisms of Solid-State Interactions in UMo/Al System”, F. Mazaudier, C. Proye and F. Hodaj, *J. Nucl. Mater.*, **2008**, *377*, 476-485.
- [184] “Interdiffusion Between U(Mo, Pt) or U(Mo, Zr) and Al or Al A356 Alloy”, C. Komar Varela, M. Mirandou, S. Arico’, S. Balar and L. Gribaudo, *J. Nucl. Mater.*, **2009**, *395*, 162-168.
- [185] “Irradiation-Enhanced Interdiffusion in the Diffusion Zone of U-Mo Dispersion Fuel in Al”, Y. Kim, G. Hofman, H. Ryu and S. Hayes, *J. Phase Equilib. Diffus.*, **2006**, *27*, 614-621.
- [186] “Reaction layer growth and reaction heat of U–Mo/Al dispersion fuels using centrifugally atomized powders”, H. J. Ryu, Y. S. Han, J. M. Park, S. D. Park and C. K. Kim, *J. Nucl. Mater.*, **2003**, *321*, 210-220.
- [187] “Irradiation behavior of ground U(Mo) fuel with and without Si added to the matrix”, A. Leenaers, S. Van den Berghe, W. Van Renterghem, F. Charollais, P. Lemoine, C. Jarousse, A. Röhrmoser and W. Petry, *J. Nucl. Mater.*, **2011**, *412*, 41-52.
- [188] “The effect of silicon on the interaction between metallic uranium and aluminum: a 50 year long diffusion experiment”, A. Leenaers, C. Detavernier and S. Van den Berghe, *J. Nucl. Mater.*, **2008**, *381*, 242-248.
- [189] “High Density Fuel Development for Research Reactors”, P. Lemoine and D. Wachs, *Proceedings of Global 2007 – Advanced Nuclear Fuel Cycles and Systems*, Report No. INL/CON-07-12889 (Preprint), **2007**. Available at <http://www.inl.gov/technicalpublications/Documents/3881536.pdf>

- [190] “Interaction Layer Characteristics in U-xMo Dispersion/Monolithic Fuels”, D. L. Porter and A. Ewh, *Report No. INL/EXT-10-17972, Revision 1*, **2010**. Available at <http://www.inl.gov/technicalpublications/Documents/4680336.pdf>
- [191] “Role of Si on the Diffusional Interactions Between U-Mo and Al-Si Alloys at 823 K (550° C)”, E. Perez, Y. H. Sohn and D. D. Keiser Jr., *Metall. Mater. Trans. A*, **2013**, *44*, 584-595.
- [192] “AlSi matrices for U(Mo) dispersion fuel plates”, A. Leenaers, S. Van den Berghe and C. Detavernier, *J. Nucl. Mater.*, **2013**, *439*, 7-18.
- [193] “Microstructural evolution of U(Mo)–Al(Si) dispersion fuel under irradiation – Destructive analyses of the LEONIDAS E-FUTURE plates”, A. Leenaers, S. Van den Berghe, J. Van Eyken, E. Koonen, F. Charollais, P. Lemoine, Y. Calzavara, H. Guyon, C. Jarousse, D. Geslin, D. Wachs, D. Keiser, A. Robinson, G. Hofman and Y. S. Kim, *J. Nucl. Mater.*, **2013**, *441*, 439-448.
- [194] “Potential annealing treatments for tailoring the starting microstructure of low-enriched U–Mo dispersion fuels to optimize performance during irradiation”, D. D. Keiser Jr., J. F. Jue, N. E. Woolstenhulme and A. Ewh, *J. Nucl. Mater.*, **2011**, *419*, 226-234.
- [195] “Characterization and Testing of Monolithic RERTR Fuel Plates”, D. D. Keiser Jr., J. F. Jue and D. E. Burkes, *RERTR-2007*, Report No. INL/CON-07-12224 (Preprint), **2007**. Available at <http://www.inl.gov/technicalpublications/Documents/3667230.pdf>
- [196] “US RERTR Fuel Development Post-Irradiation Examination Results”, A. B. Robinson, D. M. Wachs, D. E. Burkes and D. D. Keiser, *Proceedings of the 30th International Meeting on RERTR-2008*, Report No. INL/CON-08-14916 (Preprint), **2008**. Available at <http://www.inl.gov/technicalpublications/Documents/4282340.pdf>
- [197] “Irradiation Performance of U-Mo Alloy Based ‘Monolithic’ Plate-Type Fuel – Design Selection”, A. B. Robinson, G. S. Chang, D. D. Keiser Jr., D. M. Wachs and D. L. Porter, *Report No. INL/EXT-09-16807*, **2009**. Available at <http://www.inl.gov/technicalpublications/Documents/4363871.pdf>
- [198] “Diffusion of Uranium in Molybdenum, Niobium, Zirconium, and Titanium”, L. Pavlinov, A. Nakonechnikov and V. Bykov, *Atomic Energy*, **1965**, *19*, 1495-1497.
- [199] H. Baker (Ed.), *ASM Handbook, Volume 3: Alloy Phase Diagrams*, ASM International, **1992**.

- [200] “Atomic mobilities, diffusivities and their kinetic implications for U–X (X = Ti, Nb and Mo) bcc alloys”, Y. Liu, D. Yu, Y. Du, G. Sheng, Z. Long, J. Wang and L. Zhang, *Calphad*, **2012**, 37, 49-56.
- [201] “Diffusion Barriers in Thin Films”, M. A. Nicolet, *Thin Solid Films*, **1978**, 52, 415-443.
- [202] “Growth kinetics and microstructural evolution during hot isostatic pressing of U-10 wt.% Mo monolithic fuel plate in AA6061 cladding with Zr diffusion barrier”, Y. Park, J. Yoo, K. Huang, D. D. Keiser Jr., J. F. Jue, B. Rabin, G. Moore and Y. H. Sohn, *J. Nucl. Mater.*, **2014**, 447, 215–224.
- [203] “Interdiffusion and reactions between U–Mo and Zr at 650 °C as a function of time”, Y. Park, D. D. Keiser Jr. and Y. H. Sohn, *J. Nucl. Mater.*, **2015**, 456, 351–358.
- [204] J. R. Davis (Ed.), *ASM Handbook, Volume 2: Properties and Selection: Nonferrous Alloys and Special-Purpose Materials*, **1992**.
- [205] *Neutron scattering lengths and cross sections*. Available at <https://www.ncnr.nist.gov/resources/n-lengths/>
- [206] “Development and compatibility of magnesium-matrix fuel plates clad with 6061 aluminum alloy”, T. C. Wiencek, I. G. Prokofiev and D. J. McGann, *1998 International Meeting on Reduced Enrichment for Research and Test Reactors*, São Paulo, Brazil, **1998**. Available at <http://www.rertr.anl.gov/Fuels98/TWiencek.pdf>
- [207] “SGTE Data for Pure Elements”, A. T. Dinsdale, *Calphad*, **1991**, 15, 317-425.
- [208] “Algebraic Representation of Thermodynamic Properties and the Classification of Solutions”, O. Redlich and A. Kister, *Ind. Eng. Chem.*, **1948**, 40, 345-348.
- [209] “Precipitation in Zirconium-Niobium Martensites”, S. Banerjee, S. J. Vijayakar and R. Krishnan, *J. Nucl. Mater.*, **1976**, 62, 229-239.
- [210] N. F. Kazakov, *Diffusion Bonding of Materials*, New York, Pergamon Press, **1985**.
- [211] “Diffusion Bonding of Advanced Materials”, P. G. Partridge and C. M. Ward-Close, *Metals and Materials*, **1989**, 5, 334-339.
- [212] “Diffusion Bonding of Nuclear Materials”, K. Bhanumurthy, D. Joyson, S. B. Jawale, A. Laik and G. K. Dey, *BARC Newsletter*, **2013**, Issue No. 331, 19-25.

- [213] “Joining Structural Ceramics”, M. G. Nicholas, *Designing interfaces for technological applications: ceramic-ceramic, ceramic-metal joining*, S. D. Peteves (Ed.), Elsevier Applied Science, London and New York, **1989**, 49-76.
- [214] “PowderCell for Windows”, W. Kraus and G. Nolze, Version 2.4 (8.03.2000), Federal Institute for Materials Research and Testing, Rudower Chaussee 5, 12489 Berlin, Germany.
- [215] P. Villars and L. D. Calvert, *Pearson's Handbook of Crystallographic Data for Intermetallic Phases*, 1st Edition, ASM International, Materials Park, OH, **1985**, Vol. 3, 2939, 3246.
- [216] E. A. Brandes, *Smithells Metals Reference Book*, 6th Edition, Butterworth, London, **1983**, 13-25-13-26,
- [217] “Critical evaluation of the thermodynamic properties of zirconium”, A. F. Guillermet, *High Temp.-High Press.*, **1987**, 19, 119-160.
- [218] “CALPHAD Estimates of the Lattice Stabilities for High-Melting Bcc Metals: V, Nb and Ta”, A. F. Guillermet and W. Huang, *Zeitschrift für Metallkunde*, **1988**, 79, 88-95.
- [219] “Orientation relationships in precipitation systems”, U. Dahmen, *Acta Metall.*, **1982**, 30, 63-73.
- [220] “Shape-Preserving Solutions of the Time-Dependent Diffusion Equation”, F. S. Ham, *Quart. J. Appl. Math.*, **1959**, 17, 137-145.
- [221] “Dendritic and Spheroidal Growth”, G. Horvay and J. W. Cahn, *Acta Metall.*, **1961**, 9, 695-705.
- [222] “Kinetics of Growth of Platelike Precipitates”, R. Sankaran and C. Laird, *Acta Metall.*, **1974**, 22, 957-969.
- [223] T. Mura, *Micromechanics of Defects in Solids*, 2nd Edition, Martinus Nijhoff Publishers, The Netherlands, **1987**.
- [224] “The Determination of the Elastic Field of an Ellipsoidal Inclusion, and Related Problems”, J. D. Eshelby, *Proceedings of the Royal Society A*, **1957**, 241, 376–396.
- [225] “Elasticity-based model of the variant selection observed in the β to α phase transformation of a Zircalloy-4 sample”, M. Humbert and N. Gey, *Acta Mater.*, **2003**, 51, 4783-4790.
- [226] “The normal elastic modulus of alloys of zirconium with niobium”, Y. F. Bychkov, A. N. Rozanov and D. M. Skorov, *Atomic Energy*, **1957**, 2, 171-174.

- [227] “The lattice stability of metals—I. Titanium and zirconium”, L. Kaufman, *Acta Metall.*, **1959**, 7, 575-587.
- [228] “The isothermal omega transformation in zirconium-niobium alloys”, A. J. Perkins, P. E. Yaffe and R. F. Hehemann, *Metallography*, **1971**, 4, 303-323.
- [229] “The crystal structure of U₂Mo”, E. K. Halteman, *Acta Cryst.*, **1957**, 10, 166-169.
- [230] T. Hahn, *International Tables for Crystallography, Volume A (Space-Group Symmetry)*, 2nd Edition, D. Reidel Publishing Company, Dordrecht, Holland, **1987**, 468.
- [231] K. H. Eckelmeyer, *Microstructural Structure*, Vol. 7, McCall (Eds.), Fallen, **1977**.
- [232] “Study of decomposition and reactions with aluminum matrix of dispersed atomized U-10 wt.% Mo alloy”, J. S. Lee, C. H. Lee, K. H. Kim and V. Em, *J. Nucl. Mater.*, **2002**, 306, 147-152.
- [233] “Interdiffusion, Intrinsic Diffusion, Atomic Mobility, and Vacancy Wind Effect in γ (bcc) Uranium-Molybdenum Alloy”, K. Huang, D. D. Keiser Jr. and Y. Sohn, *Metall. Mater. Trans. A*, **2013**, 44, 738-746.
- [234] “Abaissement des coefficients d'autodiffusion de l'uranium en phase γ par des additions de molybdene, de zirconium ou de niobium”, Y. Adda and A. Kirianenko, *J. Nucl. Mater.*, **1962**, 6, 135-136.
- [235] P. Shewmon, *Diffusion in Solids*, Wiley, New York, **1989**.
- [236] “Discontinuous coarsening of aligned eutectoids”, J. D. Livingston and J. W. Cahn, *Acta Metall.*, **1974**, 22, 495-503.
- [237] “Discontinuous reactions in solids”, I. Manna, S. K. Pabi and W. Gust, *Int. Mater. Rev.*, **2001**, 46, 53-91.
- [238] “Eutectoid Transformations in Nonferrous and Ferrous Alloy Systems”, C. W. Spencer and D. J. Mack, *Decomposition of Austenite by Diffusional Processes*, V. F. Zackay and H. I. Aaronson (Eds.), Interscience, N.Y., **1962**, 549-606.
- [239] “A summary of the present diffusionist views on bainite”, W. T. Reynolds, H. I. Aaronson and G. Spanos, *Mater. T. JIM.*, **1991**, 32, 737-746.
- [240] “Volume Fractions of Proeutectoid Ferrite/Pearlite and Their Dependence on Prior Austenite Grain Size in Hypoeutectoid Fe-Mn-C Alloys”, Z. Q. Liu, G. Miyamoto, Z. G. Yang and T. Furuhashi, *Metall. Mater. Trans. A*, **2013**, 44, 5456-5467.

- [241] “The Formation of Pearlite”, M. Hillert, *Decomposition of Austenite by Diffusional Processes*, V. F. Zackay and H. I. Aaronson (Eds.), Interscience, N.Y., **1962**, 197-247.
- [242] “Systematics of the Cellular Precipitation Reactions”, E. Hornbogen, *Metall. Trans.*, **1972**, 3, 2717-2727.
- [243] “Mechanisms of the bainite (non-lamellar eutectoid) reaction and a fundamental distinction between the bainite and pearlite (lamellar eutectoid) reactions”, H. J. Lee, G. Spanos, G. J. Shiflet and H. I. Aaronson, *Acta Metall.*, **1988**, 36, 1129-1140.
- [244] H. I. Aaronson, M. Enomoto and J. K. Lee, *Cellular Reaction. Mechanisms of Diffusional Transformations in Metals and Alloys*, CRC Press, Boca Raton, FL, **2010**.
- [245] “A Eutectoid Reaction for the Decomposition of Austenite into Pearlitic Lamellae of Ferrite and $M_{23}C_6$ Carbide in a Mn-Al Steel”, W. C. Cheng and S. M. Hwang, *Metall. Mater. Trans. A*, **2011**, 42, 1760-1766.
- [246] “The Coexistence of Multiple “Pearlites” in Isothermally Treated Multicomponent Steels”, C. Hutchinson, *Metall. Mater. Trans. A*, **2012**, 43, 2567-2570.
- [247] “On the Eutectoid Reaction in a Quaternary Fe-C-Mn-Al Alloy: Austenite \rightarrow Ferrite + Kappa-Carbide + $M_{23}C_6$ Carbide”, W. C. Cheng, Y. S. Song, Y. S. Lin, K. F. Chen and P. C. Pistorius, *Metall. Mater. Trans. A*, **2014**, 45, 1199-1216.
- [248] V. Raghavan, *Solid State Phase Transformations*, Prentice Hall, India, **1987**.
- [249] R. W. Cahn and P. Haasen (Ed.), *Physical Metallurgy*, Vol. 2, 4th Edition, Elsevier, Amsterdam, Netherlands, **1996**.
- [250] D. A. Porter, K. E. Easterling and M. Y. Sherif, *Phase Transformations in Metals and Alloys*, 4th Edition, CRC Press Taylor & Francis Group, N.Y., **2009**.
- [251] D. E. Laughlin and K. Hono (Eds.), *Physical Metallurgy*, Vol. 1, 5th Edition, Elsevier, Oxford, UK, **2014**.
- [252] “The annealing of a quenched uranium-5 at % molybdenum alloy”, G. H. May, *J. Nucl. Mater.*, **1962**, 7, 72-84.
- [253] J. W. Christian, *The Theory of Transformations in Metals and Alloys*, 3rd Edition, Elsevier, N.Y., **2002**.
- [254] “In situ transformation of Fe_3C to Mo_2C in iron-molybdenum-carbon alloys”, D. Raynor, J. A. Whiteman and R. W. K. Honeycombe, *J. Iron Steel I.*, **1966**, 204, 1114-1116.

- [255] “Dispersed (coated particles) and monolithic (zircalloy–4 cladding) U–Mo miniplates”, E. E. Pasqualini, *The 27th International Meeting on Reduced Enrichment for Research and Test Reactors (RERTR)*, Boston, USA, **2005**. Available at http://www.rertr.anl.gov/RERTR27/PDF/S15-3_Pasqualini.pdf
- [256] “Thermal cycling effect in U-10Mo/Zry-4 monolithic nuclear fuel”, D. A. Lopes, A. J. O. Zimmermann, S. L. Silva and J. R. C. Piqueira, *J. Nucl. Mater.*, **2016**, 473, 136-142.
- [257] “Selected Observations in Phase Constituents, Growth Kinetics and Microstructural Development of Aluminides in U-Mo vs. Al and 6061 Diffusion Couples Annealed at 600 °C”, E. Perez, D. D. Keiser and Y. H. Sohn, *Defect Diffus. Forum*, **2009**, 289-292, 41-49.
- [258] “Characterization of the interaction layer grown by interdiffusion between U–7wt%Mo and Al A356 alloy at 550 and 340 °C”, M. Mirandou, S. Aricó, M. Rosenbusch, M. Ortiz, S. Balart and L. Gribaudo, *J. Nucl. Mater.*, **2009**, 384, 268-273.
- [259] “Characterization of the interaction layer in diffusion couples U-7 wt.%Mo/Al 6061 alloy at 550 °C and 340 °C: Effect of the γ U(Mo) cellular decomposition”, M. I. Mirandou, S. F. Aricó, S. N. Balart and L. M. Gribaudo, *Mater. Charact.*, **2009**, 60, 888-893.
- [260] “Thermal stability of co-extruded U–Zr/Zr–Nb alloys”, C. T. Lee, J. H. Park, T. K. Kim, U. J. Lee, B. S. Lee and D. S. Sohn, *J. Nucl. Mater.*, **2008**, 373, 275-279.
- [261] “Density-functional study of U–Mo and U–Zr alloys”, A. Landa, P. Söderlind and P. E. A. Turchi, *J. Nucl. Mater.*, **2011**, 414, 132-137.
- [262] “Stability and structure of the δ phase of the U-Zr alloys”, M. Akabori, A. Itoh, T. Ogawa, F. Kobayashi and Y. Suzuki, *J. Nucl. Mater.*, **1992**, 188, 249-254.
- [263] “The lattice stability and structure of δ -UZr₂ at elevated temperatures”, M. Akabori, T. Ogawa, A. Itoh and Y. Morii, *J. Phys.: Condens. Matter*, **1995**, 7, 8249-8257.
- [264] “On the formation mechanism of UZr₂ phase”, C. B. Basak, N. Prabhu and M. Krishnan, *Intermetallics*, **2010**, 18, 1707-1712.
- [265] “Disordered bcc γ -phase to δ -phase transformation in Zr-rich U-Zr alloy”, C. B. Basak, S. Neogy, D. Srivastava, G. K. Dey and S. Banerjee, *Philos. Mag.*, **2011**, 91, 3290-3306.
- [266] “Interdiffusion in Diffusion Couples: U-Mo vs Al and Al-Si”, E. Perez, D. D. Keiser Jr., B. Yao and Y. H. Sohn, *RERTR 2009 31st International Meeting on Reduced Enrichment for*

Research and Test Reactors (RERTR), Beijing, China, Report No. INL/CON-09-17105
(Preprint), **2009**. Available at <https://inldigitallibrary.inl.gov/sti/4408272.pdf>

Binary equilibrium phase diagrams

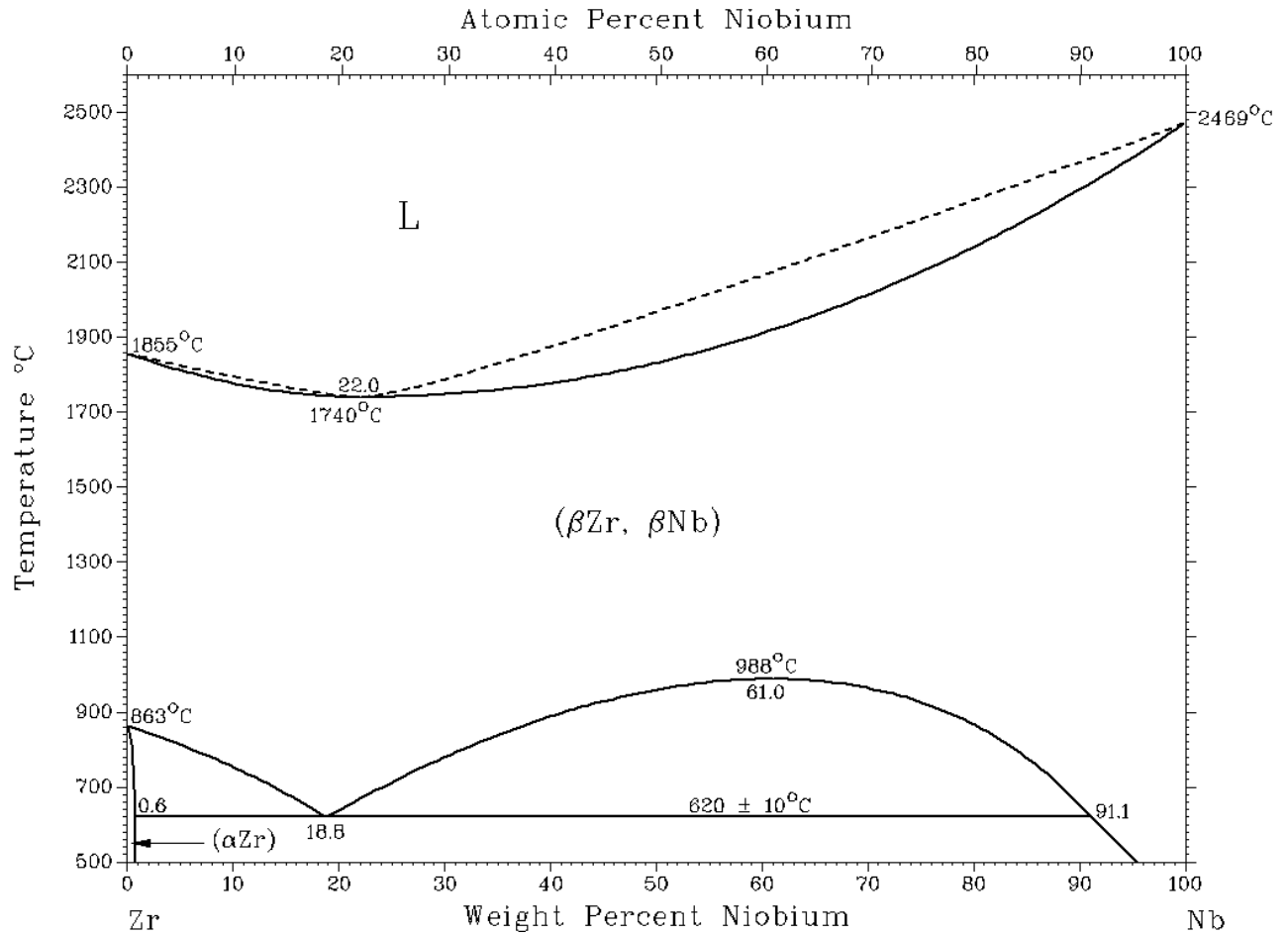


Figure AI.1 The binary Zr–Nb equilibrium phase diagram [24].

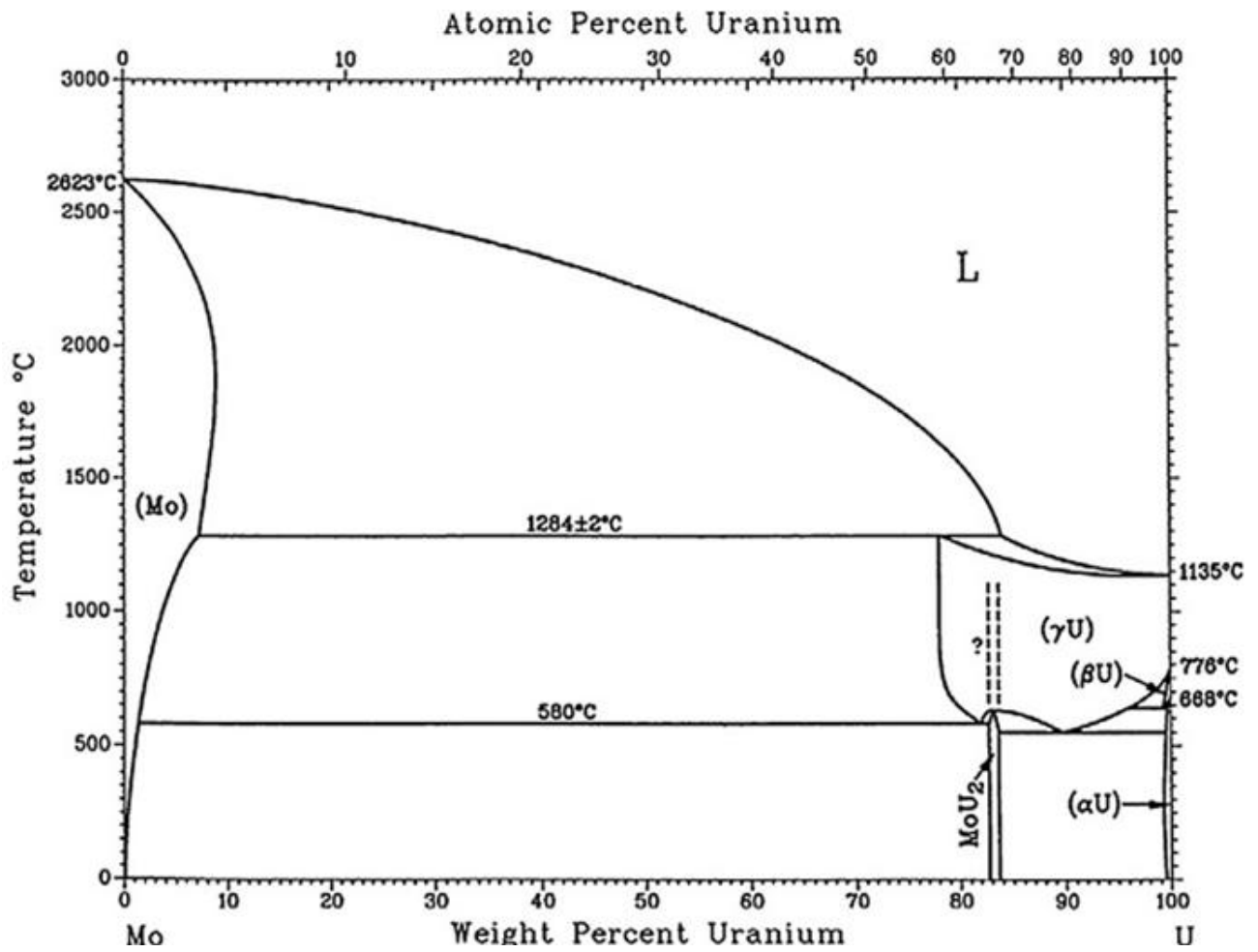


Figure A1.2 The binary Mo-U equilibrium phase diagram [24].

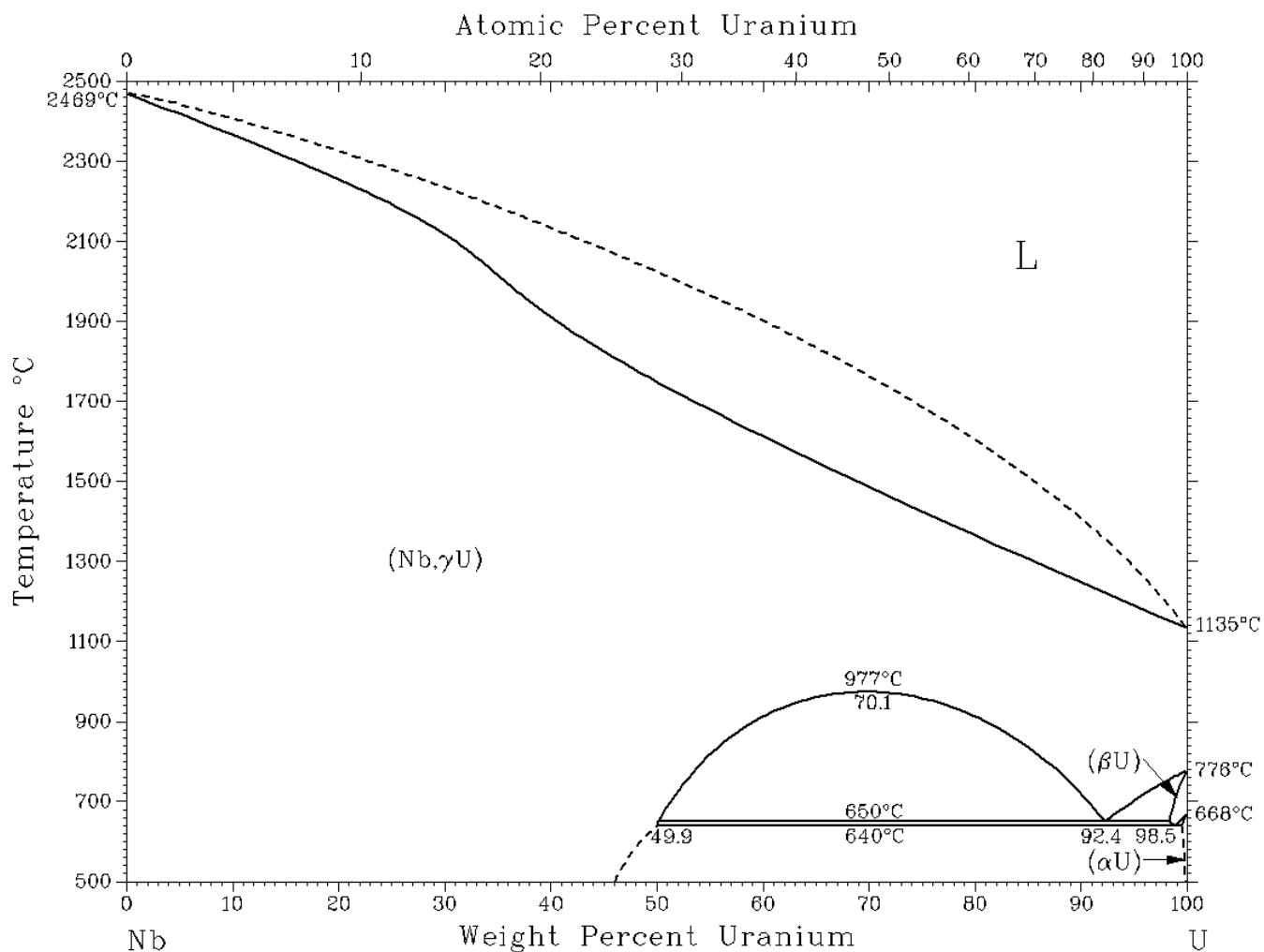


Figure A1.3 The binary Nb–U equilibrium phase diagram [24].

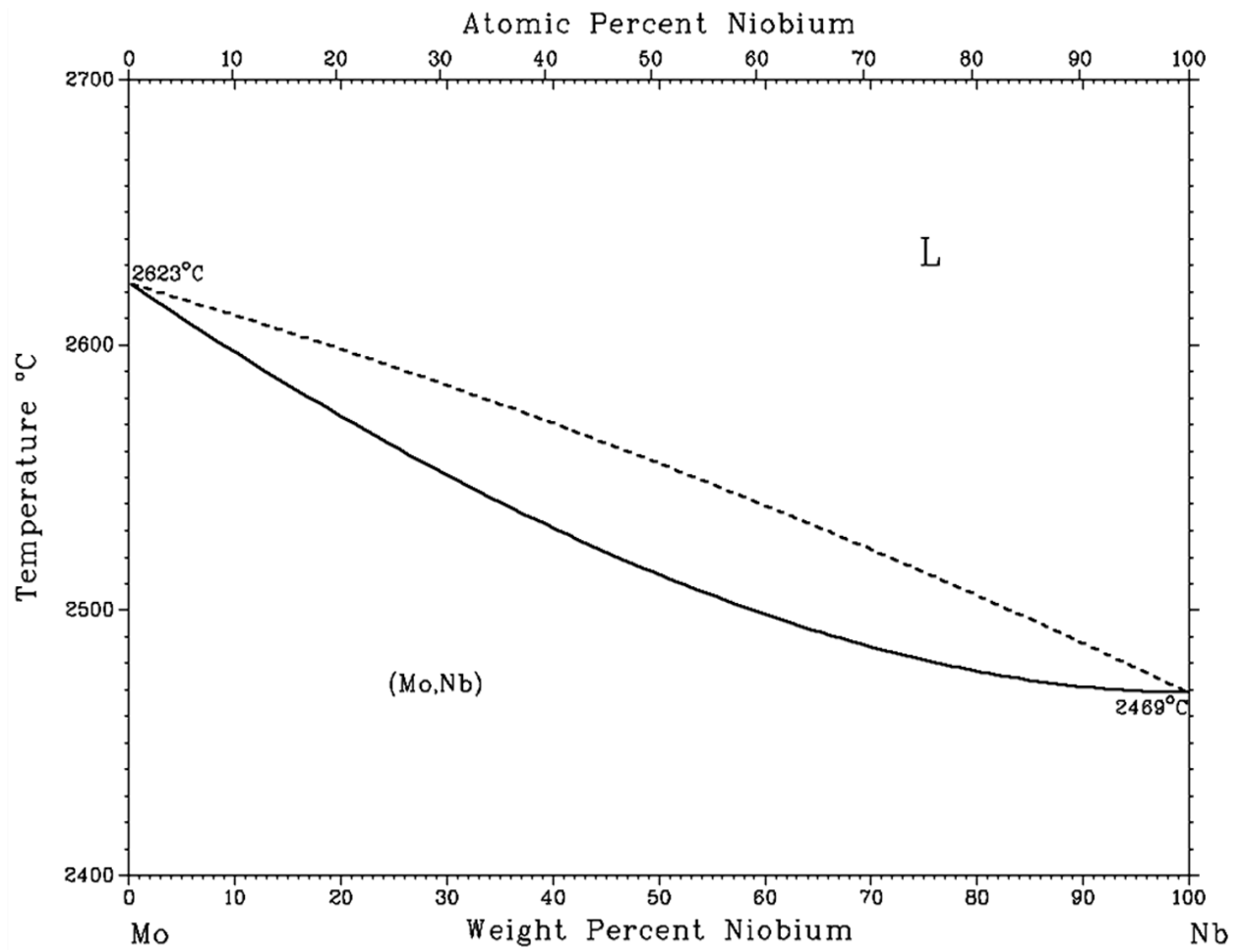


Figure A1.4 The binary Mo–Nb equilibrium phase diagram [24].

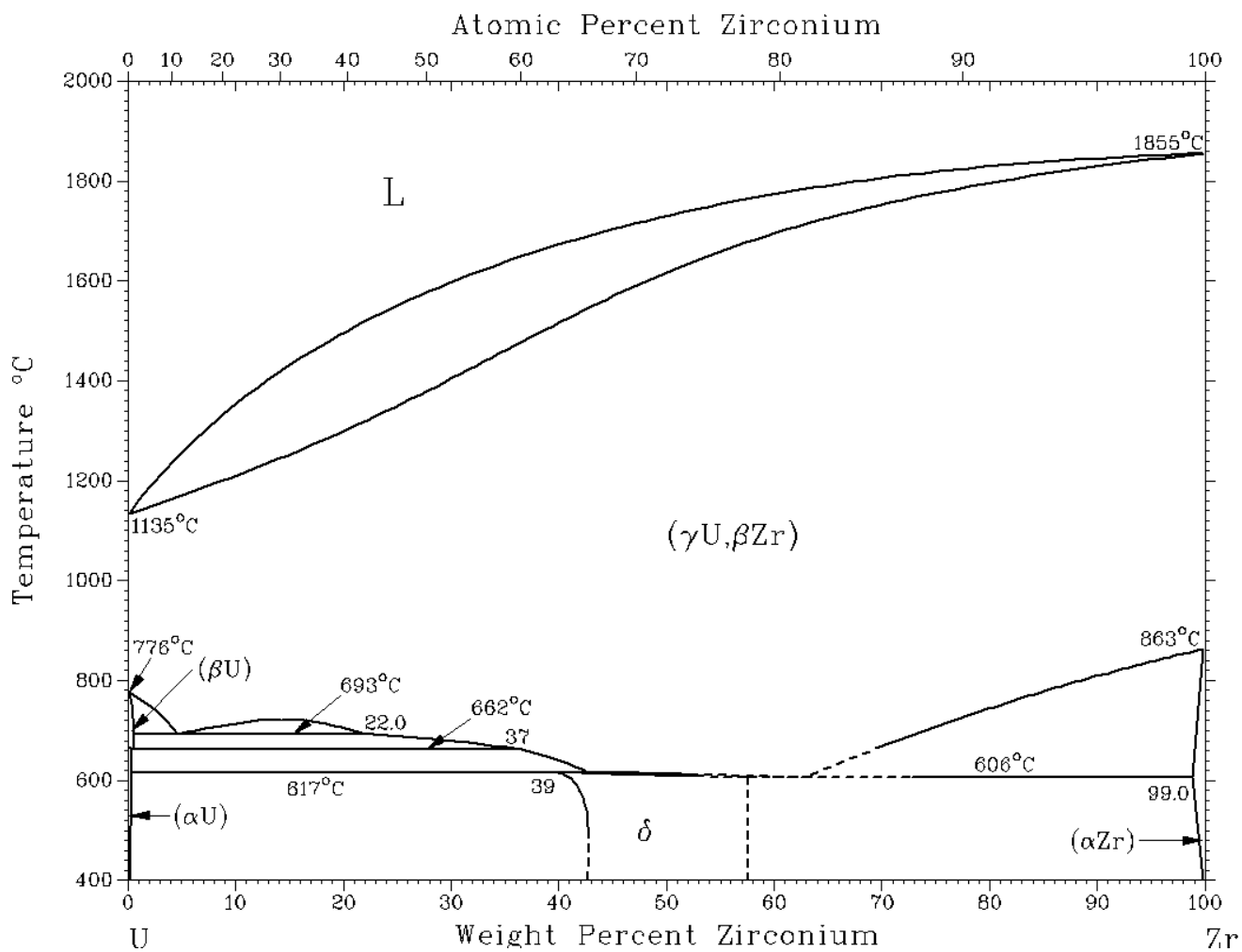


Figure A1.5 The binary U–Zr equilibrium phase diagram [24].

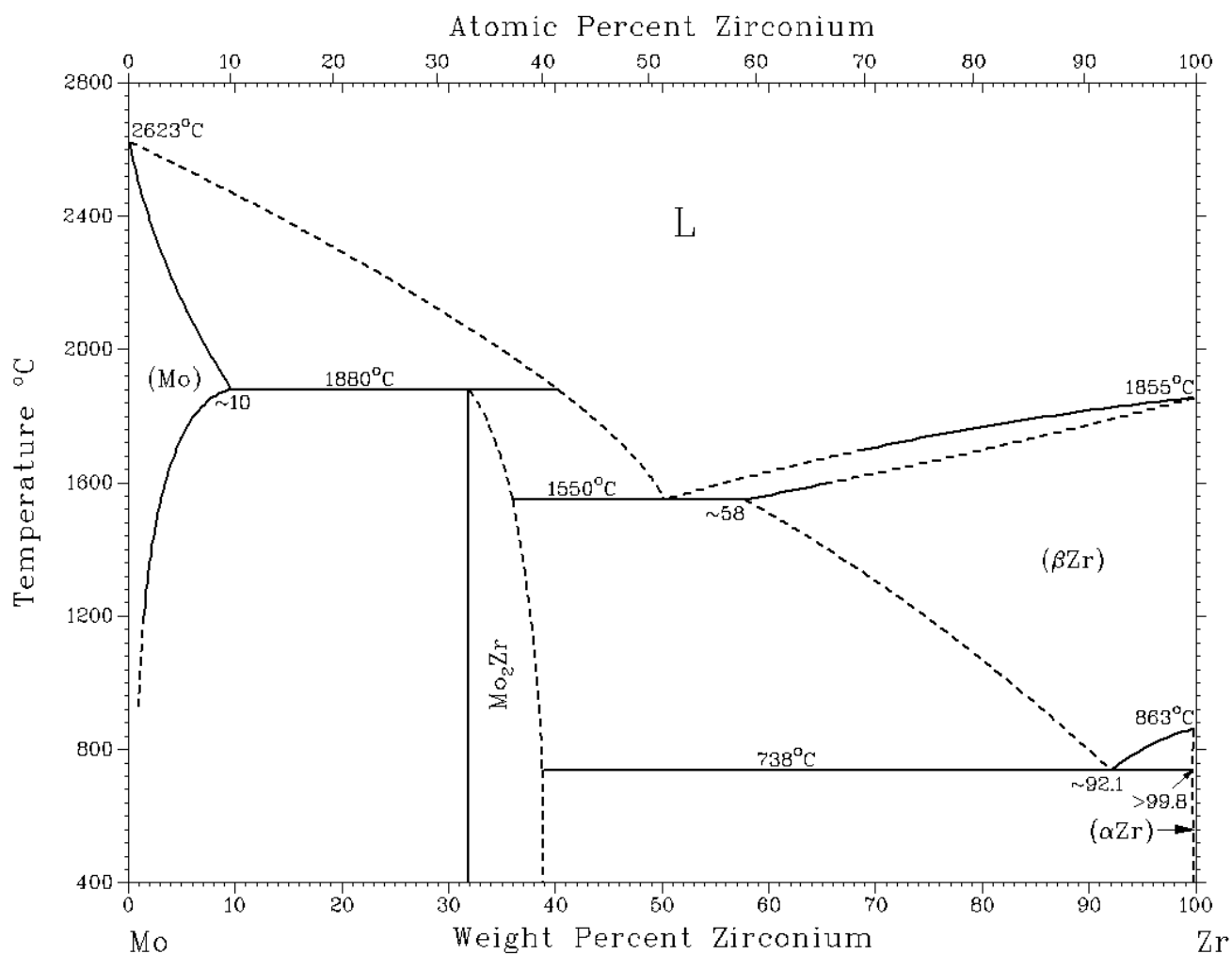


Figure A1.6 The binary Mo–Zr equilibrium phase diagram [24].

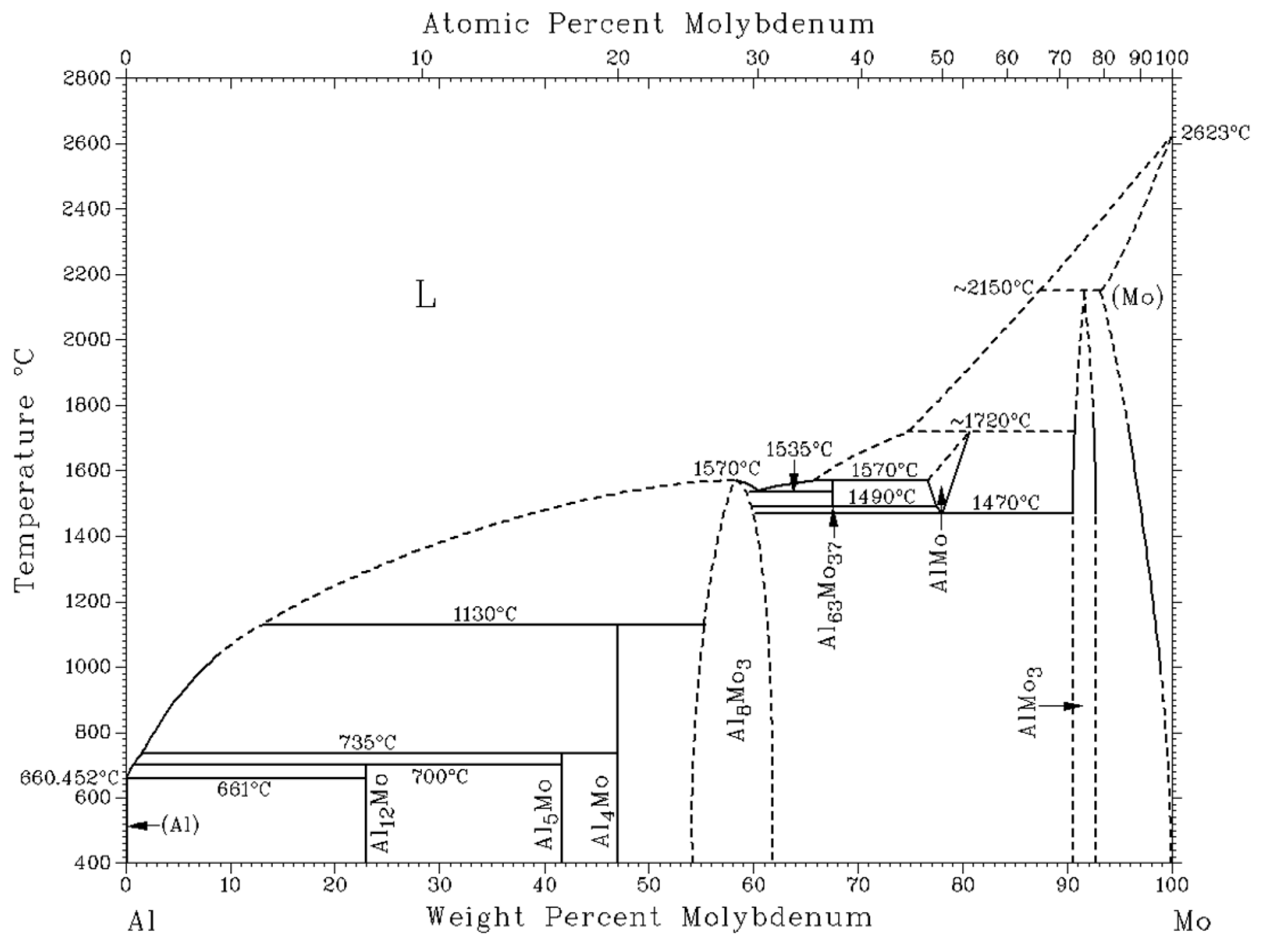


Figure A1.7 The binary Al–Mo equilibrium phase diagram [24].

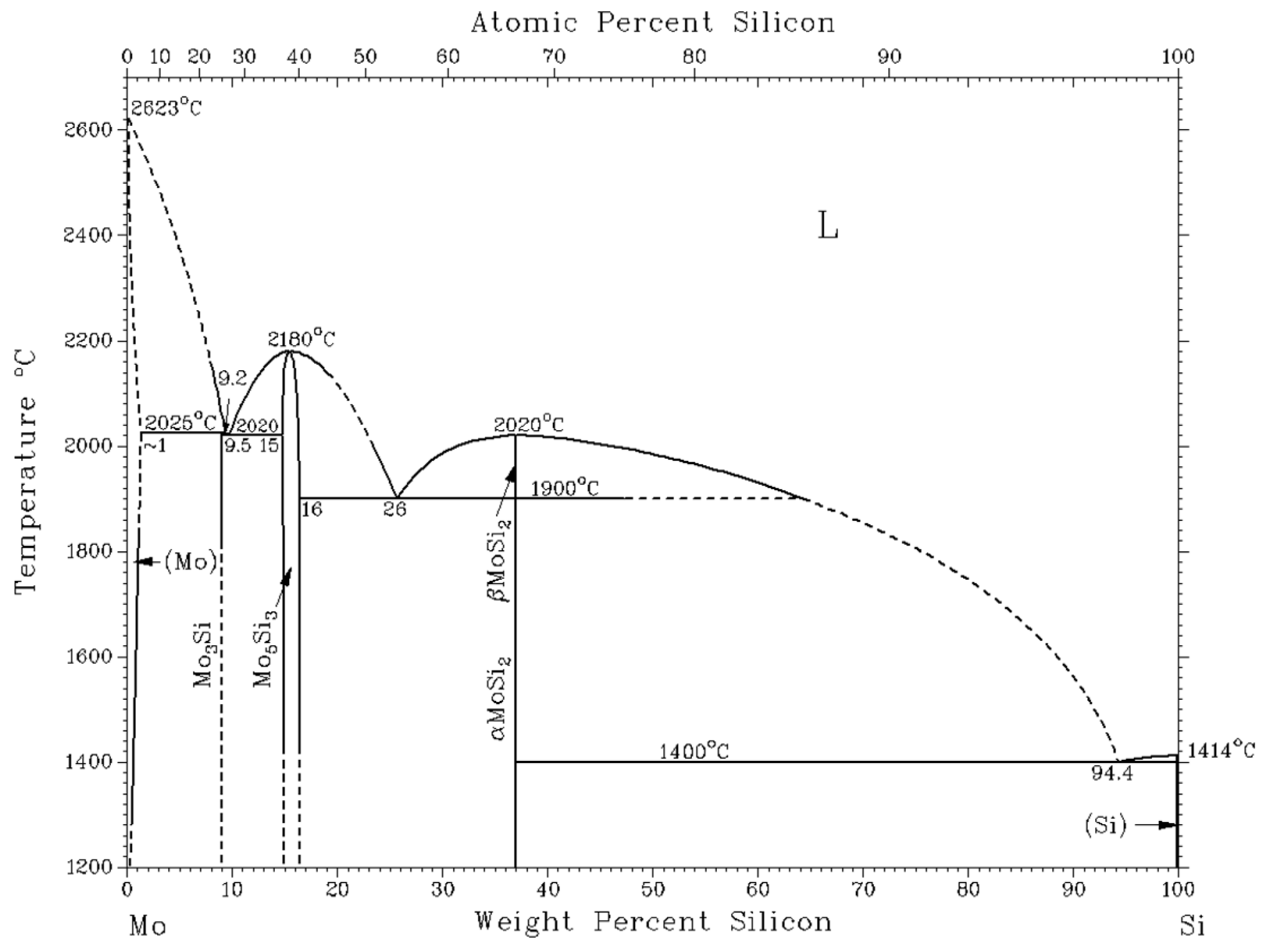


Figure A1.8 The binary Mo-Si equilibrium phase diagram [24].

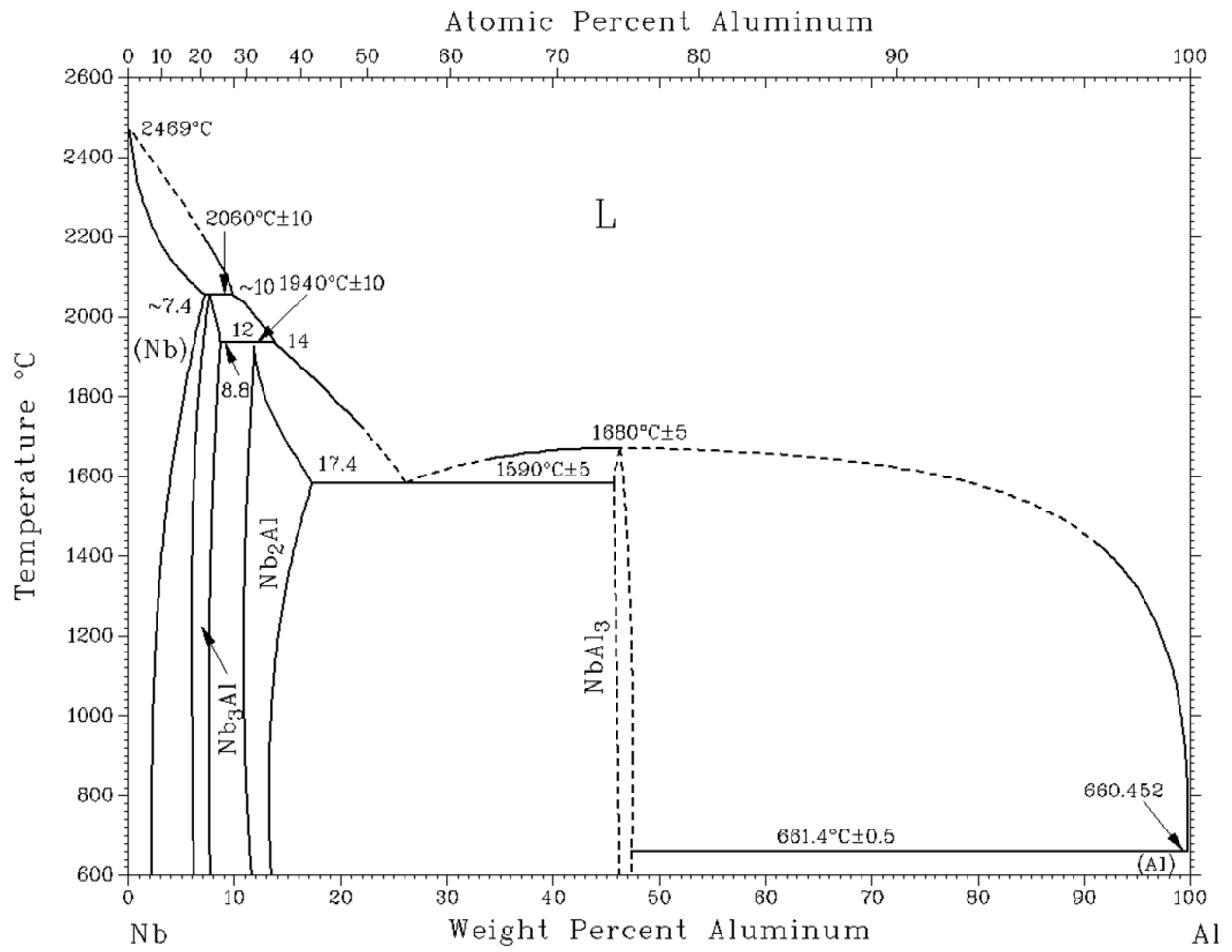


Figure AI.9 The binary Nb–Al equilibrium phase diagram [24].

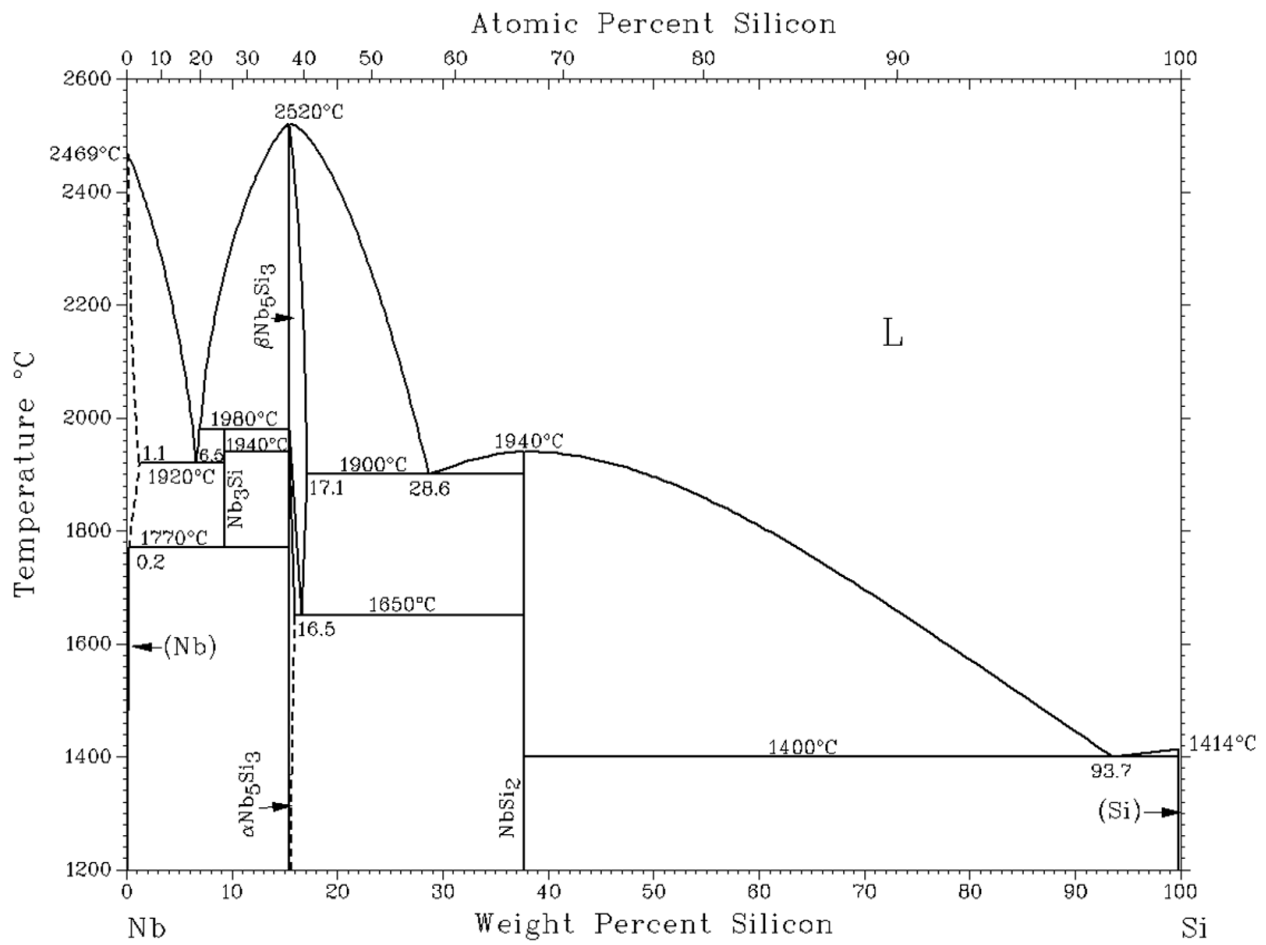


Figure A1.10 The binary Nb–Si equilibrium phase diagram [24].

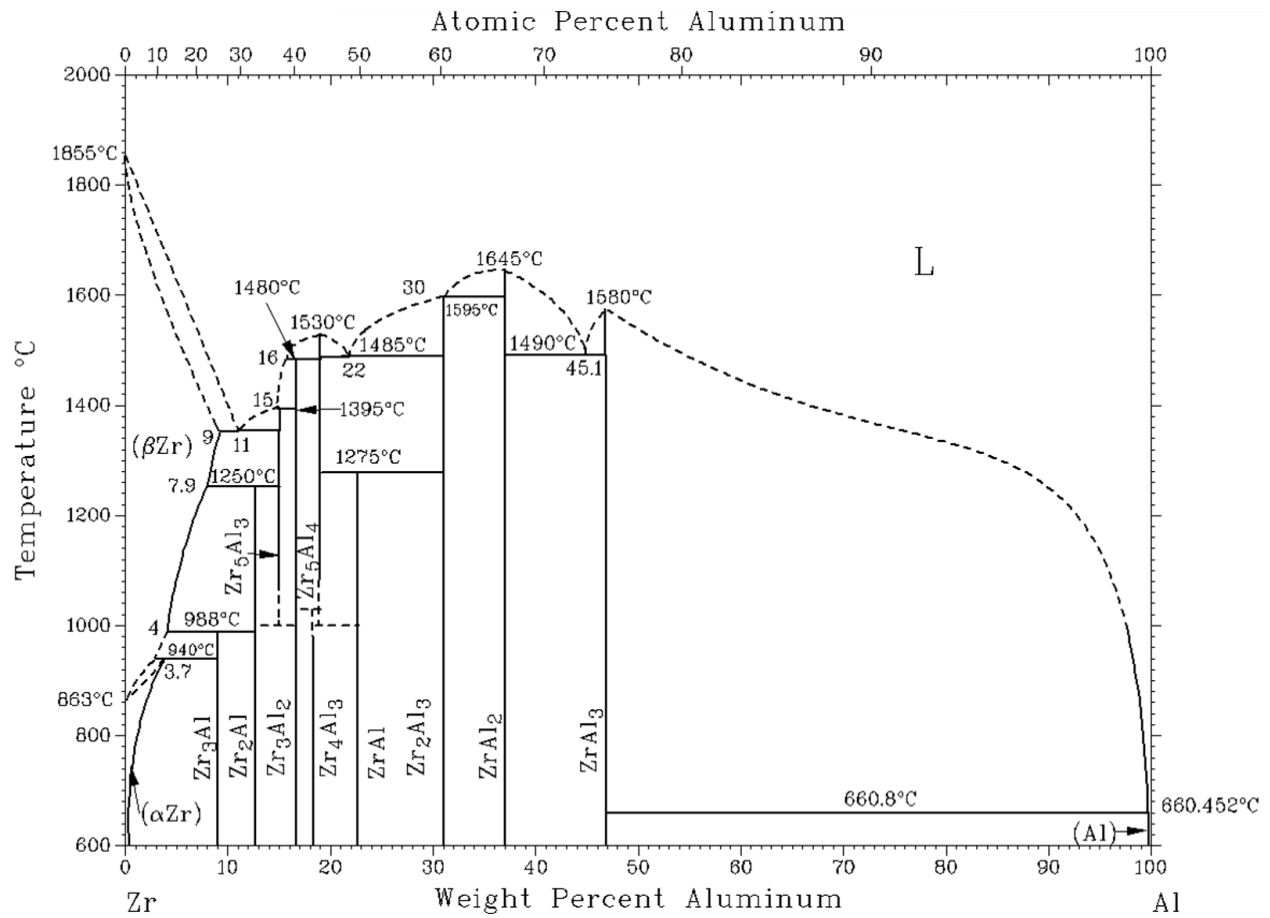


Figure A1.11 The binary Zr–Al equilibrium phase diagram [24].

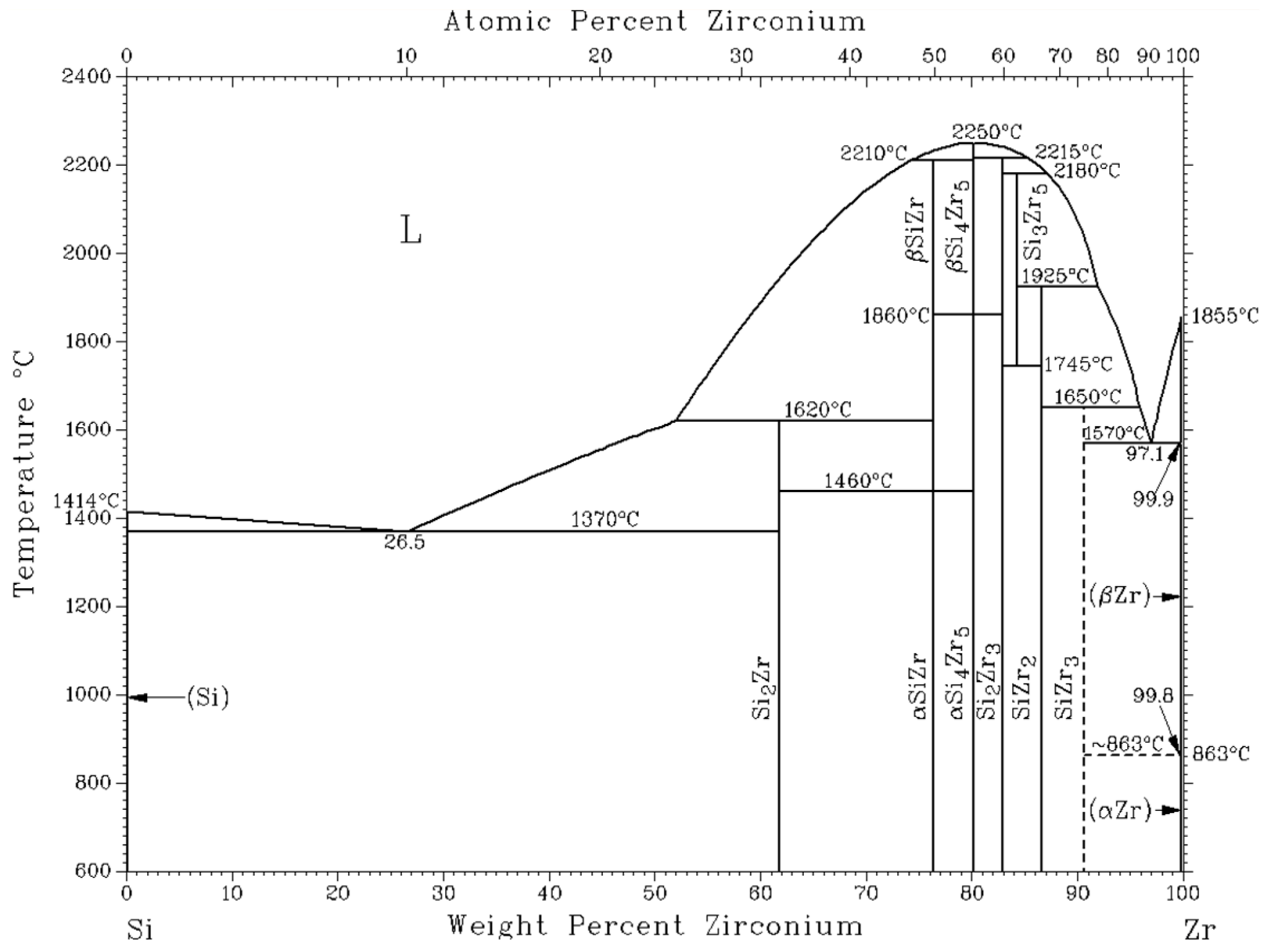


Figure AI.12 The binary Si–Zr equilibrium phase diagram [24].

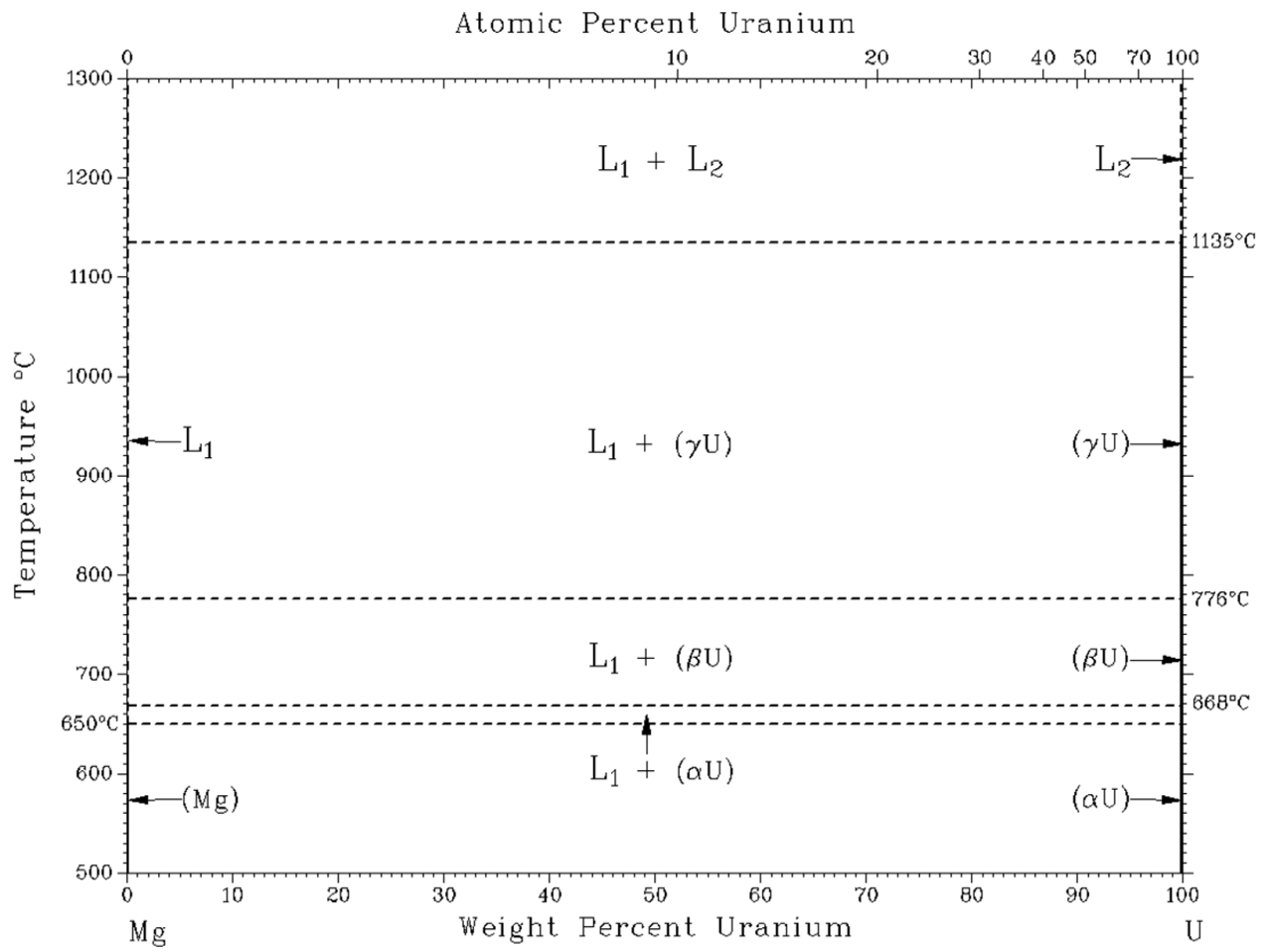


Figure A1.13 The binary Mg–U equilibrium phase diagram [24].

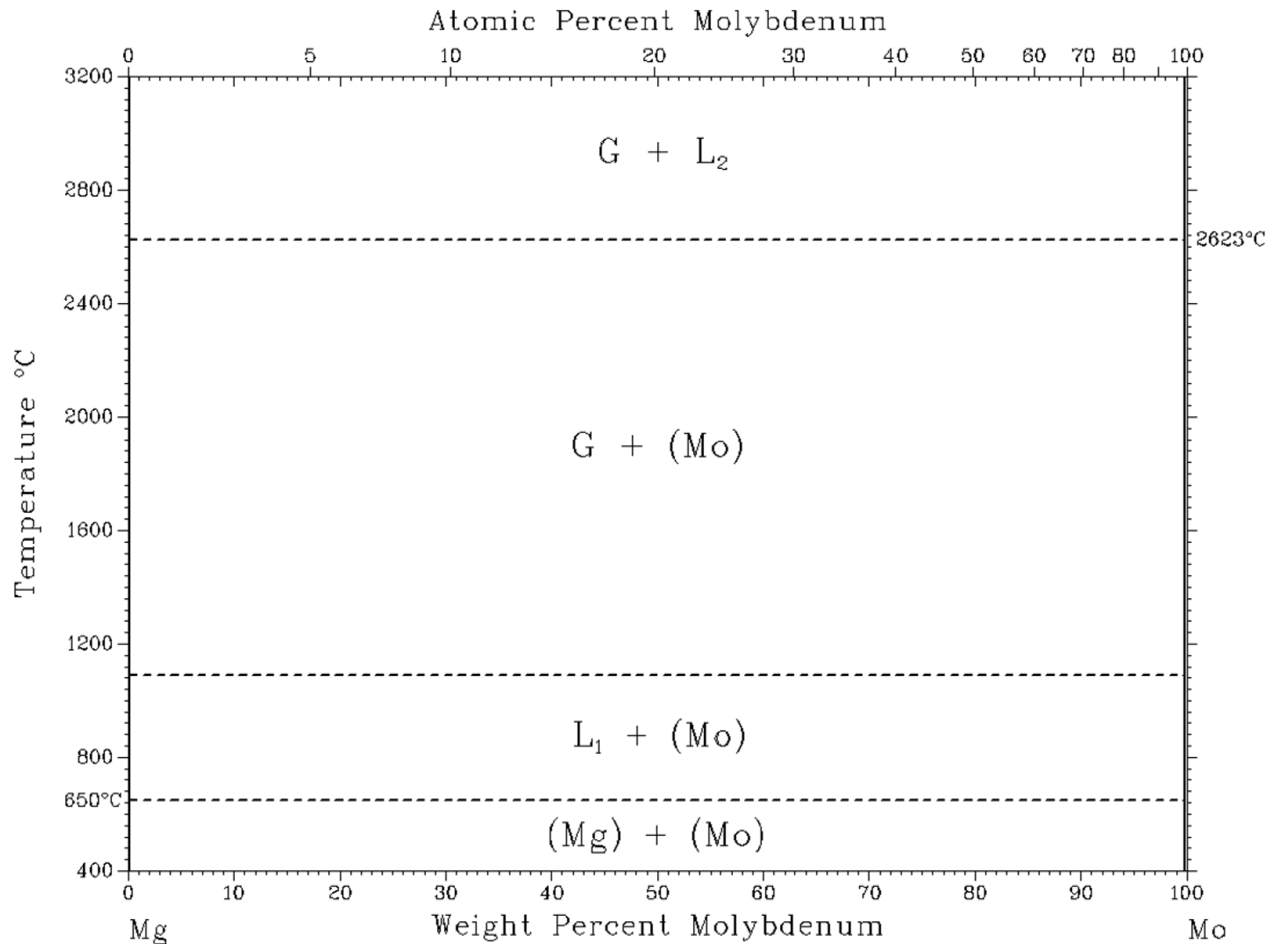


Figure AI.14 The binary Mg–Mo equilibrium phase diagram [24].

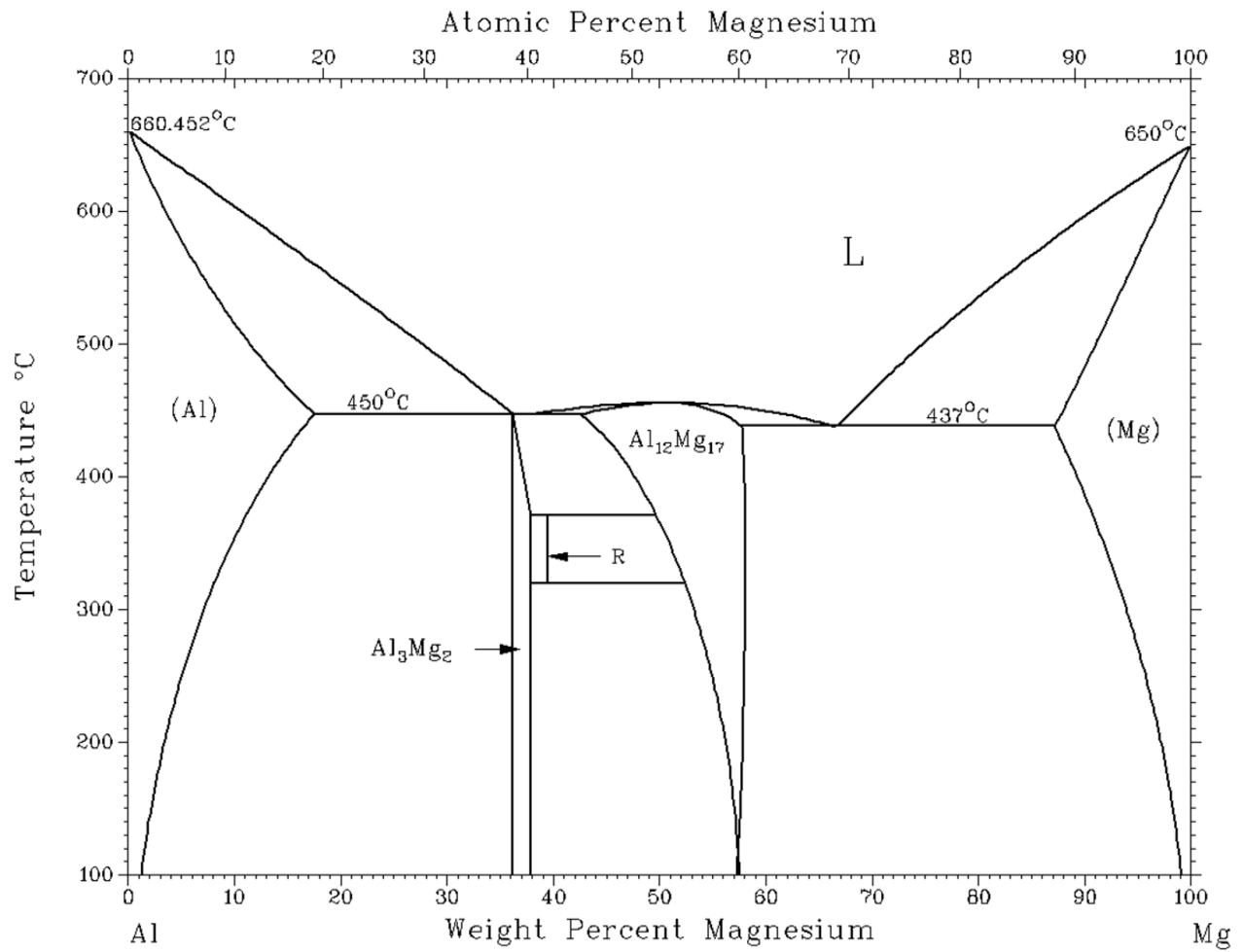


Figure AI.15 The binary Al–Mg equilibrium phase diagram [24].

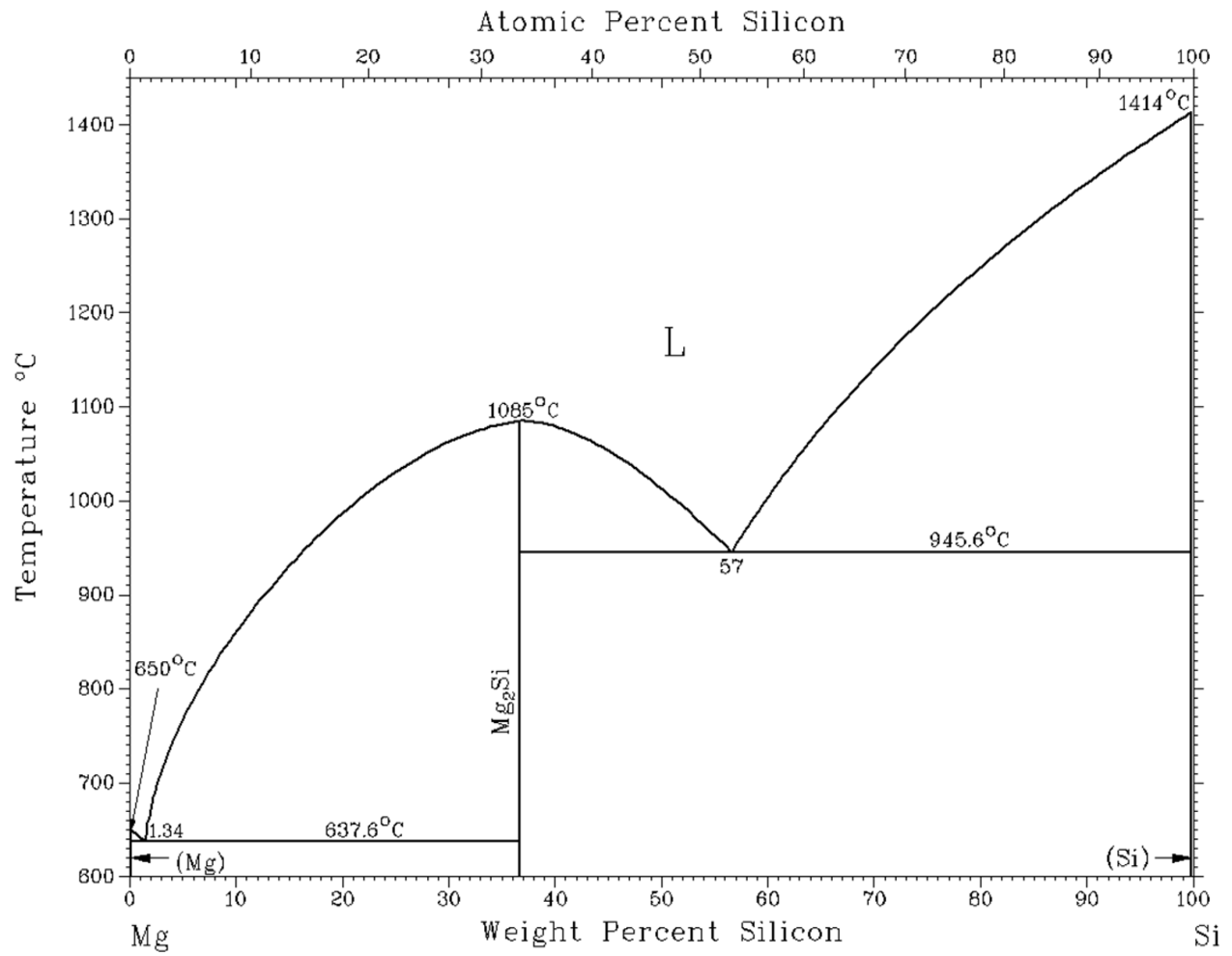


Figure A1.16 The binary Mg–Si equilibrium phase diagram [24].

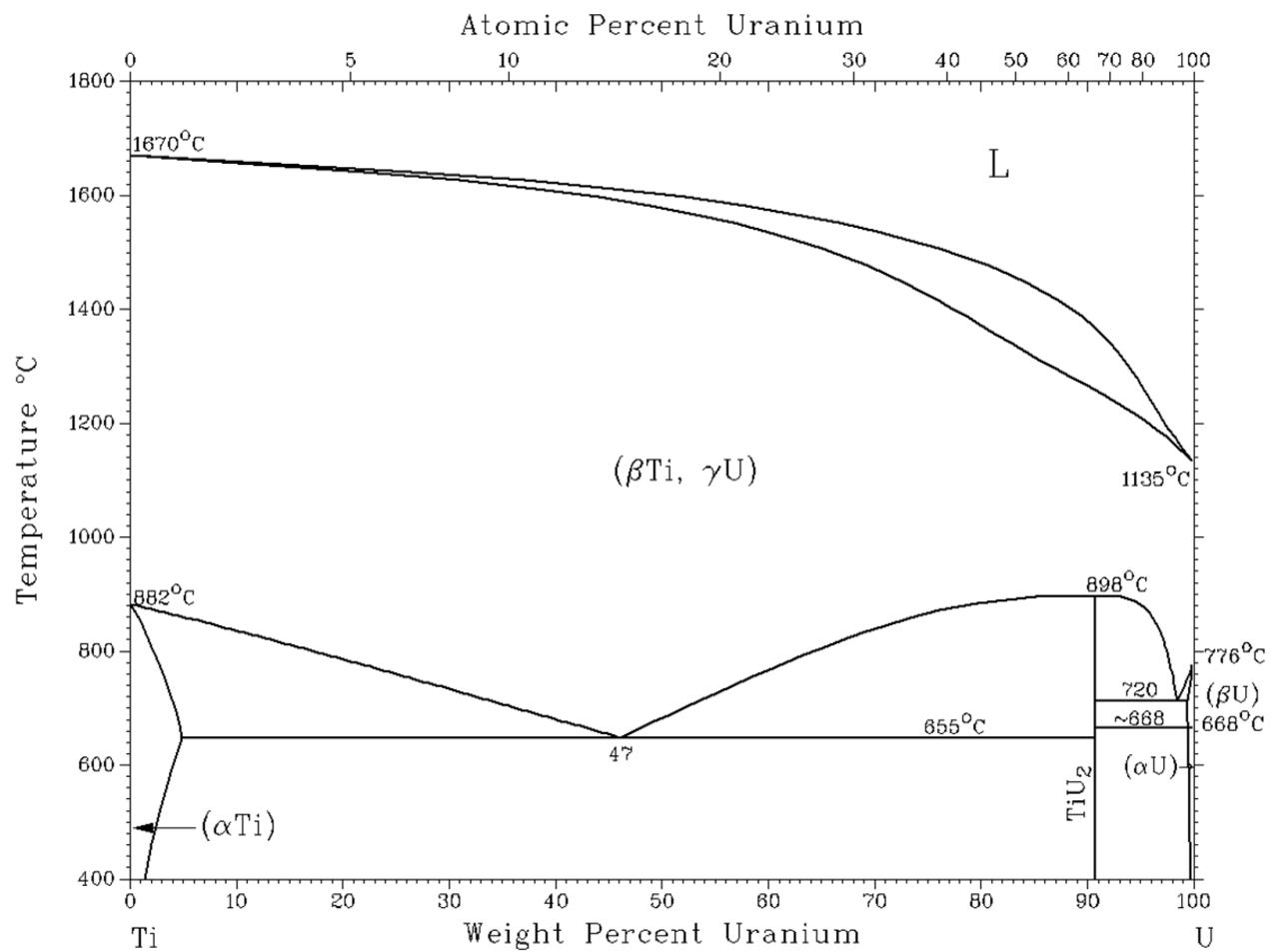


Figure AI.17 The binary Ti-U equilibrium phase diagram [24].

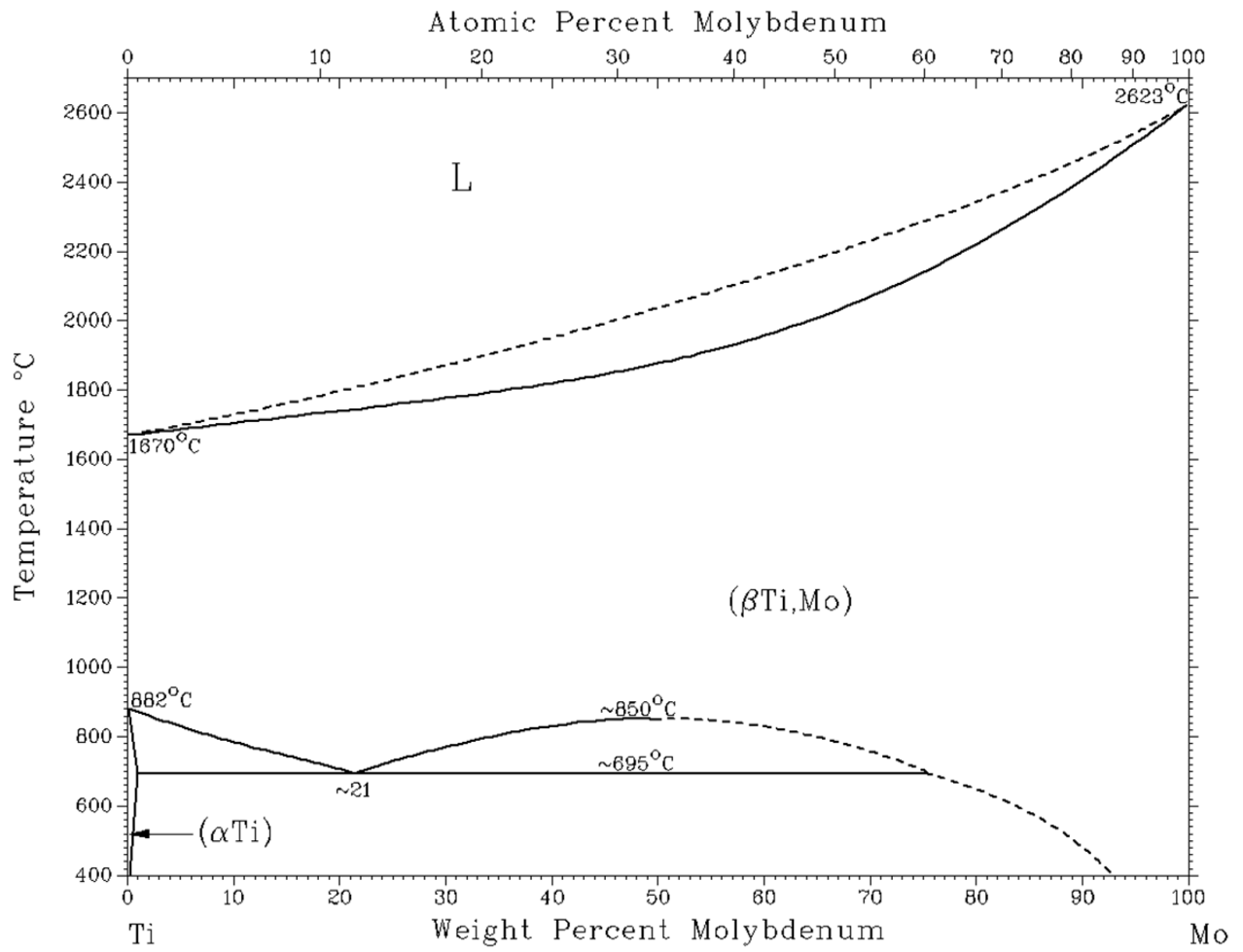


Figure A1.18 The binary Ti–Mo equilibrium phase diagram [24].

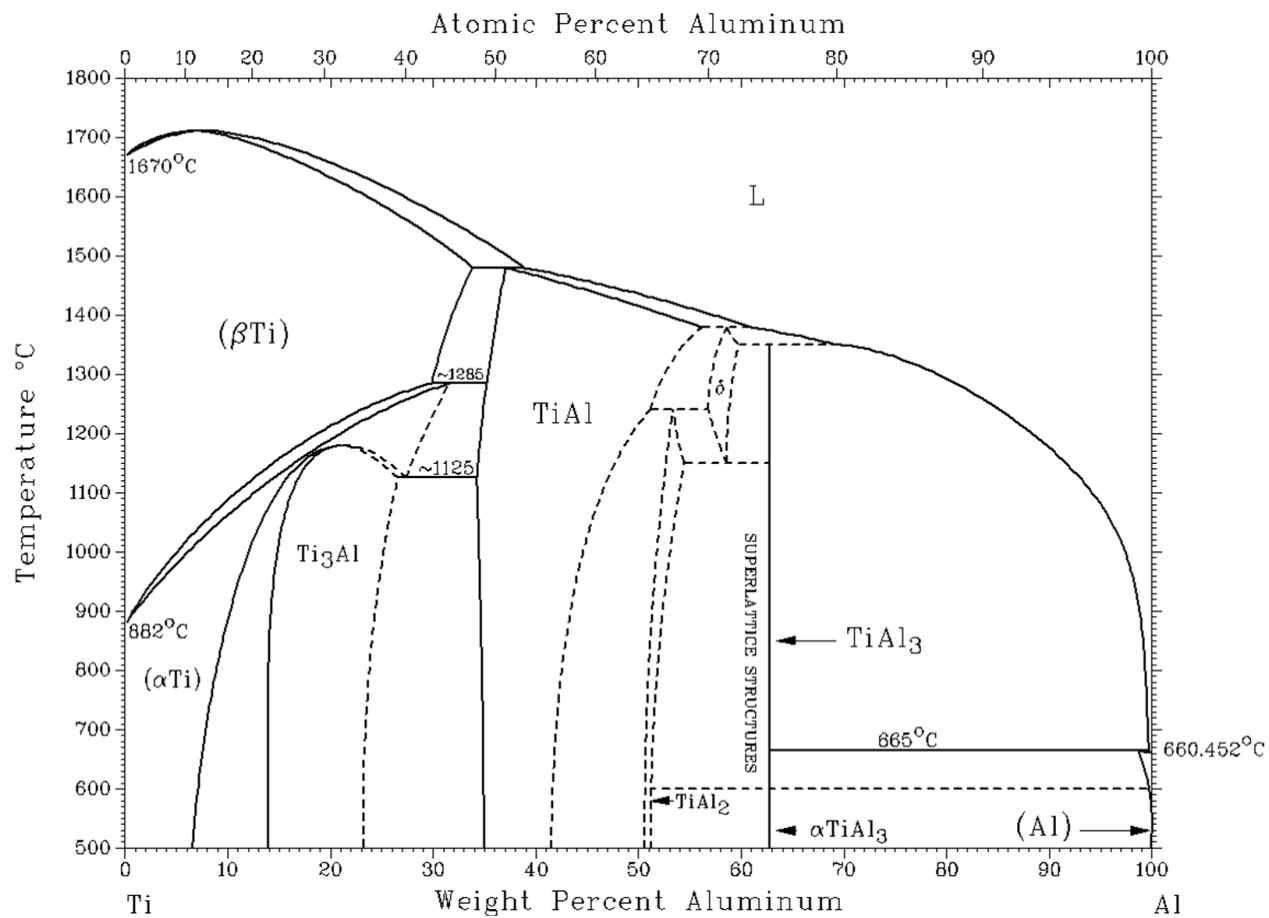


Figure A1.19 The binary Ti–Al equilibrium phase diagram [24].

Free energy (G)–Composition (X) diagrams

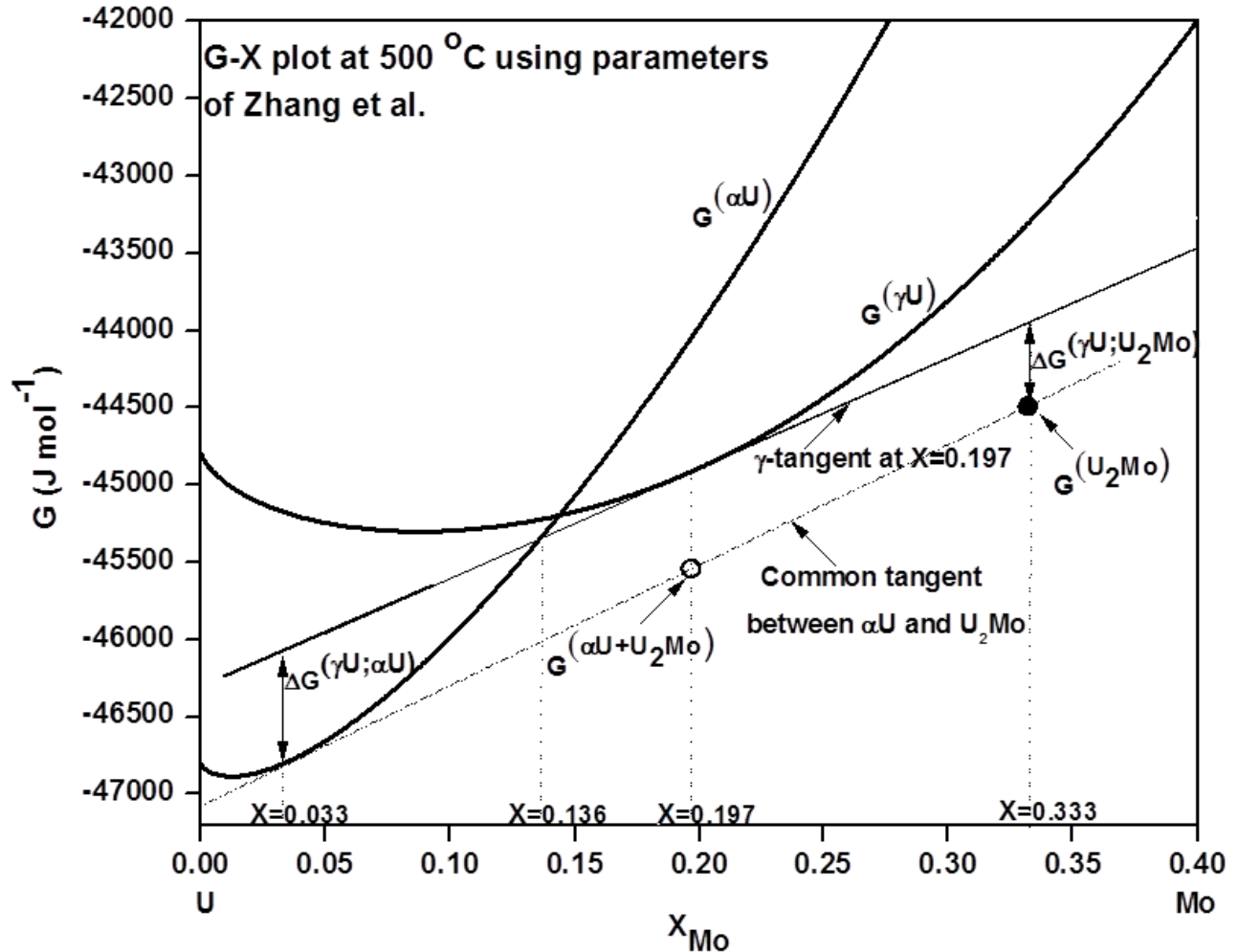


Figure AII.1 Free energy–composition diagram at 500 °C showing the variation of free energies of $\alpha\text{-U}$ and $\gamma\text{-U}$ phases as a function of Mo-content in U–Mo system constructed using the thermodynamic parameters of Zhang et al [135]. The free energy of the stoichiometric γ' (U_2Mo) phase of 33.3 at.% Mo ($G^{\text{U}_2\text{Mo}}$) is marked in the diagram by the filled circle. The free energy of the U-19.7 at.% Mo alloy existing as a mixture of $\alpha\text{-U}$ phase, of equilibrium composition, and stoichiometric γ' phase ($G^{\alpha\text{U}+\text{U}_2\text{Mo}}$) is indicated in the diagram by the open circle on the common tangent between the $\alpha\text{-U}$ and γ' phases. $X = 0.136$ (or 13.6 at.% Mo) represents the maximum Mo-content with which the $\alpha\text{-U}$ phase can nucleate.

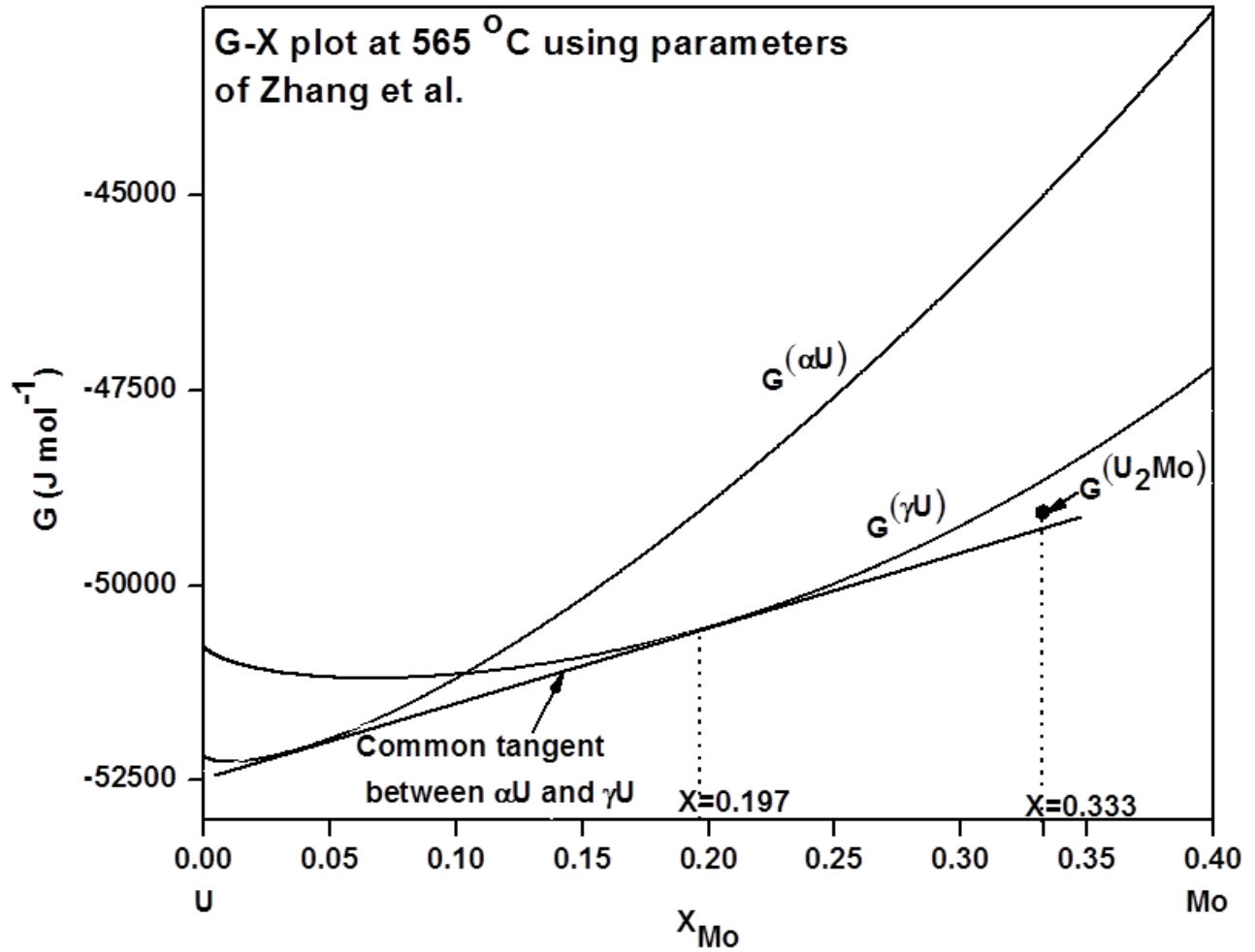


Figure AII.2 Free energy–composition diagram at 565 °C showing the variation of free energies of $\alpha\text{-U}$ and $\gamma\text{-U}$ phases as a function of Mo-content in U–Mo system constructed using the thermodynamic parameters of Zhang et al [135]. The free energy of the stoichiometric γ' (U_2Mo) phase of 33.3 at.% Mo ($G^{\text{U}_2\text{Mo}}$) is marked in the diagram by the filled circle.

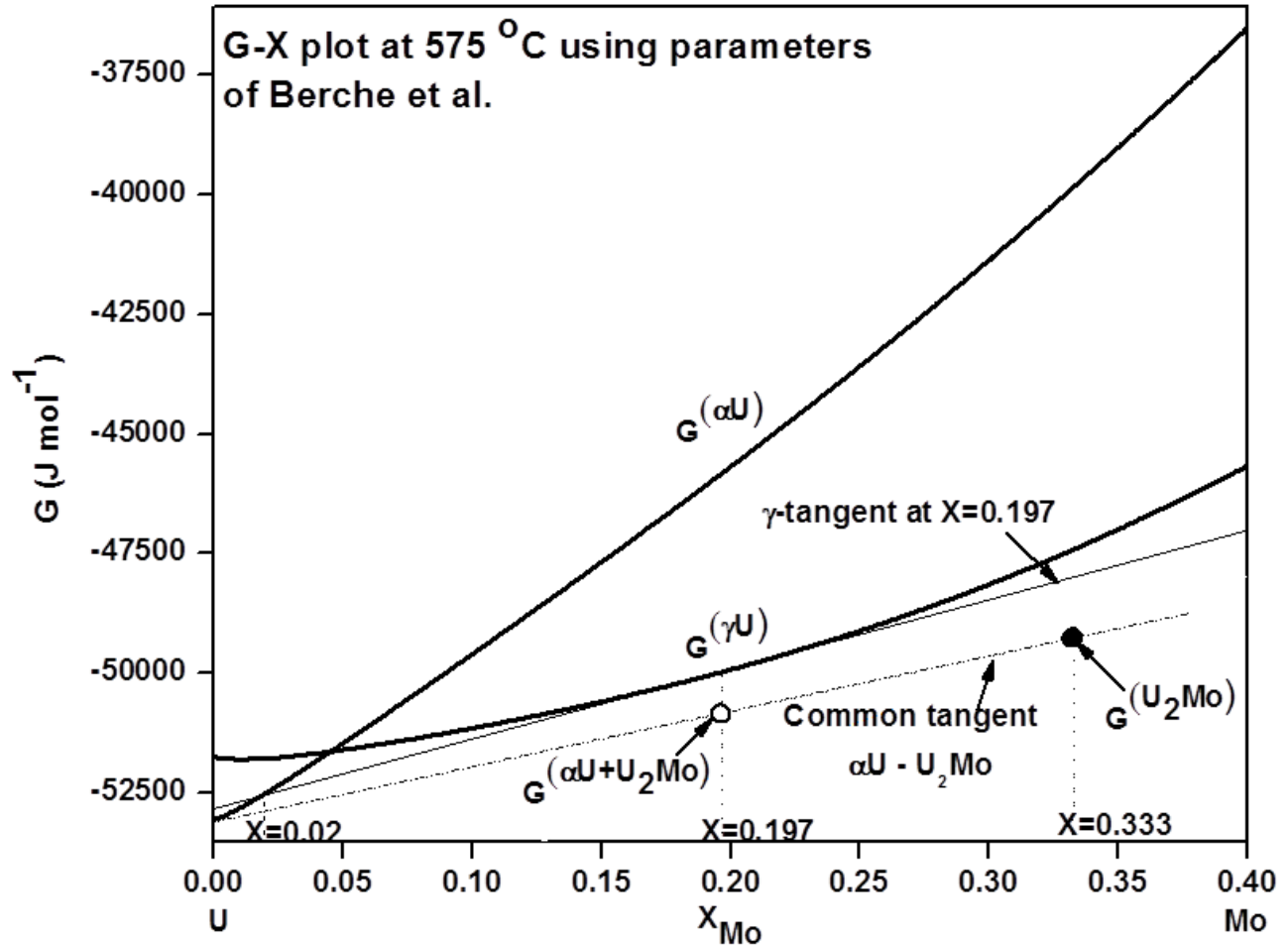


Figure AII.3 Free energy–composition diagram at 575 °C showing the variation of free energies of α -U and γ -U phases as a function of Mo-content in U–Mo system constructed using the thermodynamic parameters of Berche et al [136]. The free energy of the stoichiometric γ' (U_2Mo) phase of 33.3 at.% Mo (G^{U_2Mo}) is marked in the diagram by the filled circle. The free energy of the U-19.7 at.% Mo alloy existing as a mixture of α -U phase, of equilibrium composition, and stoichiometric γ' phase ($G^{\alpha U+U_2Mo}$) is indicated in the diagram by the open circle on the common tangent between the α -U and γ' phases. $X = 0.02$ (or 2 at.% Mo) represents the maximum Mo-content with which the α -U phase can nucleate.

Scope of further work

On the basis of the studies carried out in this dissertation, the following are a few suggestions for further work:

1. Evaluation of mechanical properties of Zr-1Nb alloy with morphologically, compositionally and transformationally evolved β -phase.
2. Examination of the effect of irradiation on Zr-1Nb alloy with morphologically, compositionally and transformationally evolved β -phase.
3. Study on discontinuous precipitation and discontinuous coarsening reactions in U-9Mo alloy in respect of decomposition of the metastable γ -phase.
4. Estimation of mechanical properties of U-9Mo/Zr-1Nb as-bonded and annealed samples.
5. Investigation on the stability of the U-9Mo/Zr-1Nb interdiffusion zone under irradiation.